

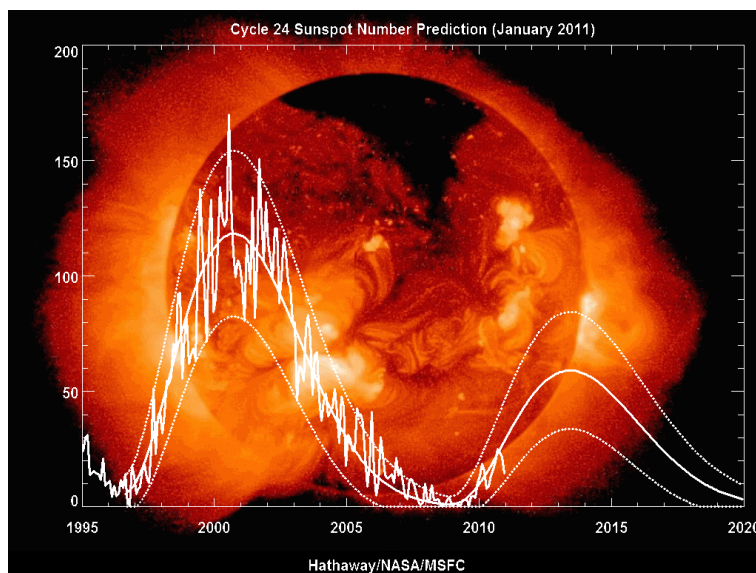
XFYS4280 Solar structure and activity

Silja Pohjolainen

Lecture Notes

Version 2.1.2

Updated Spring 2013



Course website:

<http://users.utu.fi/silpoh/xfys4280.html>

Contents

1	History of Solar Research	4
2	Solar and Stellar Structure	12
2.1	The Sun as a star	12
2.2	Energy production	14
2.3	Neutrino problem	16
2.4	Sun-like stars	17
2.5	Helioseismology	24
2.6	Solar magnetic fields	29
2.7	Hale's and Joy's laws	36
2.8	Differential rotation	37
2.9	Solar atmosphere	40
2.10	Plasma diagnostics	42
2.11	Atmospheric densities	43
2.12	Magnetic field strengths	45
3	Emission mechanisms	47
3.1	Radiation of atoms and molecules	47
3.2	Bremsstrahlung (free-free continuum emission)	52
3.3	Gyroemission	56
3.3.1	Gyrosynchrotron emission: mildly relativistic electrons	57
3.3.2	Gyrosynchrotron emission: thermal electrons	58
3.3.3	Synchrotron emission: ultrarelativistic electrons	58
3.3.4	How to distinguish between bremsstrahlung and gyrosynchrotron emission?	61
3.4	Masers	61
3.5	Absorption effects	63
3.6	Plasma emission	67
4	Radio astronomy fundamentals	71

4.1	Radio telescopes	72
4.2	Interferometers	76
4.3	Brightness temperature and flux density	78
4.4	Radiative transfer equations	83
4.5	Radio observations	86
4.5.1	Single dish antennas	87
4.5.2	Non-traditional antennas	91
4.5.3	Observed polarization	92
4.5.4	Multi-beam receivers in single dishes	94
4.5.5	Interferometers	95
4.5.6	Radio spectrometers	99
4.5.7	Solar eclipse observations using Fresnel diffraction	101
4.5.8	Burst classifications	105
5	Optical, EUV, and X-ray observations	107
5.1	Satellite orbits	107
5.2	X-ray and EUV instruments	109
5.3	Ground-based optical telescopes	119
6	Software and data archives	123
7	Shock waves in the solar corona	127
7.1	Moreton waves and EIT waves	127
7.2	Radio type II bursts	132
7.3	Solar energetic particles	137
8	Solar flares	141
8.1	Basic concepts	141
8.2	Flare models	147
8.3	Predictions for activity	152
8.4	Reconnection models	160
8.5	Accelerated particles	167
9	Coronal mass ejections	171
9.1	Basic concepts and observational constraints	171
9.2	Dimmings	178
9.3	CMEs, filaments, type IIs, and flares - all connected?	180

10 Small and large scale solar features	189
10.1 Coronal holes	189
10.2 Radio-bright coronal holes	191
10.3 Bright points	194
10.4 Plumes	196
10.5 Spicules	199
10.6 Photospheric network	199
10.7 Solar wind	201
10.8 Solar oscillations	203
10.9 Atmospheric models and coronal heating	205
11 Solar Physics in the Future	209
11.1 Instrumentation	209
11.2 Unsolved problems in solar physics	209
11.3 Solar activity	210
References and further reading	210

Chapter 1

History of Solar Research

Naked-eye observations of sunspots go back for millennia, and the first observations were done through smog or dust in order not to hurt one's eyesight. The first definite sunspot sighting was done in China in 165 BC. However, it was the invention of the telescope and Kepler's laws of planetary motion that really started solar research:

- 1610** Galileo Galilei observed dark spots on the solar surface with his telescope, and suspected them to be objects close to the surface of the solar globe. Since the Church at that time vigorously supported the idea that the sun is immaculate and blemish-free, Galileo was afraid to make his ideas public. For the next 230 years, sunspots were observed semi-regularly by several observers, but little progress was made in understanding their nature.
- 1715** The size of the solar disc was measured accurately during a solar eclipse.
- 1769** Prof. Alexander Wilson deduced that spots are depressions and the umbra of a sunspot shows the solid surface of the sun.
- 1794** Sir William Herschel reported his observations and suggested that there might be living beings inhabiting the solar interior.
- 1843** A sunspot cycle of about 10 years was discovered.
- 1851** The first photograph of a solar eclipse showed coronal structures and prominences.
- 1853** Richard Carrington, an amateur astronomer, determined solar rotation patterns.
- 1859** A solar flare was observed the first time, in white light.
- 1859** Gustav Kirchhoff found that the continuous spectrum produced by a hot solid body is transformed into a solar-like spectrum when light passes through a gas that is cooler than the solid.
- 1890s** Solar surface temperature was derived to be around 6600 K, using the newly-discovered Stefan-Boltzmann law. Researchers generally assumed that the sun is made of gas.
- 1904** The connection between geomagnetic disturbances and sunspots was discovered.
- 1908** George Hale discovered solar magnetic fields with his polarization analyser, and found that sunspots have a bipolar character.

- 1926** A hydrodynamic model was developed to explain solar magnetic fields. It was later refined to a magnetohydrodynamic model.
- 1930s** Speculation arose that the sun's energy source is nuclear. In 1939 it was proposed that the energy comes from the fusion of four hydrogen atoms.
- 1942** Solar radio emission was observed by the British Army radar operators.
- 1946** The intensity of the steady component of the solar radio emission, at different wavelengths, was explained by a 10 000 degree solar chromosphere (emitting at short wavelengths) and a million-degree solar corona (emitting at long wavelengths). It was predicted that the extremely hot solar corona would also emit in X-rays.
- 1949** Solar X-ray emission was observed during a rocket flight.
- 1958** It is proposed that the generator of solar magnetic fields is a dynamo, working inside the sun.
- 1958** The existence of a solar wind was predicted, and it was first observed a few years later.
- 1960** Solar oscillations were observed. The most typical period is 5 minutes, although many other periods exist as well. Seismic activity, with pressure modes and gravity modes, was suggested to be the explanation.
- 1960** Propagating shock fronts were observed on the solar disk in association with flare eruptions. These chromospheric signatures were later named Moreton waves, and they were explained as blast waves created in the flare processes.
- 1961** The 11-year sunspot cycle was explained to be a 22-year magnetic cycle. The model developed by Horace Babcock also explained the observed differential (non-uniform) solar rotation.
- 1964** The neutrino problem was discovered: there are less detected neutrinos than predicted by stellar models. Was this an observational problem or were the models based on fusion completely wrong?
- 1966** The first models where solar flares are explained to be the result of magnetic reconnection were developed.
- 1972** Solar gamma-ray emission was first observed.
- 1981** A detailed model of the solar atmosphere was published.
- 1981** Nano-flares were detected with new sensitive instruments and they were proposed to be the cause of coronal heating. It was later calculated that the total energy released in nano-flares is not sufficient to heat the corona, but people still searched for even smaller events (piko-flares etc.) that might go undetected because of the limits in instrument sensitivity.
- 1980's** MHD (magnetohydrodynamic) models were developed to explain coronal heating.
- 1989** An intense solar flare caused geomagnetic storms that disrupted electric power transmission in Canada and put 6 million people without electricity for 9 hours. The term "space weather" was invented, to understand and predict how and when solar eruptions occur.

1994-95 The equatorial slow-speed solar wind and the fast polar region wind were detected in satellite observations. Large-scale polar coronal holes were also observed at that time.

1999 “EIT-waves” were discovered in EUV satellite observations. It was soon discovered that they were different from the earlier-observed Moreton waves, but it was still unclear if EIT waves were associated with flares or coronal mass ejections (CMEs), or both. Shock waves became a hot topic in solar physics.

2001 The neutrino-problem was resolved: not all neutrinos can be detected as they can oscillate and change their type on their way from the sun’s interior to the earth.

2001 Sunspots on the backside of the sun were observed with holography techniques.

Solar physics entered a new era with the launch of the first spin-stabilized solar satellite in 1962 (Orbiting Solar Observatory, OSO-1). Its objective was to measure the solar electromagnetic radiation in the UV, X-ray, and gamma-ray regions. The solar observatory onboard the U.S. space station Skylab (launched in 1973), took the first full-disk X-ray images of the sun.

The GOES satellites (the first GOES-1 launched in 1975; latest GOES-13 launched in 2006) are a key element in United States’ National Weather Service operations and they provide, for example, continuous observations of the solar X-ray flux. SMM (1980-1989) ja CGRO (1991-2000) provided solar data especially in hard X-rays and gamma-rays. The Japanese solar satellite Yohkoh (1991 – 2001) combined high-resolution soft and hard X-ray imaging with spectral information, and the satellite was operational for a decade.

SOHO was launched in 1995, and with its 12 different instruments it remains the largest and most expensive solar satellite so far. TRACE (1998-) is a Small Explorer (SMEX) mission, to image the solar corona and transition region at high angular and temporal resolution, mainly in EUV. Another SMEX mission, RHESSI (2002-), is the first instrument that can image solar flares in gamma-rays. The Japanese Hinode (launched in 2006) is carrying three advanced solar telescopes: one to observe solar magnetic fields with 0.2 arc sec resolution, one to image in X-rays with a resolution three times as high as Yohkoh, and one to get imaging and spectral information in EUV with a sensitivity ten times as high as SOHO. The imaging instruments of the Solar Dynamics Observatory (launched in 2010) have better spatial resolution and far better image cadence compared to SOHO, but otherwise similar performance. Solar Orbiter (launch scheduled around 2015 or later) will be one of the main future solar missions.

Although the solar cycle shows periods of low activity, the Sun is never really “quiet”. Magnetic activity and plasma flows create structures and features that can be considered signs of activity at all times, e.g., sunspots and active regions, surges, plages, plumes, spicula, facula, moss and crinkles, bright points, radio brightenings, filaments, prominences, coronal holes, and solar wind. During activity maximum, spectacular large-scale features like flares, coronal mass ejections, filament eruptions, shock waves (Moreton waves, EIT-waves, SXT waves, etc.) and dimmings (EIT, SXT, radio, etc.) may appear daily.

Chapters 1 – 6 of these lecture notes give the basics of the structure of our nearest star, explain the radiation mechanisms that can be present, and describe the instruments that can be used in the observations. In Chapters 7 – 10 some of the observed features are discussed in more detail.

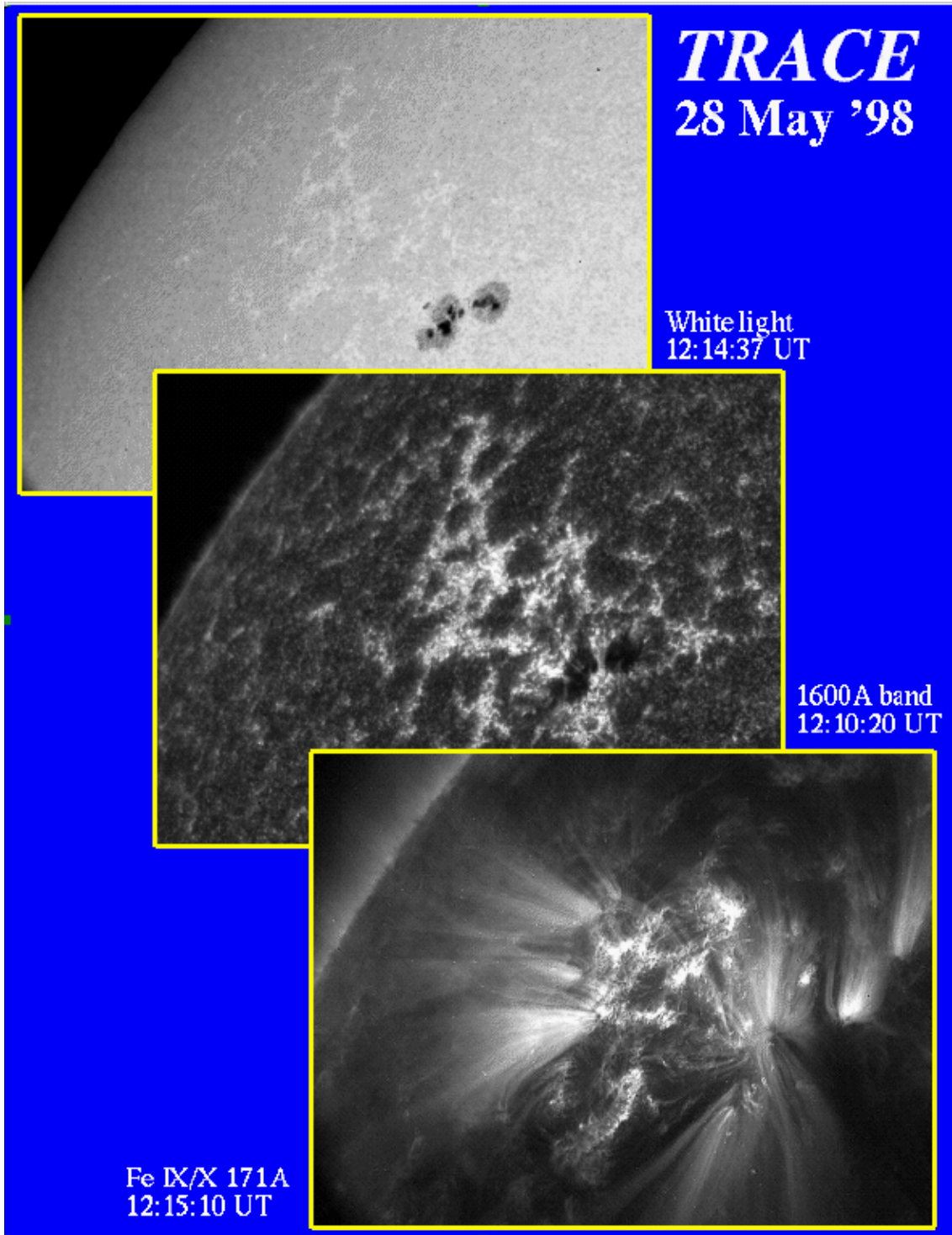


Figure 1.1: Solar features observed at three different wavelengths, at three different heights and temperatures: solar photosphere in white light (temperature 4000–6000 K), chromosphere at 1600 Å (4000–10 000 K), and corona in the Fe IX/X iron line temperature (160 000 – 2 million K). Sunspots are best observed at photospheric level, dark *umbra* in the middle and lighter *penumbra* surrounding it. Chromospheric images show fine structures and features connected with the magnetic network. In the corona magnetic loops are visible due to hot plasma flows. (TRACE satellite images)

DAILY SUNSPOT AREA AVERAGED OVER INDIVIDUAL SOLAR ROTATIONS

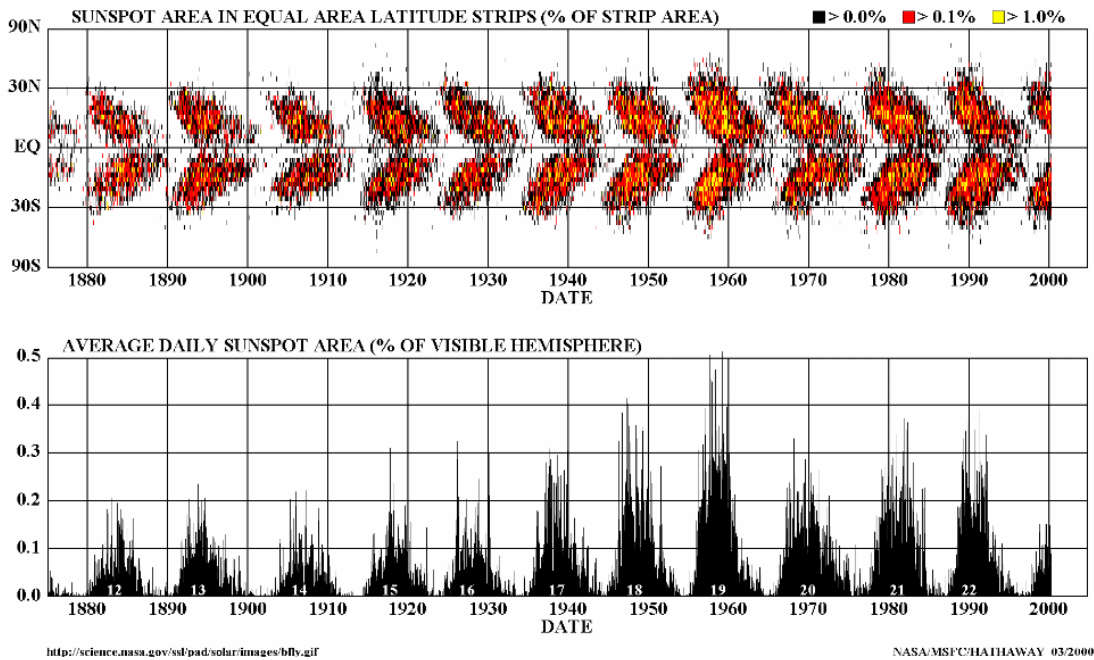


Figure 1.2: Sunspot cycles have been observed since the 1650's. The average length of one cycle is about 11 years. However, the length has been observed to vary between 9 and 14 years. 'New' sunspots, at the beginning of each cycle, are observed first at high solar latitudes. As the cycle progresses, sunspots appear closer to the solar equator. This is usually illustrated with a *butterfly diagram*. The number of sunspots and the total area covered by sunspots also show a similar cycle.

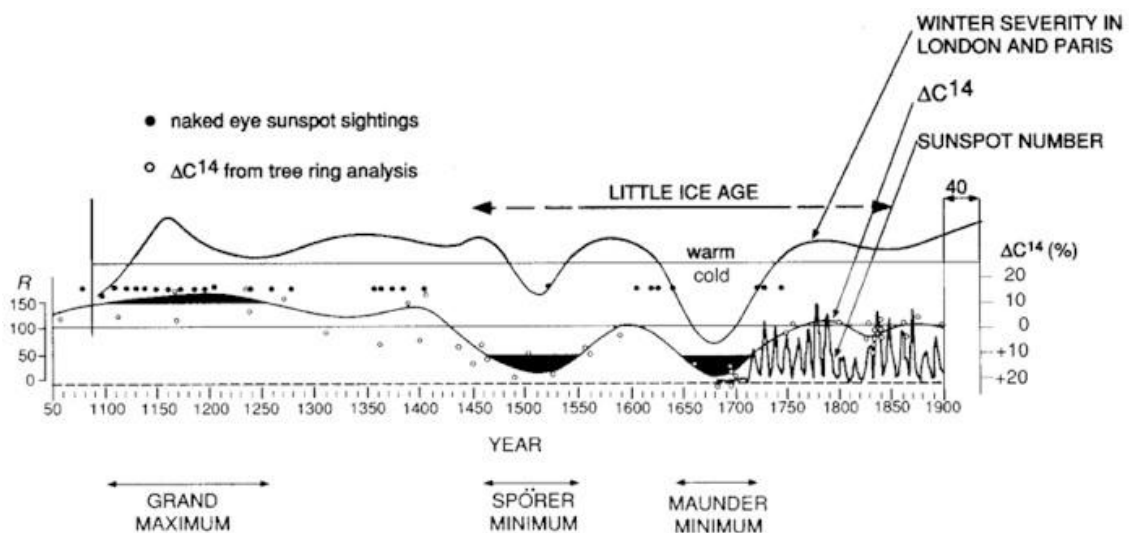


Figure 1.3: Sunspot cycles have shown so-called grand minimums, when sunspots numbers have been very low. The best-known is the Maunder minimum (1645 – 1715) which co-incided with a lengthy cold spell, 'the Little Ice Age'. Radio-carbon record from tree-ring samples show an increased amount of ^{14}C isotope during that time. It is believed that during low solar activity the impact of cosmic radiation increases (the 'shield' of sun-earth connection is missing).

Solar Cycle Variations

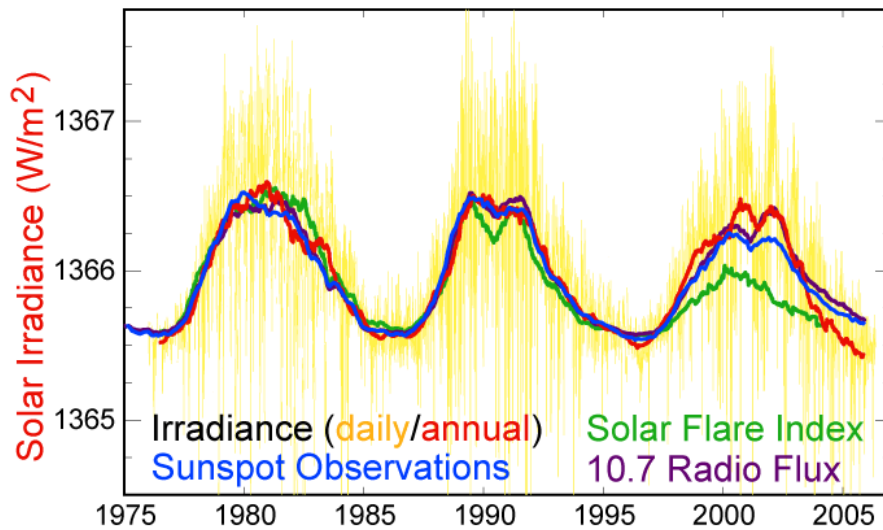


Figure 1.4: Solar activity can be monitored several different ways. In addition to daily sunspot numbers, solar irradiance, number of solar flares, and changes in the radio flux density at microwaves reflect the 11 year activity cycle. The so-called 'solar constant' is 1.37 kW/m^2 on average, but the cycle variation is visible also here. The 'constant' describes the solar radiation that falls on an area above the atmosphere at a vertical angle; on earth it varies with the time of day and year as well as with the latitude and weather. (Image courtesy of Wikipedia, Robert A. Rohde, Global Warming Art project)

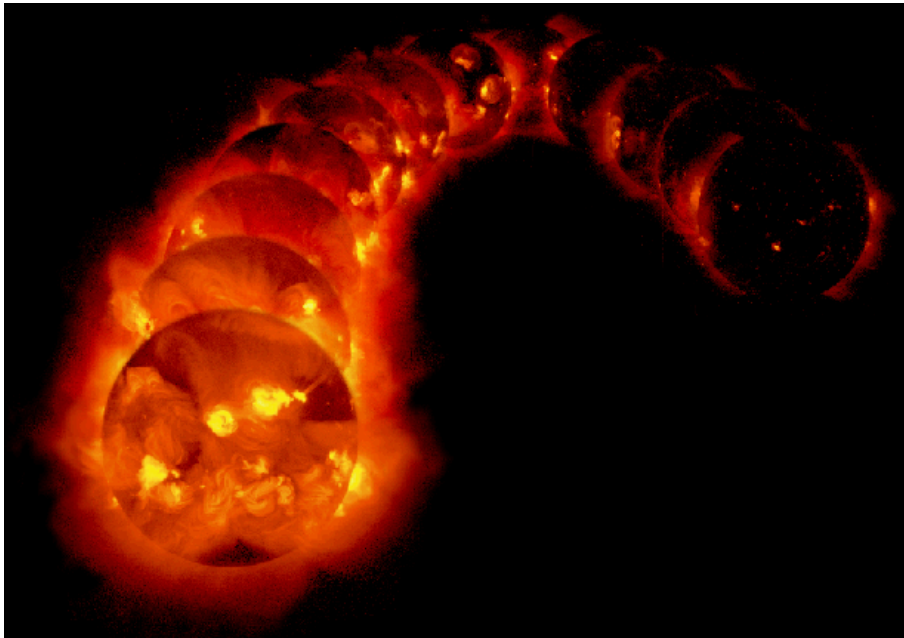


Figure 1.5: The changes in solar activity are well-observed also in soft X-ray images. During activity minimum, only a few bright points and some simple, isolated active regions are visible. During activity maximum the sun is covered with complex, multipolar active regions, and plasma flows along large-scale loops make the sun appear bright also high in the solar corona. (Image courtesy of Yohkoh SXT)

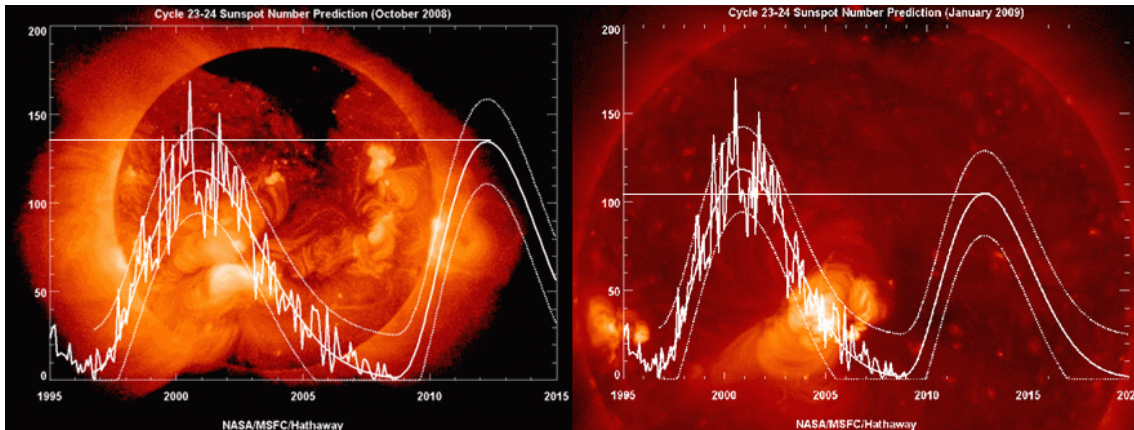


Figure 1.6: Solar cycle predictions by NASA’s David Hathaway, in October 2008 and updated in January 2009. For the new solar cycle 24, the prediction for the number of sunspots has gone down quite a lot: Hathaway’s predicted maximum in March 2006 was 145, in October 2008 it was 137, and in January 2009 it was 104. Also, the start of the new cycle was delayed. (image courtesy of <http://www.klimadebat.dk/forum/attachments/>).

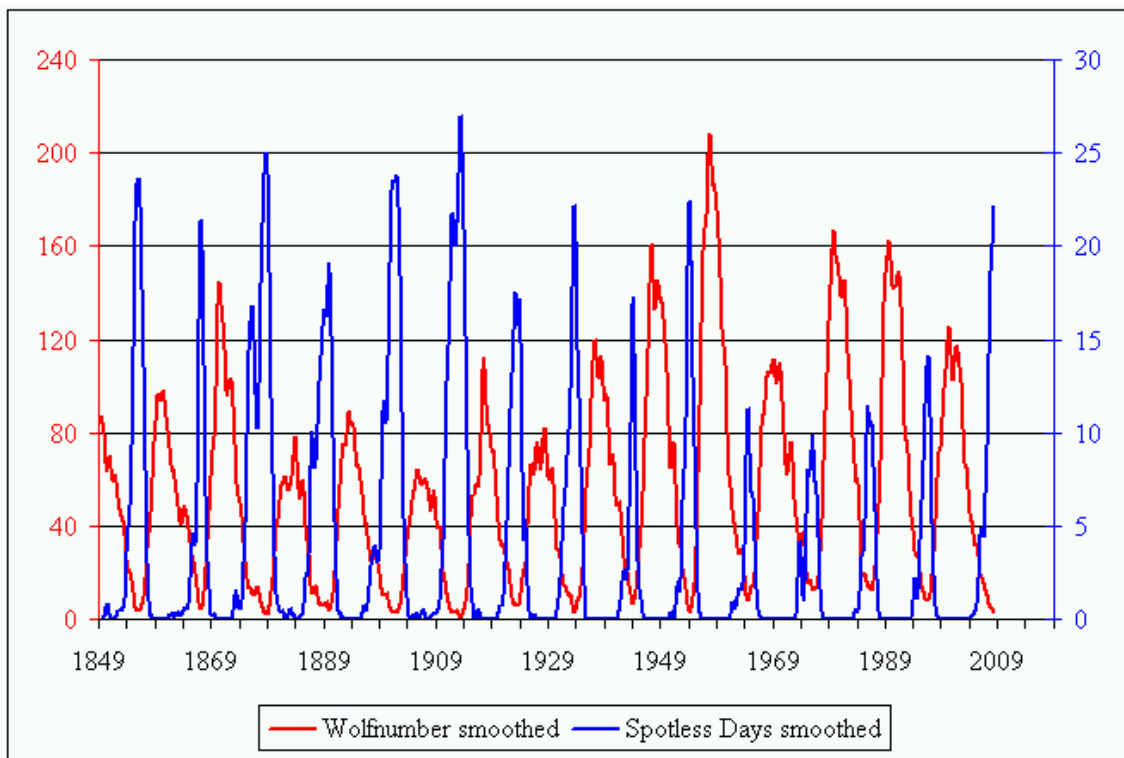


Figure 1.7: The graph shows the smoothed monthly Wolf number (red) and smoothed monthly number of spotless days (blue) since 1849. The current Wolf number is already at 2,9 and still decreasing, implying high smoothed number of spotless days of around 25. This is comparable with the low activity transits in the early 20th-century, and certainly contrasts with the previous 4 cycle transits. (Image and text courtesy of Solaemon’s Spotless Days Page, at <http://users.telenet.be/j.janssens/Spotless/Spotless.html>)

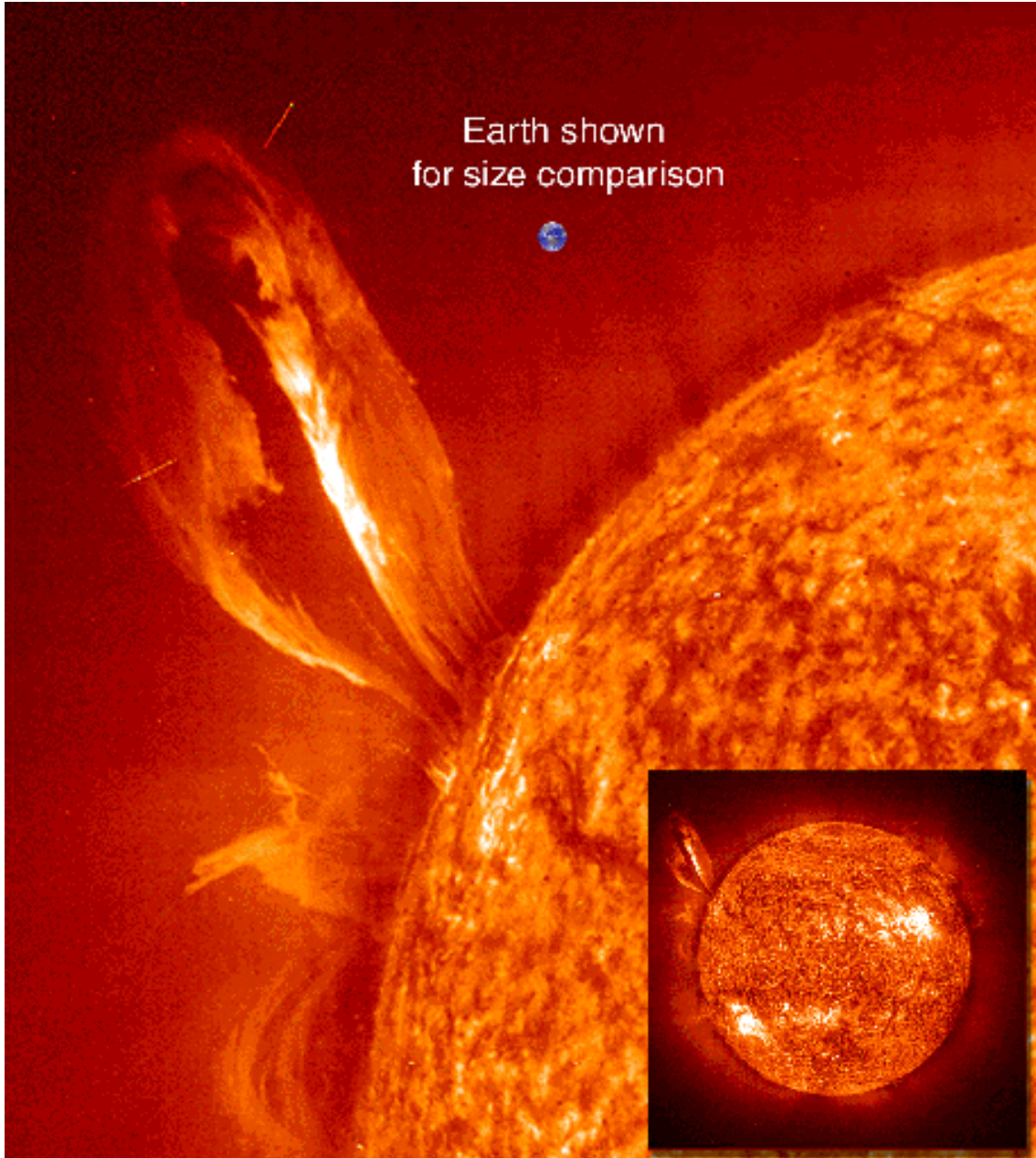


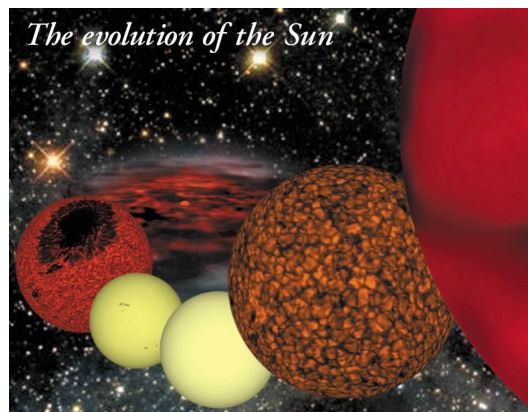
Figure 1.8: SOHO EIT image at He II (304 \AA) wavelength, showing a large loop-like prominence located over the solar limb. The temperature range in this EUV image is approximately $60\,000\text{--}80\,000 \text{ K}$. The spatial resolution of EIT is 2.6 arc sec ; one arc sec on the sun corresponds to about 700 km .

Chapter 2

Solar and Stellar Structure

2.1 The Sun as a star

All stars in our galaxy have been formed from clouds of gas and dust. Eventually, gravity causes the clouds to collapse, and since the clouds are spinning, centrifugal forces result in accretion disks. The material that concentrates into the disk centers forms new stars. While the stars continue to grow, lumps form in the disks which will ultimately become planets. The disks become thinner as more material falls onto the stars and the protoplanets.



Our sun was formed some 4.5 billion (american) / 4.5 milliard (british) years ago. The first tens of millions of years, the sun was extremely magnetically active. Gigantic starspots covered its surface, at times even in its polar regions. Then, the sun settled into a long stable life as a common, yellow star (spectral class G2V; G2 means that it has a surface temperature of approximately 5780 K). In the next 6.5 billion/milliard years, the activity continues to subside, and the sun will slightly increase in size and brightness. Then it will run out of the hydrogen that fuels the fusion reactor in its core. For a while it will find new ways of nuclear fusion, as it swells up to an orange giant. Because surface gravity weakens as the star grows, the convective bubbles (that span only approximately 1000 km on the present sun) will become much larger. Within the following few million years, the sun will grow into a huge red giant, one hundred times its present size. In that phase, only a handful of huge convection cells will cover its surface, that will be undulating by millions of miles as the convective flows evolve; the Sun will generally look oddly distorted from the average spherical state shown on the front. This brief phase heralds the end of the earth, which will be cooked in

the intense radiation, and most likely be engulfed by our star. After that, the sun will shrink to a size only somewhat larger than the earth, and eventually slowly fade out. (The evolution of the Sun, image and slightly edited text are from Karel Schrijver's Cool Star Homepage at <http://www.lmsal.com/schryver/Public/homepage/coolstarimages.html>).

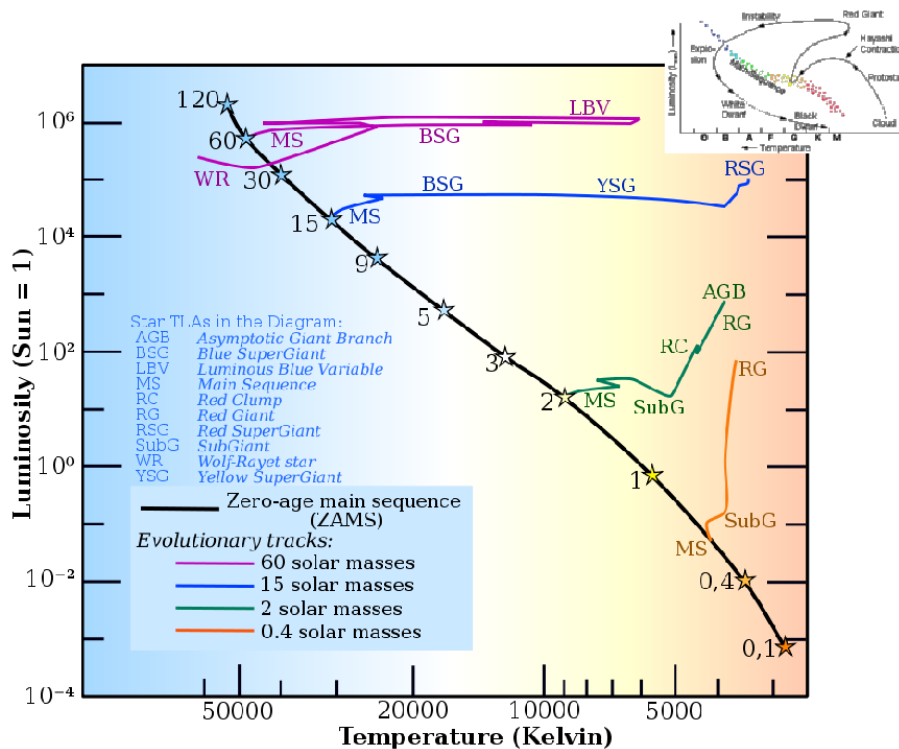
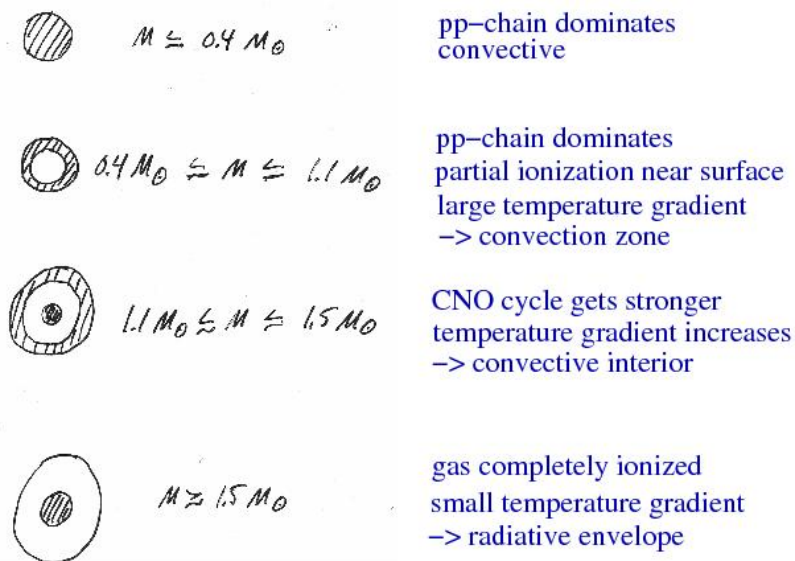


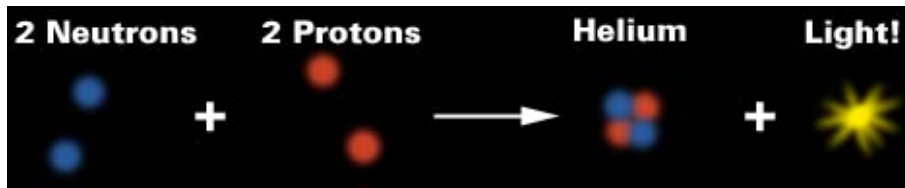
Figure 2.1: Stellar evolution (H-R diagram by Rursus, Wikimedia Commons; insert solar track image from Gene Smith's Astronomy Tutorial)



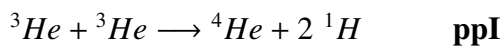
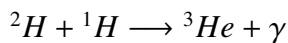
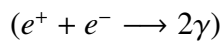
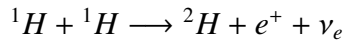
The End: if $M < 3 M_{\text{sun}}$ \rightarrow white dwarf

Figure 2.2: Stellar structure during the main sequence, for stars with different masses.

2.2 Energy production



The proton-proton chain reaction (pp-chain) goes as follows:



The pp-chain is one of several fusion reactions by which stars convert hydrogen to helium. The first step involves the fusion of two hydrogen nuclei into deuterium, releasing a positron and a neutrino. The positron immediately annihilates with an electron, and their mass energy is carried off by two gamma ray photons. The deuterium produced in the first stage can then fuse with another hydrogen nuclei, to produce an isotope of helium, ${}^3\text{He}$. From here there are three possible ways to generate ${}^4\text{He}$, but the ppI chain is the most probable process in the Sun: the ${}^4\text{He}$ is created from fusing two of the ${}^3\text{He}$ that were produced in earlier processes. The ppI branch is dominant at temperatures of 10–14 MK. The temperature at the center of the sun is approximately 15 MK, and about 90% of the sun's energy production is from the ppI branch.

Comparing the mass of the final helium-4 atom with the masses of the four protons reveals that 0.7% of the mass of the original protons has been lost. This mass is converted into energy, in the form of gamma rays and neutrinos released during each of the individual reactions. The total energy we get in one whole pp-chain is 26.7 MeV.

We can write the difference in atomic mass units (AMU) as

$$4 \times M_H \approx 4 \times 1.0075 \text{ AMU} = 4.0300 \text{ AMU},$$

$$M_{He} \approx 4.0013 \text{ AMU} \implies \Delta M = 0.0287 \text{ AMU}$$

$$\Delta E = \Delta M c^2 = 0.0287 \times 1.6604 \times 10^{-27} \text{ kg} \times (2.99 \times 10^8 \text{ m/s})^2 \approx 4.283 \times 10^{-12} \text{ J}$$

To keep the sun's present luminosity L_\odot we need

$$\frac{L_\odot}{\Delta E} \approx \frac{3.8 \times 10^{26} \text{ W}}{4.283 \times 10^{-12} \text{ J}} \approx 0.89 \times 10^{38} \text{ reactions/s} \quad (2.1)$$

One reaction uses four hydrogen nuclei: $4 \times 0.89 \times 10^{38} \approx 3.6 \times 10^{38}$ atoms/s

$$N_H \approx \frac{M_\odot}{m_H} \approx \frac{1.989 \times 10^{30} \text{ kg}}{1.6734 \times 10^{-27} \text{ kg/atom}} \approx 1.2 \times 10^{57} \text{ atoms} \quad (2.2)$$

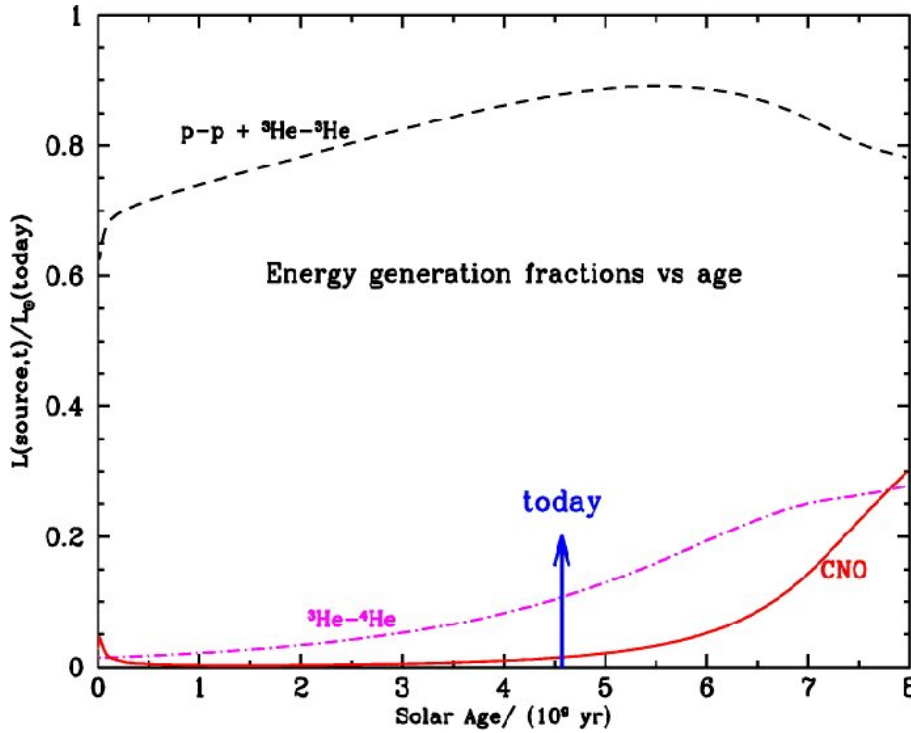


Figure 2.3: Fraction in the standard model of the solar luminosity produced by different nuclear fusion reactions vs. solar age. The luminosity generated by the p-p nuclear fusion branch that is terminated by the ${}^3\text{He}-{}^3\text{He}$ reaction is marked by a dashed curve in the figure, and the luminosity produced by the p-p branches that proceed through the ${}^3\text{He}-{}^4\text{He}$ reaction is denoted by a dot-dashed curve. The luminosity generation by the CNO cycle is indicated by a solid line. The unit of luminosity is the present-day total solar luminosity. At the present epoch, the p-p + ${}^3\text{He}-{}^3\text{He}$ reactions produce 87.8% of the solar luminosity and the branches terminating through the ${}^3\text{He}-{}^4\text{He}$ reaction generate 10.7% of the solar luminosity. The CNO cycle produces 1.5% of the present-epoch luminosity. (From Bahcall et al. ApJ 555, 990, 2001).

The sun could then be using its hydrogen supplies for

$$t_{max} \approx \frac{1.2 \times 10^{57}}{3.6 \times 10^{38}} \text{ s} \approx 10^{11} \text{ years.} \quad (2.3)$$

But, we believe that only 70% of the original solar mass was hydrogen, and only 10% of that hydrogen is usable in nuclear reactions. Hence, only about 0.7% of the total mass is converted into energy. For a main sequence star, we can use the timescale for nuclear reactions,

$$\tau_n = \frac{0.007 \times 0.1 M c^2}{L}. \quad (2.4)$$

For the sun, the timescale $\tau_n \approx 10^{10}$ years. The sun is estimated to be now about $4.5 - 4.6 \times 10^9$ years old. For more massive stars, that also have much higher luminosity, the timescale is much shorter.

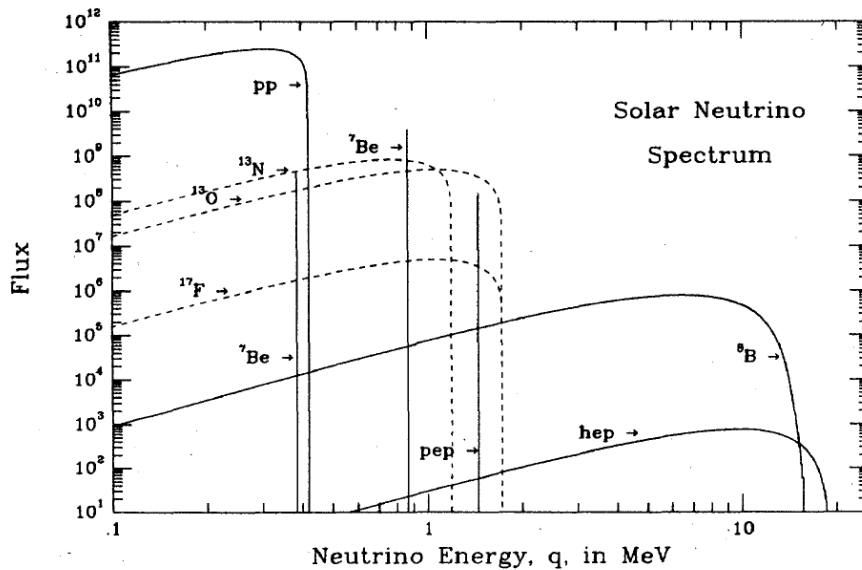


Figure 2.4: The energy spectrum and flux of solar neutrinos which should be received at earth according to the standard solar model of Bahcall and Ulrich. It can be seen that the neutrinos from ${}^7\text{B}$ and $p e^- p$ have discrete energies and the others have continuous distribution. The majority of high-energy neutrinos are released by decay of ${}^8\text{B}$ (From Bahcall and Ulrich, Rev. Modern Phys. 60, 297, 1988).

2.3 Neutrino problem

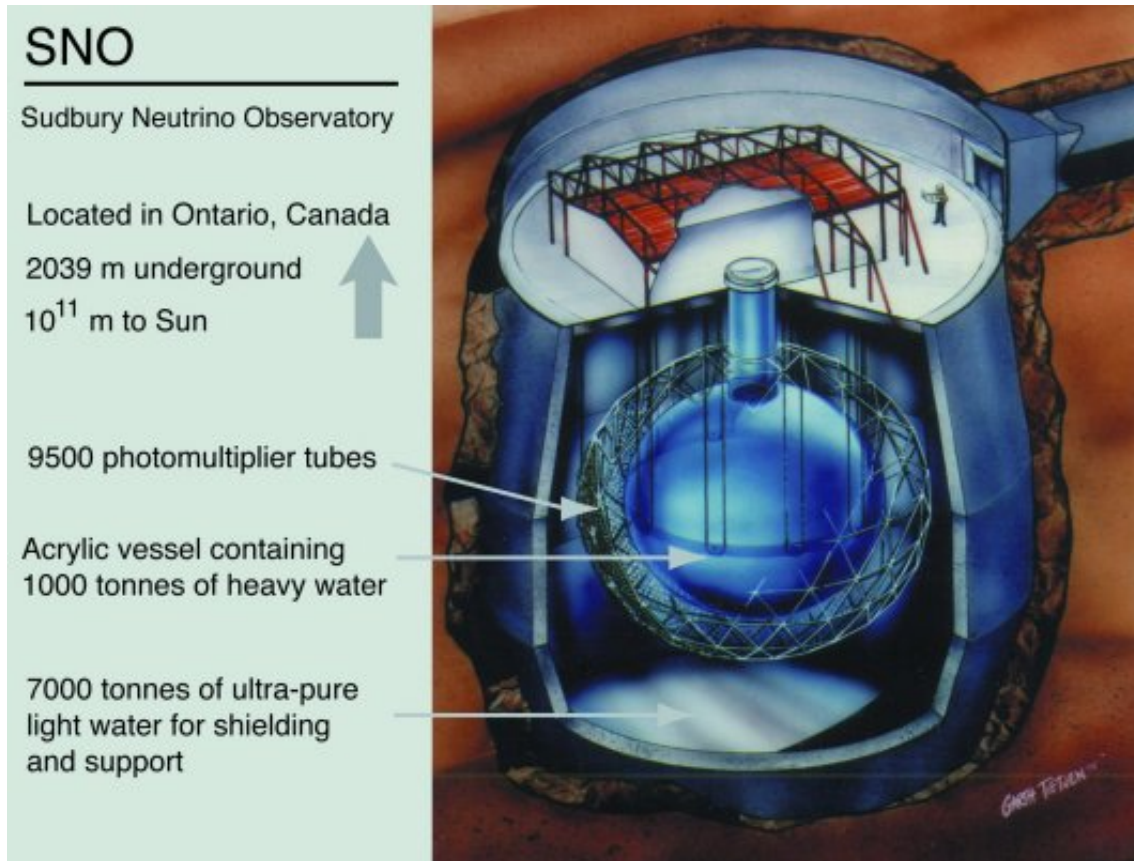
The neutrinos emitted in the first reaction of the pp-chain can have energy values between zero and 0.42 MeV. The decay of ${}^8\text{B}$ can produce neutrinos with a maximum energy of about 15 MeV. All neutrinos interact weakly with matter, but the probability of absorption increases with energy. Despite the large value of mean free path, we should observe neutrinos (when they interact with matter at earth) because there are so many of them. There should be something like $10^{15} \text{ m}^{-2} \text{ s}^{-1}$ reaching the earth. A neutrino detector should then observe about one per month per cubic meter of the detector.

Neutrino detections are measured in solar neutrino unit, SNU, which is equal to 10^{-36} captures per target atom per second. The original theoretical detection rate was estimated to be about 30 SNU (Bahcall, 1966), but in the 1990s this value was lowered to 8–6 SNU. The experimental result is about 2 SNU. So, is the standard solar model wrong, or are neutrinos behaving oddly?

The news in June 2001 stated: the neutrino problem has been solved!

According to the standard model of particle physics, there are three different kinds of neutrinos: electron neutrinos, muon neutrinos, and tau neutrinos. Already in late 1960s it had been proposed that if neutrinos had mass, then they could change from one type to another. Neutrino oscillation means that the probability of measuring a particular flavour for a neutrino varies periodically as it propagates. The first strong evidence for neutrino oscillation came in 1998 from the Super-Kamiokande collaboration in Japan, which produced observations consistent with muon-neutrinos (produced in the upper atmosphere by cosmic rays) changing into tau-neutrinos. More evidence came in 2001 from the Sudbury Neutrino Observatory (SNO), when it detected all types of neutrinos coming from the sun and was able to distinguish between

electron-neutrinos and the other two flavors. Statistical analysis showed that about 35% of the arriving solar neutrinos were electron-neutrinos and the others muon or tau neutrinos. The total number of detected neutrinos agreed quite well with the earlier predictions from nuclear physics, based on the fusion reactions inside the sun. At energies above 5 MeV, solar neutrino oscillation actually takes place in the sun. So, the standard solar model was not wrong, although we still do not know the composition and processes inside the sun nor the behavior of traveling neutrinos in detail.



SNO was a heavy-water Cherenkov detector designed to detect neutrinos produced by fusion reactions in the sun. It used 1000 tonnes of heavy water loaned from Atomic Energy of Canada Limited (AECL), and contained by a 12 meter diameter acrylic vessel. Neutrinos reacted with the heavy water (D_2O) to produce flashes of light called Cherenkov radiation. This light was then detected by an array of 9600 photomultiplier tubes mounted on a geodesic support structure surrounding the heavy water vessel. The detector was immersed in light (normal) water within a 30 meter barrel-shaped cavity. Located in the deepest part of the mine, the overburden of rock shielded the detector from cosmic rays. (More details in http://nobelprize.org/nobel_prizes/physics/articles/bahcall/)

2.4 Sun-like stars

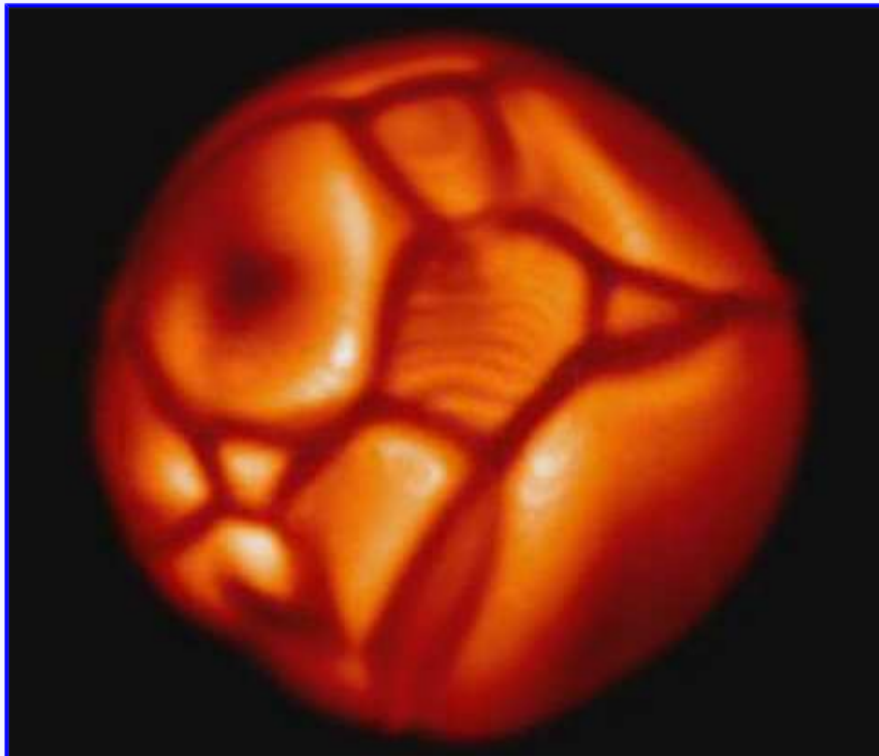
The results from solar physics have been used also in stellar physics. We know that stars may have 'starspots', similar to sunspots, and stellar flares, similar to solar eruptions. Hot coronae and stellar winds much like the solar wind have been predicted, although not observed yet.

The information we have of stellar objects is based on interpretations from light curves, eclipses, Doppler effects, and simulations, since the other stars are too far away to be imaged in detail. Therefore our knowledge on solar processes helps to reveal the structure and behaviour of stars in general.

Astronomy Picture of the Day

[Discover the cosmos!](#) Each day a different image or photograph of our fascinating universe is featured, along with a brief explanation written by a professional astronomer.

2000 December 22

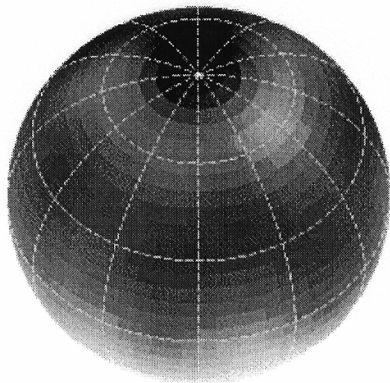


Simulated Supergiant Star

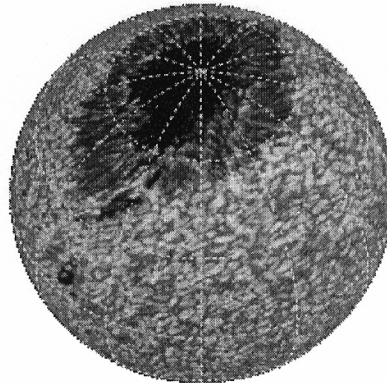
Credit: [B. Freytag](#), ([Institute for Astronomy and Space Physics](#), Univ. Uppsala)

Explanation: Looking for that perfect holiday gift for an astronomer? Consider this "star in a box". Of course, the box is actually a computational box consisting of a three dimensional grid of points, and the star is a virtual one whose [physical](#) properties and internal [dynamics](#) are numerically simulated at the points on the grid. While computers and software capable of a totally realistic numerical simulation of a complete star don't presently exist, researchers have been making progress. [This picture is](#) a movie frame from a recent numerical simulation of a [supergiant star](#) with properties intended to approximate the real star [Betelgeuse](#). The single frame shows large convection cells and bright spots mottling the virtual supergiant's surface. [Simulation movies](#) show these surface features changing substantially with time.

Doppler Imaging of Stellar Surface Structure



Typical Doppler Image (HD218153 by M.Weber). That's what's possible today.



SISP simulation (by K.Schrijver). That's what we hope for from future space interferometry. This image was composed by remapping a solar image onto a sphere.

Scientific Goals of this Project

One of the most challenging observational goals of today's stellar activity research is to obtain two-dimensional images of inhomogeneous stellar surfaces to relate disk integrated observations to spatially resolved surface features. Spots cooler than the undisturbed photosphere of a late-type star are a manifestation of surface magnetic fields and a time-dependent study of their latitudinal and longitudinal behavior provides a direct link to the internal stellar dynamo. Our long-term objective is thus to provide conclusive observational constraints for a generalized theory of stellar magnetism.

The near-term goal, however, is to enlarge the available sample of stars with a Doppler map and to investigate the surface spot morphology as a function of stellar rotation.

What is Doppler imaging?

Doppler imaging is an inversion technique to recover a 2-D image of a rapidly rotating star from a series of high-resolution spectral line profiles. The inverse problem for stars with cool spots amounts to solving the integral equation relating the surface temperature distribution to the observed line profiles and light and color curve variations, while controlling the effects of noise in the data through a regularizing functional. Note that we solve for the photometric variations simultaneously with the line profiles, but that we can handle only one line per solution. If the spectroscopic phase coverage contains gaps of more than 25 degr on the stellar surface more weight is shifted to the photometry. In a recent application to the K-dwarf LQ Hya (Strassmeier, Rice, Wehlau et al. 1993, A&A 268, 671) we made up an average map from nine spectral lines and two broad-band colors. This ensured that spurious features from a single line, caused by noise or any other systematic error, will be suppressed in the final map.

Optical, Ultraviolet, and X-ray Observations Planned and in Progress

Mapping starspots and magnetic fields on cool stars

Andrew Collier Cameron, Ron Hilditch, Moira Jardine and David James, Tim Lister, Sandra Jeffers

Recent highlights:

- **2001: AB Dor does the twist!** Differential rotation discovered to be changing with time.
- **1997: First measurement of differential rotation** on a star other than the Sun.
- For images illustrating these highlights, go to the [AB Dor Picture Gallery](#)

The cool stars group at St Andrews uses indirect imaging methods, including Doppler tomography, Zeeman-Doppler imaging, eclipse mapping and prominence tomography to make maps of cool starspots and other magnetic structures on and above the surfaces of rapidly rotating stars. With Jean-Francois Donati (Toulouse) and Meir Semel (Meudon) we have established a world-leading long-term programme of Zeeman-Doppler imaging at the Anglo-Australian Telescope. This enables us to map changes in magnetic-field patterns on stellar surfaces from year to year. This programme also produced the first detailed measurements of surface differential rotation on stars other than the Sun, by enabling us to use starspots as tracers of large-scale fluid shear. We find that even in stars rotating 50 times faster than the Sun, the differential rotation rate is similar. We are using these powerful new observations to extend what we know about physics of similar structures on the Sun (spots, prominences, etc) to the much more densely-packed magnetic structures we see on other, more active stars. We now suspect that 40% or more of some stars' surfaces are covered in dark magnetic spots, and we are developing sensitive new eclipse-mapping methods to determine the packing fraction and size distribution of these structures.

How Doppler imaging works:

The term ‘‘Doppler imaging’’ was coined by Vogt & Penrod (1983), who demonstrated that travelling starspot bumps were observable in the line profiles of HR 1099, and that an image of the stellar surface could be derived from them. A photospheric absorption line in which rotation is the dominant broadening mechanism displays time-variable irregularities if the visible surface of the star is mottled by dark spots. The effect of a cool, dark region on a rotationally-broadened line profile is illustrated in Fig. 1.

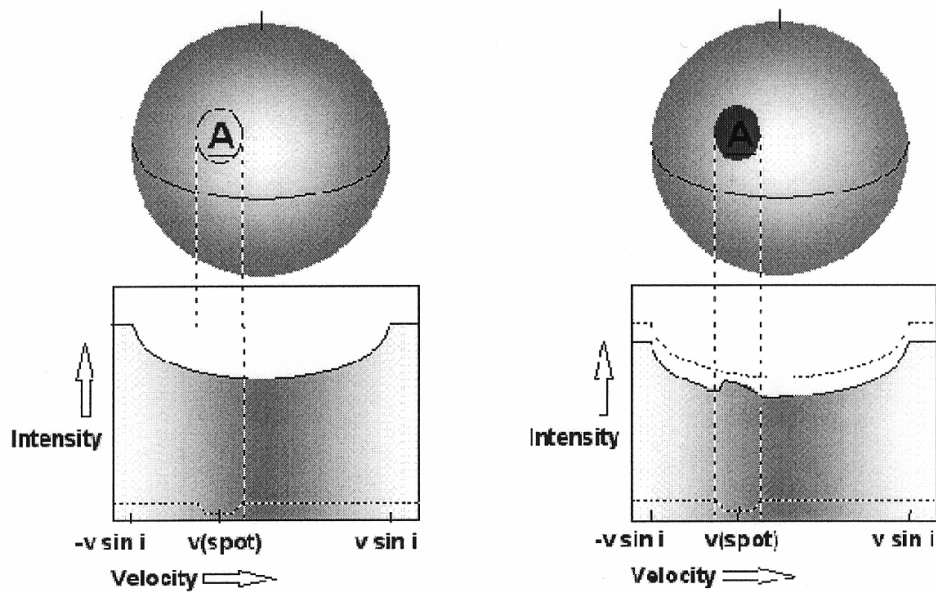


Fig. 1: The ‘‘missing’’ light of the spot consists of a continuum contribution that spans the line profile, plus a narrow line contribution that is Doppler shifted by an amount that depends on the projected distance of the spot from the stellar rotation axis. Removing this light causes an overall depression of the continuum, but less light is removed at the Doppler shift of the spot relative to the centre of the line. The observable signature of a dark spot on the stellar surface is therefore a bright bump in every photospheric absorption line in the star’s spectrum.

As the star rotates, the spots are carried across the stellar disc, causing the bumps to change their Doppler shifts in accordance with their projected distances from the star’s rotation axis. Spots near the equator remain visible for half the stellar rotation cycle, tracing out a sinusoidal velocity variation with an amplitude equal to the stellar equatorial rotation velocity, $V \sin i$. Spots at progressively higher latitudes follow progressively lower-amplitude sinusoids. The fraction of the rotation cycle for which a spot remains visible depends on its latitude and the inclination of the stellar rotation axis to the line of sight. The times at which spot signatures cross the centre of the line profile thus reveal their longitudes, while the amplitudes of their sinusoids (or equivalently, their radial accelerations at line centre) tell us their latitudes.

For a fuller account of the technical details and recent results, the following resources are available:

- Slides from review talk given at International Workshop on Astro-tomography, Brussels (July 2000)
- Review paper to appear in proceedings of Brussels workshop

Zeeman-Doppler imaging

This is a variant on the Doppler imaging technique. It uses circular and linear polarization information to measure the small shifts in wavelength and profile shape that arise in the presence of a magnetic field. Both the strength of the field and its orientation relative to the line of sight can be determined. As in conventional Doppler imaging, the rotation of the star is used to resolve different magnetic regions on the stellar surface. Jean-Francois Donati has an excellent web page describing this technique.

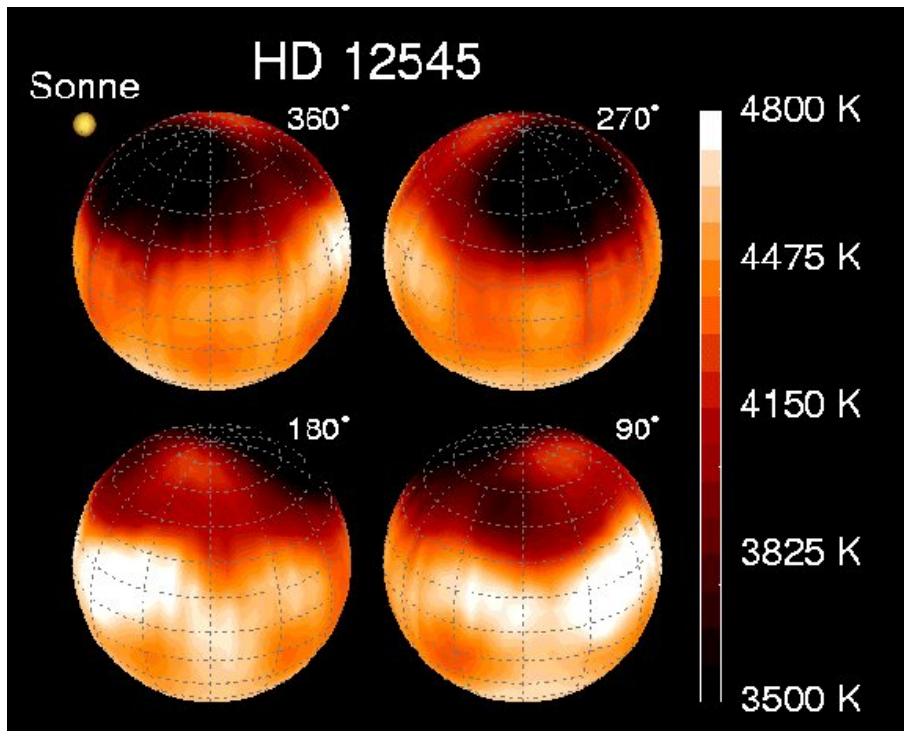


Figure 2.5: Doppler images of the giant star HD 12545 (= XX Triangulum) and its superstarspot. It is a K0 giant star, a cool star that is approximately ten times larger and two times more massive than the Sun. In order to observe spots on the surfaces of other stars, astronomers need to "resolve" the stellar disk. This cannot be done with even the largest (existing and planned) telescopes but here the researchers applied an indirect imaging technique called Doppler imaging. The star was observed for 24 consecutive (clear) nights, to cover the whole stellar rotation period. The color coding in the image is proportional to temperature. Dark means cooler than the effective temperature and white means hotter. An image of the solar disk is shown to scale as a comparison. Surprisingly, HD 12545 had a warm spot (350 K above photospheric temperature; the white area in the picture) on the hemisphere adjacent to the cool super spot. It is speculated that the warm spot harbors the same magnetic field as the cool spot but being of opposite polarity. (Text from the press release of a paper by Strassmeier, *A&A*, 347, 225, 1999.)

For more on this topic, see for example A. Collier Cameron: Spot Mapping in Cool Stars. *Lecture Notes in Physics*, Vol. 573, s. 183-206, 2001.

Doppler image gallery is available at
<http://www.aip.de/groups/activity/DI/maps/>

See Doppler imaging movie at Svetlana Berdyugina's website, Starspots and Stellar cycles,
<http://www3.kis.uni-freiburg.de/~sveta/Starspots/starspots.html>

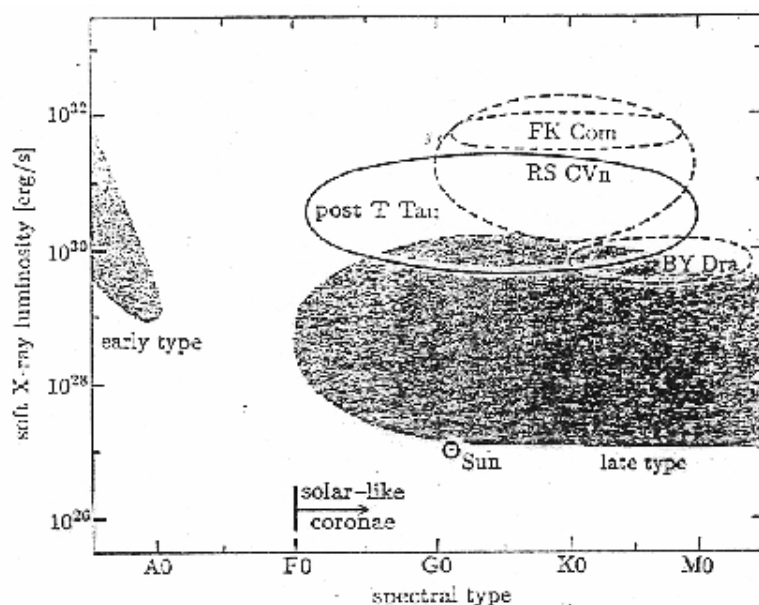
Flare Stars

Many of the flare stars are dim, red (class-M) dwarfs that exhibit unusually violent flare activity. A solar-flare-sized flare occurring on Proxima Centauri would emit about as much light as Proxima Centauri itself. From our standpoint here on the Earth, it would appear that, during

the flare, Proxima Centauri doubled in brightness. Flares on flare stars occur sporadically, with successive flares spaced anywhere from an hour to a few days apart. Flares on such dim dwarfs may emit up to 10 000 times as many X-rays as a comparably sized flare on our own sun. They would be lethal to any life forms otherwise developing on planets near the flare star, so life around such stars is unlikely. (Even if life could spring up despite the flares, flare stars are red dwarfs anyway, meaning that they have very narrow comfort zones due to their dimness and may be too red in color for plants to perform photosynthesis.) Some flare stars have also been observed emitting radio bursts simultaneously with the flares.

Note that since flare stars are variable stars, they will usually have a variable star designation such as UV Ceti or V645 Centauri. As more and more red dwarfs are observed in detail, more and more of them are being classified as flare stars. It may turn out that most red dwarfs are flare stars, and that red dwarfs without violent flare activity are the exception rather than the rule. Some of the flare stars included in this compendium are: UV Ceti, Alpha Centauri Proxima, Wolf 359, and FL Virginis.

(Text from <http://www.stellar-database.com/>)



O...B stars: hot stellar winds **F...M stars: hot corona**

Conditions for the solar-type corona:

- convection layer below the photosphere
- stellar rotation (the faster, the larger luminosity)

Studied stars:

Proxima Centauri (nearest star to the Sun, M5.5, flares, red dwarf)

AB Doradus (K1, starspots(?), fast-rotating orange dwarf)

2.5 Helioseismology

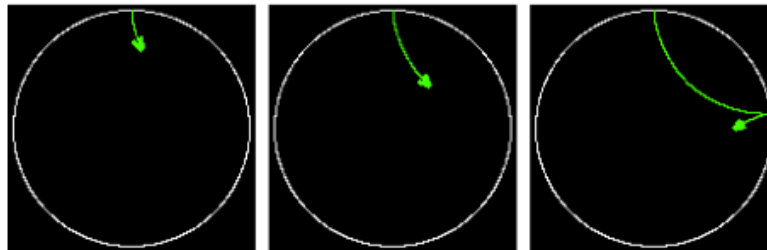
Helio- and Asteroseismology

INTRODUCTION | OBSERVATIONS : the SUN | OBSERVATIONS : STARS | MODELS | SOLAR OSCILLATIONS | RESULTS
WHO ARE WE ?

Solar oscillations

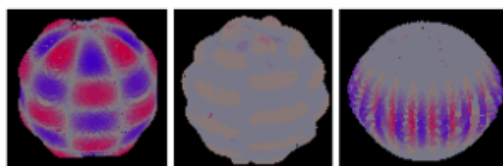
The oscillations in the Sun are sound waves, generated by the convection much like a guitar is played by plucking the strings.

If we follow where a sound wave goes, starting from the surface, it first moves into the Sun almost straight towards the centre. Its path then slowly bends around, because of the increasing sound speed, so that it misses the centre of the Sun. How exactly it moves therefore depends on the details of the sound speed inside the Sun. The point of closest approach is known as the *turning point* of the mode. After the turning point the wave moves out again until it reaches the surface. At the surface it is reflected as if by a mirror and it goes back in again.



Here are a few examples of how sound waves propagate into the Sun, with some animated sequences.

These sound waves give rise to so-called *standing waves*, in the same way that a vibrating string shows standing waves. In the Sun we are talking about standing waves in three dimensions of course. Here we show some examples of how the waves look on the solar surface (the amplitude is very much enhanced).



This page contains more information about oscillations on the solar surface.

The oscillation pattern on the surface can be characterised by node lines, on which the motion vanishes. The total number of node lines is called the degree l . The oscillation modes can also have node lines at constant longitude. There are a number m of those which is always less than or equal to the degree l . Inside the Sun the amplitude of the standing waves can have a number n , called the radial order of the mode, of nodes at certain radii from the centre.

HELIOSEISMOLOGY

- p modes (outer layers)
- g modes (core)
- f modes (surface gravity waves)

Observations

- 5 minute p modes
- 160 min oscillation (?)
- 13 day oscillation etc.

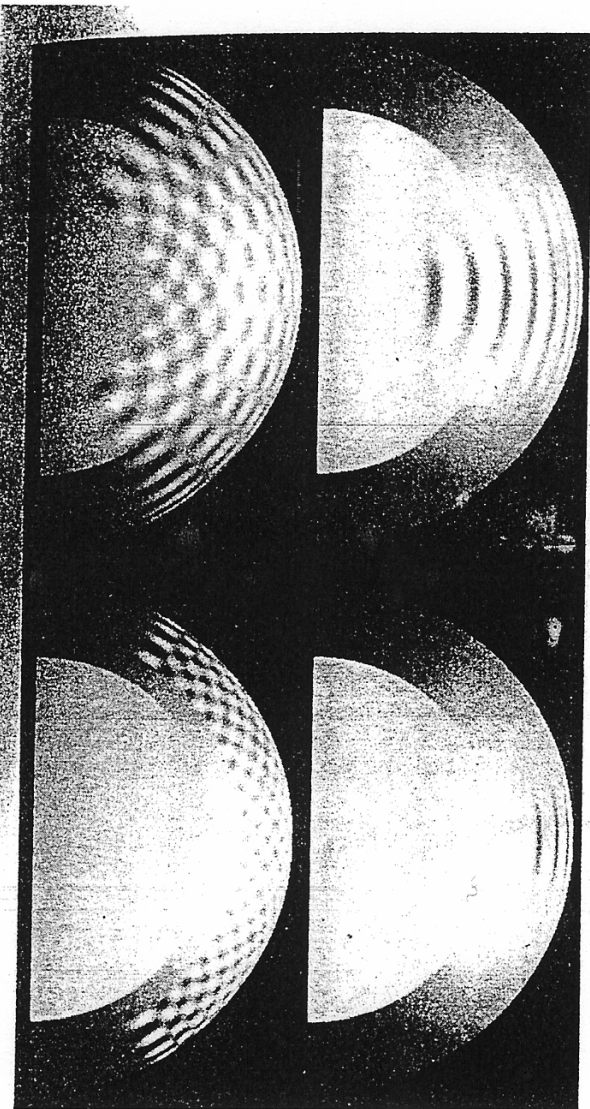
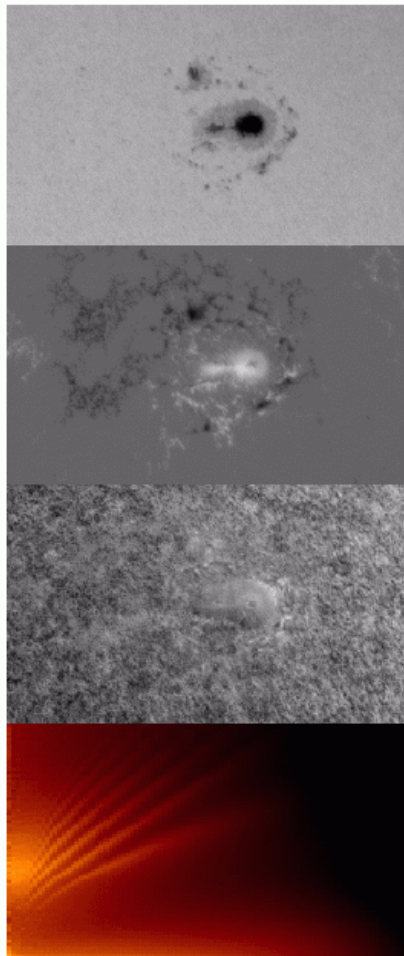
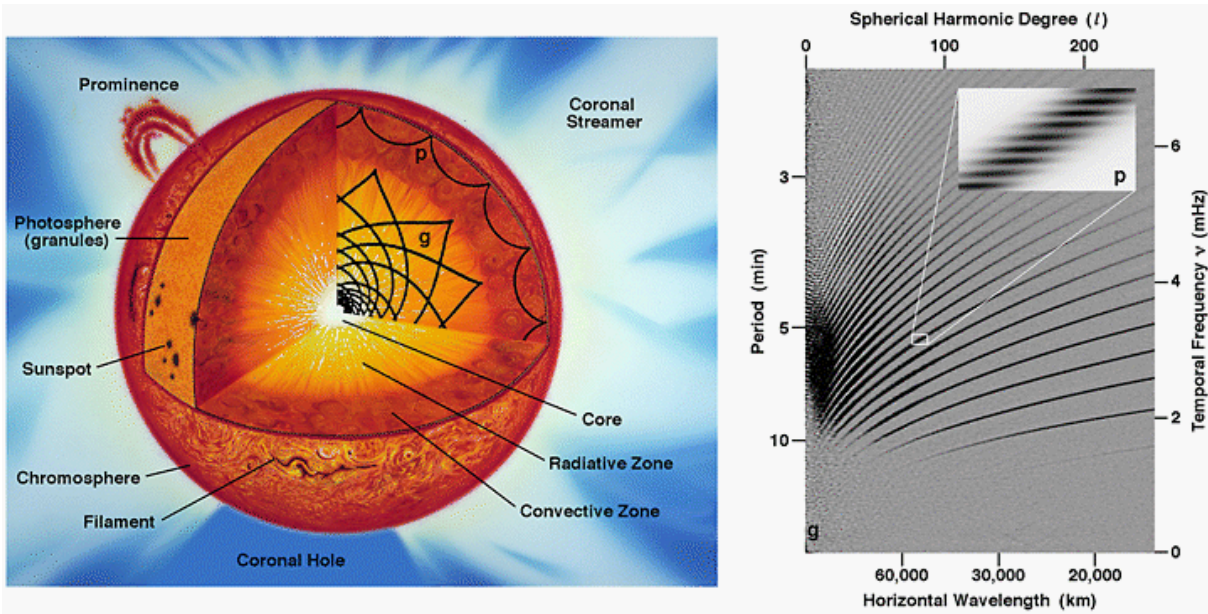


Figure 3. Superimposed on the model of Figure 2 are oscillation patterns arising from p modes with frequencies of about 3 mHz. These plots show the rough extent in depth and latitude of modes of $l=20$ (top) and 60 (bottom). The left column shows modes with m values = $l/2$ and the right column shows sectoral modes.



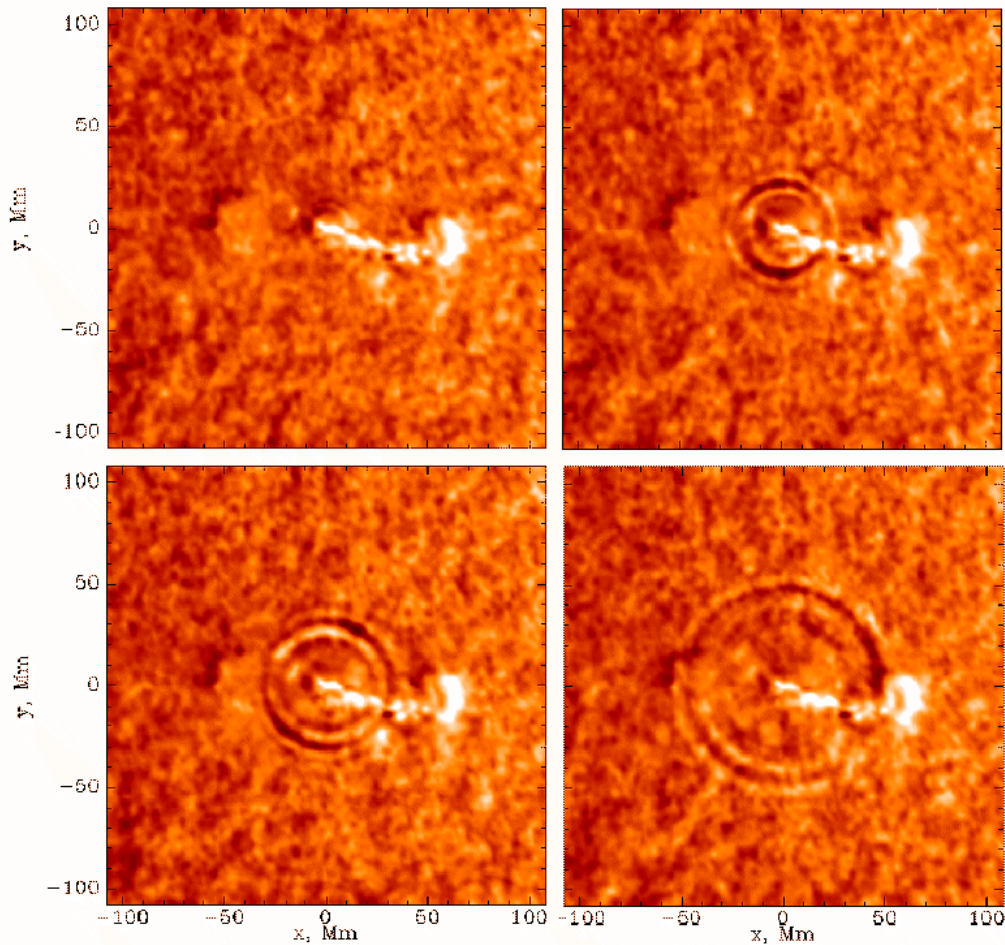
**MDI High Res.
Observations**
5 November 1998

Filtergram

Magnetogram

Dopplergram

f & p mode spectrum
K=0 to 6.4/Mm
(l=0 to 4400, 0 to 8.3mHz
12.5hrs, hr_V data)



Scientists have shown for the first time that solar flares produce seismic waves in the Sun's interior that closely resemble those created by earthquakes on our planet. The researchers observed a flare-generated solar quake that contained about 40,000 times the energy released in the great earthquake that devastated San Francisco in 1906. The amount of energy released was enough to power the United States for 20 years at its current level of consumption, and was equivalent to an 11.3 magnitude earthquake, scientists calculated.

The solar seismic waves appear to be compression waves like the "P" waves generated by an earthquake. They travel throughout the Sun's interior. The solar quake that the science team recorded looks much like ripples spreading from a rock dropped into a pool of water. But over the course of an hour, the solar waves traveled for a distance equal to 10 Earth diameters before fading into the fiery background of the Sun's photosphere. Unlike water ripples that travel outward at a constant velocity, the solar waves accelerated from an initial speed of 22,000 miles per hour to a maximum of 250,000 miles per hour before disappearing.

Images were taken with the Michelson Doppler Imager (MDI) onboard the Solar and Heliospheric Observatory (SOHO) spacecraft, immediately following a moderate-sized flare on July 9, 1996 (reported at the Conference of the American Geophysical Union, 27 May 1998).

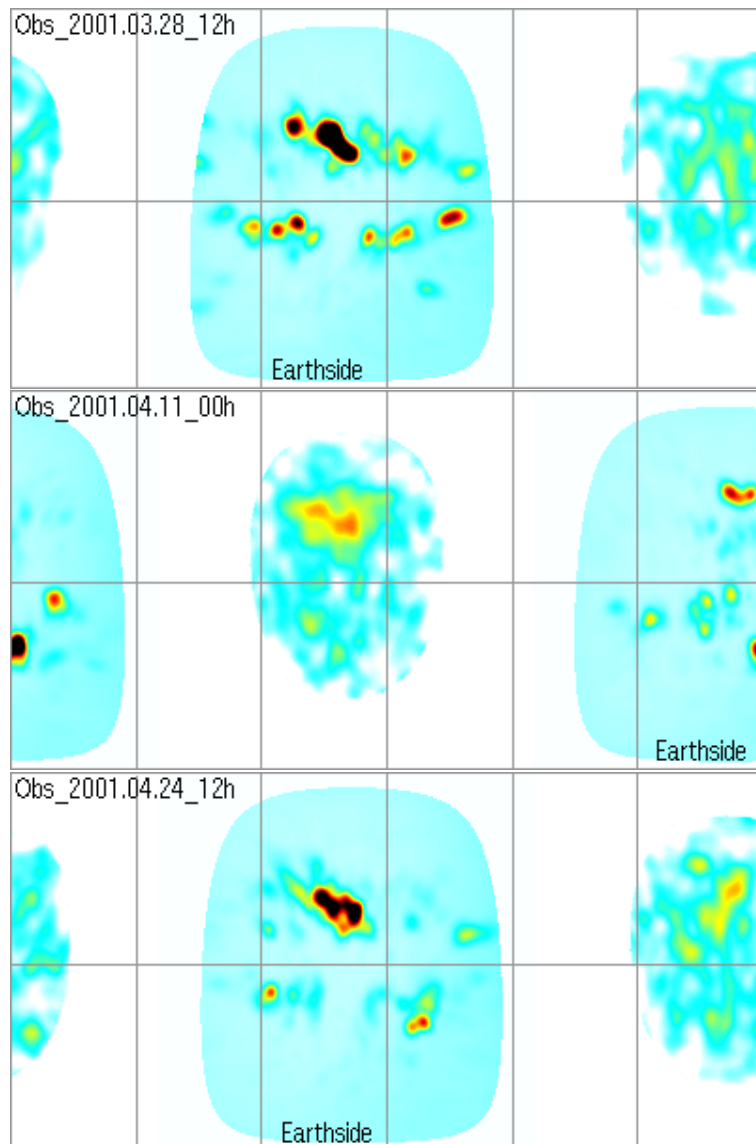
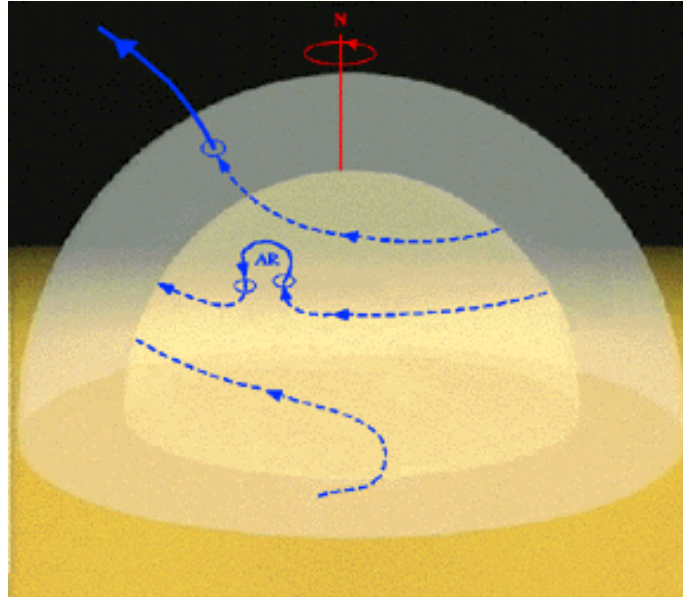


Figure 2.6: In March 2000 the SOHO/MDI science team announced the first images of an active region on the far side of the Sun. Since mid-2001 these far side images of the central area of the back side of the Sun have been prepared for each 12-hours and made available on the web. Since the Sun rotates on its axis in about 27 days, regions facing the Earth rotate off the visible surface after at most 13 days. They can emerge at any longitude, surprising solar observers if they form on the back side of the Sun and rotate into view as already very active centers. The method is using the travel time of sound waves which are bounced from the underside of the surface (Earth-side) going to and coming from each location on the farside (back-side). Because the sound speed beneath active regions is a bit faster than other places and because the reflecting layer beneath active regions is a bit deeper than other places, waves that include an active region at one of their bounce places will return to the front side a bit sooner than other waves. To make these backside images, surface motion maps are taken each minute and each map contains about 30 000 measurements. The computation for each farside map takes about 2.5 hours on a fast computer. (Text and more details in, e.g., http://soi.stanford.edu/press/farside_Feb2006/web/)

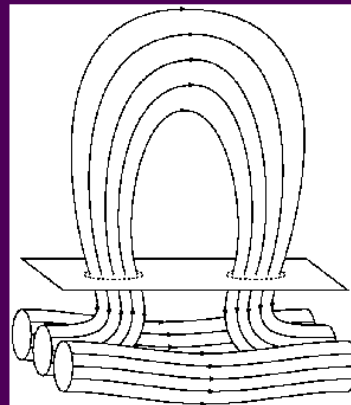
2.6 Solar magnetic fields

Magnetic fields play a dominant role in solar activity. Solar eruptions are powered by the energy stored in the magnetic fields, and to understand what triggers the eruptions, we have to know first where the energy comes from. Observations show how magnetic fields are raised from the solar interior to the sun's surface, but the primary energy release happens high in the chromosphere and corona.



Winding of the Sun's magnetic field by differential rotation leads to the formation bands of strong magnetic field on the Sun

Active regions occur where the field breaks the surface



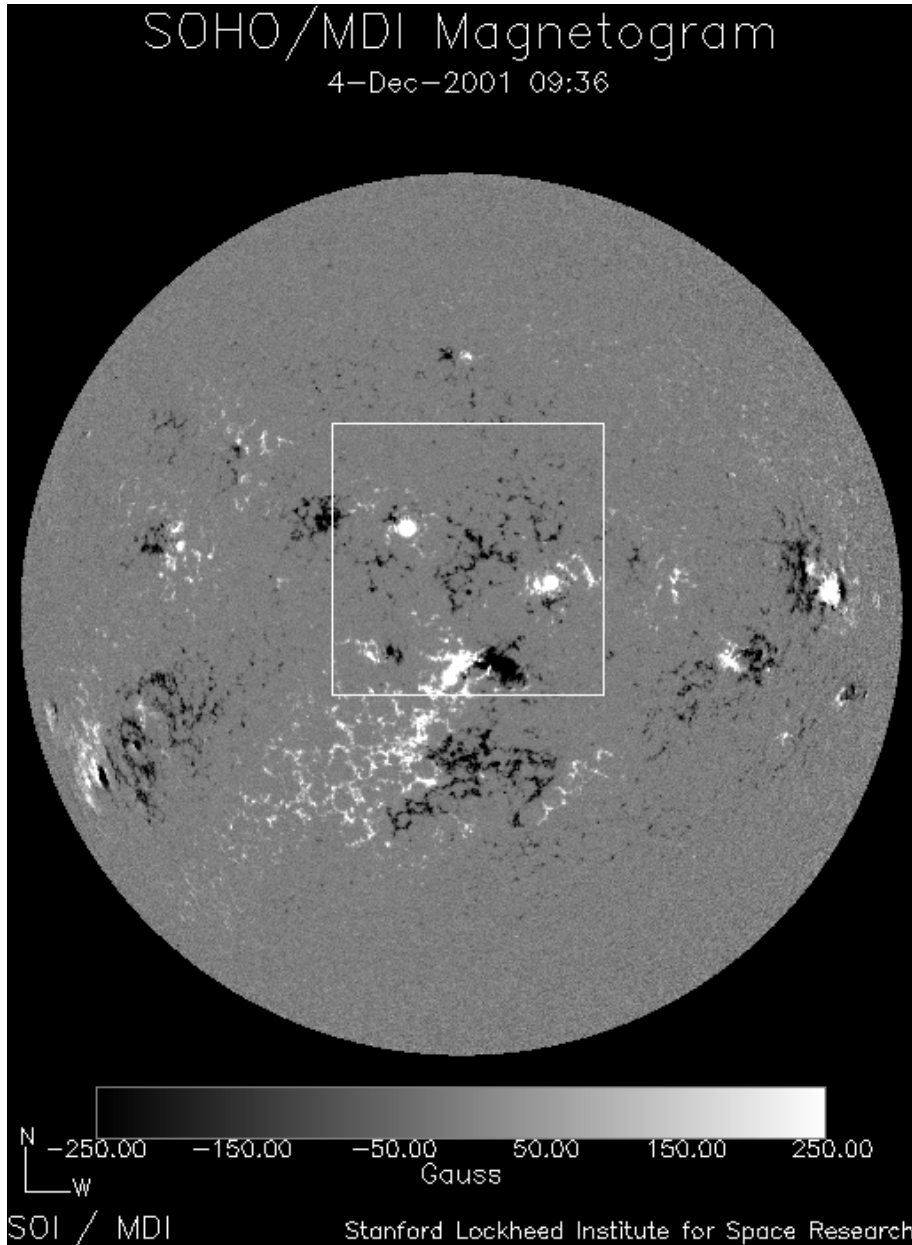


Figure 2.7: A magnetogram from SOHO MDI shows the photospheric fields between -250 and +250 Gauss. Within the active regions the field strength can be as high as 2000–3000 G. Magnetic field observations are done using the Zeeman splitting of photospheric spectral lines.

One scenario – although the idea is not supported much these days – is that when the sun was formed by contraction of a gas cloud, a 'primordial' magnetic field was dragged in, and that the interior still holds this relic field. In support to this model, researchers have found 'active longitudes' (i.e., longitudes where repeated activity is observed) that could be a sign of the relic fields.

However, it is now widely accepted that the field regenerates itself continuously, and to do this a dynamo mechanism is needed. A dynamo converts kinetic energy of an electrically conducting body (like the plasma inside the sun, in motion because of convection, for example) into magnetic energy. It has been found that a 'seed' magnetic field can form much larger fields if certain motions are present. These fields can also oscillate, with periods that possibly explain the 22-year solar magnetic cycle and the 11-year activity cycle.

There are many models that try to explain where and how the dynamo works. One basic thing that needs to be explained is the switching between the poloidal and toroidal field (i.e., how to generate fields that are first parallel to lines of longitude, then change into fields parallel to latitude, and then regenerate back the fields that are parallel to longitude). The migration of sunspots and the formation of the butterfly diagram is part of this problem.

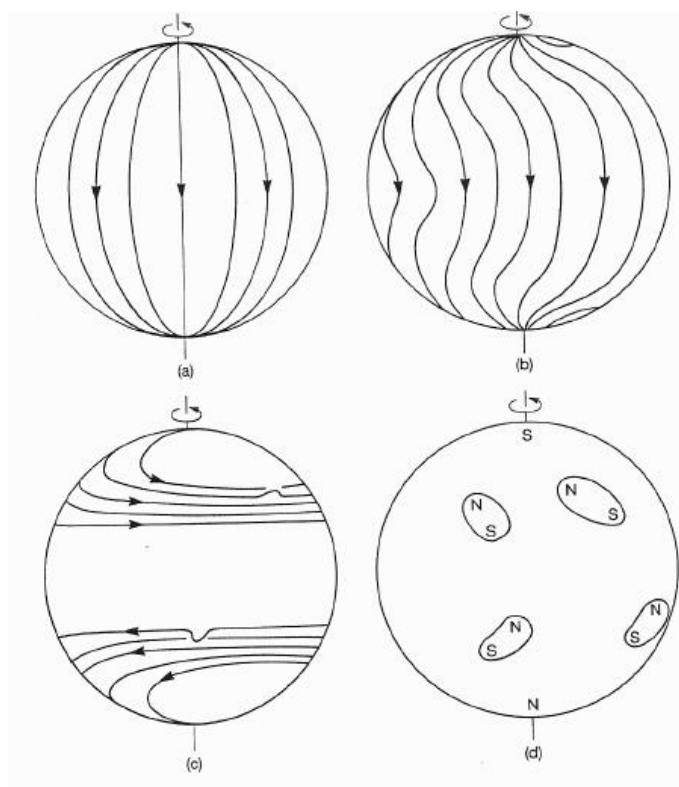


Figure 2.8: Simplified scheme for the generation of sunspot magnetic fields; the first model was developed by H.W. Babcock in 1961. The scheme shows how the entirely poloidal field (a) is deformed by differential rotation (b,c), and the active regions with bipolar sunspot groups get formed (d). Sunspot migration then neutralizes the field, and the poloidal field is regenerated – but now with opposite polarity sunspots. This explains the full 22-year magnetic cycle. (From K.J.H. Phillips: Guide to the Sun, Cambridge University Press, 1992)

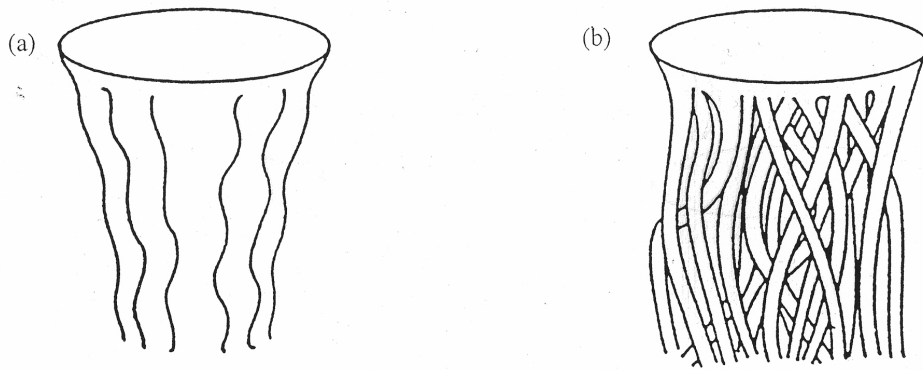


Fig. 37. Two possible magnetic field behaviours below a sunspot. (a) coherent flux tube and (b) tight cluster (diagram courtesy of Thomas, J H and Weiss, N O).

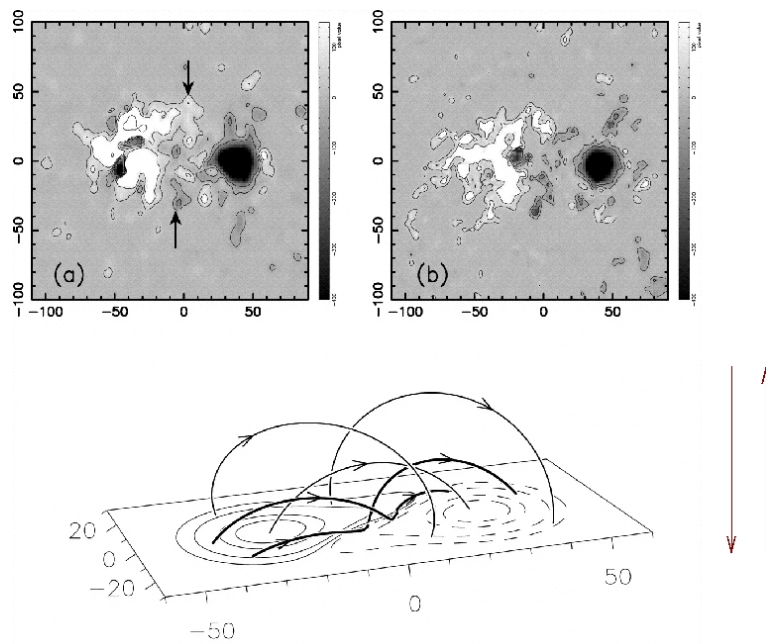
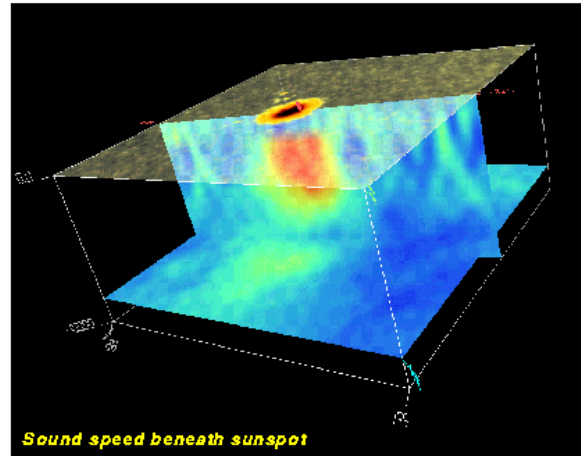


Figure 2.9: Magnetic flux is measured along the line-of-sight, and twisted fields are observed only in projection. When the flux tube is twisted, an asymmetry appears in the magnetogram because of the contribution of the azimuthal component to the observed vertical component of the field. The vertical projection of the azimuthal component produces two elongated polarities ("tongues"), which extend between the main ones. The strength of these tongues is directly proportional to the magnitude of the twist and their position depends on the sign of the twist. (Image and part of the text from Lopez Fuentes et al. ApJ 544, p. 540-549, 2000.)



Sunspot data from MDI High Resolution, 18 June 1998

Figure 2.10: An image of the sound speed below a sunspot derived from dopplergrams observed with the Michelson Doppler Imager onboard the Solar and Heliospheric Observatory spacecraft using the technique of time-distance helioseismology. Three planes are shown, on top the intensity at the surface which shows the sunspot with the dark central umbra surrounded by the somewhat brighter, filamentary penumbra. The second plane is a vertical cut from the surface to a depth of 24000 km showing areas of faster sound speed as reddish colors and slower sound speed as bluish colors. The sound speed is affected both by the temperature of the gas and the magnetic field, which we know to be strong in the sunspot at the surface. The normal increase of sound speed with depth in the sun has been subtracted so that we are only looking at deviations from the average. The third plane (bottom) is a horizontal cut at a depth of 22000 km showing the horizontal variation of sound speed over a region of 150000x150000 km.

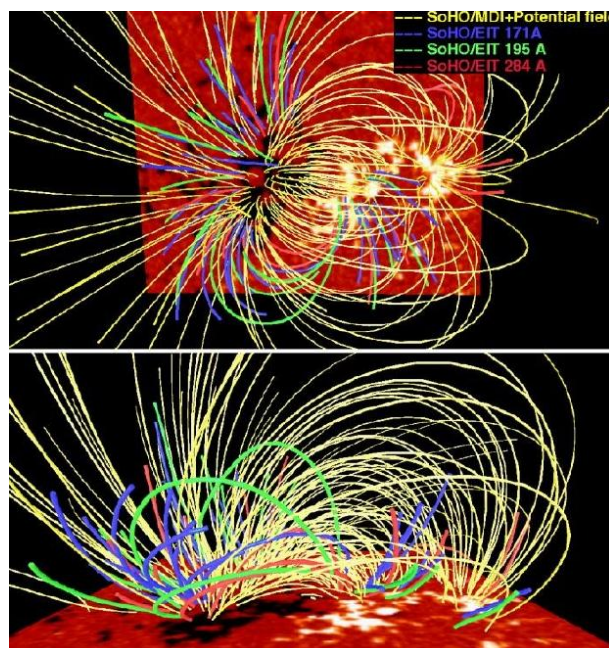


Figure 2.11: 3-D simulation of an active region (Aschwanden et al., 2000).

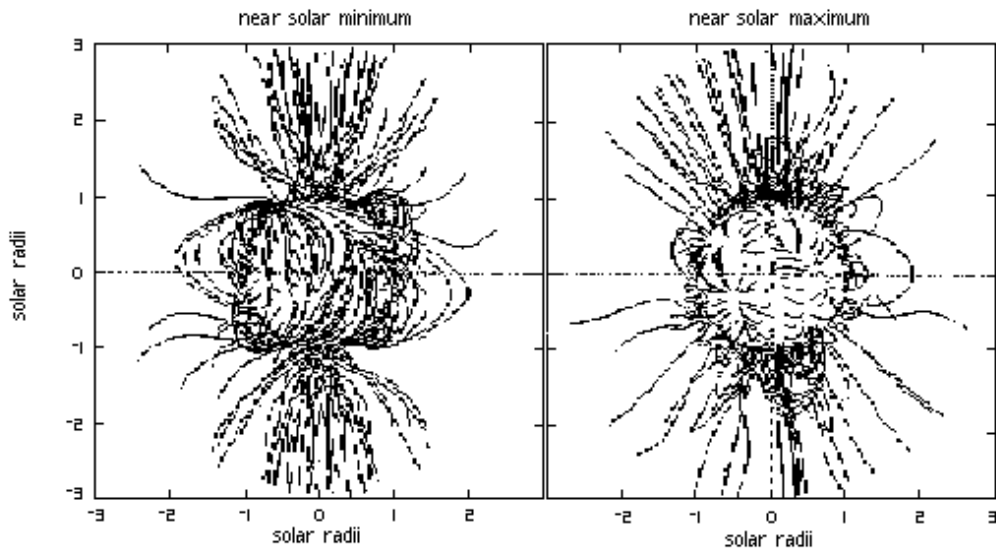


Figure 2.12: Solar magnetic field during activity minimum and maximum.

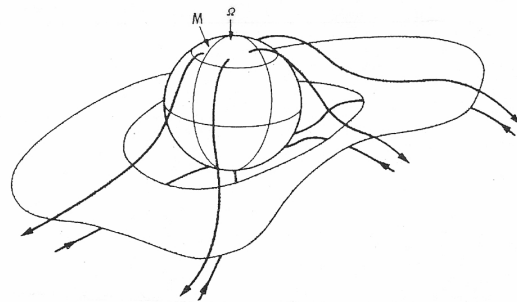


Fig. 8.11. Current sheet in the inner heliosphere in the Ballerina model. The thick lines indicate the magnetic field lines. Reprinted from Smith et al. [8.82], *J. Geophys. Res.* 83, Copyright 1978, American Geophysical Union

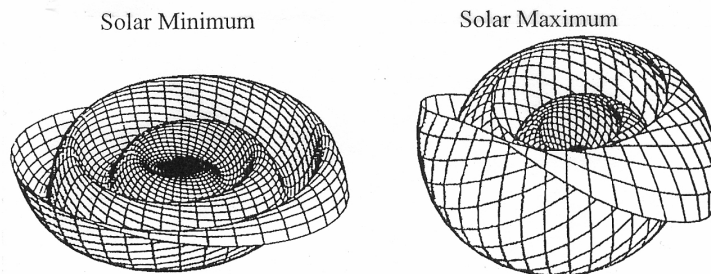


Fig. 8.20. Waviness of the heliospheric current sheet during solar minimum and maximum conditions, based on a sketch by R. Jokipii, University of Arizona

Figure 2.13: Solar magnetic field is often described as the 'ballerina skirt'. The skirt looks different during activity minimum and maximum.

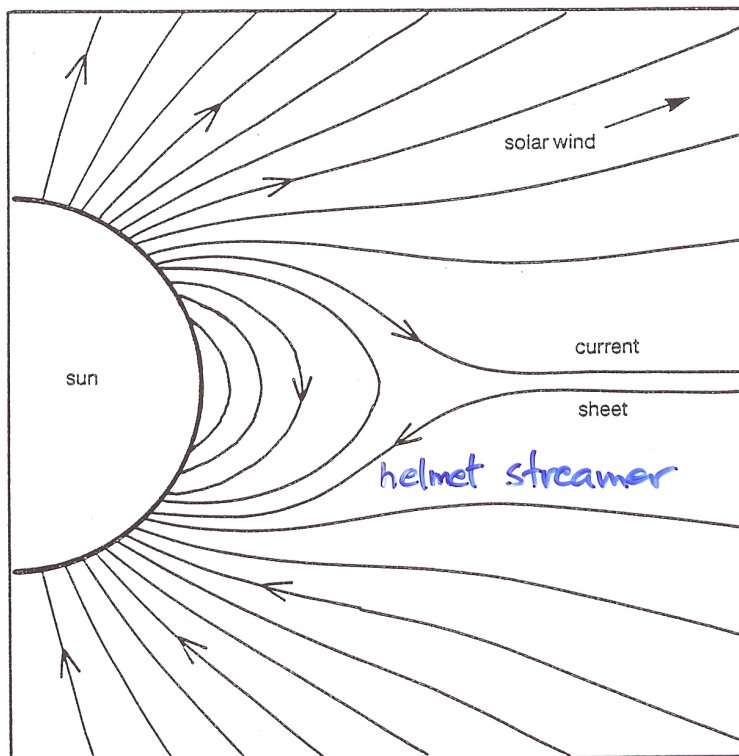


Fig. 5.15 Calculated magnetic field configuration at the time of solar minimum: a dipolar field stretched out by the solar wind to form a helmet structure near the equator and a current sheet. (After Pneuman and Kopp (1971). Reprinted by permission of Kluwer Academic Publishers)

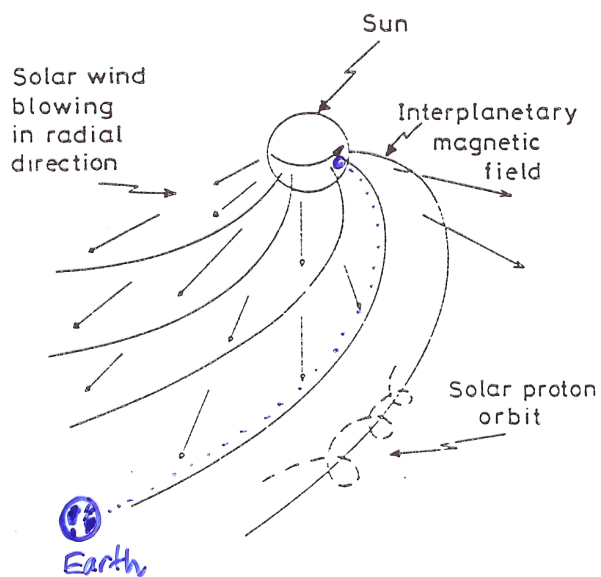


Figure 2.14: Some solar longitudes are “well-connected” to the Earth (~ W70–80).

2.7 Hale's and Joy's laws

Hale's Polarity Law:

The polarity of the leading spots in one hemisphere is opposite that of the leading spots in the other hemisphere and the polarities reverse from one cycle to the next.

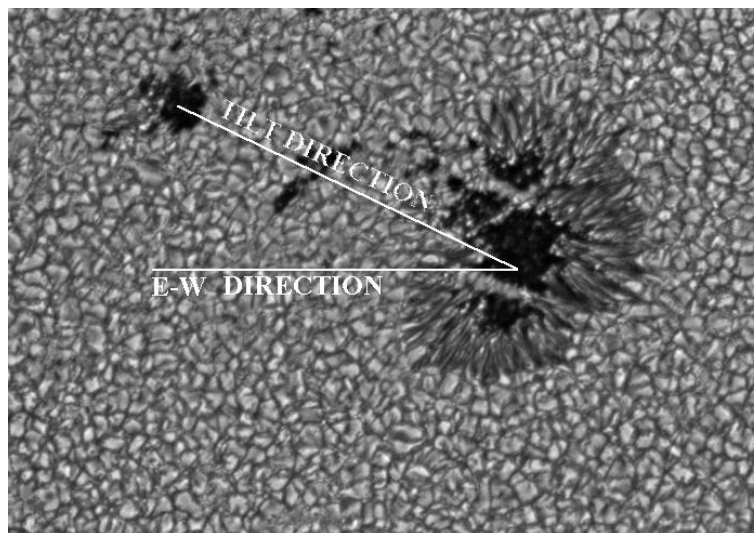
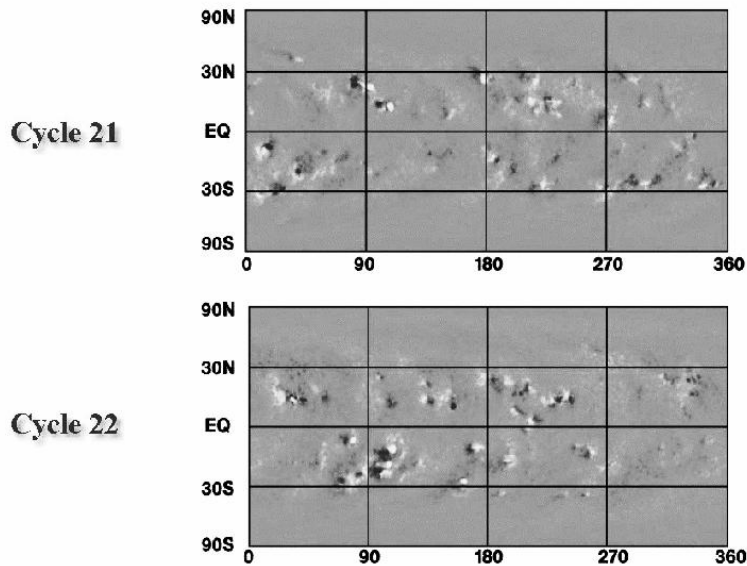
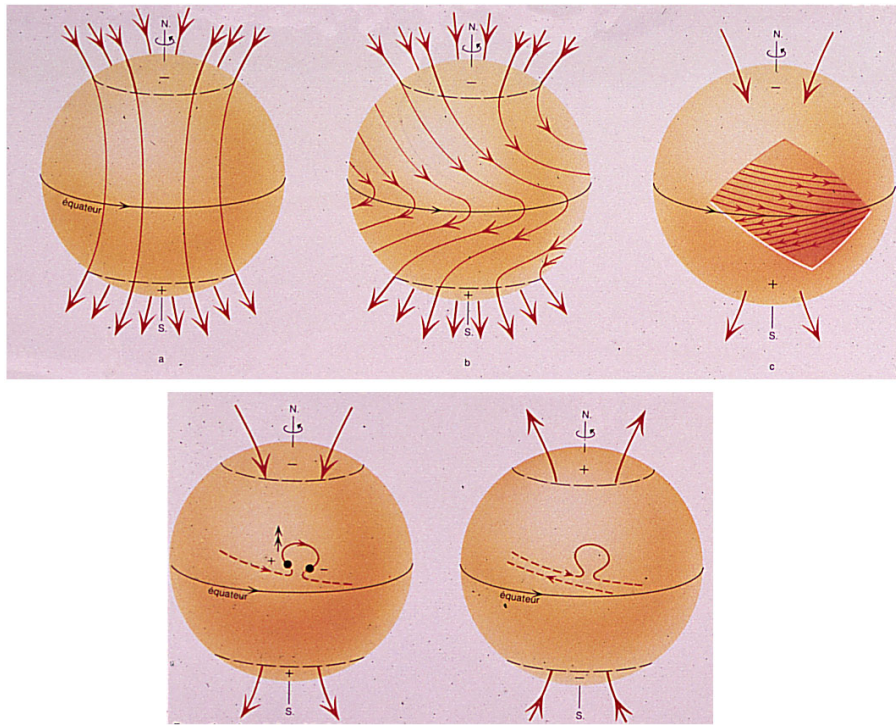


Figure 2.15: Joy's law: The magnetic axis of the sunspot group is usually slightly inclined to the solar east-west line, running from 3 degrees near the equator to 11 degrees at latitude 30 N/S, with the preceding polarity spot being slightly closer to the equator. If the axis is highly tilted initially, the group will tend to rotate until the axis is more parallel to the equator.



2.8 Differential rotation

Magnetic fields within the Sun are stretched out and wound around the Sun by differential rotation - the change in rotation rate as a function of latitude and radius within the Sun. This is called the *omega-effect* after the Greek letter used to represent rotation. Twisting of the magnetic field lines is caused by the effects of the Sun's rotation. This is called the *alpha-effect* after the Greek letter that looks like a twisted loop (see schematic drawings at <http://solarscience.msfc.nasa.gov/dynamo.shtml>). Recent dynamo models assume that the twisting is due to the effect of the Sun's rotation on the rising magnetic field flux tubes. The twist produced by the alpha effect makes sunspot groups that obey Joy's law and also makes the magnetic field reverse from one sunspot cycle to the next (Hale's law). But, there is differential rotation also *inside* the sun.

The sidereal rotation rate Ω (degrees/day) can be expressed as

$$\Omega = A + B \sin^2 \theta + C \sin^4 \theta \quad (2.5)$$

where θ is the solar latitude in degrees, and A , B and C are the fitted constants.

Sidereal (true) rotation rate is calculated from the observed, *synodic*, rotation rate by correcting for Earth rotation.

Surface rotation rates can be calculated using relatively stable features like sunspots, quiescent filaments and radio bright regions. First, solar images must be made comparable by rotating the images so that North is up and West is to the right. This is called correcting for the P angle. Correction for the B_0 angle is more demanding, and it is usually done by superposing a grid on the disk (after fitting the solar limb). After the corrections, the latitude and longitude values of each feature can be recorded and followed at suitable intervals. It should be noted that for example sunspots tend to disintegrate and/or merge together, so the time between observations should not be too long.

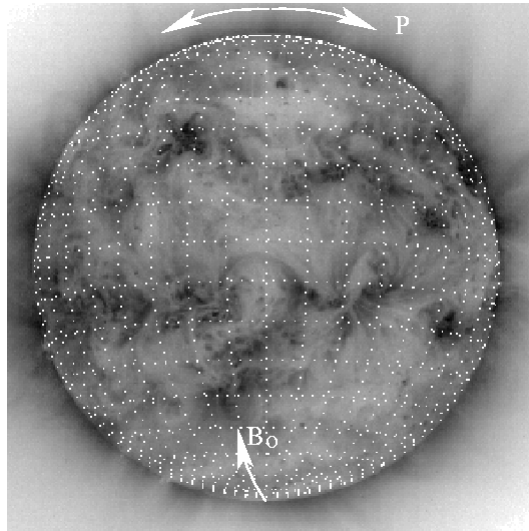


Figure 2.16: The sun at 195 Å:n observed in February 2000. Grid separation is 10 degrees and the value of B_0 is -6 degrees, which means that the south pole is tilted towards us. North is up (a correction for the P angle has been made).

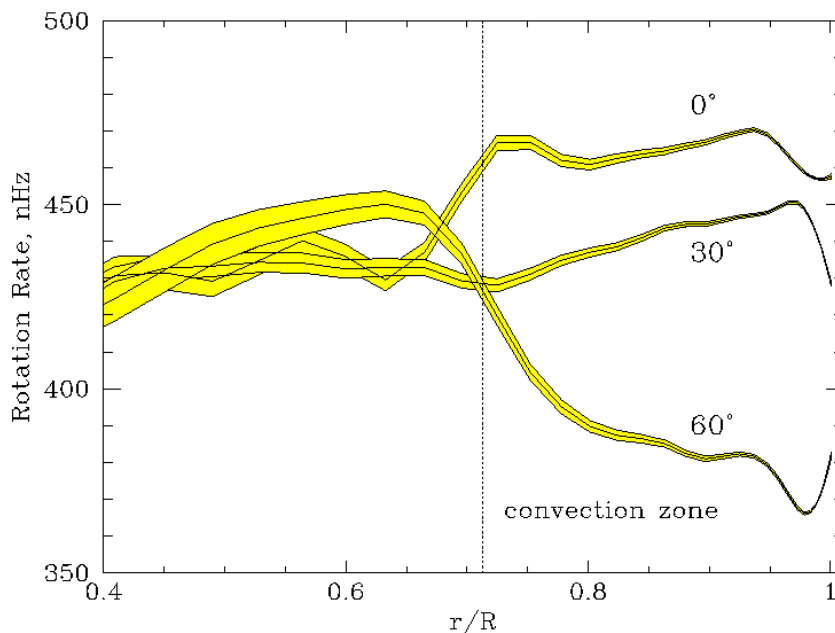


Figure 2.17: The diagram shows the solar rotation rate inferred from two months of SOHO/MDI data as a function of radius at three latitudes, 0 degrees, 30 degrees, and 60 degrees. 350 nHz corresponds to a 33-day rotation rate and 450 nHz to a 26-day rate. The data are spatial averages of the full-disk Doppler velocity out to ninety percent of the Sun's radius, measured each minute. This MDI observational program results in 23,000 bins of approximately ten arcsecond resolution, which, in turn, provides sensitivity to solar p mode frequency oscillations up to degree $l=300$ of the spherical surface harmonic modes. (From Internal Structure and Rotation of the Sun: First Results from the MDI Data, by A.G. Kosovichev et al., see <http://soi.stanford.edu/results/srotation.html>)

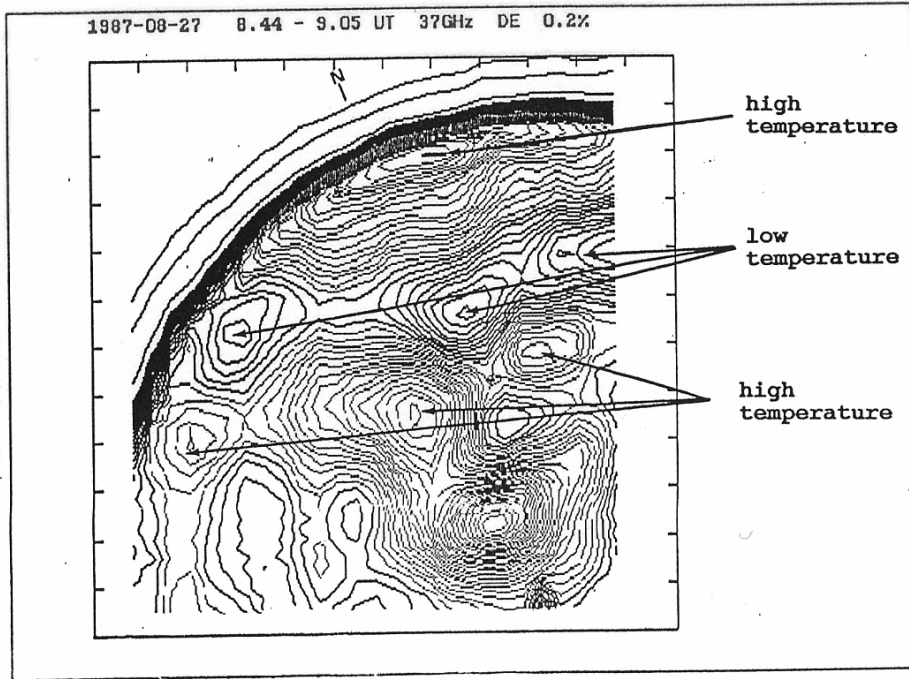


FIGURE 2: Enlarged solar map showing the north pole with low temperature areas below the enhanced polar region. Map measured at Metsahovi on August 27, 1987. Contours 0.2 % of the quiet Sun level.

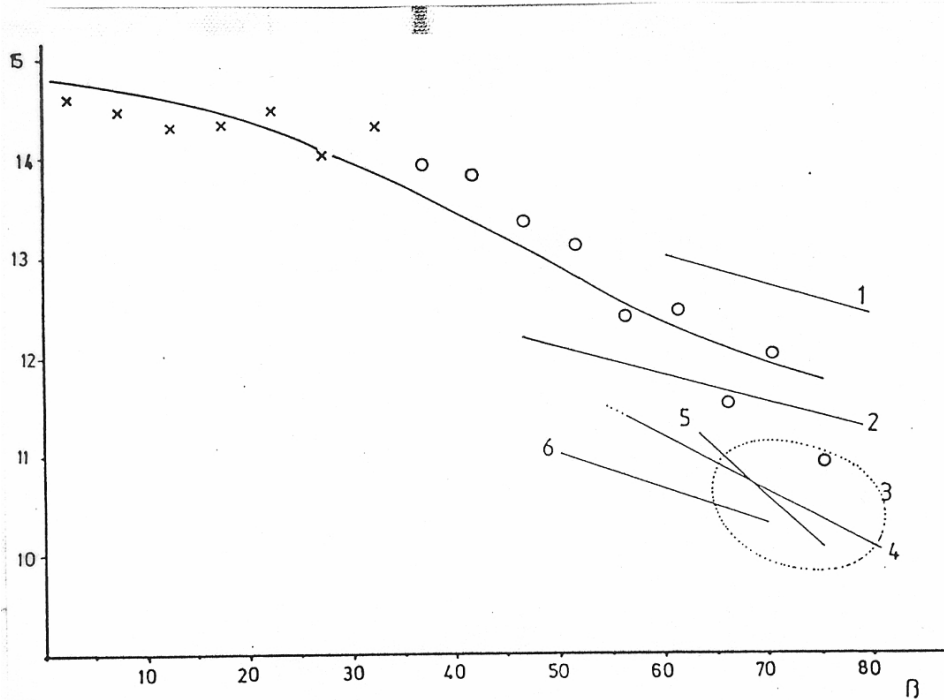


FIGURE 3: Curves of the sidereal rotation rate (deg/day) vs. solar latitude.

- +) filaments, Adams & Tang (1977)
- circles) polar crown filaments, Brajsa et al. (1990)
- 1) filaments, d'Azambuja (1948), after Schroter (1985)
- 2) & 3) polar faculae, after Makarova & Solonsky (1987)
- 4) photosphere, spectroscopic, Howard & Harvey (1970)
- 5) polar faculae, Waldmeier (1955) & Muller (1954), after Hansen et al. (1969)
- 6) high temperature regions at 37 GHz, present work

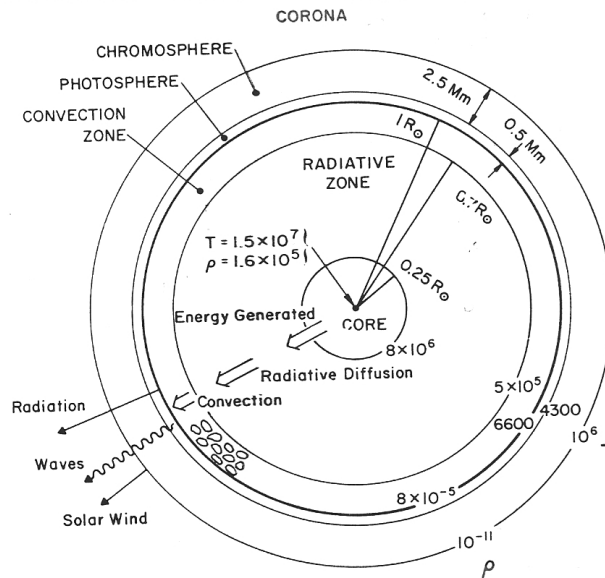


Figure 2.18: A schematic drawing of the solar structure.

2.9 Solar atmosphere

Solar atmosphere can be divided into three different layers (based on the temperature and density variation), and they are called photosphere, chromosphere, and corona. Photosphere is the 'light sphere', a thin layer (500 km) which is often taken as the sun's surface as it is what we see when we look at the sun in white (= visible) light. Within the photosphere, the temperature drops from 6400 K to about 4400 K, and then starts to rise again. When we measure magnetic fields using Zeeman splitting, the lines are photospherically-formed Fraunhofer lines, and the magnetic field strengths are only valid for the photosphere. Chromosphere, the 'colour sphere', is a 1500 km thick layer above the photosphere, where temperature first rises gradually and then sharply. (In fact the thin region between the chromosphere and corona is called the transition region, to emphasize the change.) The rich variety of chromospheric spectral lines provides a lot of observational material, especially in EUV. Corona, the 'crown', has a temperature of a few million degrees, and it emits strongly in radio and X-rays. Why the corona has such a high temperature is not known exactly, and this is called the coronal heating problem. Coronal gas has a low density and the gas is almost fully ionized. Electrons are 'frozen' into the solar magnetic field, but they can move away from the sun within the solar wind or during coronal mass ejections and other eruptions.

The structure of the solar magnetic field changes within the activity cycle. During minimum activity, a streamer belt is observed near the equator, but it changes into a more complex structure during activity maximum. Current sheets can be observed in association with helmet streamers. Since a neutral line separates magnetic fields of opposite polarity, a current must flow inside it, and thus a neutral line is a current sheet - and the sheet is observed to extend outward through the tips of the helmet streamers.

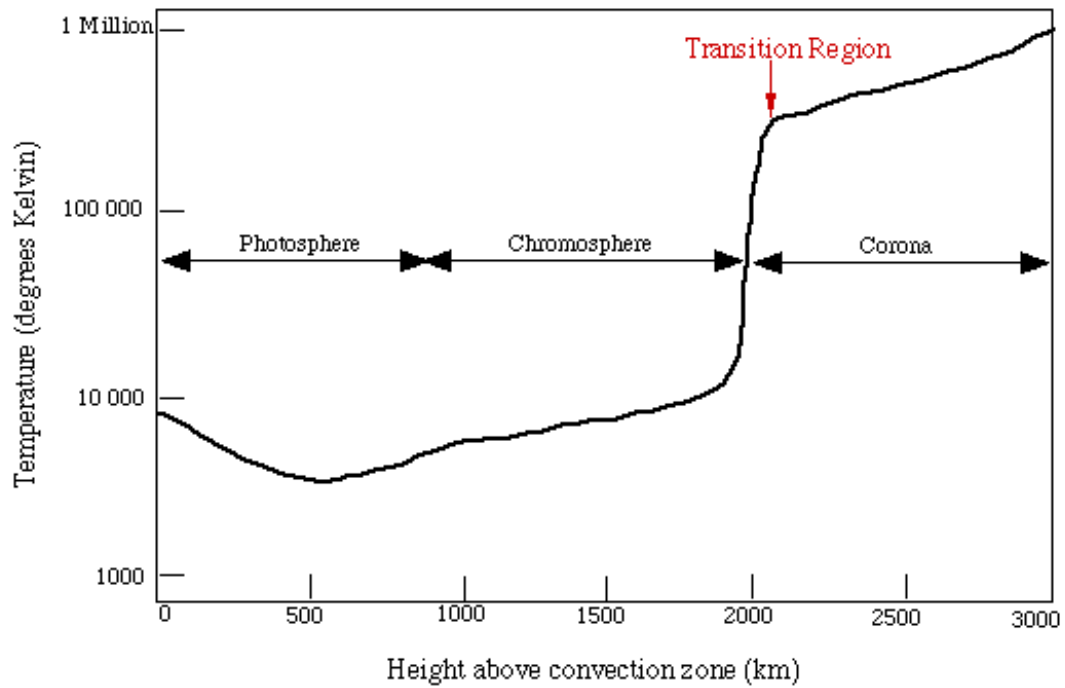


Figure 2.19: The solar atmosphere (adapted by M.B. Larson from Kenneth Lang: Sun, Earth, Sky).

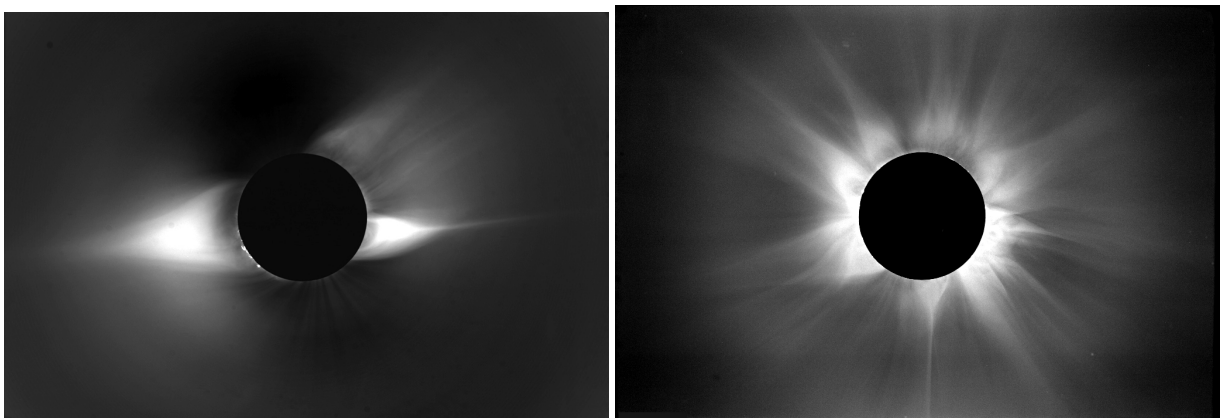


Figure 2.20: Coronal streamers are permanent features but their number also depends on the activity cycle. Left: eclipse photograph during activity minimum and Right: during activity maximum (High Altitude Observatory).

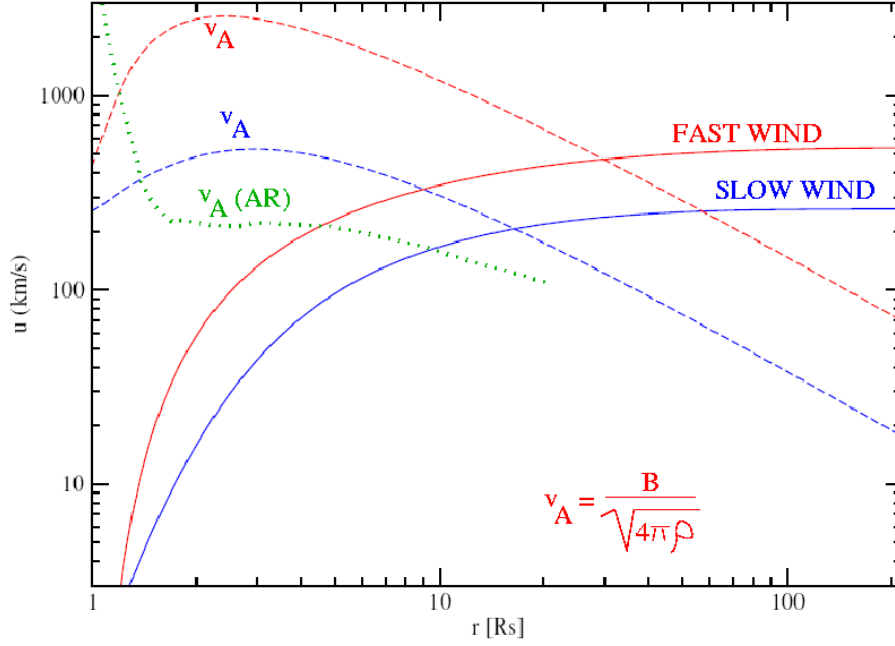


Figure 2.21: Alfvén speed (v_A) and solar wind speed in the (quiet sun) solar atmosphere and above an active region (AR). Speeds are in km/s. In X-axis is the distance R_s from the solar surface (limb) in solar radii (at the limb, $R_s = 1$). Alfvén speed depends on the magnetic field strength B and electron density ρ . Within an active region and low in the atmosphere, magnetic field strengths are high and thus also Alfvén speeds are high. Outside the active regions (in 'quiet sun' atmosphere), density decrease is faster than the decrease in B , and hence the Alfvén speed rises in the low corona, up to a distance of 3–5 R_s . (Original plot from Timo Laitinen)

2.10 Plasma diagnostics

For a fully ionized plasma, in known conditions within the solar system, we can use the following approximations (all in gaussian units; density in cm^{-3} and field strength in G):

plasma frequency

$$\nu_p \approx 9 \times 10^3 \sqrt{n_e} \quad (\text{Hz}), \quad (2.6)$$

Alfvén speed (in hydrogen plasma, primordial abundances; transverse wave that propagates parallel to the magnetic field and does not compress the plasma)

$$v_A \approx \frac{2 \times 10^{11} B}{\sqrt{n_e}} \quad (\text{cm/s}), \quad (2.7)$$

sound speed (longitudinal wave that propagates parallel to the magnetic field and compresses the plasma)

$$v_s \approx 1.5 \times 10^4 \sqrt{T} \quad (\text{cm/s}), \quad (2.8)$$

magnetosonic speed (longitudinal wave that propagates perpendicular to the magnetic field, also known as the compressional Alfvén wave or magnetoacoustic wave)

$$v_{ms} = \sqrt{v_s^2 + v_A^2}, \quad (2.9)$$

plasma β is the ratio of the plasma pressure to the magnetic pressure

$$\beta = \frac{16\pi nkT}{B^2}. \quad (2.10)$$

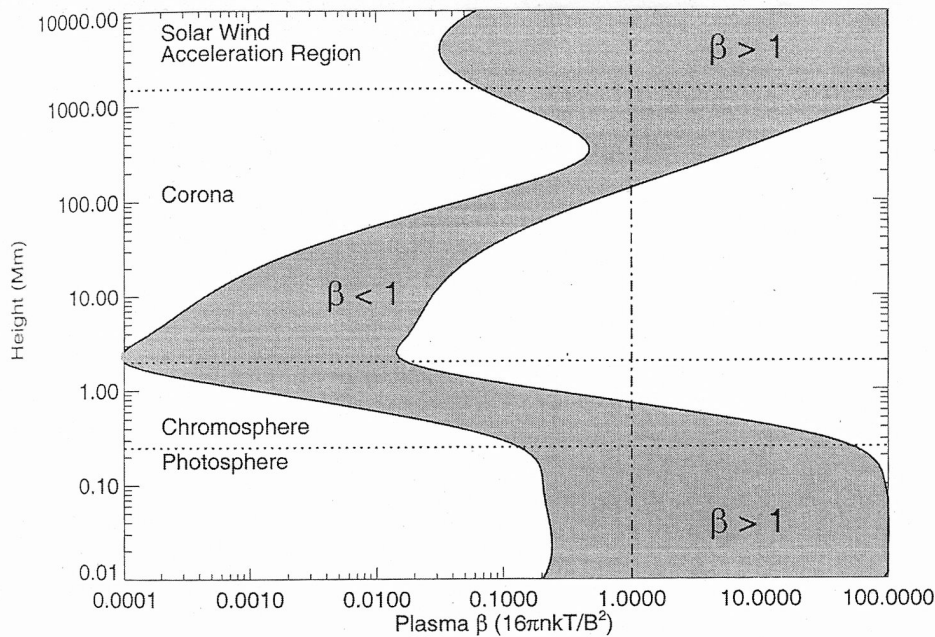


Figure 2 Plasma β in the solar atmosphere for two assumed field strengths, 100 G and 2500 G. In the inner corona ($R \lesssim 0.2R_\odot$), magnetic pressure generally dominates static gas pressure. As with all plots of physical quantities against height, a broad spatial and temporal average is implied. (Courtesy of G. Allen Gary.)

Figure 2.22: Plasma β in the solar atmosphere. Coronal loops contain hot and dense plasma (high value of β) while the corona itself is less dense but extremely hot and only weakly magnetized (low β value). This may give rise to instabilities (so-called ballooning instability). The 'high- β disruption' has been proposed to be the reason why plumes disintegrate.

2.11 Atmospheric densities

Atmospheric density models are used to describe density changes at different heights. As plasma frequency depends on the local density, these values are of interest especially to solar radio astronomers.

The Newkirk (1961) density model is based on hydrostatic equilibrium and the density values stay high also at large distances from the sun

$$n = 4.2 \times 10^4 \times 10^{4.32/r}, \quad (2.11)$$

here the distance r is expressed in solar radius R_{\odot} , measured from the center of the sun, and electron density is in cm^{-3} .

The Saito (1970) model describes best quiet sun densities near the equator,

$$n = k1 \times r^{-16} + k2 \times r^{-6} + k3 \times r^{-2.5} \quad (2.12)$$

where $k1 = 3.09 \times 10^8$, $k2 = 1.58 \times 10^8$, and $k3 = 0.0251 \times 10^8$, units as in the Newkirk model.

Because both of these 'basic' density models fail to work in active region densities, they are usually multiplied with selected constants: for example a 2-times Newkirk model means $n = 2 \times 4.2 \times 10^4 \times 10^{4.32/r}$. A 10×Saito can be used within active regions, but it does not work at large distances from the sun. Measurements of coronal densities would be most useful, but they are infrequent and the analysis of coronal images is difficult (coronal images show scattered white light).

The interplanetary (IP) approximation is based on the relation $n_e \sim R^{-2}$, and gives

$$n_e = \frac{n_0}{R_d^2} \quad (2.13)$$

where n_0 (cm^{-3}) is the plasma density near Earth (at 1 AU) and R_d (AU) is the distance from the sun. This model does not work well in the solar corona, since the densities it gives are too low. There are also 'hybrid' models that try to combine the different characteristics, e.g. by Vrsnak et al. (2004) which starts as a 5-times Saito at solar surface and continues as the modified IP model by Leblanc et al. (1998) towards the Earth.

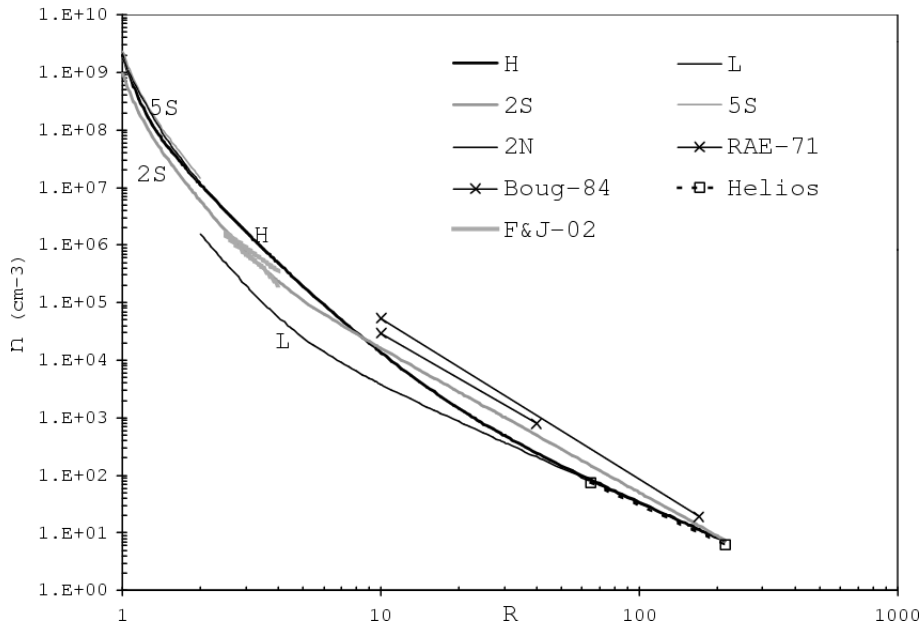


Figure 2.23: Density models from the AR-corona to IP space: H - the hybrid density model by Vrsnak et al. (A&A 413, 753, 2004); L - the model by Leblanc et al. (1998); 2S and 5S - two-fold and five-fold Saito (1970) model; RAE-71 - Fainberg & Stone (1971); Boug-84 - the results by Bougeret et al. (1984b) as given in Bougeret et al. (1984a); Helios - in situ measurements (Bougeret et al. 1984a); F&J-02 - Frazin & Janzen (2002).

Table 2.1: Calculated electron densities and plasma frequencies (wavelengths in parenthesis) at different distances h (R_\odot) from the center of the sun ($R_\odot=1$ at the limb).

f_p (MHz)	λ (m)	n_e (cm^{-3})	h Saito	h Hybrid	h 2×Newkirk	h 10×Saito	h Leblanc ^a	h IP ^a
500	0.6	3.1×10^9	-	-	-	1.035	-	-
400	0.75	2.0×10^9	-	-	-	1.076	-	-
300	1	1.1×10^9	-	1.044	1.050	1.142	-	-
200	1.5	4.9×10^8	-	1.117	1.147	1.258	-	-
100	3	1.2×10^8	1.131	1.305	1.368	1.560	-	-
70	4.3	6.0×10^7	1.226	1.453	1.514	1.758	-	-
50	6	3.1×10^7	1.342	1.637	1.682	1.989	1.10	-
30	10	1.1×10^7	1.584	2.010	2.040	2.403	1.31	-
14	21.4	2.4×10^6	2.07	2.78	2.96	3.33	1.71	-
12	25	1.8×10^6	2.19	2.96	3.24	3.57	1.80	-
10	30	1.2×10^6	2.36	3.24	3.74	3.97	1.93	-
9	33.3	1.0×10^6	2.44	3.38	4.00	4.17	2.00	-
8	37.5	7.9×10^5	2.56	3.57	4.44	4.47	2.09	-
7	42.9	6.0×10^5	2.72	3.81	5.05	4.86	2.20	-
6	50	4.4×10^5	2.90	4.10	6.00	5.38	2.33	-
5	60	3.1×10^5	3.13	4.46	7.61	6.06	2.49	-
4	75	2.0×10^5	3.49	4.96	11.46	7.09	2.72	1.02
3	100	1.1×10^5	4.07	5.75	>30	8.88	3.07	1.37
2	150	4.9×10^4	5.18	7.07	>>	12.17	3.69	2.06
1	300	1.2×10^4	8.58	10.36	>>	21.30	5.42	4.16

a) $n_0=4.5 \text{ cm}^{-3}$ at 1 AU

2.12 Magnetic field strengths

We can approximate the magnetic field strengths in the solar corona as in Vainio & Khan (ApJ, 2004), the approximation is valid for equatorial regions:

$$B \sim 1.7 \left(\frac{R_\odot}{R} \right)^3 + 1.3 \left(\frac{R_\odot}{R} \right)^2 (G). \quad (2.14)$$

The empirical scaling law presented by Dulk & McLean (Solar Physics, 1978) gives the strength of the coronal magnetic field above active regions and it works best at distances $1.02 - 10 R_\odot$:

$$B = 0.5 \times h^{-1.5} (G), \quad (2.15)$$

where h is the height above the photosphere expressed in solar radii. Field strengths of 22 G would then appear at about heights of 56 000 km and 10 G at about 95 000 km.

Using radio observations of gyrosynchrotron emission, the field strengths can be calculated if other source parameters (volume, density and viewing angle) are known. However, in most cases we can just give most probable range values for the fields.

Magnetic field strengths at sunspot centers can be approximately 1000–3000 Gauss. In the solar corona the field strengths are 10–300 G (similar to fridge magnets, at 200 G). At Earth, the magnetic field strength is about 0.5 G.

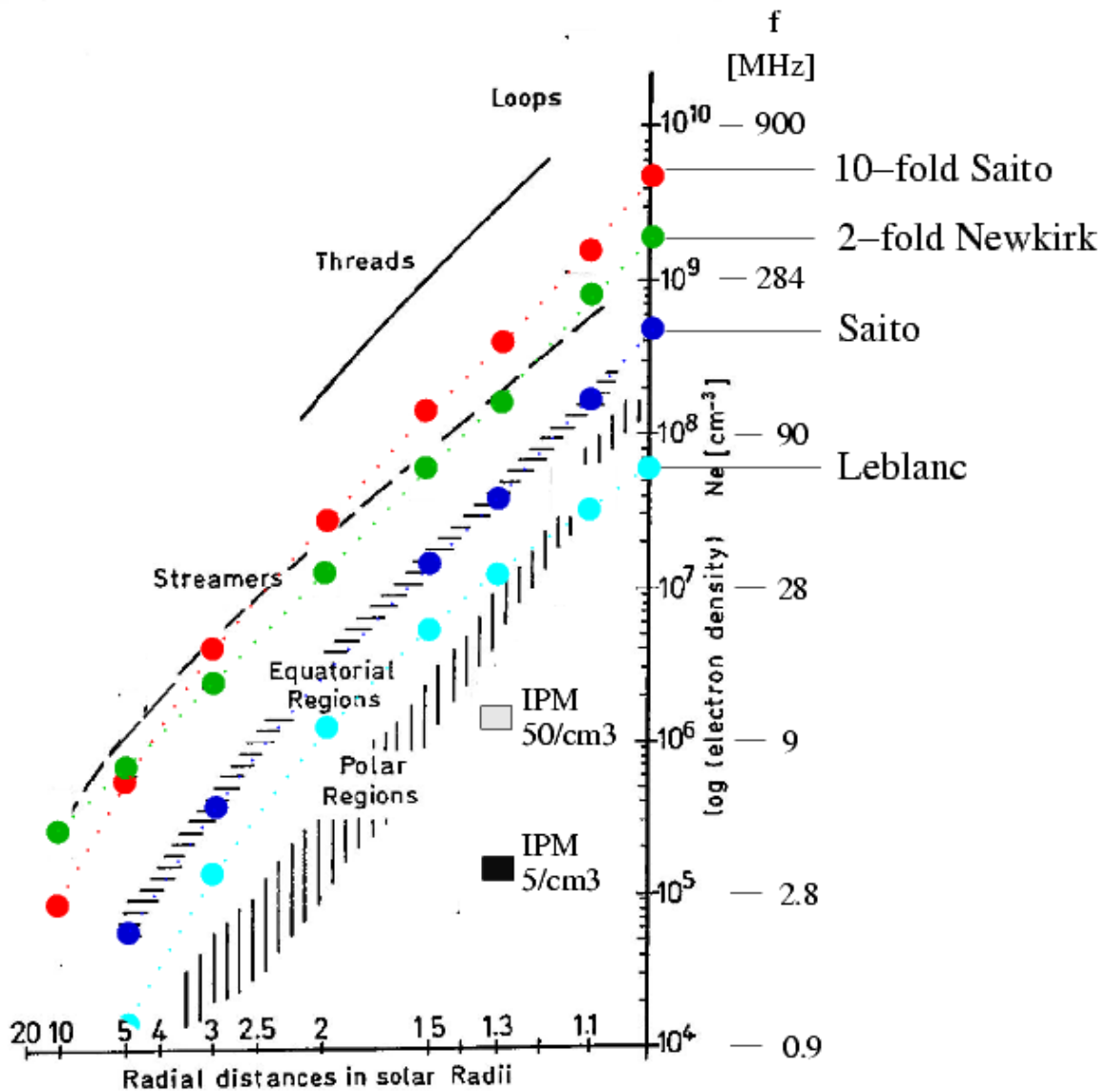


Figure 2.24: Electron densities in the solar corona: dashed areas are based on eclipse observations (S. Koutchmy) and the filled circles describe the densities given by different models (Saito, Newkirk, Leblanc et al.). The two filled boxes show densities given by the IP density models, with two different densities near Earth: 5 cm^{-3} during activity minimum and 50 cm^{-3} during activity maximum.

Chapter 3

Emission mechanisms

3.1 Radiation of atoms and molecules

Bound-bound (energy quantized – line spectrum)

- **Absorption**
- **Emission**

Bound-free (continuum emission)

- **Ionization**

Free-bound (continuum emission)

- **Recombination**

Free-free (continuum emission)

- **Bremsstrahlung**

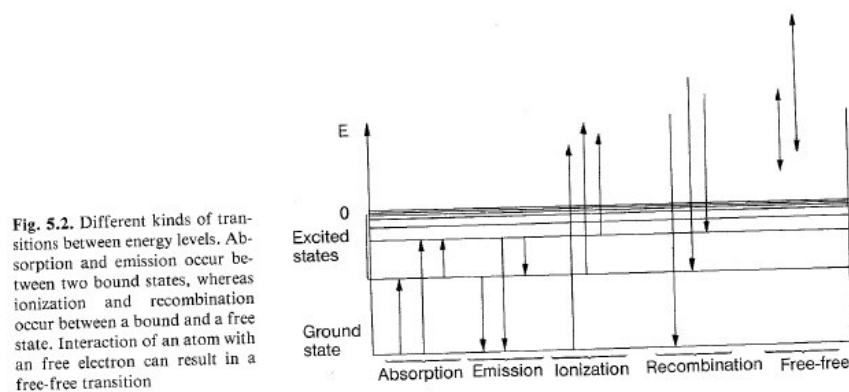


Figure 3.1: From Karttunen et al.: Fundamental Astronomy (Springer)

Spectral lines

- **Electron-positron annihilation (511 keV)** $e^+ + e^- \rightarrow 2\gamma$
- **Neutron capture (2.22 MeV)** $^1H + n \rightarrow ^2H + \gamma$
- **De-excitation (radiative or collisional)**

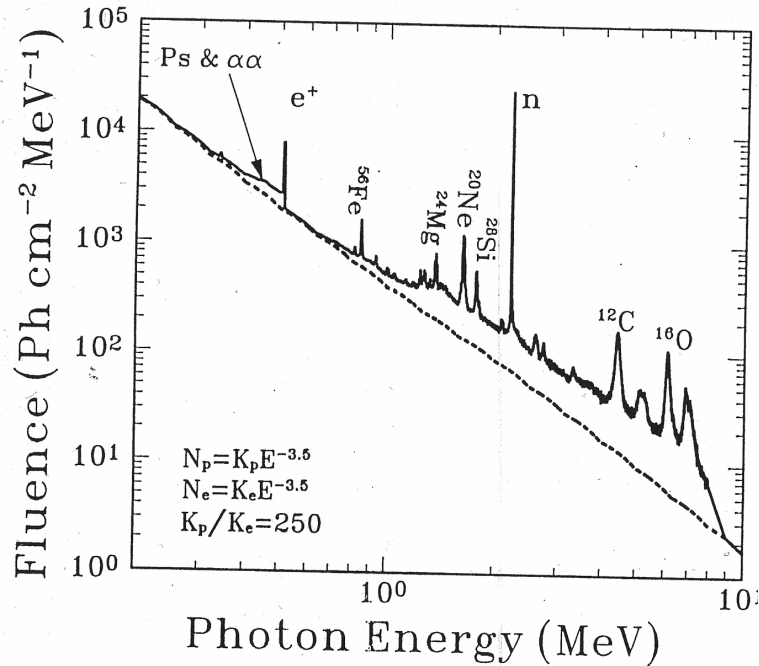


Figure 3.2: Neutron capture 2.223 MeV (delayed; attenuated near solar limb); e^+ annihilation 511 keV; De-excitation ^{16}O – 6.129 MeV; ^{12}C – 4.438 MeV; ^{20}Ne – 1.634 MeV etc.; Ps (positron continuum) + $\alpha\alpha$ -interactions; Ions are due to accelerated particles (solar flares), break-up of He

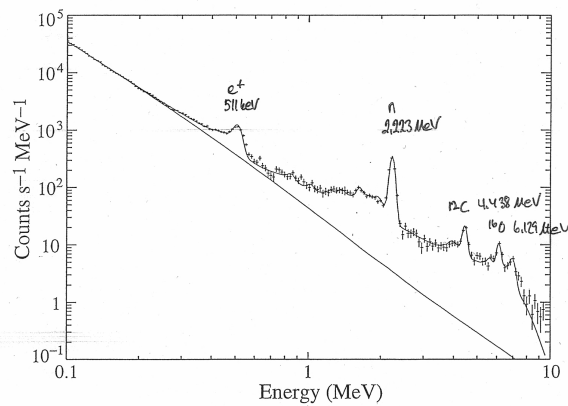


Figure 3.3: June 4, 1991 event: Radio flux at 80 GHz 140 000 sfu (1.4 billion Jansky)!

> 16 MeV

	Date	Time (UT)	GOES Class	>50 keV	>300 keV	Narrow Lines >1 MeV	2.223 MeV
<i>γ-rays</i>	22-Nov-1998	6:39	X3.7	*	*		
	18-Aug-1998	22:16	X4.9	1830+/-21**	70+/-4**		
	29-May-1998	00:56	M6.7	916+/-15	13+/-1.5		
	08-May-1998	01:57	M3.1	398+/-4			
	01-Dec-1997	13:27	C6.6	<1			
	01-Dec-1997	2:34	M1.2	48.0+/-1.6			
	28-Nov-1997	5:02	M6.8	165.1+/-6.3			
	27-Nov-1997	16:13	C3.8	125.6+/-2.0			
*	27-Nov-1997	13:15	X2.6	680+/-34	25.2+/-4.1	1.2+/-0.6	1.2+/-0.3
	26-Nov-1997	18:32	M2.0	20.6+/-1.2			
	17-Nov-1997	15:05	C8.6	47.4+/-3.4			
	27-Oct-1991	13:15	X6.1	*	*	63+/-3	141+/-3
<i>γ-rays</i>	30-Jun-1991	2:56	M5.0	*	*	2.8+/-0.9	
* <i>γ-rays and neutrons</i>	04-Jun-1991	3:41	X12+	*	*	831+/-24	1050+/-19
<i>neutrons</i>	01-Jun-1991	15:05	X12+	+	+	+	+

Figure 3.4: CGRO-OSSE solar flare observations (previous solar max)

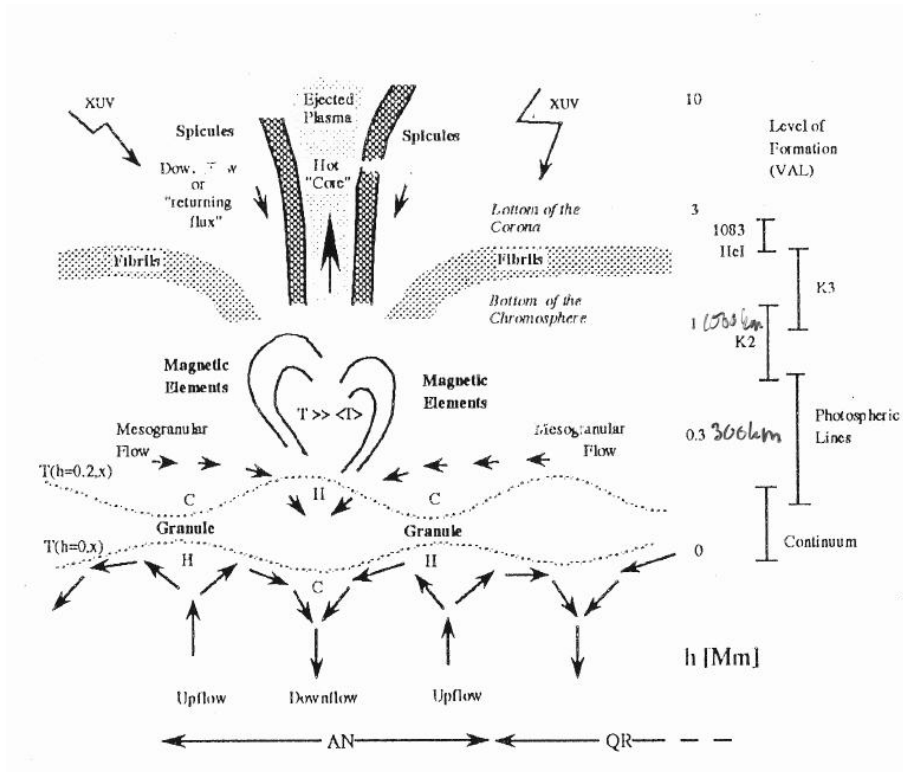


Figure 3.5: Formation heights of UV and EUV spectral lines

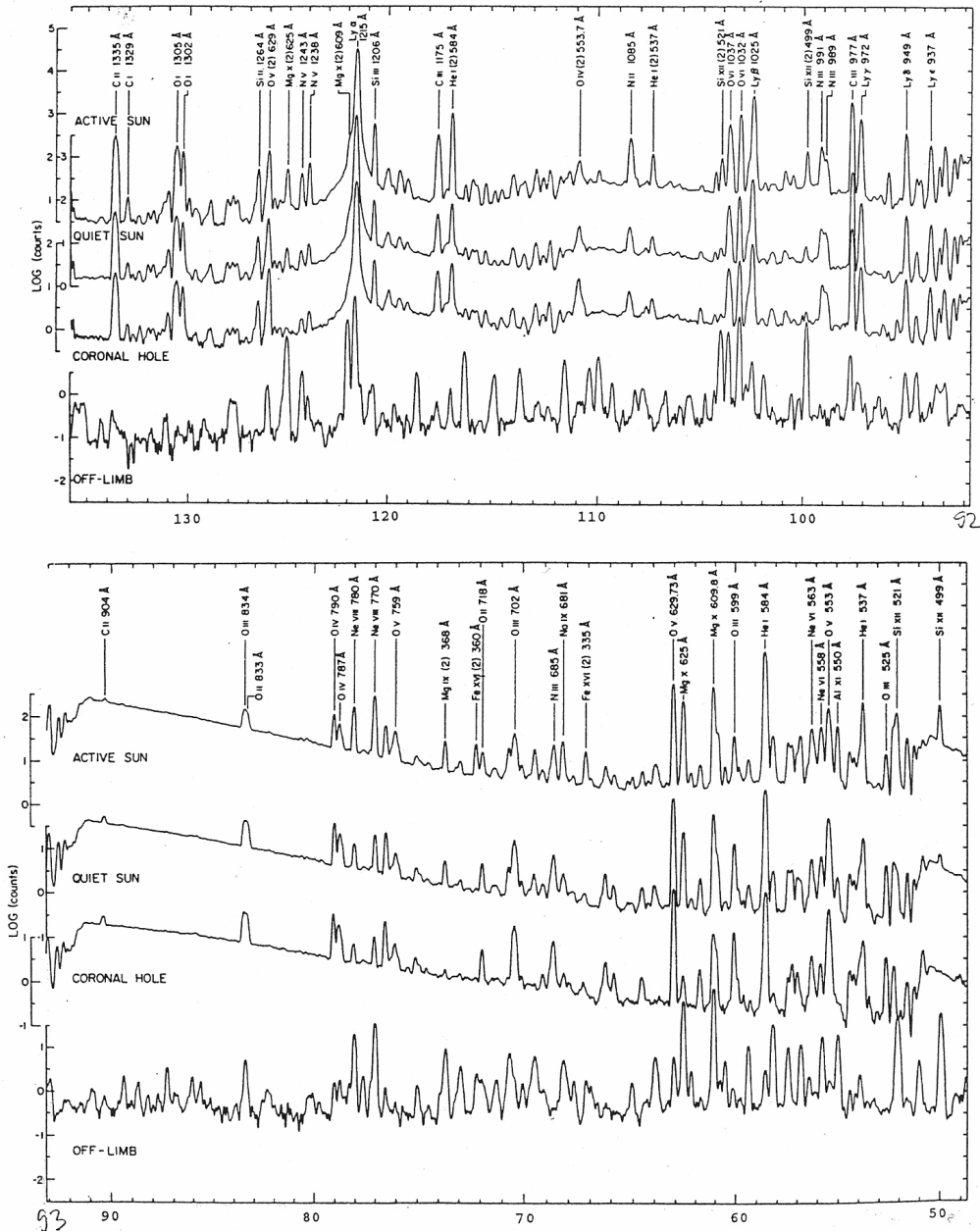


Figure 3.6: Solar spectra in far UV, Spacelab data (Vernazza & Reeves, 1978)

Plasma diagnostics with spectral lines

- **Line identification (CHIANTI database)**
- **Temperature T**, in K, from spectral fit
- **Emission measure EM**, in cm^{-3} , from spectral fit or filter ratio
- **Electron density N**, in cm^{-3} , $\text{EM} = \int_0^V N^2 dV = N^2 V$

Mason & Monsignori Fossi, *Astron. Astrophys. Rev.* 6 (1994), 123-179

Table 4.1. *Some prominent ultraviolet emission lines*

Wavelength (nm)	Identification	Temperature of formation (K)
17.1	Fe IX	900 000
17.48	Fe X	1 100 000
18.04	Fe XI	1 300 000
19.5	Fe XII	1 500 000
21.9	Fe XIV	1 800 000
23.4	Fe XV	2 000 000
24.9	Ni XVII	2 500 000
25.1	Fe XVI	2 200 000
25.6	He II	50 000
26.3	Fe XVI	2 200 000
26.5	Fe XIV	1 800 000
28.4	Fe XV	2 000 000
30.4	He II	50 000
33.5	Fe XVI	2 200 000
36.8	Mg IX	1 000 000
46.5	Ne VII	500 000
55.4	O IV	160 000
62.5	Mg X	1 100 000
99.7	C III	70 000
103.2	O VI	320 000
117.6	C III	70 000
120.6	Si III	30 000
121.5	H I ^a	20 000
124.0	N V	200 000
133.5	C II	20 000
139.4	Si IV	60 000
140.3	Si IV	60 000
153.3	Si II	14 000
155.0	C IV	110 000
164.0	He II	50 000
165.7	C I	<10 000
167.0	C I	<10 000
180.8	Si II	14 000
181.7	Si II	14 000

Note:

^a Lyman- α of neutral hydrogen.

Figure 3.7: Table from K.J.H. Phillips, *Guide to the Sun*, Cambridge Univ. Press, 1992

3.2 Bremsstrahlung (free-free continuum emission)

- Thermal bremsstrahlung
- Nonthermal bremsstrahlung

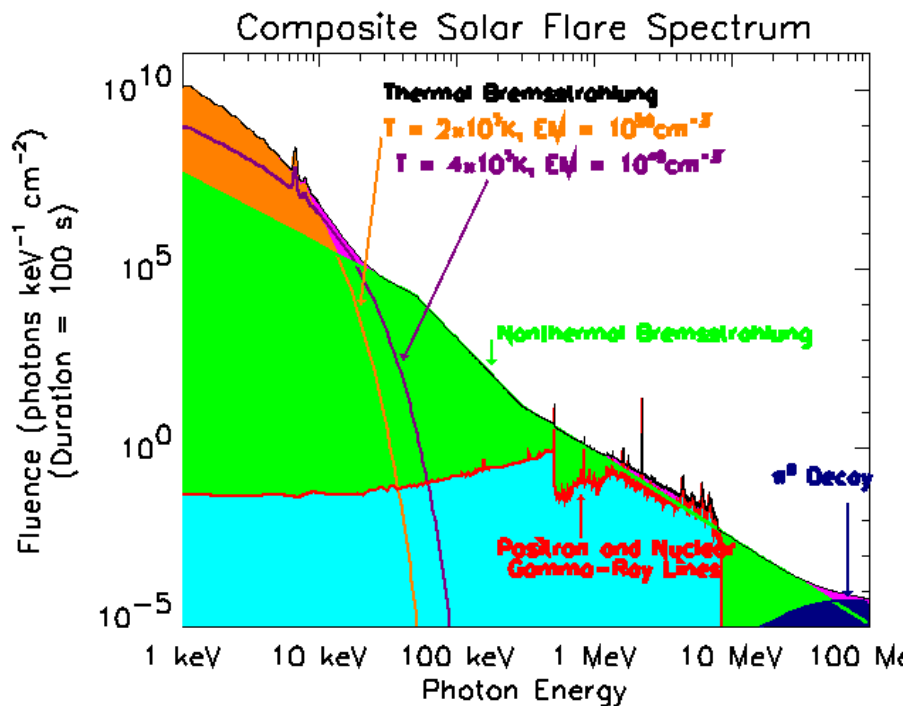
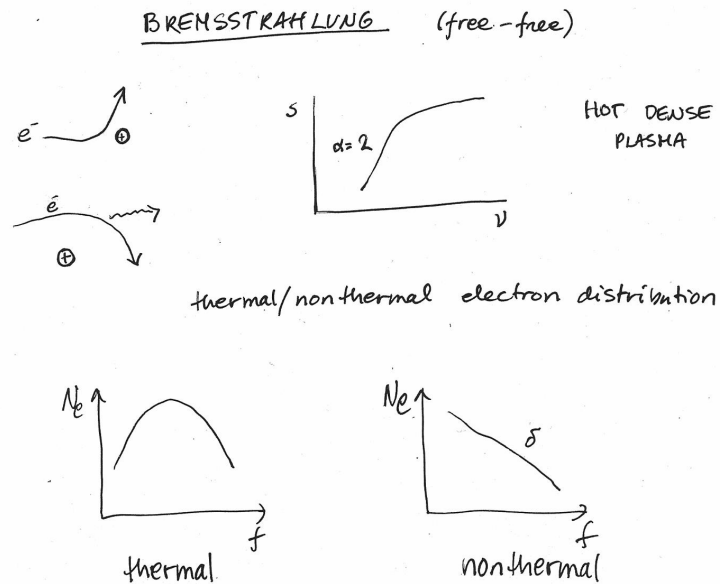


Figure 3.8: $E = hc/\lambda$, $1 \text{ keV} = 12 \text{ \AA}$; from RHESSI website

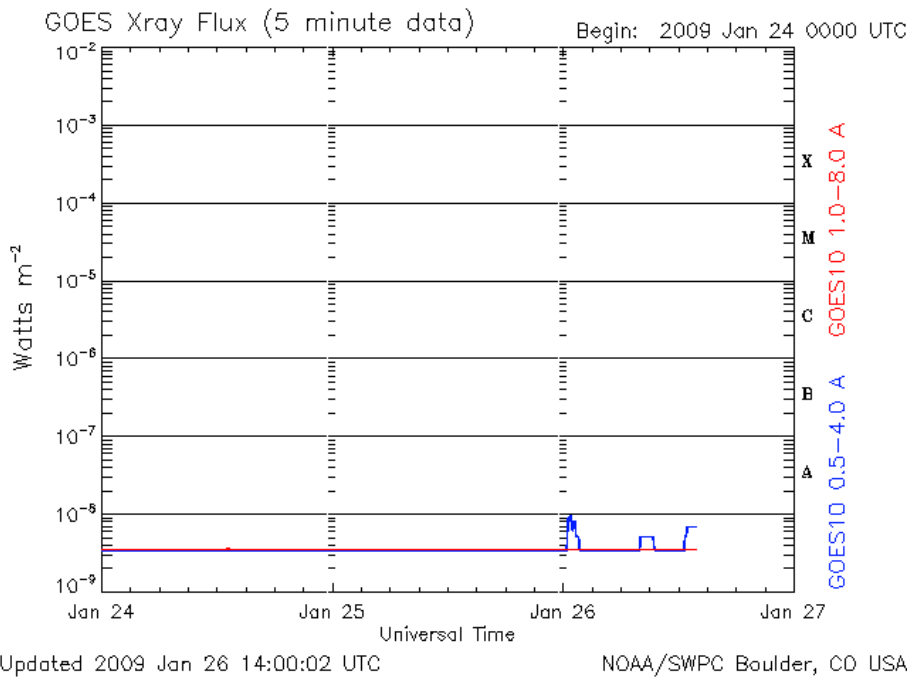
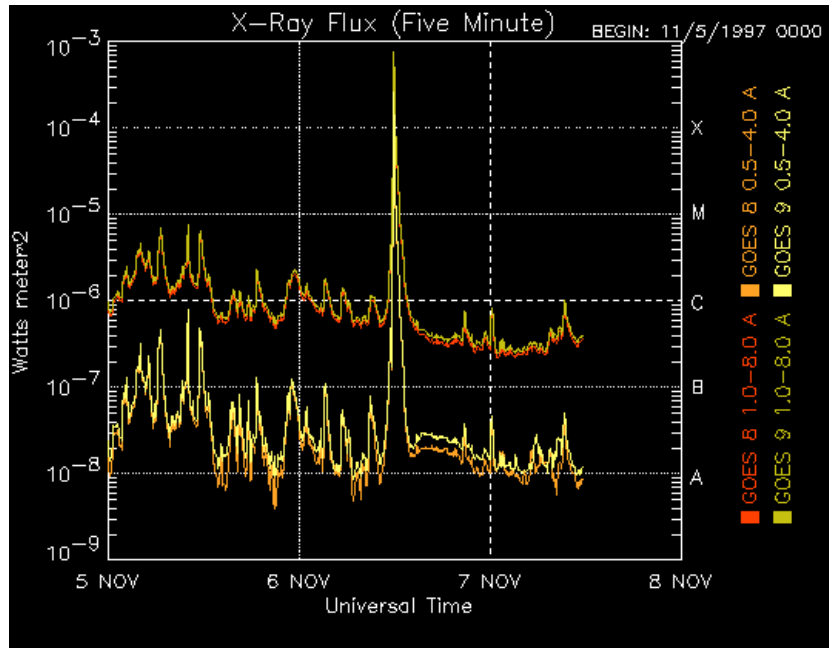
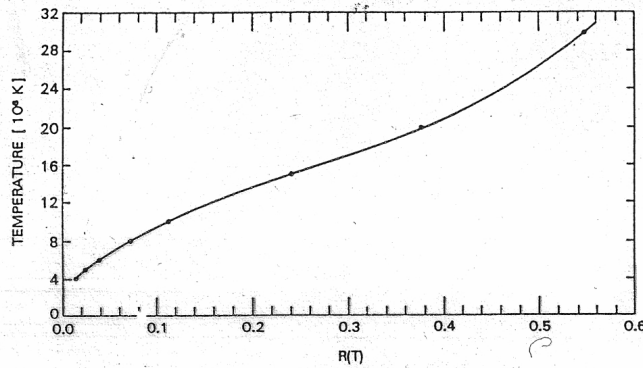


Figure 3.9: Thermal example: soft X-rays from the Sun. GOES satellites (1974–) are on geosynchronous orbits; 2-3 satellites cover 24 hours/day of continuous observations. Ion chamber detectors: 1–8 Å (12–1.5 keV) and 0.5–4 Å (25–3 keV). Flares are classified according to their flux: C, M, X classes. **Note that these are full disk observations – all events get detected and mixed if there are many happening at the same time!**

EXPRESSIONS TO DETERMINE TEMPERATURES AND
EMISSION MEASURES FOR SOLAR X-RAY EVENTS FROM
GOES MEASUREMENTS



NOAA-NGDC
GOES-satellite,
full sun

Fig. 3. Calculated points for the effective plasma temperatures as a function of detector ratios, and our analytic fit to them given by Equation (9).

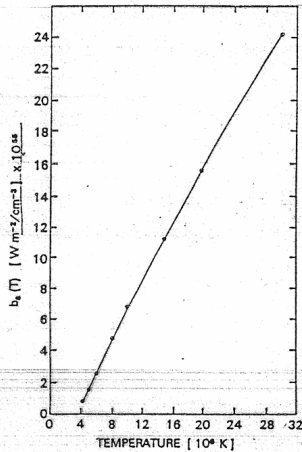


Fig. 4. Calculated points for the response per unit emission measure of the 1 to 8 Å GOES detector as a function of temperature of the emitting plasma. Our analytic fit to these points as given by Equation (10) is also shown.

$$R(T) = B_4/B_8 = b_4(T)/b_8(T).$$

$$T(R) = 3.15 + 77.2R - 164R^2 + 205R^3,$$

$$10^{25} b_8(T) = -3.86 + 1.17T - 1.31 \times 10^{-2} T^2 + 1.78 \times 10^{-4} T^3$$

$$EM = B_8/b_8(T).$$

$$EM = 10^{25} B_8 / (10^{25} b_8(T)).$$

B_i - flux value above flare background
 b_i - temperature dependent part of the detector's response

$$\begin{cases} B_8 = 1-8 \text{ \AA} \\ B_4 = 0.5-4 \text{ \AA} \end{cases}$$

T - plasma temperature, 10^6 K
 EM - emission measure, cm^{-3}

© Solar Phys. 95 (1985) 323-329

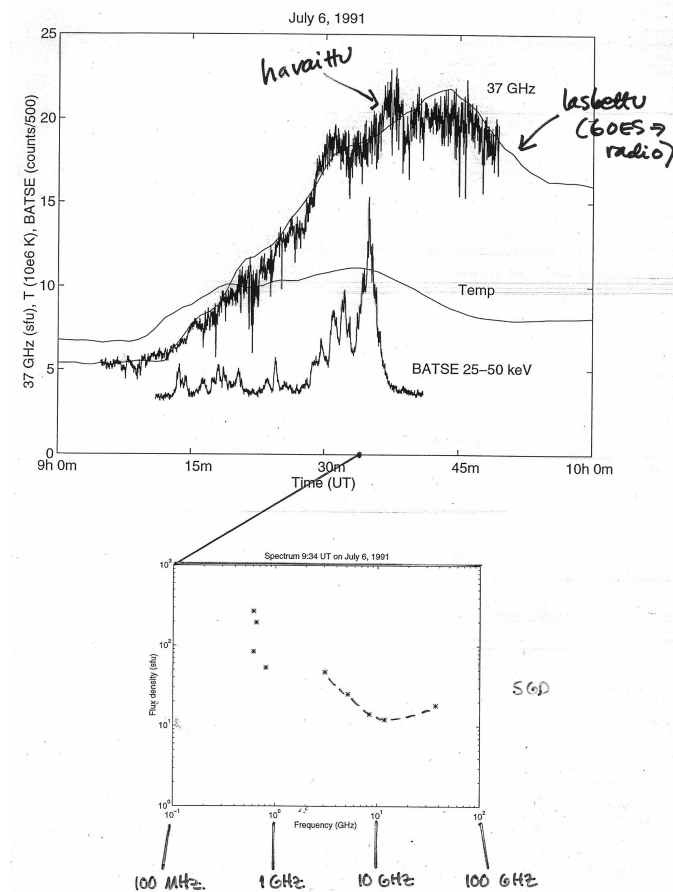


Figure 3.10: Gradual solar event: observed radio flux ('havaittu') and calculated radio flux ('laskettu') using the filter ratio from GOES X-rays.

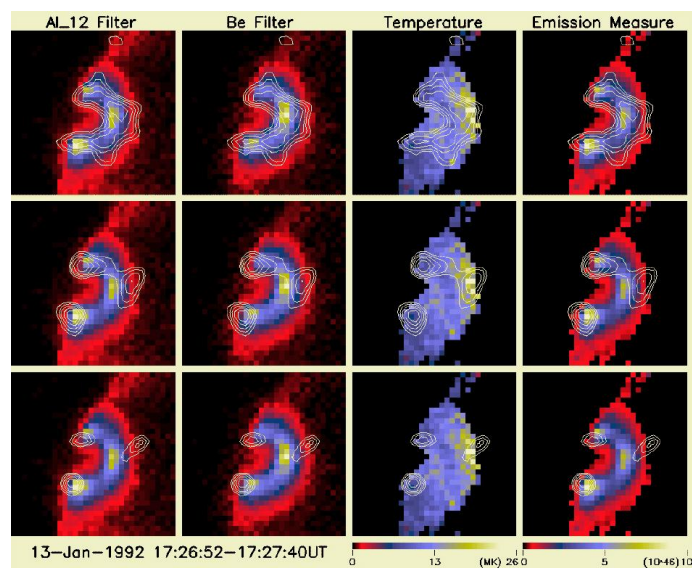


Figure 3.11: Masuda-flare: non-thermal source at the loop top? Loop is filled with hot plasma radiating in soft X-rays, with hard X-ray sources at loop footpoints (First Yokoh results, 1992)

3.3 Gyroemission

The gyrofrequency ω_B for a particle with a charge q , mass m , and Lorentz factor γ , gyrating in a magnetic field B , pitch angle ψ being the angle between the B vector and the velocity vector, is in Gaussian units (Lang, 1980)

$$\omega_B = \frac{qB}{\gamma m c} \sin \psi \quad (3.1)$$

The gyrofrequency thus depends on the magnetic field strength B (in Gauss) and for non-relativistic electrons the gyrofrequency becomes

$$\nu_B = 2.8 \times 10^6 B \text{ (Hz)} \quad (3.2)$$

The particles gyrating in the magnetic field can have thermal or non-thermal velocity distributions. Emission can be classified as:

Gyroresonance(cyclotron) emission:

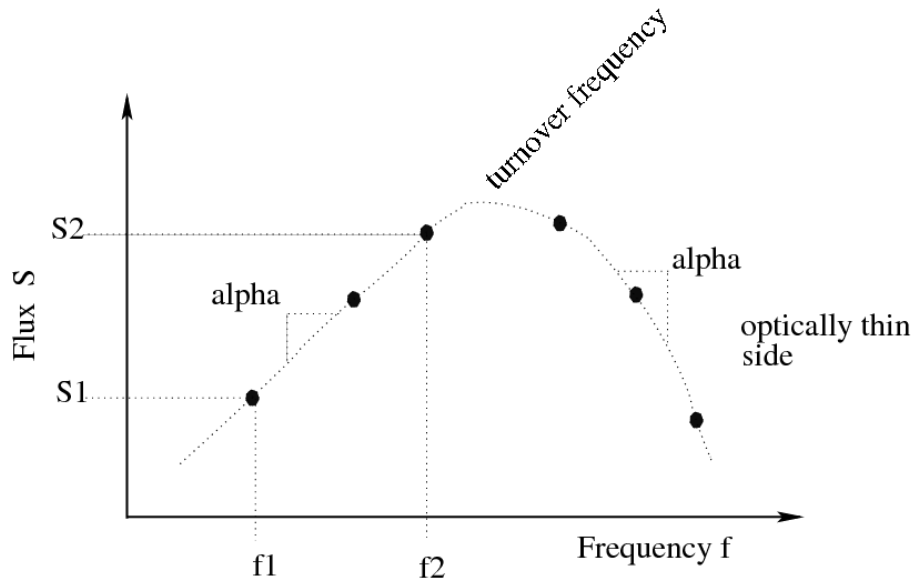
- non-relativistic ($\gamma = 1$) particles
- gyroresonance emission is concentrated at the fundamental frequency ($\omega = \Omega_e$) and at harmonics $s = \nu/\nu_B < 10$
- thermal electron distribution
- radiation is directed mainly along the magnetic field

Gyrosynchrotron emission:

- mildly relativistic ($\gamma < 2-3$) particles
- gyrosynchrotron emission is strong at harmonic numbers $s = 10 < \nu/\nu_B < 100$
- both thermal and power-law electron distributions
- emission has a broad maximum perpendicular to the magnetic field

Synchrotron emission:

- relativistic particles
- broad continuum at high harmonics $s \sim (\gamma \sin \theta)^3$, i.e. near $\omega = \Omega_e \gamma^2 \sin \theta$
- power-law electron distributions only
- emission directed in the direction of instantaneous electron motion; peak of radiation perpendicular to the magnetic field



SPECTRAL INDEX $\alpha = \frac{\log S_2 - \log S_1}{\log f_2 - \log f_1}$

GYROSYNCHROTRON RADIATION

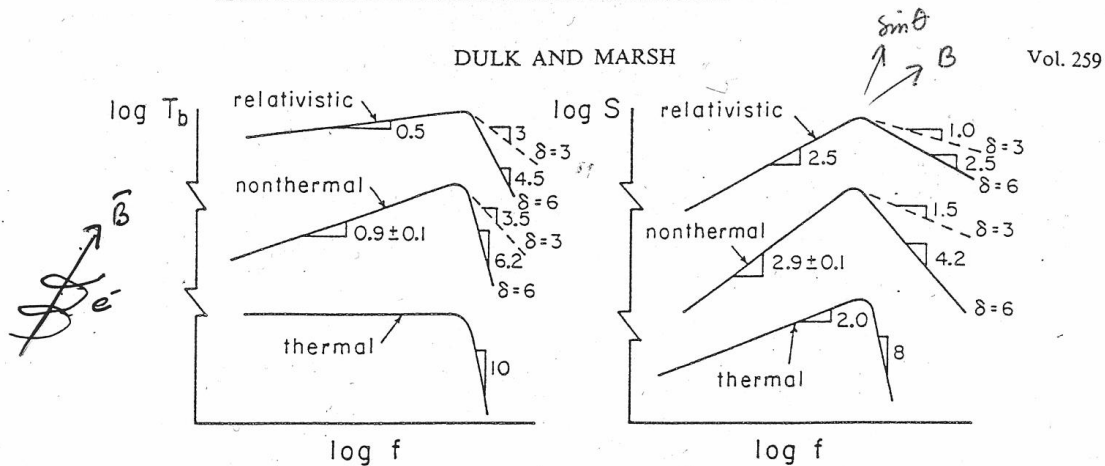


FIG. 2.—Shapes of brightness and flux spectra for thermal and nonthermal electron distributions. The shapes of the curves for relativistic power-law distributions were taken from Ginzburg and Syrovatskii (1965).

δ -electron power law

Astrophys. J. 259
(350-358)

3.3.1 Gyrosynchrotron emission: mildly relativistic electrons

For optically thin ($\tau \ll 1, \nu > \nu_{peak}$) sources the radio flux density reduces to

$$S_\nu = \frac{2k\nu^2}{c^2} \int \tau T_{ef} d\Omega = \eta L \Omega \tag{3.3}$$

$$\eta \approx 3.3 \times 10^{-24} 10^{-0.52\delta} (\sin \theta)^{-0.43+0.65\delta} \left(\frac{\nu}{\nu_B}\right)^{1.22-0.90\delta} BN$$

where $d\Omega$ = source solid angle, L = source length along the line of sight, N = particle density. These approximations are valid for power-law indices $2 \leq \delta \leq 7$, viewing angles $\theta \geq 20^\circ$, and harmonic numbers $\nu/\nu_B \geq 10$. The original calculations for gyrosynchrotron emission were presented by Ramaty (1969), and are now widely used because computers are more powerful!. These are simplified expressions by Dulk and Marsh (Astrophysical Journal, Vol. 259, 1982, p. 350-358).

There is a way to determine B in the corona, using radio observations:

$$\nu_{peak} \approx 2.72 \times 10^3 10^{0.27\delta} (\sin \theta)^{0.41+0.03\delta} (NL)^{0.32-0.03\delta} B^{0.68+0.03\delta} \quad (3.4)$$

But you then need δ (from spectral hard X-ray observations), NL and θ (from soft X-ray, EUV, and/or radio imaging)... Note: these are valid if the numbers are given in cgs units.

3.3.2 Gyrosynchrotron emission: thermal electrons

For thermal electrons with a Maxwellian energy distribution Dulk and Marsh present a simplified expression suitable for semiquantitative analytical modelling for the optically thin spectral region

$$S_\nu = \frac{2k\nu^2}{c^2} \int \tau T_{ef} d\Omega = \eta L \Omega, \quad \eta \approx 60 \times 10^{-24} \left(\frac{\nu^8}{\nu_B^2}\right) T^8 \sin^6 \theta B^{11} N. \quad (3.5)$$

The spectral peak of thermal gyrosynchrotron emission depends heavily on the plasma temperature and two expressions are given for different temperature ranges:

$$\nu_{peak} \approx 1.4 \left(\frac{NL}{B}\right)^{0.1} (\sin \theta)^{0.6} T^{0.7} B \quad (10^8 < T < 10^9 \text{ K}) \quad (3.6)$$

$$\nu_{peak} \approx 475 \left(\frac{NL}{B}\right)^{0.05} (\sin \theta)^{0.6} T^{0.5} B \quad (10^7 < T < 10^8 \text{ K}) \quad (3.7)$$

3.3.3 Synchrotron emission: ultrarelativistic electrons

In the case of ultrarelativistic electrons the emission is very strongly beamed in the direction of the electron motion and collisions are rare. The expressions for emissivity and peak frequency in the range $2 \leq \delta \leq 5$ can be written as

$$\eta \approx 8.6 \times 10^{-24} (\delta - 1) \sin \theta \left[\frac{0.175}{\sin \theta} \left(\frac{E_0}{1 \text{ MeV}}\right)^{-2} \frac{\nu}{\nu_B} \right]^{-(\delta-1)/2} BN, \quad (3.8)$$

$$\begin{aligned} \nu_{peak} &\approx 3.2 \times 10^7 \sin \theta \left(\frac{E_0}{1 \text{ MeV}}\right)^{(2\delta-2)/(\delta+4)} \\ &\times \left[8.7 \times 10^{-12} \frac{\delta-1}{\sin \theta} NL \right]^{2/(\delta+4)} B^{(\delta+2)/(\delta+4)} \end{aligned} \quad (3.9)$$

The emission occurs over a broad band centered at $\nu \approx \nu_B \gamma^2 \sin \theta / 2$, i.e. at harmonic numbers $s \approx (\gamma \sin \theta)^3$.

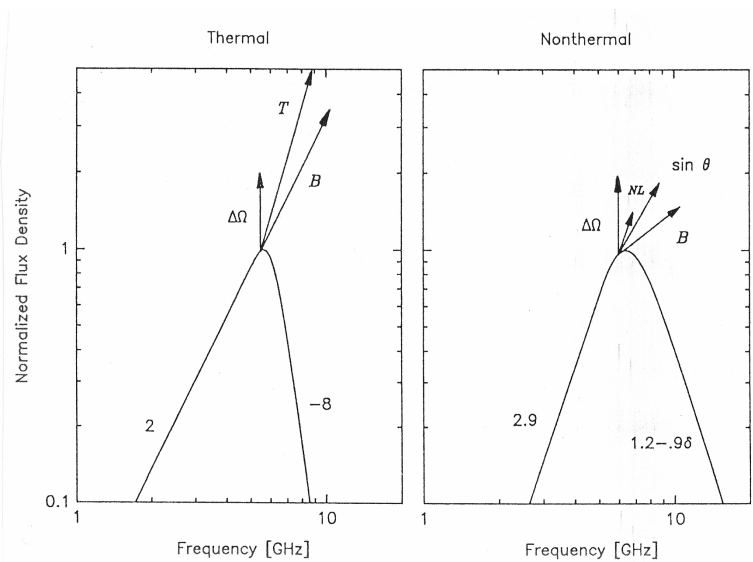
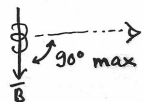


Figure 3.12: Parameters that change the spectral shape: temperature T , magnetic field strength B , source solid angle Ω , density \times source length NL (along the line of sight), viewing angle $\sin \theta$. (From Stähli, Gary & Hurford, Solar Phys. 120, 1989)

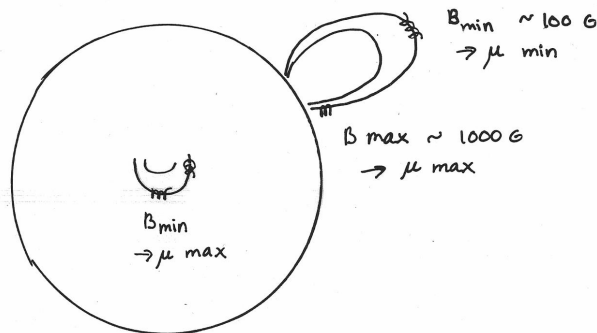
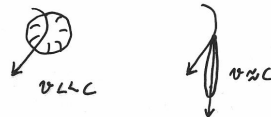
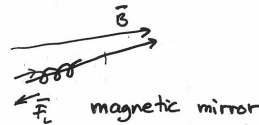
RADIO EMISSION DIRECTIVITY

GYROSYNCHROTRON RADIATION:

- TRAPPING (FLARE LOOPS)
- BEAMING
- VIEWING ANGLE



- RADIATED POWER $P \propto B^2$



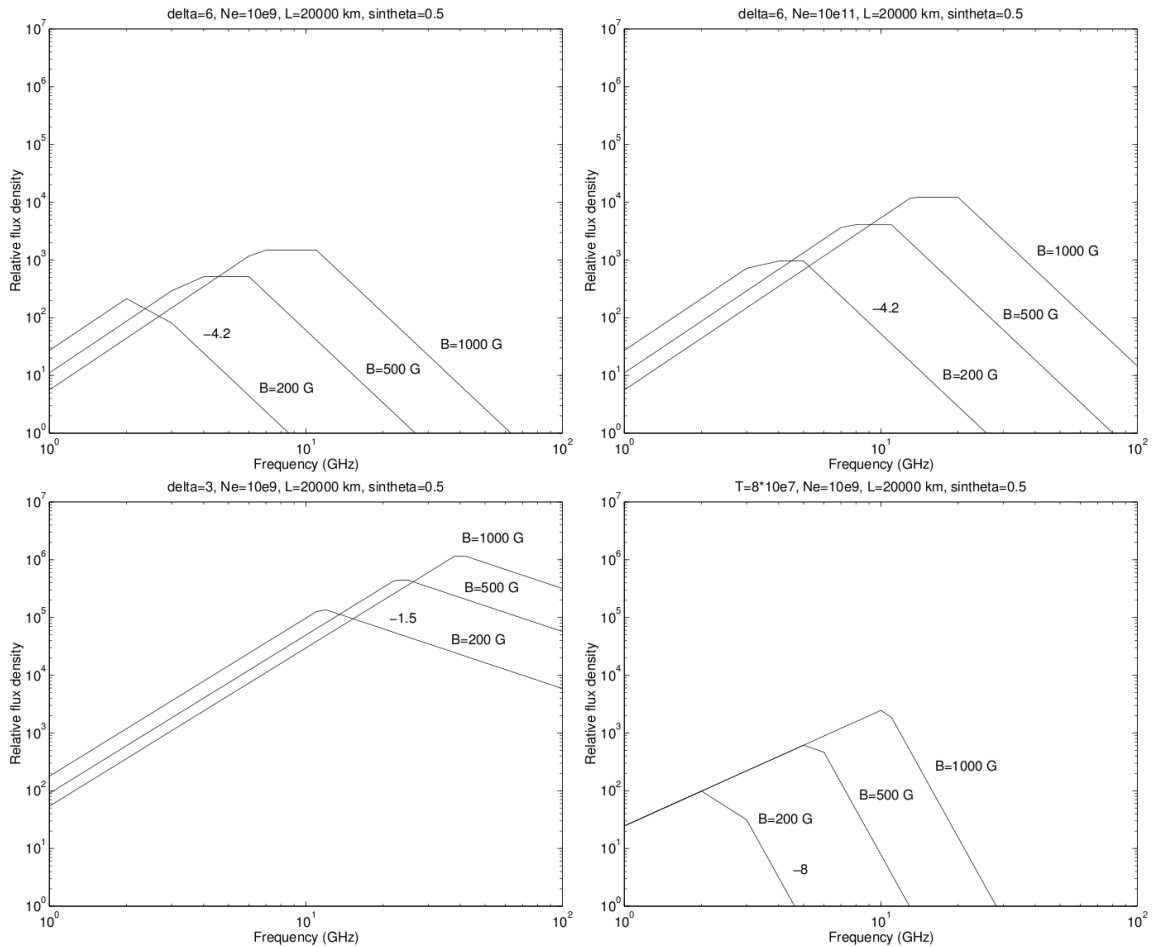


Figure 3.13: Examples of flux density spectra for gyrosynchrotron emission calculated from the given approximations, for magnetic field values of 200, 500, and 1000 Gauss. Path length L and viewing angle θ remain the same in all cases.

Top left:

flux density spectra for non-thermal gyrosynchrotron emission for $\delta = 6$, $N_e = 10^9 \text{ cm}^{-3}$, $\theta = 30^\circ$, $L = 20\,000 \text{ km}$

Top right:

otherwise similar to top left but now $N_e = 10^{11} \text{ cm}^{-3}$ (electron density increased)

Bottom left:

otherwise similar to top left but now $\delta = 3$ (population of more energetic electrons present)

Bottom right:

flux density for thermal gyrosynchrotron emission, at plasma temperature $T_{ef} = 8 \times 10^7 \text{ K}$

The figures show how an increasing magnetic field strength and a decreasing electron power law index move the spectral peak towards the higher frequencies, while changes in the source electron density alter the flux density, but do not change significantly the general spectral shape.

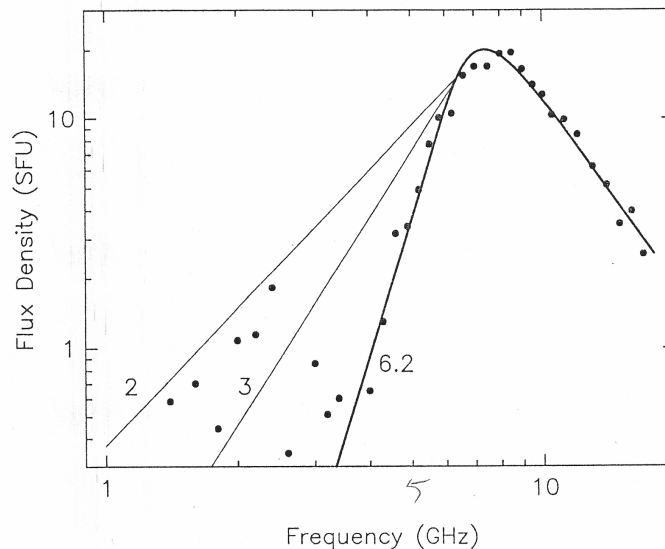


Fig. 8. Example of a spectrum with a steep low-frequency slope. The observed data points and the fit are shown together with the slopes expected from theory for a homogeneous source (about 2 for thermal and about 3 for nonthermal gyrosynchrotron emission).

Figure 3.14: Determining the spectral shape: especially at the optically thick side this can be difficult. A spectrum can always be a combination of several sources, at different T and N_e . This plot is made from Owens Valley observations, at several single frequencies between 1 and 18 GHz.

3.3.4 How to distinguish between bremsstrahlung and gyrosynchrotron emission?

- Thermal bremsstrahlung is only weakly polarized
- If plasma is isothermal and optically thick, polarization is zero
- Polarization in the optically thick side of gyrosynchrotron spectrum is extremely difficult to interpret
- On the optically thin side the degree of circular polarization in gyrosynchrotron emission is approximately 10...30%
- Polarization can be right (RCP) or left (LCP) handed and it can change during flare emission - depending on which end of the plasma loop electrons are gyrating
- Linear polarization has not been observed from the Sun (according to theory, it cannot propagate through the solar atmosphere)

3.4 Masers

Maser = amplification of radio waves by stimulated emission of radiation

Solar case for maser emission:

Electron cyclotron maser occurs when the resonance between electrons spiraling around a magnetic field and circularly polarised waves leads to growth of the waves.

The condition of growth is certain form of **anisotropy** → loss cone anisotropy at loop footpoint.
Occurs at ν_B and second harmonic.

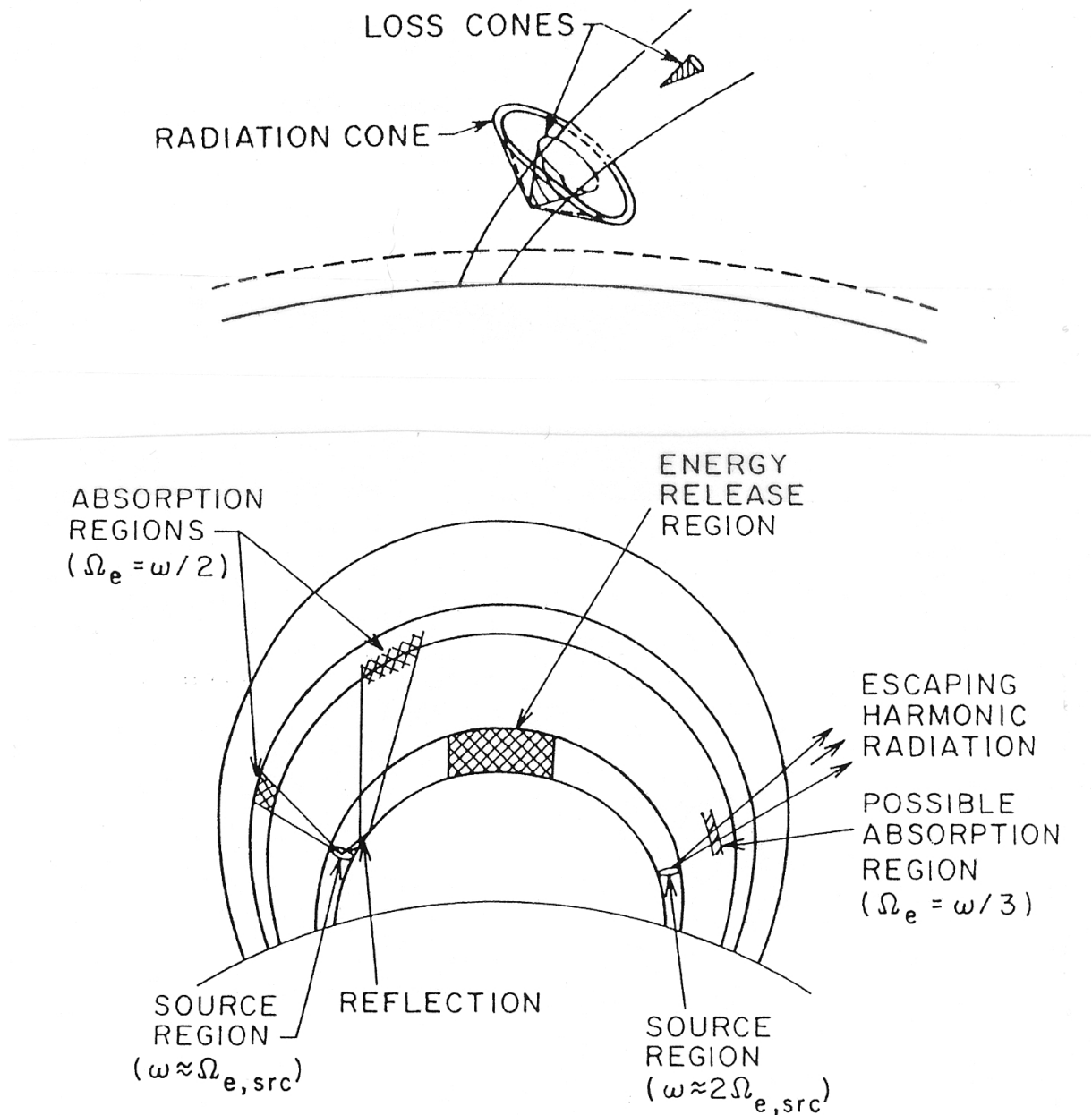
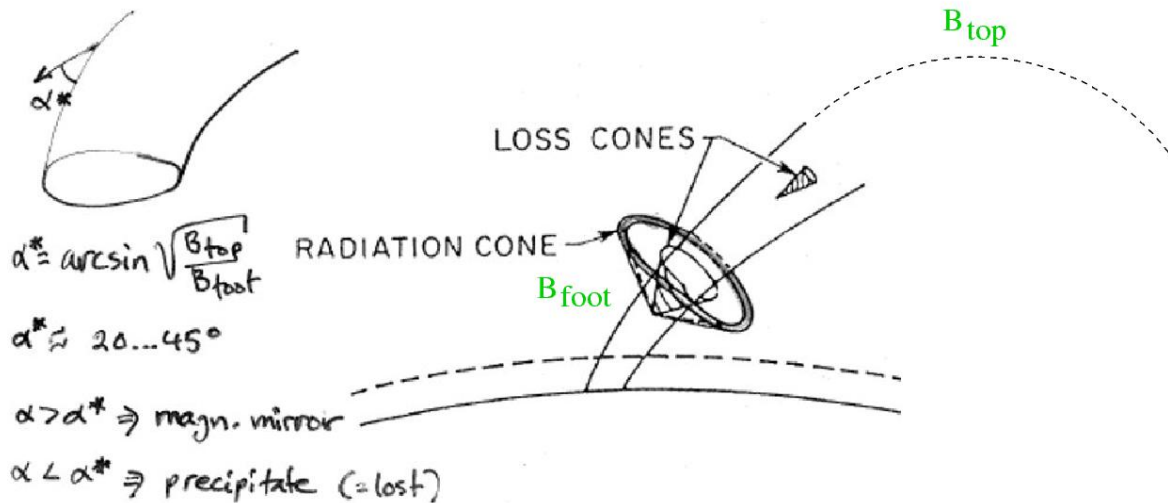


Figure 4 Schematic drawing of a sequence of magnetic flux tubes. At the top of a loop is a region where energy release is occurring. On the left is sketched a maser source region emitting at frequency $\omega = \Omega_e + \Delta$ at a location where the field strength is B_{src} . The cone of radiation is shown, including a reflection of the portion directed toward higher field strength; this radiation is reabsorbed at locations where $B = B_{\text{src}}/2$. At the right is sketched a maser operating at $2\Omega_e + \Delta$, perhaps being reabsorbed where $B = 2B_{\text{src}}/3$.



3.5 Absorption effects

Razin effect

The presence of a medium, tends to suppress synchrotron and gyrosynchrotron radiation at low frequencies. The Razin frequency ν_R in a plasma with an electron density N_e is defined as

$$\nu_R = \frac{20N_e}{B} = \frac{2\nu_p^2}{3\nu_B} \quad (3.10)$$

For ultra-relativistic electrons the suppression occurs at $\nu \leq \nu_R$ and for mildly relativistic and non-relativistic electrons at harmonics $s = \nu/\nu_B \leq \nu_p^2/\nu_B^2$ (Melrose, 1985; Dulk, 1985).

An illustrative example: in order to have Razin suppression effective up to 5 GHz, the electron density N_e (cm^{-3}) must be greater than $\sim 1.7 \times 10^8 B$. The required density is high even with the minimum expected magnetic field strength $B = 100$ G in the solar case.

Gyrosynchrotron self-absorption

Absorption by the population of radiating electrons itself. The process requires a strong magnetic field and a high column density of electrons.

Free-free absorption

Collisional damping (free-free absorption) occurs when electrons begin to oscillate in resonance with the electric field and then collisions destroy the oscillation: the wave energy decreases and heats the plasma. Can happen when electromagnetic waves travel through cool dense structures in the solar atmosphere

Solar burst spectra

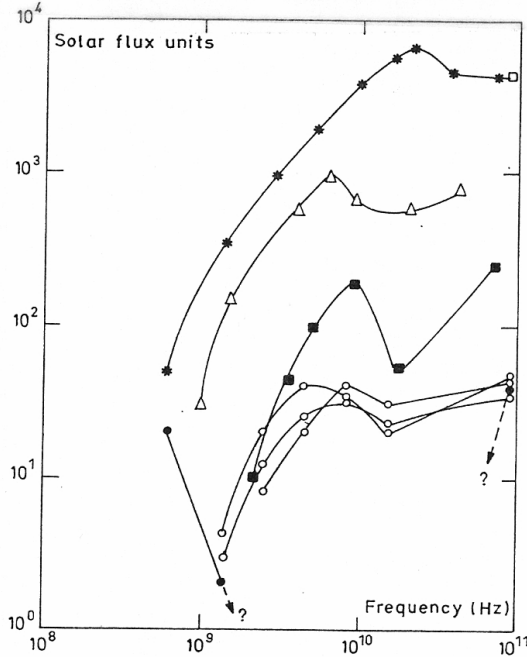


Fig. 3. Examples of solar burst spectra published in the literature, exhibiting a "flattening" towards mm-wavelengths or the superposition of a mm-wave spectral component. These results were obtained by the authors indicated is below. The measurements were taken with relatively poor time resolution and sensitivity. * Croom (1970); □ Cogdell (1972); ○ Shimabukuro (1972); ● Shimabukuro (1970); ■ Akabane et al. (1973); △ Zirin and Tanaka (1973)

P. Kaufmann et al.: Synchrotron/inverse Compton solar burst emission

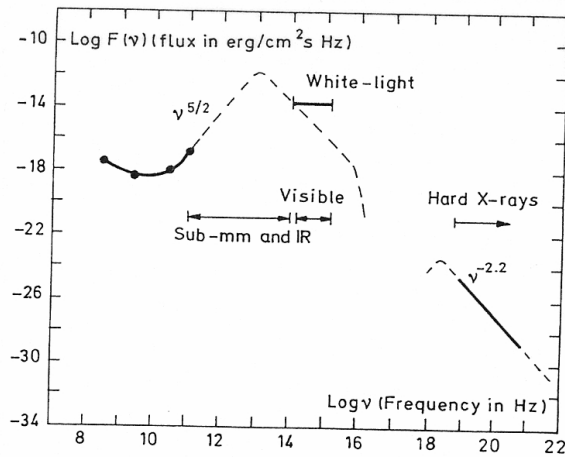


Fig. 4. The presently suggested interpretation associates the observed mm-wave spectrum (solid line for $\lambda \gtrsim 3$ mm) to a synchrotron spectrum peaking in the infrared range. Dashed lines are for a predicted qualitative spectrum at a time $t_0 < t < t_c$. The reported fluxes for white-light continuum in flares are close to the predicted synchrotron fluxes in the visible. Observed hard X-rays (solid line) are explained by inverse Compton quenching on the synchrotron produced photons, accounting for the short time scale durations (≈ 60 ms)

Figure 3.15: Examples of peculiar radio spectra where flux rises towards the high frequencies (there is no spectral turnover around 10–20 GHz).

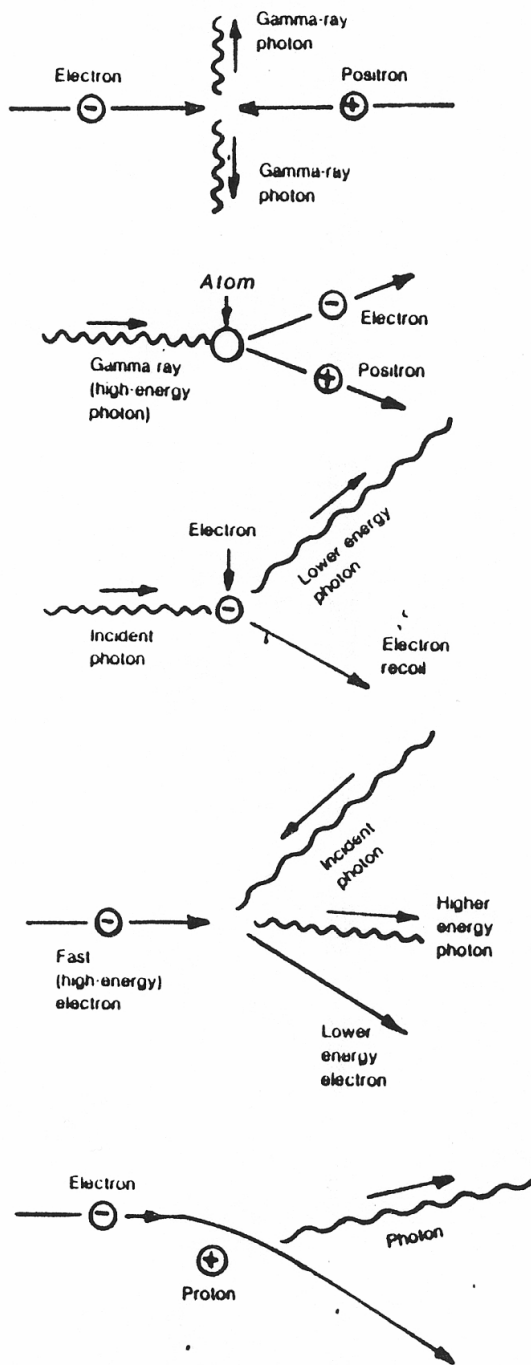


Fig. 10-14. Some particle-particle and particle-photon interactions.

Matter into radiation. Annihilation of an electron-positron pair produces gamma-ray photons (511 000 electron volt line).

Radiation into matter. Photon transforms into an electron-positron pair on impact with atom. (Radiation into matter).

Compton scattering. Photon wavelength increased. Photon gives up some of its energy to electron. A Compton scattering event is a down-converter of the photon frequency.

Inverse Compton scattering. Photon wavelength decreased (light to x-ray or gamma ray). Electron gives up some of its energy to photon. An inverse Compton scattering event is an up-converter of photon frequency.

Bremsstrahlung. Free-free interaction of electron deflected by proton produces photon radiation. The electron leaving the interaction has less energy by the amount imparted to the photon. Typical radiation mechanism of an ionized hydrogen cloud.

Figure 3.16: Inverse Compton scattering was proposed to be the reason for the peculiar radio spectra - but emission at microwaves should then be less.

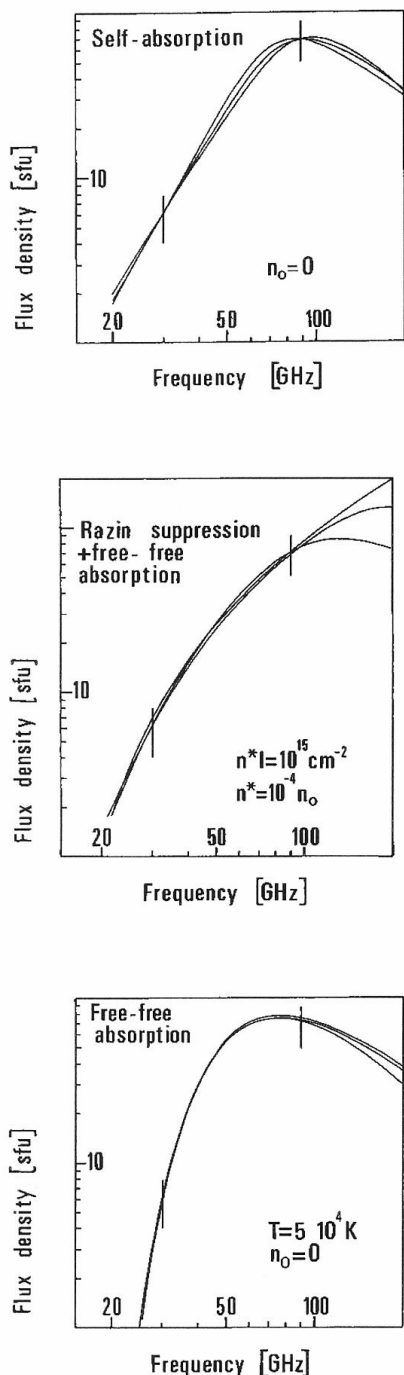


Fig. 4a-c. Gyrosynchrotron flux spectra computed for the mechanisms of absorption and suppression discussed in section 4 with the parameters of table 1 ($1 \text{ sfu} = 10^{-22} \text{ W m}^{-2} \text{ Hz}^{-1}$). Spectra are plotted for magnetic fields of 500 G, 1000 G and 2000 G (a), (c) and 250 G, 500 G and 1000 G (b) respectively. The vertical bars represent the observed flux densities at 30 and 90 GHz with an assumed error of 30%

outside the source of emission do not depend very much on the chosen parameters. This is different in the case where Razin suppression and free-free absorption inside the emissive source shape the spectrum: Most of the radiation above the spectral turnover frequency is then due to free-free emission, which is most intense at high electron densities and low temperatures.

In order to compare the numbers of energetic electrons in the microwave and the hard X-ray sources, we extrapolate the power-law spectrum (6) down to 10 keV and obtain the instantaneous number of nonthermal electrons at the peak of the microwave burst

$$N_{\mu}^*(10 \text{ keV}) = 10^{32} - 10^{34}.$$

The number $N_{\mu}^*(10 \text{ keV})$ of nonthermal electrons emitting hard X-rays through bremsstrahlung can be estimated from a power-law fit to the observed photon spectrum published by McClements and Brown (1986). With a spectral index of 3.2, Brown's (1971) Eq. 14, corrected by a factor π (Lin and Hudson, 1976), gives the instantaneous number

$$N_{\mu}^*(10 \text{ keV}) = \frac{3 \cdot 10^{45}}{n_0},$$

where n_0 is the density in the hard X-ray source in cm^{-3} . For densities above 10^{11} cm^{-3} , the instantaneous numbers of nonthermal electrons in the microwave and hard X-ray sources are thus in a fairly good agreement. The electron lifetime of 60 ms and the total duration of the event of 20 s inferred from Kaufmann et al. (1985) give a total number of $3 \cdot 10^{34}$ to $3 \cdot 10^{36}$ electrons accelerated during the event to more than 10 keV, which represent an energy of 10^{27} to 10^{29} erg.

The close temporal association of microwaves and hard X-rays down to the limits of temporal resolution of the hard X-ray spectrometer (Kaufmann et al., 1985) and the quantitative agreement between the instantaneous numbers of electrons suggest that the emissions come from a common source. As the hard X-rays are most efficiently emitted in a medium with high density of ambient electrons, this indicates that the plasma in the high-frequency source may be sufficiently dense, cool and magnetized to affect the microwave radiation by Razin suppression, free-free absorption and self-absorption. Each of these mechanisms can act with different efficiency at different points of a magnetic loop. It is to be emphasized, however, that both the derived parameters and the steep observed spectrum favour a very compact source with a small amount of inhomogeneity. The decimetric observations show that some of the accelerated particles are not confined in this source, but escape into structures with density below 10^{10} cm^{-3} . The absence of significant microwave radiation below 30 GHz requires that the escaping electrons be highly anisotropic or that their number be very small.

As an alternative explanation of the observations, free-free absorption outside the flaring loop requires a cool and dense structure between the loop and the observer. Radio maps at 35 GHz (Hachenberg et al., 1978) show that small-scale structures exist which are not optically thin to millimetre wavelengths (Raoult et al., 1979) and were shown long time ago to shield occasionally microwave emitting loops (cf. Kundu, 1965). Furthermore, Mouradian et al. (1983) showed that during flares cold arches rise into the solar atmosphere with parameters ($T = 10^4 - 5 \cdot 10^5 \text{ K}$, $n_0 \sim 10^{11} \text{ cm}^{-3}$) that can account for the efficient absorption of microwaves in the millimetre band. In the

Figure 3.17: Ludwig Klein (1987) proved with his calculations that different absorption mechanisms can change the spectral shape (decrease emission at microwaves so that at mm and sub-mm waves emission looks to increase) - no need for "exotic" emission mechanisms.

3.6 Plasma emission

$$\nu_p = \frac{q}{2\pi} \sqrt{\frac{N}{\epsilon_0 m}} \quad (\text{Hz}) \quad (3.11)$$

where N is the particle density (m^{-3}), q is the charge of particle (C), m is the mass of particle (kg), and ϵ_0 is the permittivity of vacuum.

In the case of plasma with electron density N_e (m^{-3}) the plasma frequency becomes

$$\nu_p \approx 9 \sqrt{N_e} \quad (\text{Hz}) \quad (3.12)$$

An electron in an ionized gas is subjected to a linear displacement and it behaves as an oscillator with the characteristic plasma frequency ν_p . This disturbance is known as plasma oscillations or **Langmuir waves**

Radio emission can be produced by a two-stepped process, where electrostatic oscillations are first excited at or near the plasma frequency (e.g. by an energetic electron beam) and after that the Langmuir wave energy is converted to electromagnetic radiation via non-linear wave-wave interactions.

Plasma radiation occurs at or just above the plasma frequency ν_p and its second harmonic $2\nu_p$, but rarely if ever at higher harmonics.

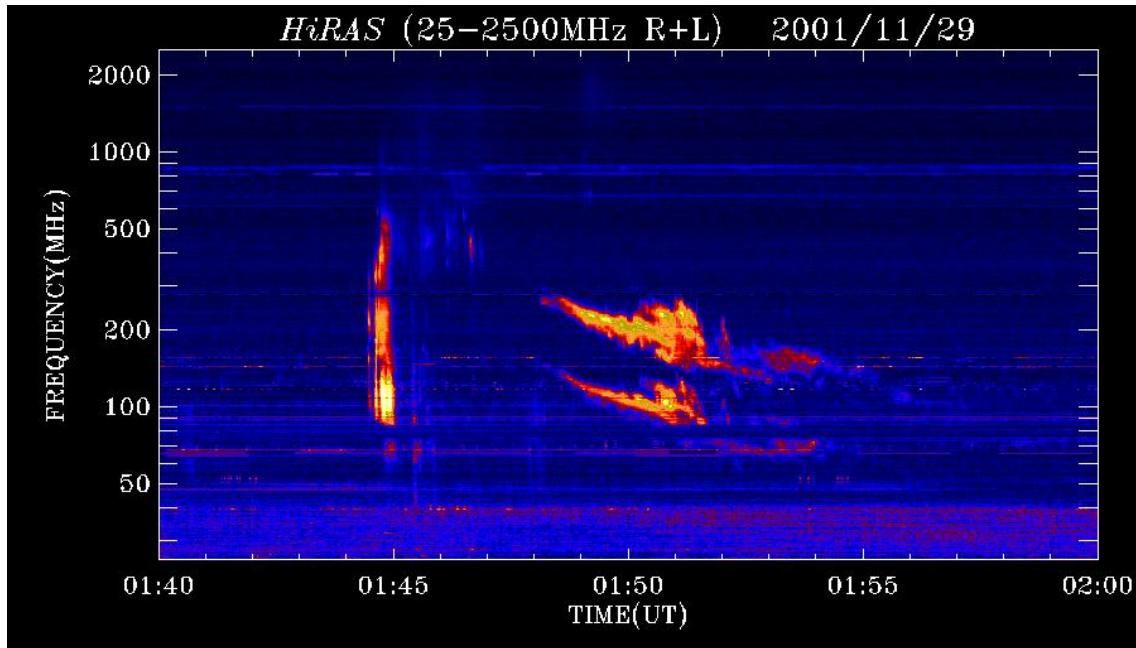


Figure 3.18: Radio dynamic spectrum at 25 MHz – 2 GHz. Plasma emission at the fundamental plasma frequency and its harmonic frequency (often called the 'second harmonic') are observed, frequency-drifting towards the lower frequencies (i.e., lower electron densities). The emission source speed is around 500–1000 km/s. A fast-drift structure in the spectrum is due to an electron beam, travelling at speed $\sim 0.3c$.

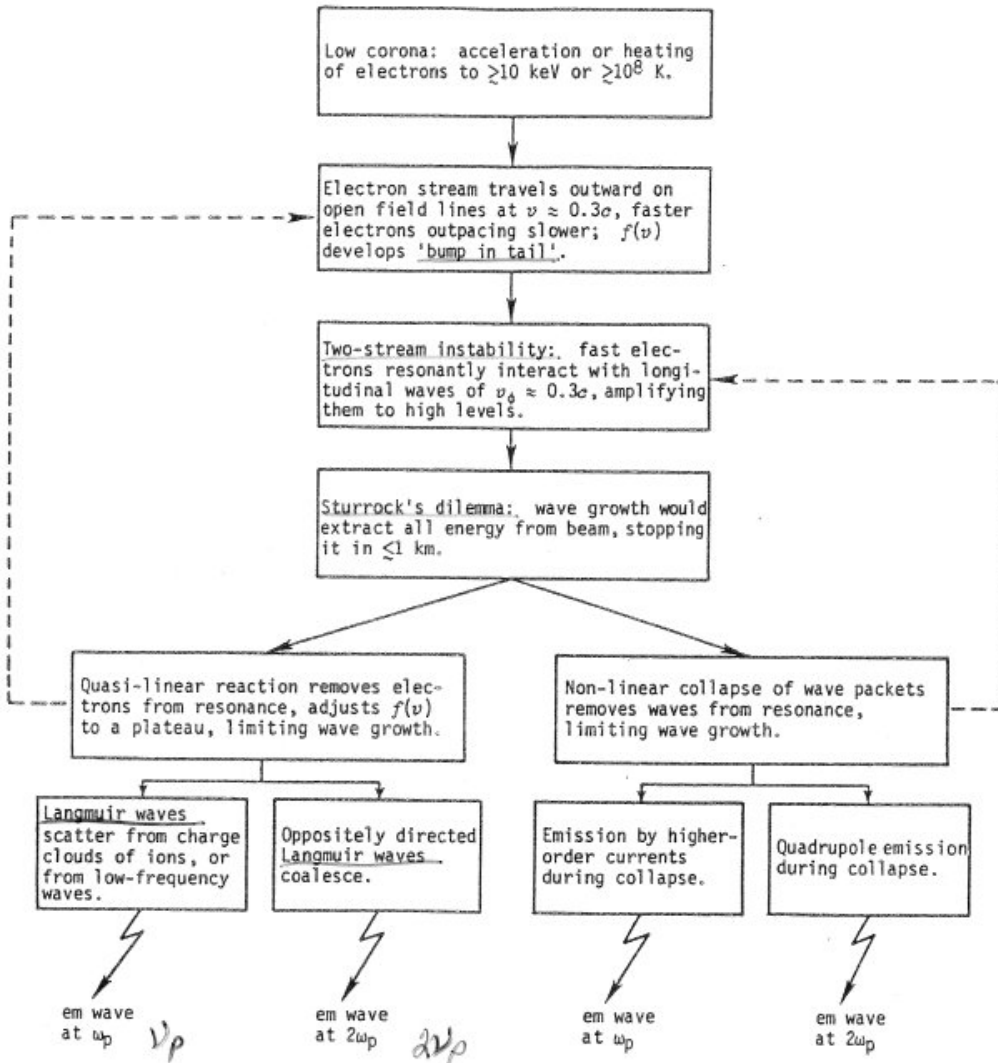


Fig. 8.1 - Steps in the theoretical description of emission of electromagnetic radiation by an electron stream in a plasma. The bottom half of the figure splits into two alternative theoretical lines of argument.

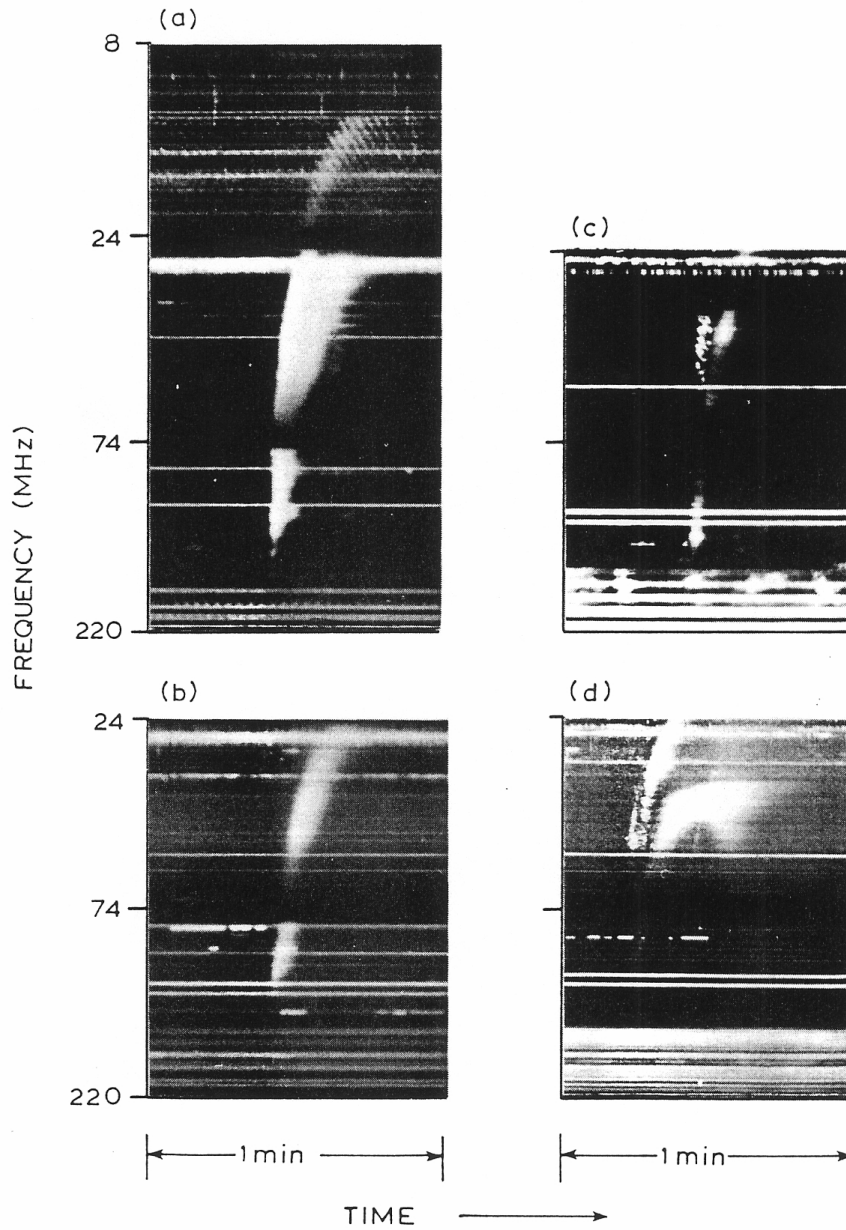


Fig. 12.1 - Dynamic spectra of several varieties of Type III bursts (examples from the Culgoora spectrograph records).
 (a) Fundamental-harmonic pair, with 'ordinary' Type III bursts for both components (III-III pair).
 (b) Structureless Type III burst.
 (c) Type IIIb fundamental with smooth Type III harmonic (IIIb-III pair).
 (d) Inverted-U burst.

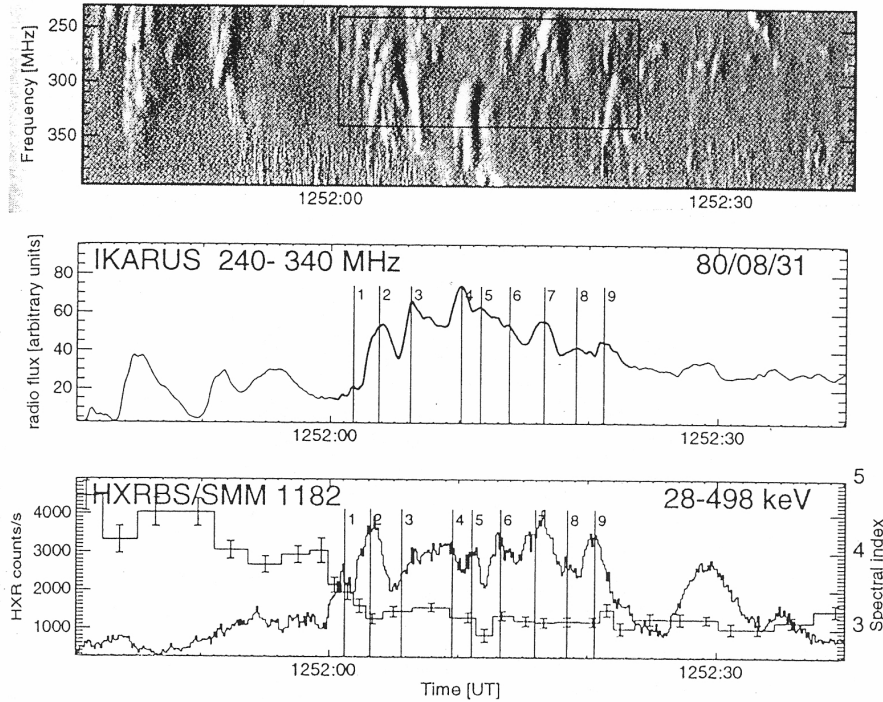


Figure 18 Correlated hard X-ray and decimeter structures (Aschwanden et al 1993). The upper panel shows an enhanced gray-scale representation of the decimeter dynamic spectrum during one minute of a flare observed jointly by the ground-based Ikarus spectrometer and by the hard X-ray instrument on the *Solar Maximum Mission*. The rapid fluctuations agree well with one another, as illustrated by the time series in the middle and lower panels.

Figure 3.19: Radio type III bursts correlate well with hard X-rays since both emissions are caused by the same particle populations. Radio emission traces the electron beams and hard X-rays are created when the beams collide with dense matter. (From Hudson & Ryan, 1995)

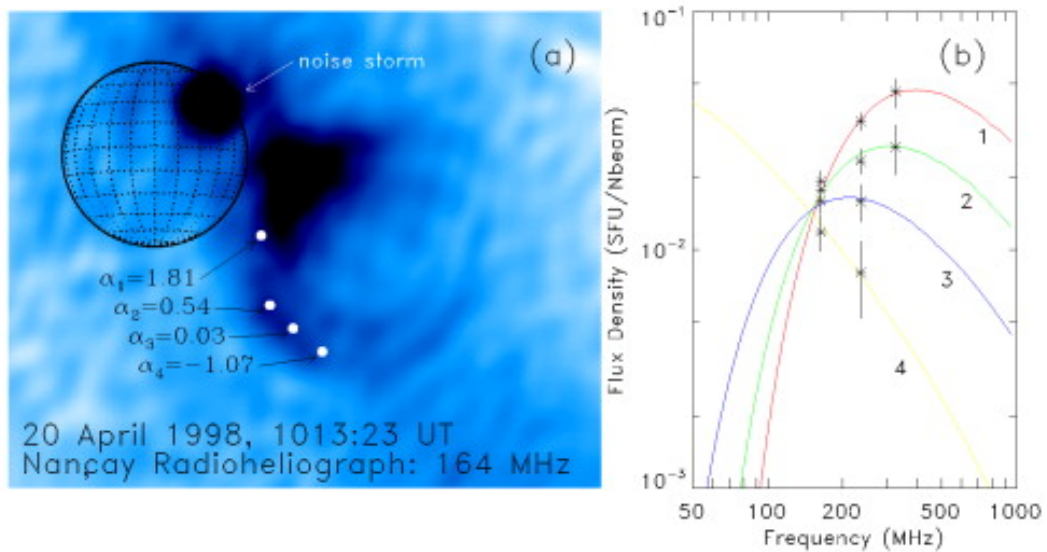
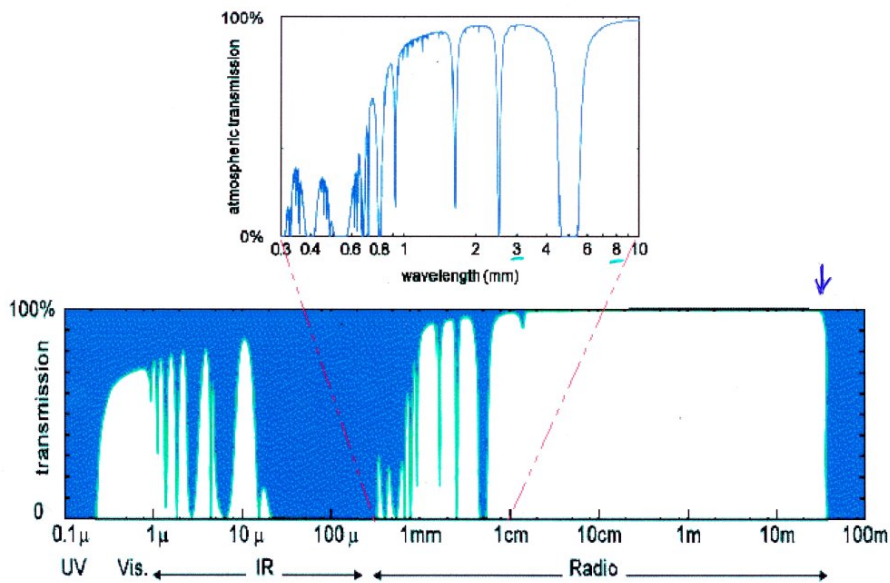
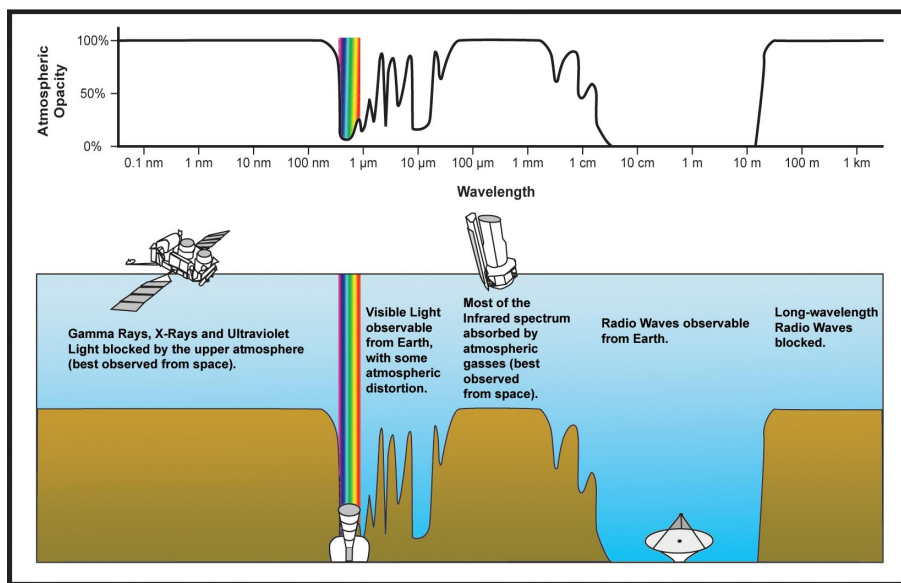


Figure 3.20: This is not plasma radiation! Emits at 164 MHz at heights over $4 R_{\odot}$ \rightarrow synchrotron radiation $E_e \approx 0.5 - 5$ MeV, $B \approx 0.1$ G (Bastian et al., 2001)

Chapter 4

Radio astronomy fundamentals



4.1 Radio telescopes



Tuorla 2-meter solar radio telescope

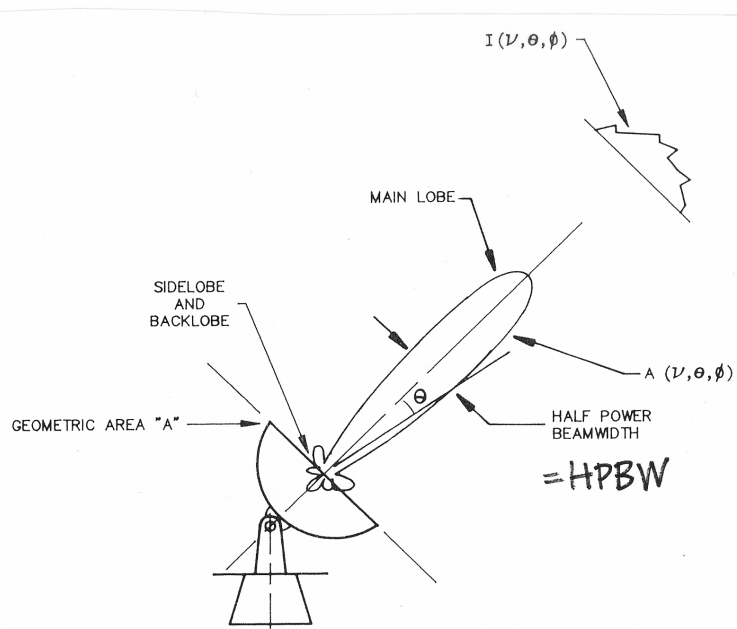


Figure 3-2. The reception pattern of an antenna.

Figure 4.1: HPBW 'half power beam width', FWHM 'full width half maximum', true (efficient) antenna area = aperture efficiency $\eta \times$ geometric area. η varies $\approx 0.3-0.7$. Surface accuracy of the dish has to be better than the wavelength used.

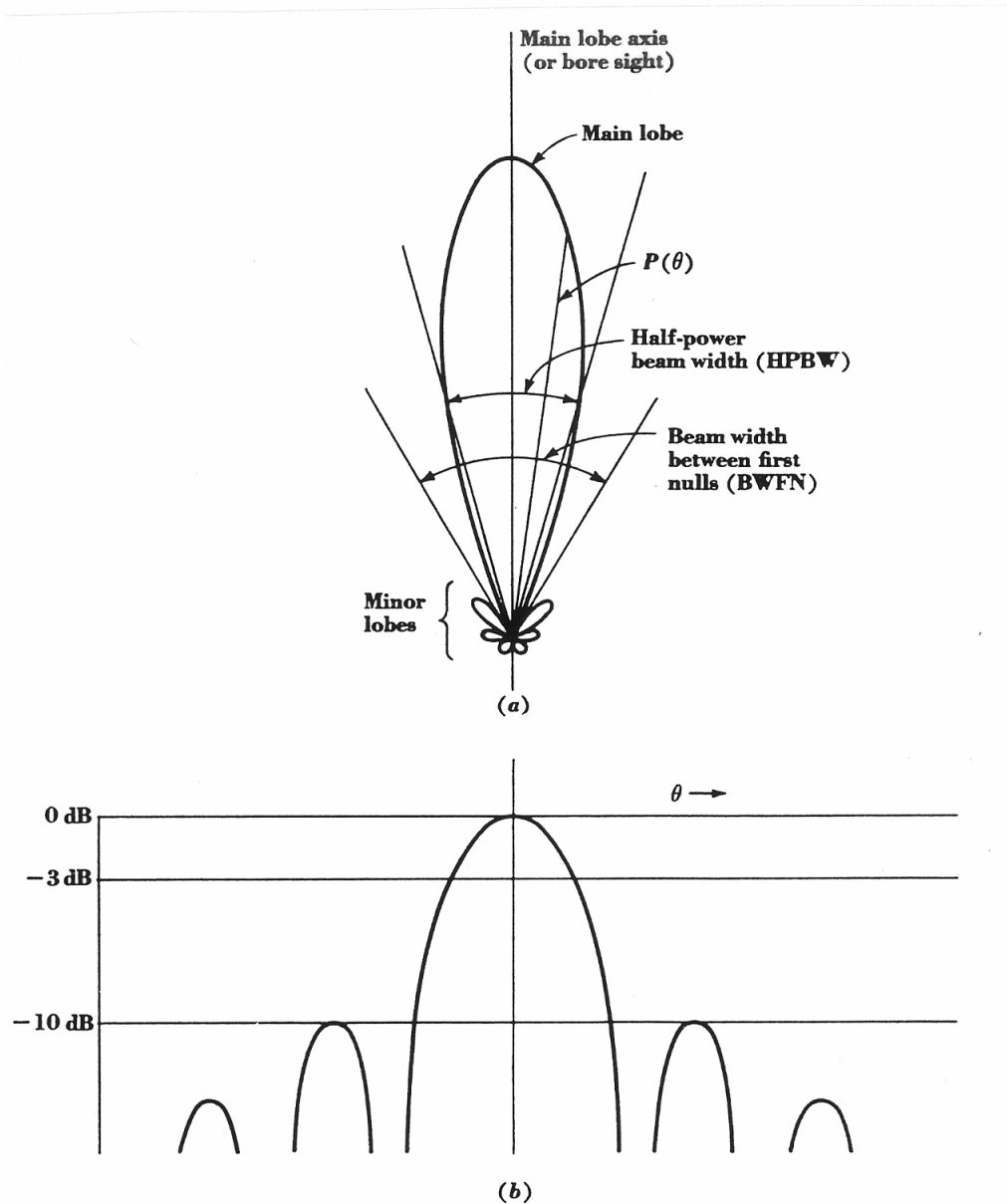


Fig. 6-1. (a) Antenna pattern in polar coordinates and linear power scale; (b) antenna pattern in rectangular coordinates and decibel power scale.

Figure 4.2: $HPBW \sim BWFN/2$ (beam width between first nulls). $dB = 10 \times \log P1/P0$; if $P1 = P0 \rightarrow 0$ dB, if $P1/P0 = 0.5 \rightarrow 3$ dB (Fig. from Kraus: Radio Astronomy)

where $\Omega_A =$ beam solid angle of antenna, rad^2

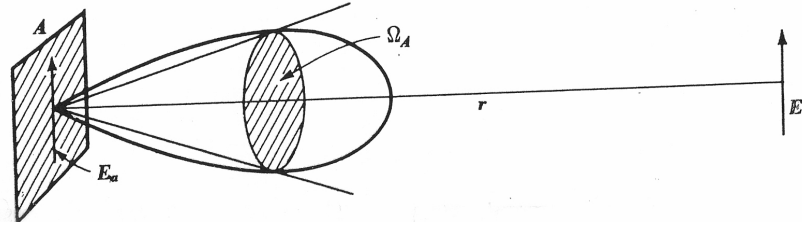
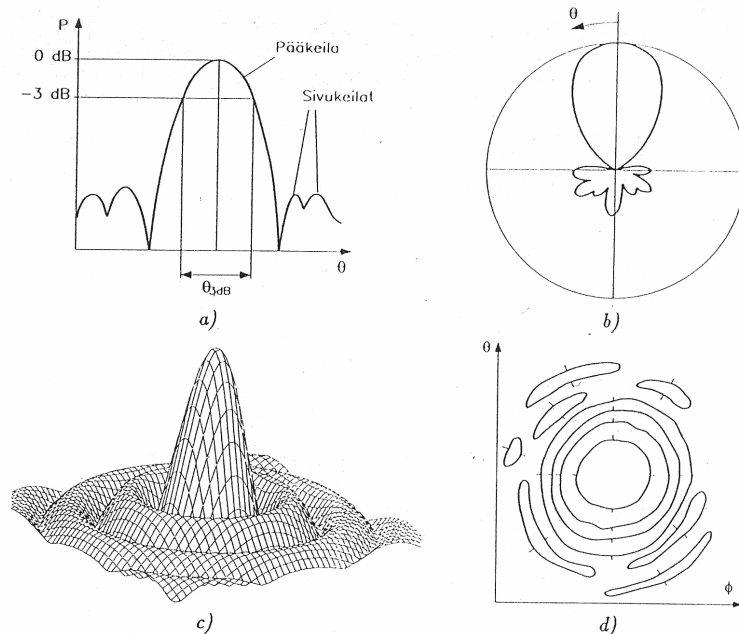


Figure 4.3: Antenna beam: The angle in **radians** (rad) is related to the arc length it cuts out: $\theta = \frac{s}{r}$, where s is arc length, and r is the radius of the circle. A squared radian is also called a **steradian** (sr), which is defined as the solid angle subtended at the center of a sphere of radius r by a portion of the surface of the sphere having an area r^2 . (Fig. from Kraus: Radio Astronomy)

Taulukko 9.1. Viivalähteiden suuntakuvioiden ominaisuuksia.

Kentänjakauma apertuurissa	Keilanleveys (-3 dB)	1. sivukeila	1. nollakohta
Tasainen 	$0,89\lambda/a$	-13,3 dB	λ/a
$\cos(\pi x/a)$ 	$1,19\lambda/a$	-23,1 dB	$1,5\lambda/a$
$\cos^2(\pi x/a)$ 	$1,44\lambda/a$	-31,5 dB	$2,0\lambda/a$
$1 - 0,5(2x/a)^2$ 	$0,97\lambda/a$	-17,1 dB	$1,14\lambda/a$
Taylor, $n = 3$, reuna -9 dB 	$1,07\lambda/a$	-25,0 dB	



Kuva 9.3. Suuntakuvioiden esitysmuotoja: a) suorakulmainen, b) polaarinen, c) kolmiulotteinen. d) vakioarvokäyrästä

Figure 4.4: Spatial resolution: Antenna beamwidth – which basically means the spatial resolution – can be approximated with $\theta = 1.2 \frac{\lambda}{D}$. (Fig. from Räisänen - Lehto: Radiotekniikka)

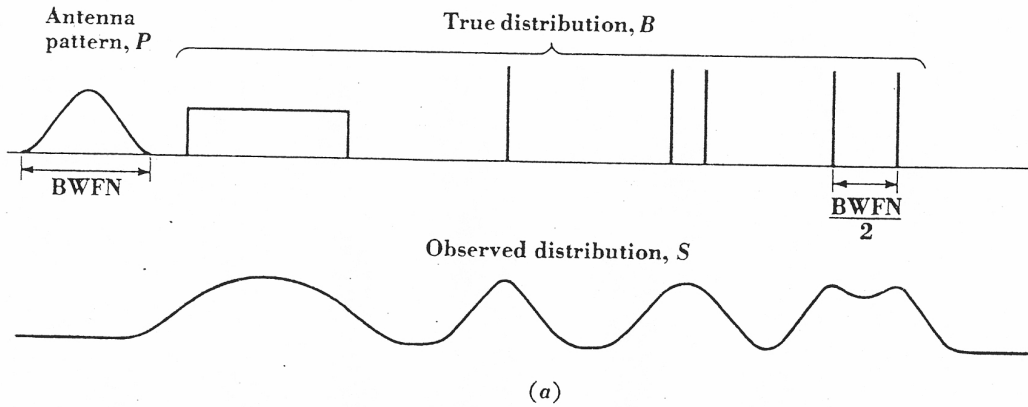


Fig. 6-11a. Smoothed distribution S observed with antenna pattern P .

(Fig. from Kraus: Radio Astronomy)

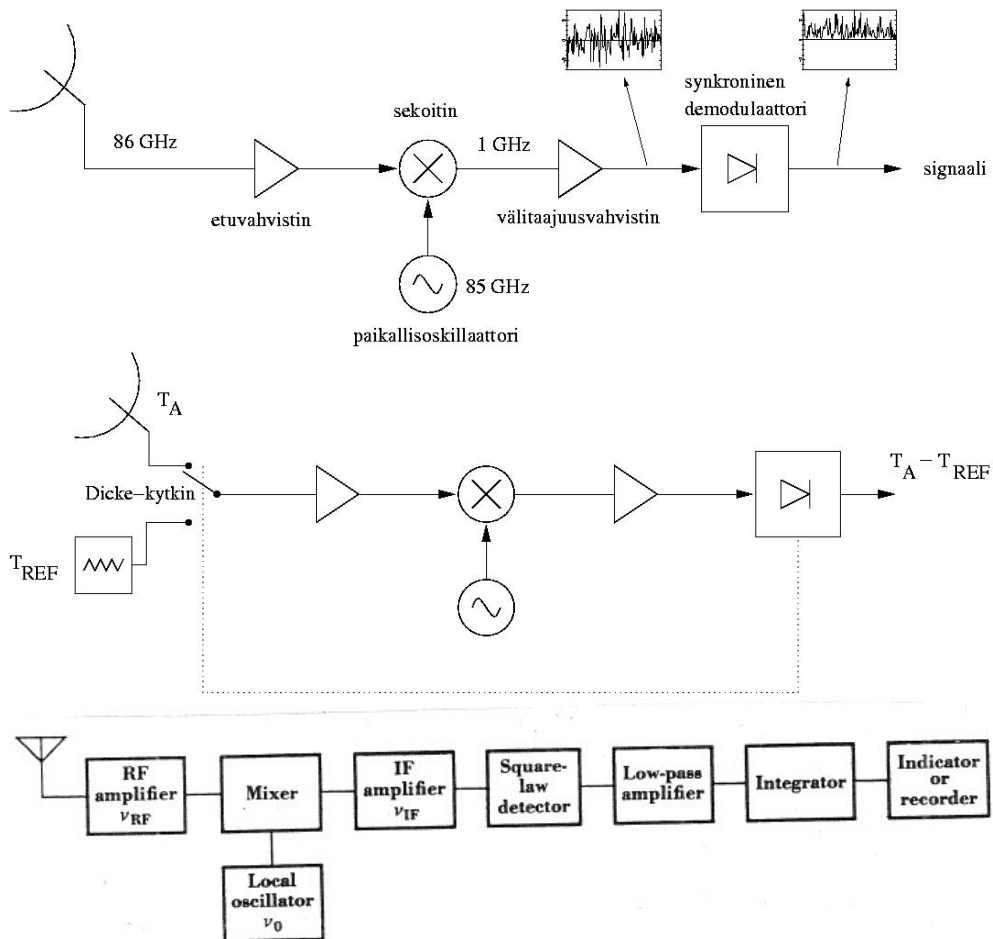


Figure 4.5: The basics of radio receivers

4.2 Interferometers

The benefit of interferometers in solar observations: better spatial resolution and removal of atmospheric disturbances (can observe in cloudy weather). Baseline = distance between the farthest antennas $\sim D$.

Fig. 3.26. The principle of an interferometer. If the radio radiation reaches the radio telescopes in the same phase, the waves amplify each other and a maximum is obtained in the combined radiation (cases 1 and 3). If the incoming waves are in opposite phase, they cancel each other (case 2)

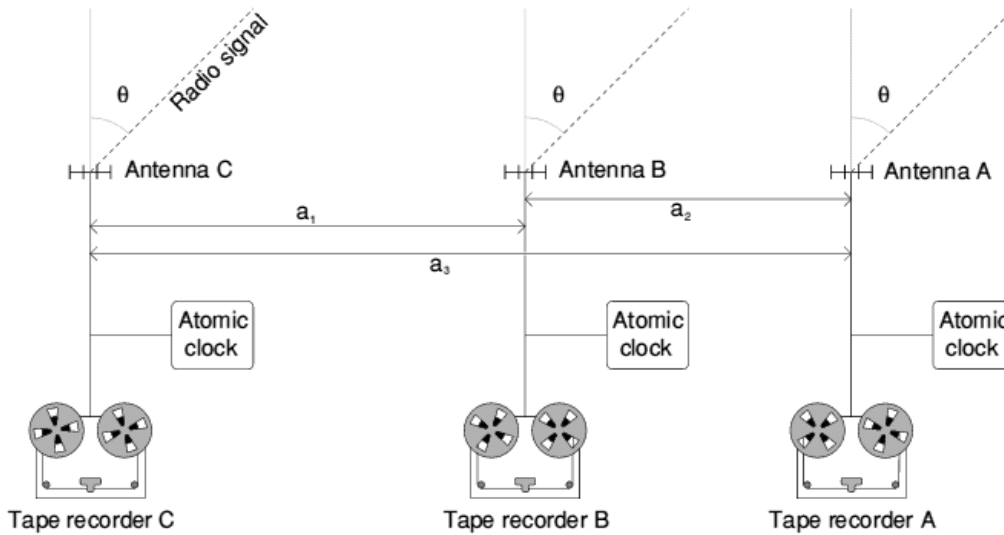
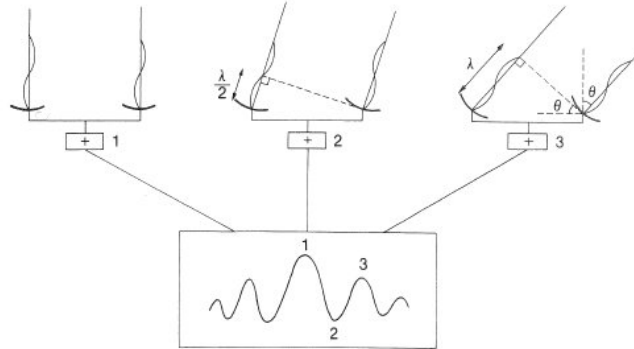


Figure 4.6: The Nobeyama radioheliograph is a traditional T-shape array of telescopes, in the future Frequency Agile Solar Radiotelescope (FASR) will consist of telescopes in no particular array form.

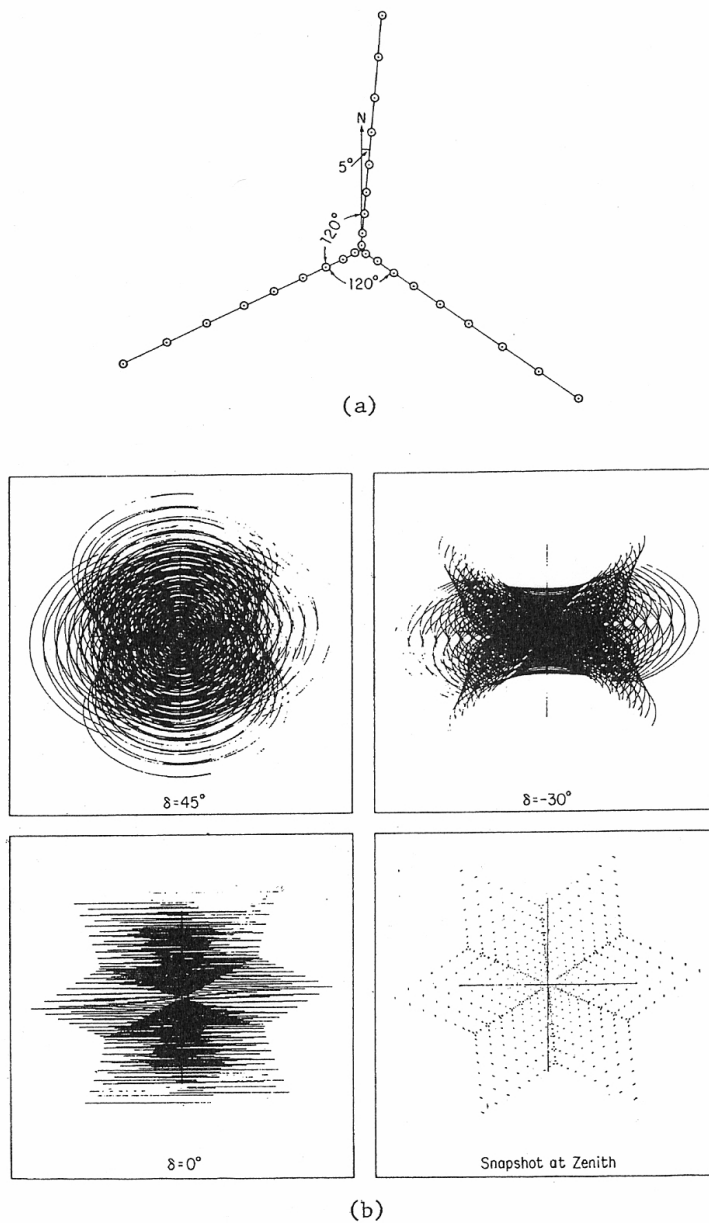


Figure 2-14. (a) The configuration of the 27 antennas of the VLA. (b) The transfer functions for four declinations with observing durations of $\pm 4^h$ for $\delta = 0^\circ$ and 45° , $\pm 3^h$ for $\delta = -30^\circ$, and $\pm 5^m$ for the snapshot. [From Napier, Thompson & Ekers (© 1983 IEEE).]

Figure 4.7: Solar observations are almost always done in the snapshot mode (no Earth rotation is used for the aperture synthesis).

4.3 Brightness temperature and flux density

An ideal (blackbody) radiator at temperature T radiates with intensity

$$B_\nu(T) = \frac{2h\nu^3}{c^2} \frac{1}{e^{h\nu/kT} - 1} \quad (\text{W m}^{-2} \text{ Hz}^{-1} \text{ sr}^{-1}) \quad (4.1)$$

At radio frequencies we can use the Rayleigh-Jeans approximation ($e^{h\nu/kT} \sim 1 + h\nu/kT + \dots$)

$$B_\nu = \frac{2kT\nu^2}{c^2} \quad (\text{W m}^{-2} \text{ Hz}^{-1} \text{ sr}^{-1}) \quad (4.2)$$

for the brightness (regardless of the emission mechanism).

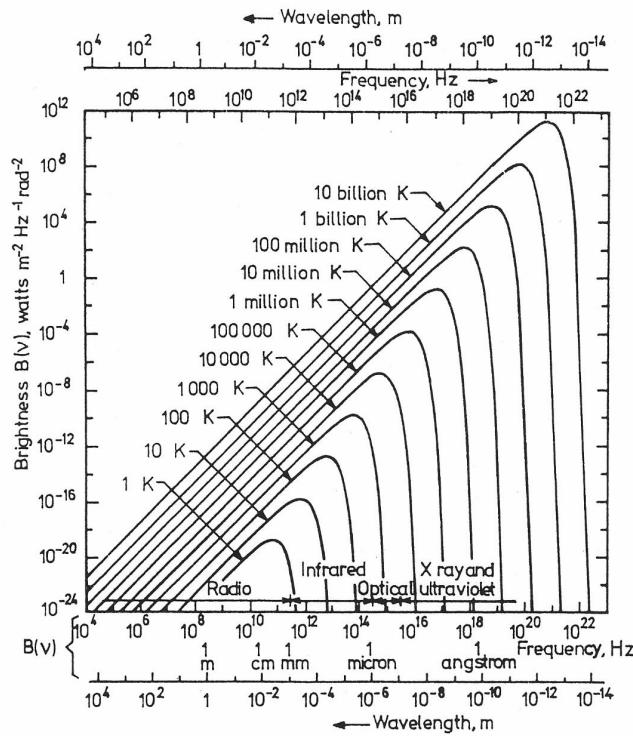


Fig. 1.6. The Planck spectrum for black bodies of different temperatures

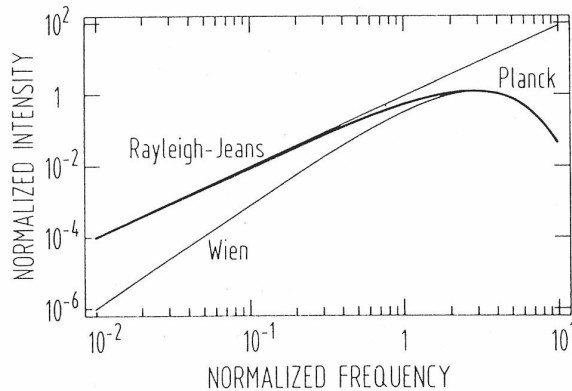


Fig. 1.7. Normalized Planck curve and the Rayleigh-Jeans and Wien approximation

Flux density S of a source is determined from the source brightness and the source solid angle

$$S = \int \int_{\Omega_S} B_S(\theta, \phi) d\Omega \quad (4.3)$$

If the source brightness is constant over the telescope beam area, the received power is

$$P_r = 1/2 A_{ef} S_0 \Delta f \quad (4.4)$$

where Δf is the frequency bandwidth, A_{ef} is the effective aperture of the antenna, and S_0 is the observed flux density within the antenna beam ($S_0 = B_S \Omega_A$).

Antenna temperature can be solved from

$$P_r = k T_A \Delta f \quad (4.5)$$

The antenna temperature T_A due to the source can be expressed as

$$T_A = \frac{1}{\Omega_A} \int \int T(\theta, \phi) P_n(\theta, \phi) d\Omega \quad (4.6)$$

$T(\theta, \phi)$ is the source temperature

$P_n(\theta, \phi)$ is the normalized antenna power pattern (dimensionless)

Ω_A is the antenna beam area (rad^2)

Flux density S of a source (for the two polarizations) is related to the source brightness temperature

$$S = \frac{2k\nu^2}{c^2} \int T_b d\Omega \quad (\text{W m}^{-2} \text{ Hz}^{-1}) \quad (4.7)$$

where $d\Omega$ is a differential solid angle and the integral is over the projected area of the source.

The observed flux density can then be written as

$$S_0 = \frac{2kT_A}{A_{ef}} \quad (\text{W m}^{-2} \text{ Hz}^{-1}) \quad (4.8)$$

Simplified Example

$D = 14 \text{ m}$

$A = \pi r^2 = 154 \text{ m}^2$

$A_{ef} = 0.5 \times 154 = 77 \text{ m}^2$

$T_A \approx T_b \approx 7200 \text{ K}$ at 37 GHz (source > beam, no absorbing atmosphere)

$$S_0 = \frac{2kT_A}{A_{ef}} = 2 \times 1.3805 \times 10^{-23} \times 7200 / 77 \quad (4.9)$$

$$= 2.58 \times 10^{-21} \text{ W m}^{-2} \text{ Hz}^{-1} = 26 \text{ sfu}$$

For a 2-m antenna with similar efficiency $S_0 = 1266 \text{ sfu}$

Example. Mayer, McCullough, and Sloanaker (1958a, b) at the Naval Research Laboratory measured an antenna temperature of 0.24 K at a wavelength of 3.15 cm, when their radio-telescope antenna was directed at Mars. At the time of the measurements the disk of Mars subtended an angle of 18 sec of arc. Assuming that the antenna has a pencil beam of 0.116° between half-power points, find the equivalent temperature of the source (Mars).

Solution. The radius of the disk of Mars is 9 sec of arc or $9/3,600 = 0.0025^\circ$. Hence, the solid angle of the disk is given by

$$\Omega_s = \pi r^2 = \pi (0.0025^\circ)^2 = 2 \times 10^{-5} \text{ deg}^2$$

The beam area Ω_A of the antenna is given approximately by (see Chap. 6)

$$\Omega_A = \frac{1}{2}(0.116^\circ)^2 = 0.018 \text{ deg}^2$$

Hence, assuming a constant temperature over the disk, the average equivalent temperature of Mars by this measurement is, from (3-118),

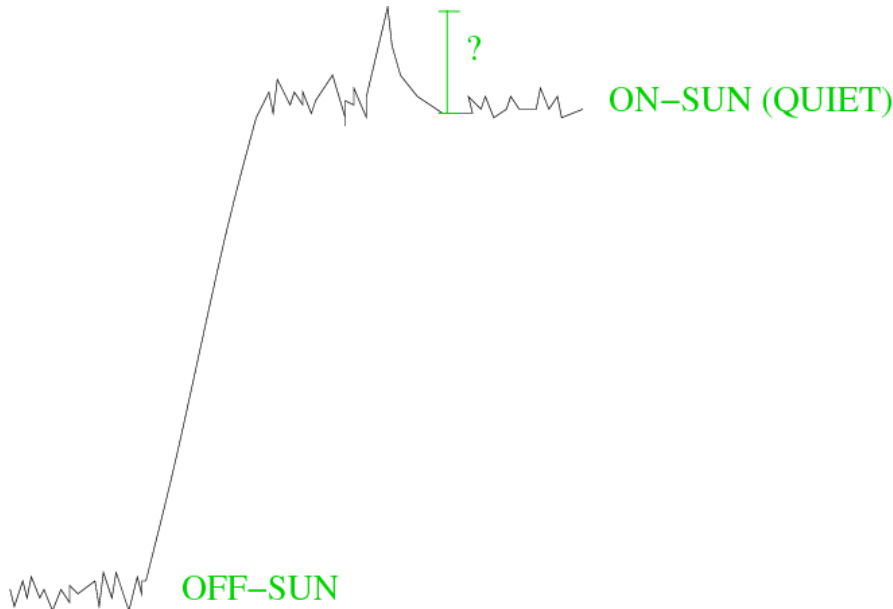
$$T = T_A \frac{\Omega_A}{\Omega_s} = 0.24 \frac{0.018}{2 \times 10^{-5}} = 216^\circ$$

(from Kraus: Radio Astronomy)

If the source size (Ω_s) is smaller than the antenna beam size (Ω_A), the observed antenna temperature reduces to:

$$T_A = \frac{\Omega_s}{\Omega_A} T_b \quad (4.10)$$

Relative radio flare brightness:



$T_{b,\nu} = X$ Kelvin (quiet Sun brightness temperature at frequency ν from literature or absolute calibrations)

On-Sun – Off-Sun = Y mV

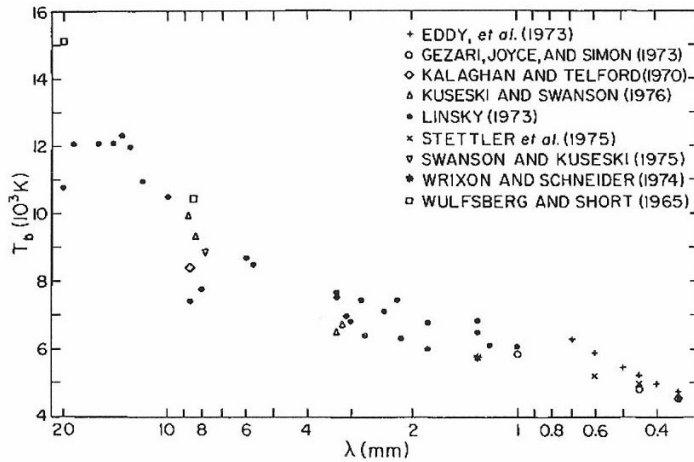
$\Rightarrow Y \text{ mV} \equiv X \text{ Kelvin}$

Calibration

- Absolute calibration using radio sources and hot+cold loads
- No calibration, using units relative to 'quiet Sun' level

The method of using relative solar flux units provides the advantage of removing atmospheric and radome effects (variable attenuation) and instrumental effects, but it is more sensitive to errors in quiet Sun level determination.

Furthermore, the true source size of the radio emitting region in solar flares is not always known and it can vary from a few arc seconds to several arc minutes.



T_b from
Sun-Moon
Calibrations

FIG. 5.— Selected brightness temperature observations of the Sun at millimeter wavelengths

Figure 4.8: (Vernazza, Avrett & Loeser, 1981)

Sensitivity

The sensitivity of radio observations depends on the receiver noise temperature, i.e. the receiver must be able to detect small differences in the total noise. The sensitivity of the system is calculated from the total or system noise temperature T_{sys}

$$T_{sys} = T_A + T_R \quad (4.11)$$

where T_R is the receiver noise temperature (K). The smaller the antenna (source) temperature, the smaller should the receiver noise temperature be.

In some cases the sensitivity limitation can be overcome by longer integration time or larger bandwidth.

The minimum detectable temperature ΔT of a radio telescope is

$$\Delta T = \frac{K_s T_{sys}}{\sqrt{\Delta f t}} \quad (4.12)$$

where K_s is a sensitivity constant that depends on the receiver type, Δf is the receiver bandwidth (Hz) and t is the post-detection integration time (s).

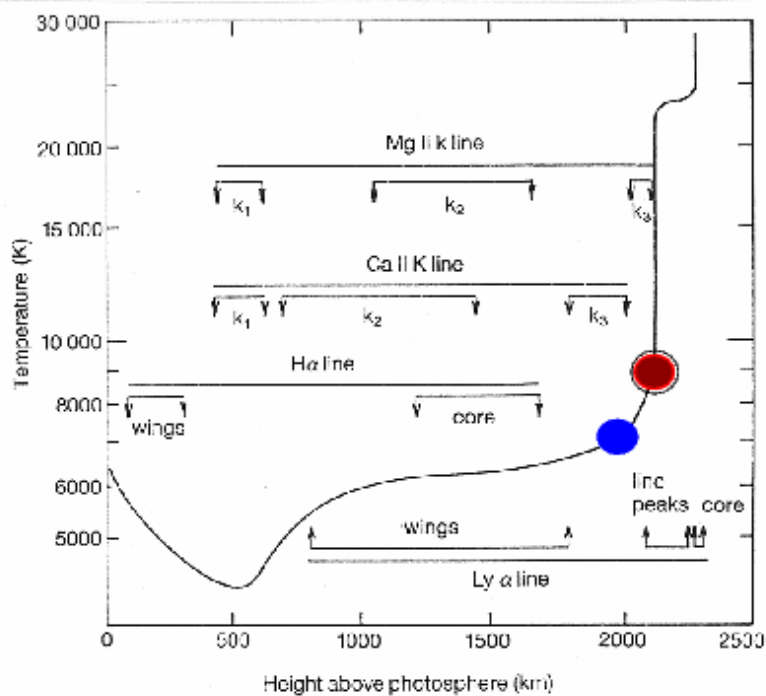


Fig. 4.12 The variation of temperature with height in the solar atmosphere up to the transition region for an average quiet-sun region. Also indicated are the height ranges over which the $H\alpha$ and $Ly-\alpha$, Ca II H and K, and Mg II h and k lines are formed. (After Vernazza, Avrett and Loeser (1981))

- 13 mm radio emission (quiet Sun, plasma limit)
- 3 mm radio emission (quiet Sun, plasma limit)

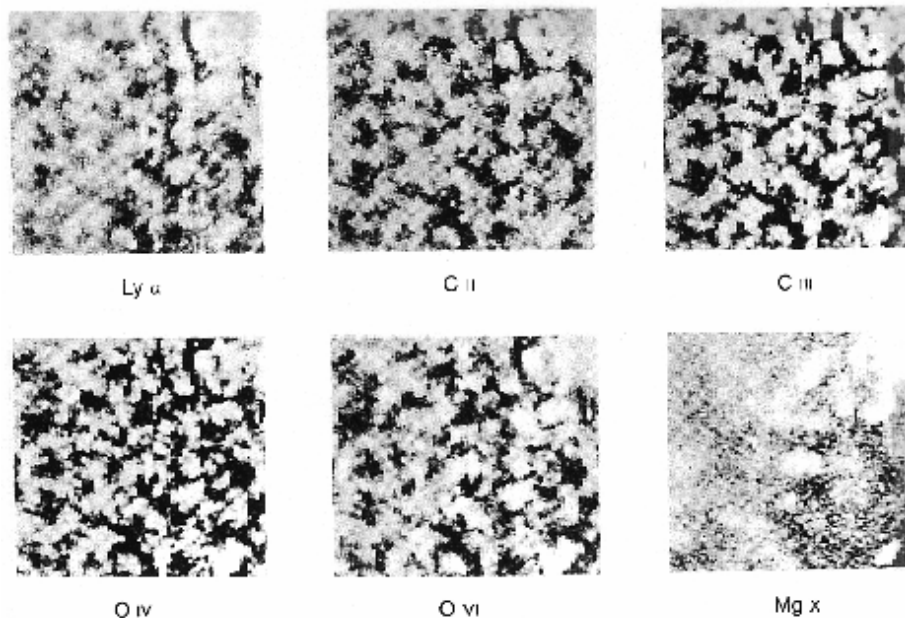
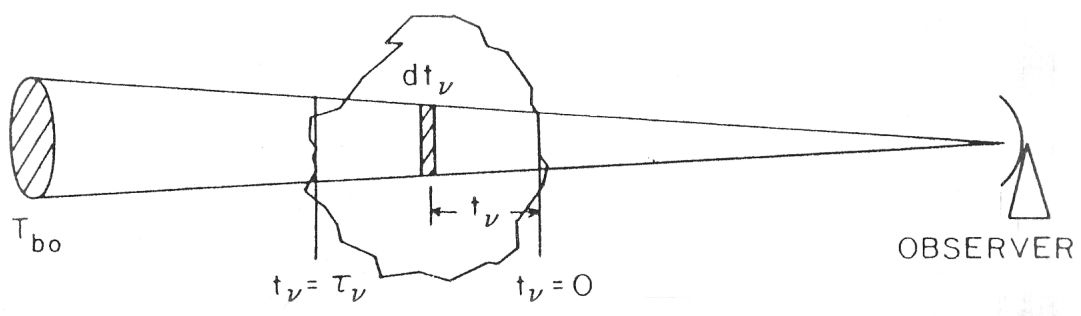
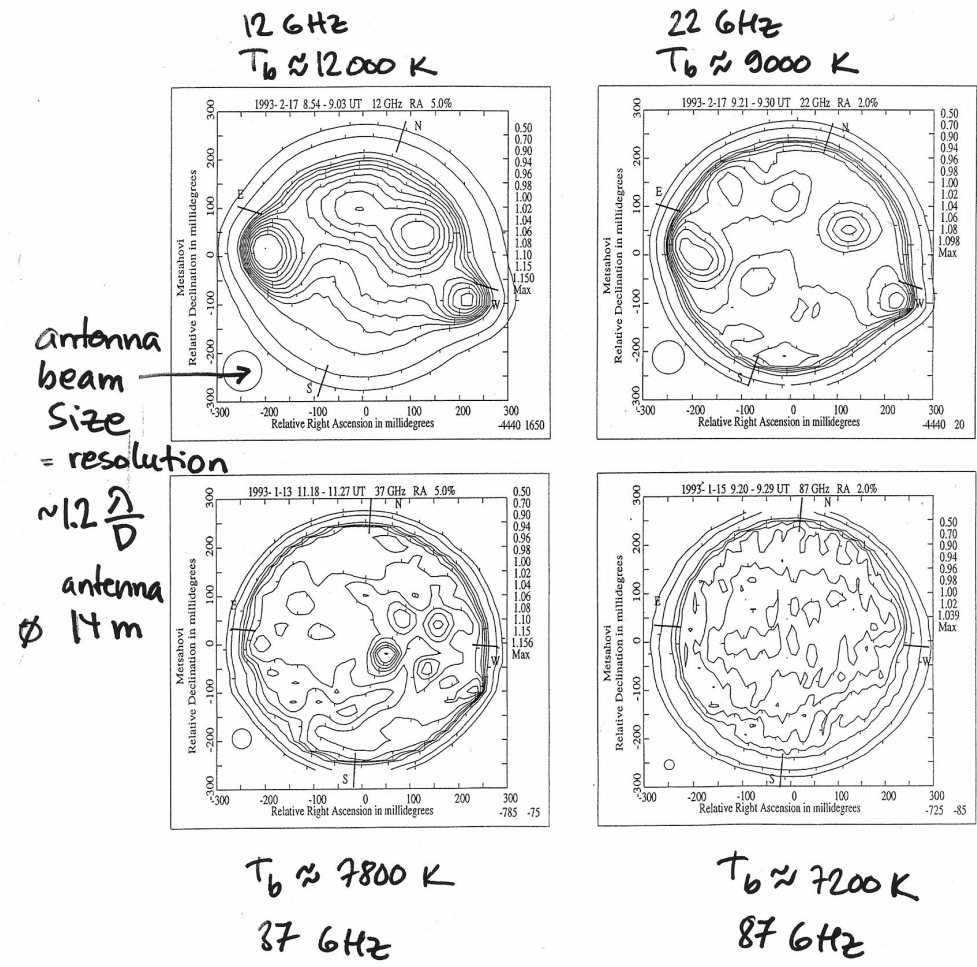


Fig. 4.11 Six *Slylab* images of a quiet-sun region taken in ultraviolet: spectral lines in a temperature range from the chromospheric Lyman- α to the coronal Mg X. The chromospheric network becomes progressively more blurred. (Courtesy R. Noyes, Harvard College Observatory and NASA)

Solar maps measured at different wavelengths



4.4 Radiative transfer equations

Geometry of a source with effective temperature T_{eff} and optical depth τ , located in front of a background with brightness temperature T_{bo} .

$$T_b = \int_0^{\tau_\nu} T_{eff} e^{-t_\nu} dt_\nu + T_{bo} e^{-\tau_\nu} = T_{eff}(1 - e^{-\tau_\nu}) + T_{bo} e^{-\tau_\nu} \quad (4.13)$$

Just the source, with no background:

$$T_b = \int_0^{\tau_v} T_{eff} e^{-t_v} dt_v \quad (4.14)$$

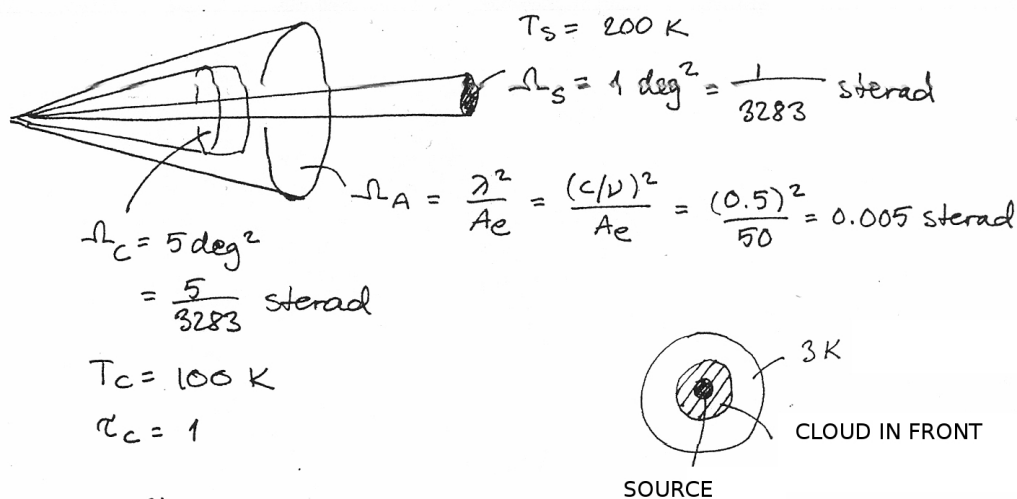
$$T_b = T_{eff}(1 - e^{-\tau_v}) \quad (4.15)$$

if $\tau_v \gg 1$, $e^{-\tau_v} \rightarrow 0$: $T_b = T_{eff}$ (optically thick)

if $\tau_v \ll 1$, $(1 - e^{-\tau_v}) \rightarrow \tau_v$: $T_b = T_{eff} \tau_v$ (optically thin).

Example:

An emission source, with brightness temperature of 200 K and source solid angle of 1 deg^2 is observed through a cloud. The brightness temperature of the cloud is 100 K and its solid angle is 5 deg^2 . The effective area of the radio telescope is 50 m^2 . Observations are done at 600 MHz and the optical depth of the cloud is 1. Calculate the antenna temperature when the telescope is pointing to the source (you can ignore the 3 K cosmic background radiation).



$$T_A = T_s e^{-\tau_c} + T_c (1 - e^{-\tau_c})$$

$$T_{SA} = \frac{\Omega_s}{\Omega_A} T_s = \frac{1/3283}{0.005} \cdot 200 \text{ K} = 12.18 \text{ K}$$

$$T_{CA} = \frac{\Omega_c}{\Omega_A} T_c = \frac{5/3283}{0.005} \cdot 100 \text{ K} = 30.46 \text{ K}$$

$$T_A = T_{SA} \cdot e^{-1} + T_{CA} (1 - e^{-1}) = 23.73 \text{ K}$$

Bremsstrahlung emissivity

64

$$E_\nu = \frac{8}{3} \left(\frac{2\pi}{3}\right)^{1/2} \frac{Z^2 e^6}{m^2 c^2} \left(\frac{m}{kT}\right)^{1/2} N_i N_e g(\nu, T) e^{-h\nu/kT}$$

$$= 5.4 \cdot 10^{-39} \frac{N^2}{T^{1/2}} e^{-h\nu/kT} g(\nu, T) \quad \text{erg/s cm}^3 \text{ Hz rad}$$

radio $h\nu \ll kT \Rightarrow e^{-h\nu/kT} \approx 1$

$$\Rightarrow E_\nu(\text{radio}) = 5.4 \cdot 10^{-39} \frac{N^2}{T^{1/2}} g(\nu, T)$$

For $T > 3.6 \cdot 10^5 \text{ K}$, $g(\nu, T) \approx \frac{\sqrt{3}}{\pi} \ln\left(\frac{4kT}{8h\nu}\right)$

$$\approx (24.5 + \ln T - \ln \nu) \frac{\sqrt{3}}{\pi}$$

$$\Rightarrow E_\nu(\text{radio}) = 2.98 \cdot 10^{-39} \frac{(24.5 + \ln T - \ln \nu)}{T^{1/2}} N^2$$

Brightness

$$\Rightarrow I_\nu = \int E_\nu ds = 2.98 \cdot 10^{-39} \frac{(24.5 + \ln T - \ln \nu)}{T^{1/2}} \cdot EM$$

$$(EM = \int N^2 ds)$$

Flux density

$$S = \int I_\nu d\Omega = I_\nu \left(\frac{L}{D}\right)^2$$

$$\left(\begin{array}{l} \text{radio: } EM = \int N^2 dL = /N^2 L \\ \text{x-ray: } EM = \int N^2 dV = /N^2 L^3 \end{array} \right)$$



$$D = 1.5 \cdot 10^{13} \text{ cm}$$

$$\Rightarrow S_{\text{radio}} = E_\nu \cdot L \cdot \left(\frac{L}{D}\right)^2 = E_\nu \frac{L^3}{D^2} = \frac{2.98 \cdot 10^{-39} f(T, \nu) \cdot EM_{\text{x-ray}}}{D^2}$$

$$= 1.32 \cdot 10^{-65} f(T, \nu) \cdot EM_{\text{x-ray}}, \quad \text{erg/cm}^2 \text{ Hz}$$

$$= 1.32 \cdot 10^{-68} f(T, \nu) EM_{\text{x-ray}}, \quad \text{W/m}^2 \text{ Hz}$$

$$= 1.32 \cdot 10^{-46} \left(\frac{24.5 + \ln T - \ln \nu}{T^{1/2}}\right) EM_{\text{x-ray}}, \quad \text{STU}$$

4.5 Radio observations

- Large single dish antennas (Metsähovi and Itapetinga 14 m, Nobeyama 45 m)
- Small dish complexes (Bern/Tuorla, Nobeyama polarimeters NoRP)
- Non-traditional antennas (RATAN-600)
- Multi-beam receivers in single dish (Brazil, Argentina)
- Interferometers (Nancay radioheliograph NRH, Nobeyama radioheliograph NoRH, Owens Valley Solar Array OVSA, future FASR)
- Radio spectrographs (Zurich ETHZ, Tretsdorf OSRA, Artemis-IV in Greece, HiRAS in Japan, Culgoora in Australia, etc.)
- Radio spectrometers in space (Wind WAVES and STEREO WAVES)
- Solar eclipse observations

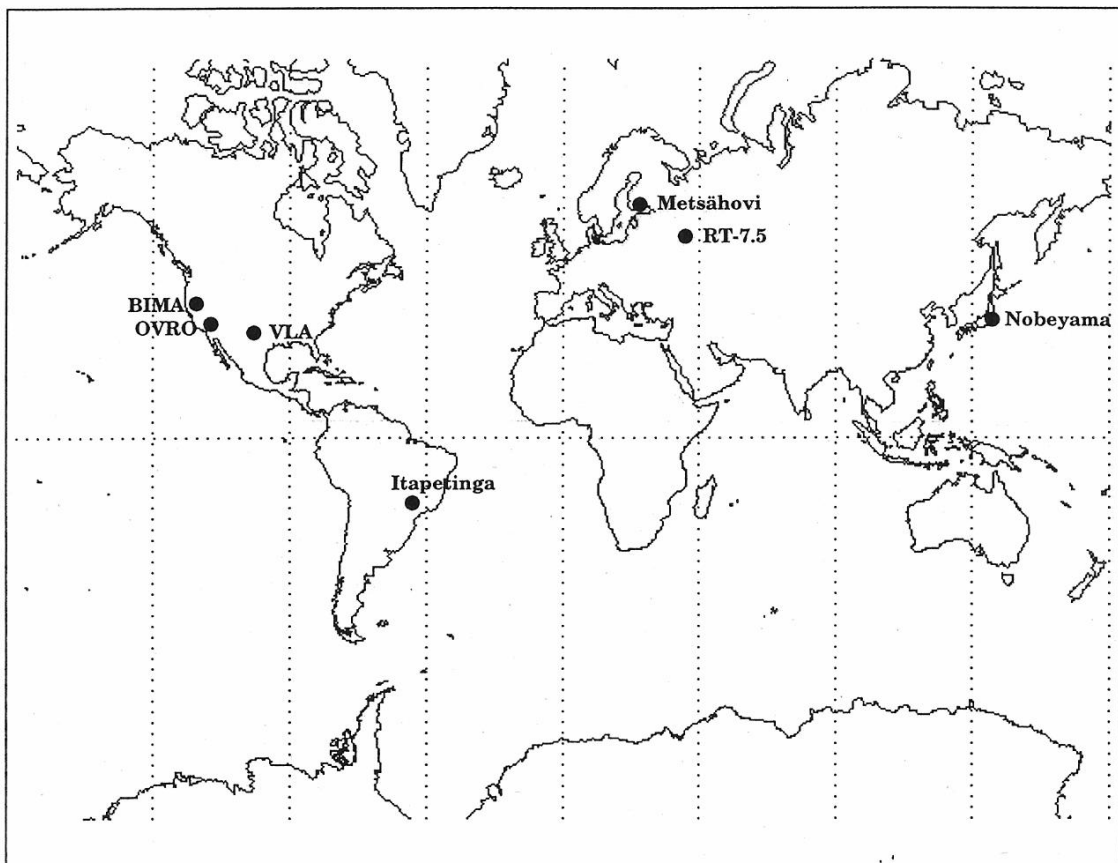


Figure 4.9: Radio facilities at cm- and mm-wavelengths (note the time difference, limited common observing time).

TABLE I
World-wide microwave spectrometers *in the 1980's...*

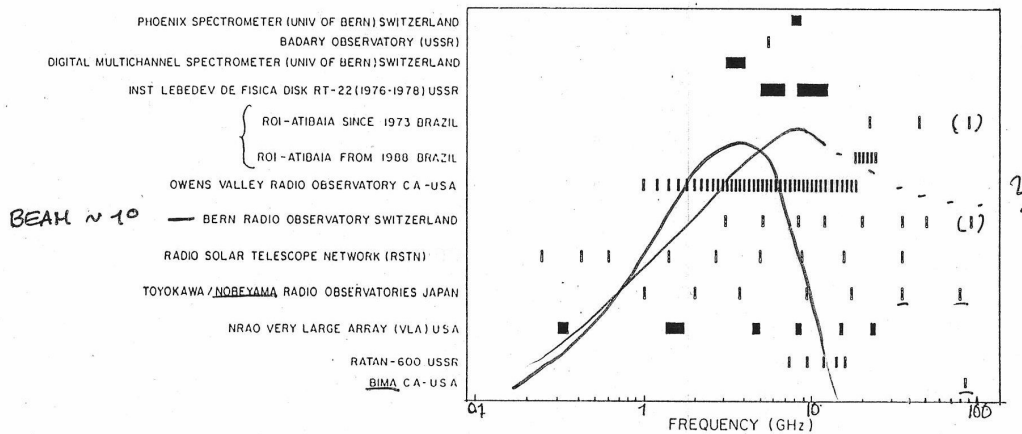
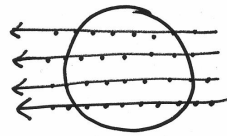


Figure 4.10: Fixed frequency coverage in the 1980s..

4.5.1 Single dish antennas



Figure 4.11: Single dish antennas - Metsähovi Radio Observatory, a 14-m antenna in Kirkkonummi, operated by Helsinki University of Technology



Skannaus läpi Auringon
 KA-suunnassa, deklinaatiota
 muuttaen

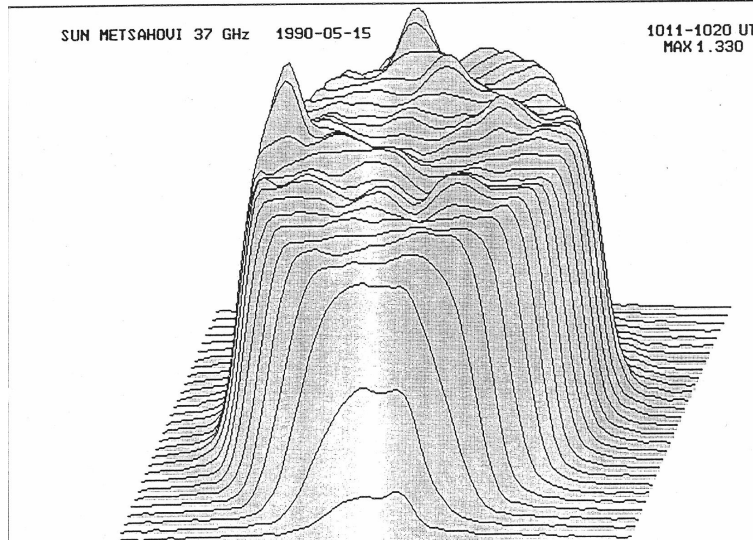


Figure 4.12: Imaging with scanning technique, the scans are made along right ascension, changing declination between scans.

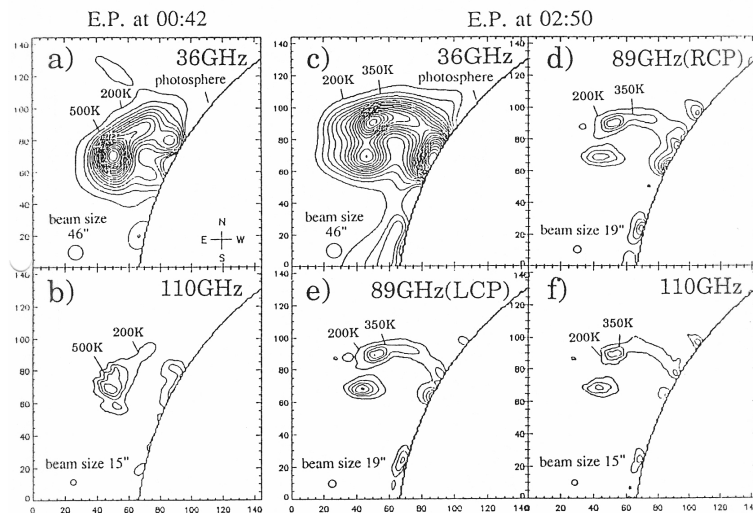


Fig. 1. Contour maps of the eruptive prominence at millimeter wavelengths observed with the 45-m radio telescope at Nobeyama Radio Observatory. (a) and (b) show 'E.P. at 00:42' observed from 00:42 to 00:55 UT (May 28) at 36 and 110 GHz, respectively. The minimum contour level is 200 K. The contour step is 300 K. (c-f) show 'E.P. at 02:50' observed from 02:50 to 02:59 UT (May 28) at 36 GHz, 89 GHz (RCP), 89 GHz (LCP), and 110 GHz, respectively. The minimum contour level is 200 K and the contour step is 150 K. The unit for each axis is 5". The area of the maps is 12' x 12', and the spatial resolutions are 46", 19", and 15" at 36, 89, and 110 GHz, respectively. The heights of the prominence are about 1.5×10^5 km and 1.7×10^5 km above the photosphere for 'E.P. at 00:42' and 'E.P. at 02:50', respectively.

Figure 4.13: Nobeyama 45-m scanning observations of a prominence (full disk needs 240 scans, which is done in 2 hours time!) From Irimajiri et al. 1995

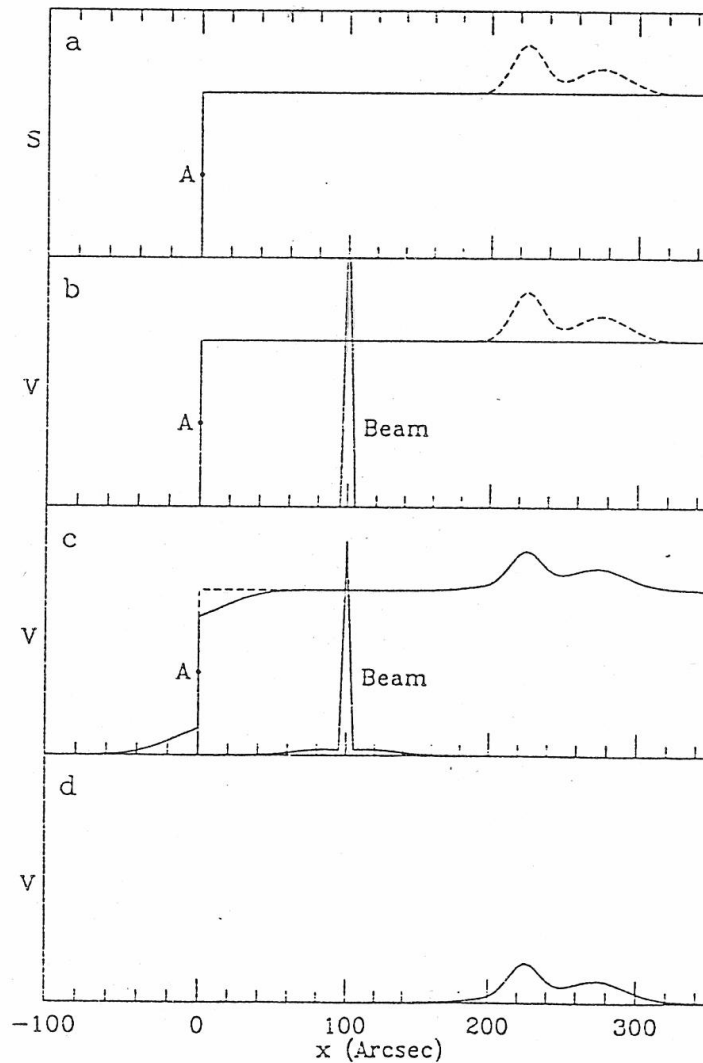


FIG. 3.—Diagrams illustrating the result of convolving sources with beams that have a sharp core and symmetric far wings. (a) Shows a source consisting of a simple step-function discontinuity (*solid curve*) at x (i.e., a Heaviside function). The dashed curve shows continuous variations introduced well inside the discontinuity. (b) Shows the result, V , of convolving the source in (a) with a simple Dirac delta function with no wings, which duplicates the source exactly. (c) Illustrates artificial limb darkening with an equal measure of artificial sky brightening, which results when the source profile is convolved with a beam that has symmetric wings. (d) Shows only continuous variation far to the right without the limb discontinuity. If we are given that the far wings of the beam are symmetric, we can conclude that the signal profiles in (b) and (c) can only have come from the source plotted in (a). The source that gave rise to the smooth signal profile shown in (d) remains ambiguous without further knowledge of the beam profile.

Figure 4.14: Artificial limb darkening (Lindsey and Roellig)

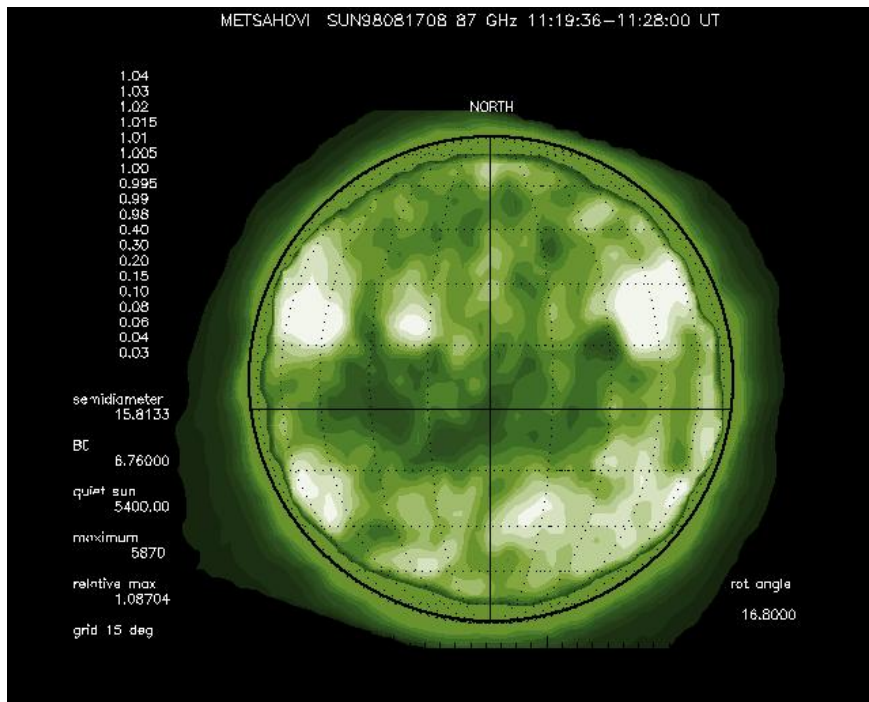


Figure 4.15: Artificial limb darkening observed in a Metsähovi solar map.



Figure 4.16: Small dish complexes: Tuorla-Bern polarimeters (TUBE)

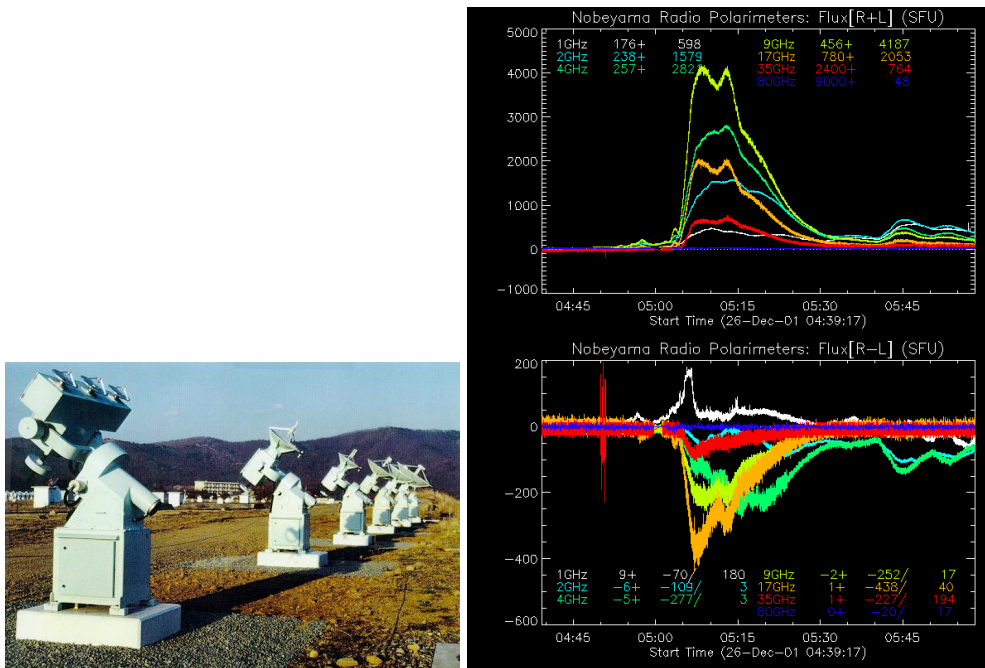


Figure 4.17: Nobeyama polarimeters: Fixed frequencies at 1, 2, 3.75, 9.4, 17, 35, 80 GHz, full disk observations, automatic recording

4.5.2 Non-traditional antennas

RATAN 600 (Russia)

RATAN 600 consists of 895 antenna elements (2×11.5 m each), constructed in the shape of a ring with a diameter of 576 m. One-dimensional scans of the Sun are observed near 09 UT, at 30-40 wavelengths ranging from 1.67 cm up to 32 cm with left (LCP) and right (RCP) circular polarization.



Figure 4.18: RATAN-600 in Zelenchukskaya, North Caucasus, Russia

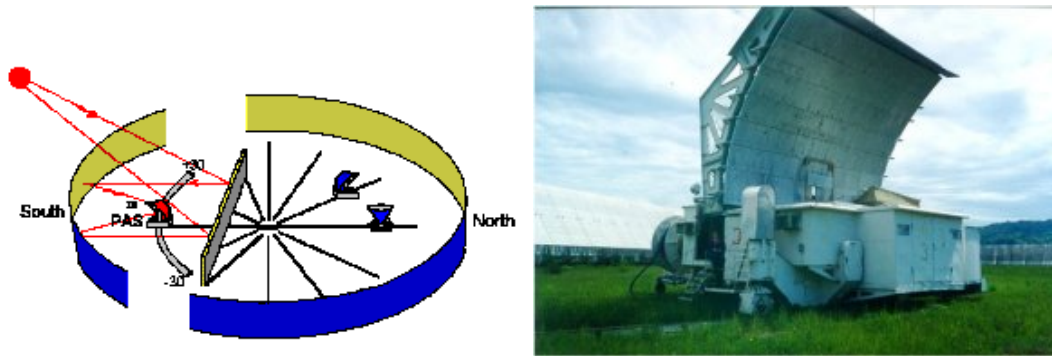


Figure 4.19: The RATAN-600 is a reflector-type radio telescope, advantages being a broad wavelength range, ability to use wide bandwidths, etc., but it is non-traditional in design. In order to obtain high resolution at rather short wavelengths, the mirror of a radio telescope must have rather large linear dimensions and the reflecting surface must be extremely accurate. These requirements are clearly contradictory; in order to resolve this contradiction, the main mirror of the telescope was built in the shape of a ring. Left: the southern sector can operate in combination with the flat periscope reflector. It is possible to track a source by moving the secondary mirror along the arc-shaped railway tracks or to perform azimuthal 2D map synthesis. Right: the secondary mirror and receiver cabins.

4.5.3 Observed polarization

Stokes parameters

Stokes parameters (I,Q,U,V) describe the degree of polarization. In solar radiation only circular polarization is observed (linear polarization disappears because of Faraday rotation).

For a completely polarized wave:

Left-hand circular ('L'): $I=S$, $Q=0$, $U=0$, $V=S$

Right-hand circular ('R'): $I=S$, $Q=0$, $U=0$, $V=-S$

Note: for engineers and physicists the directions are different!

Flux density S is often described with intensity $I = R+L$ and polarization with $R-L$.

Degree of polarization = polarized power/total power = $\frac{\sqrt{Q^2+U^2+V^2}}{I}$; (0...1)

Measurement of magnetic fields

In the presence of a temperature gradient, free-free radiation becomes circularly polarized:

$$P = (n \nu_B \cos \alpha) / f ,$$

$$n = -(\partial T_B / \partial f) f T_B^{-1} = \frac{\partial \lg T_B}{\partial \lg f} ,$$

where

P is the observed circular polarization degree (per cent, %),

n is the logarithmic spectral index,

ν_B is the gyrofrequency and f is the observing frequency,

T_B is the brightness temperature.

The intensity of polarized emission is proportional to the longitudinal (line-of-sight) component of the magnetic field B ($\cos \alpha = 1$).

A practical estimate is: $B = 107 P (n\lambda)^{-1}$, B in Gauss and λ in cm.

For optically thin plasma, $n = 2$, and $B = 54 P / \lambda$.

See details in e.g., Grebinkij et al., *Astronomy and Astrophysics Supplement Series* Vol. 144, pp. 169-180, 2000, and/or

Bogod and Gelfreikh, *Solar Physics* Vol. 67, pp. 29-46, 1980.

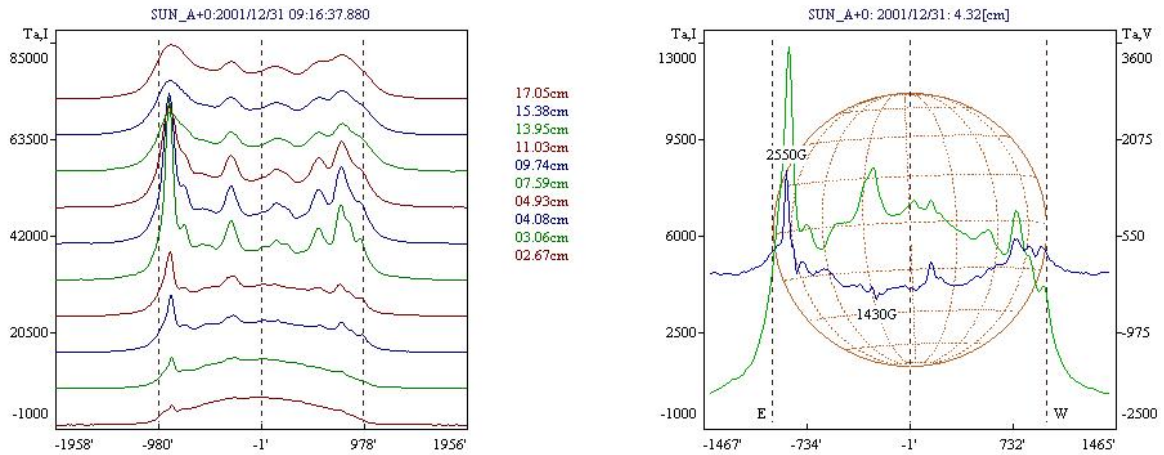


Figure 4.20: RATAN intensity profiles over the solar disk; Calculated magnetic field strength from observed polarization.

Faraday rotation

Faraday rotation observations are unique among remote diagnostics of the solar corona in that they provide information on the coronal magnetic field. The polarized radiation from natural radio sources (i.e., linear polarization of sources like quasars that get occulted by the solar corona) are observed and the magnitudes of the rotation measures together with the estimated electron number densities are used for determining the magnetic field strengths ($\beta = C \times N B \lambda^2 \Delta d$).

See more details in Mancuso and Spangler, *Astrophysical Journal*, Vol 539, pp. 480-491.

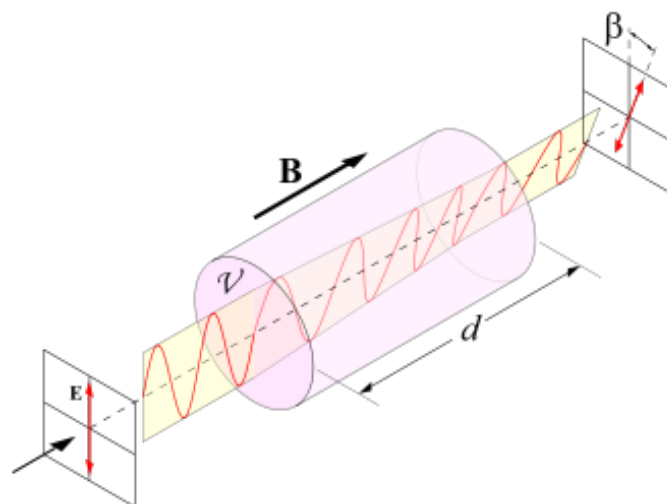


Figure 4.21: Faraday effect (image: Wikimedia Commons)

4.5.4 Multi-beam receivers in single dishes



Figure 4.22: El Leoncito, Argentina (at height 2550 m)

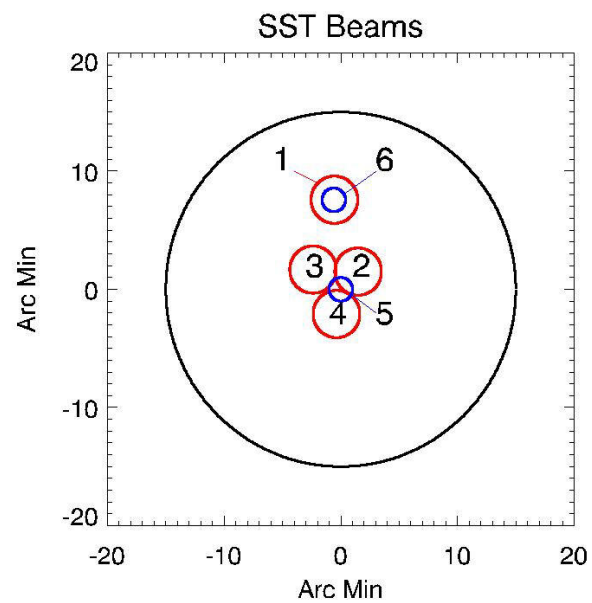
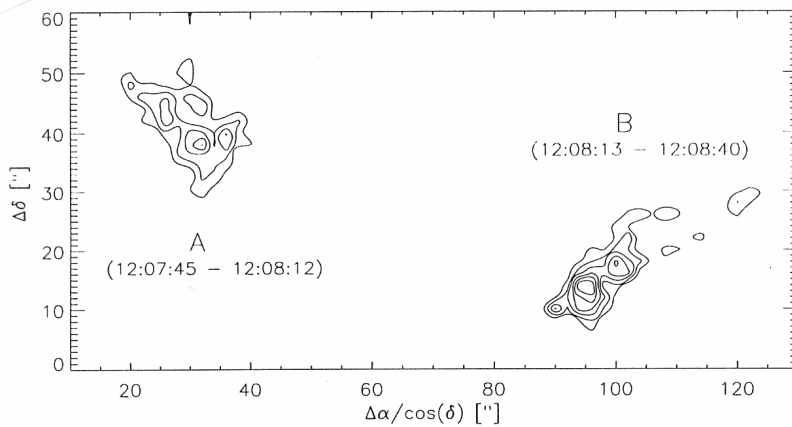


Figure 4.23: A cluster of six beams, shown in the diagram, is directed to the active region selected for tracking. Observing frequencies are 212 and 405 GHz.



A & A, 317, 232,
1997

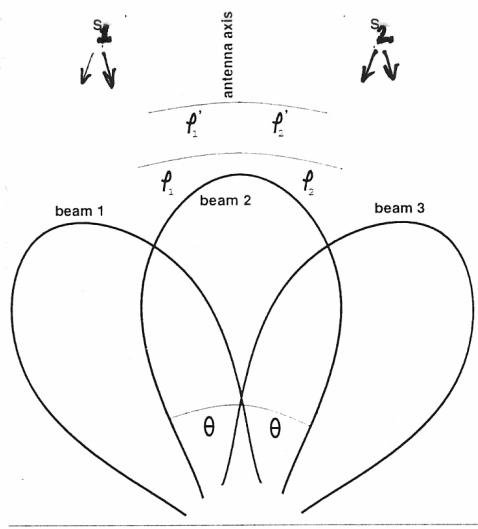


Fig. 8. Dynamic burst map of the emission center distribution during the whole event. The grid spacing is 2" and approx. 17000 positions each one calculated within 4 ms during the time interval from 12:07:45 UT until 12:08:50 UT have been used. Before 12:08:12.5 UT emission from source A dominates while for later times source B is dominant. Coordinates refer to offsets in right ascension and declination relative to the antenna pointing.

Fig. 1. Sketch of a simple antenna beam pattern of three intersecting beams observing two sources that emit at the same time.

4.5.5 Interferometers

Nobeyama Radioheliograph (NoRH) in Japan is a radio telescope dedicated to observe the Sun. "Helio" means the Sun, "graph" means an imaging telescope. It consists of 84 parabolic antennas with 80 cm diameter, sitting on lines of 490 m long in the east/west and of 220 m long in the north/south. Its construction took 2 years and cost 1.8 billion yen. The first observation was in April, 1992 and the daily 8-hours observation has been done since June, 1992. The observing frequencies are 17GHz (right and left circular polarization) and 34GHz (only intensity). Field of view is full solar disk, with spatial resolution of 10 arcsec (17GHz) and 5 arcsec (34GHz). Temporal resolution is 0.1 sec (event mode) or 1 sec (regular mode).

As the NoRH is a radio interferometer, original data are sets of correlation values of all the combination of antennas. They correspond to the spatial Fourier components of the brightness distribution of the solar disk. In most cases, it is necessary to synthesize images from the original raw data.

NoRH image synthesis is done with IDL software. All computers use Linux as the operating system. The synthesis programs available are:

- Hanaoka (standard CLEAN algorithm, support 17 and 34 GHz, full/partial Sun images)
- Koshix (CLEAN + Steer algorithm, support 17 GHz, better for diffuse radio sources, full/partial Sun)
- Fujiki (high spatial resolution, support 17 GHz, only partial Sun images)
- C2FITS (for reconstructing the NoRH raw data to visibility data that can be utilized for AIPS synthesizing software)

Nancay radioheliograph (NRH) in France consists of a cross-shaped multi-antenna array, comprising an East-West branch with 19 antennas along a 3200 meter long baseline and a North-South branch of 24 antennas over a total length of 1250 meters. It can image the Sun at wavelengths between 60 cm and 2 meters. It has been equipped with a digital correlator, which permits the true two-dimensional imaging of the solar corona, using all possible baselines of the cross-shaped array, at a rate of 5 images per second in each of 5 fixed wavelengths between 60 cm and 2 meters. Observations at different wavelengths probe different heights in the corona, in the case of the Nancay radioheliograph regions between 0.1 and 0.5 solar radius above the visible surface.



Figure 4.24: Nancay radioheliograph imaging at five selected frequencies

It is an instrument dedicated to solar observations, and presently it is the only instrument to provide daily radio observations of the **solar corona** (the other dedicated solar radio telescope, at Nobeyama Radio Observatory in Japan, observes at much shorter, centrimetric, wavelengths which probe the solar atmosphere much closer to the visible surface, and other radio telescopes, like the Very Large Array (VLA) in the U.S.A., observe the Sun only infrequently, and have not been designed for such specialized observations of a highly variable, very intense radio source).

During 1994-1998 the system has been renovated: a new, powerful correlator allowing rapid multifrequency two-dimensional imaging of the Sun has been installed, and a new 7.5 meter diameter antenna is raised at a site 1.5 km to the South of the southernmost existing antenna, thus allowing a twice better resolution. This renovation cost somewhat over a million US dollars, co-financed by the French State (CNRS) and the administrative council of the Region to which Nancay belongs.

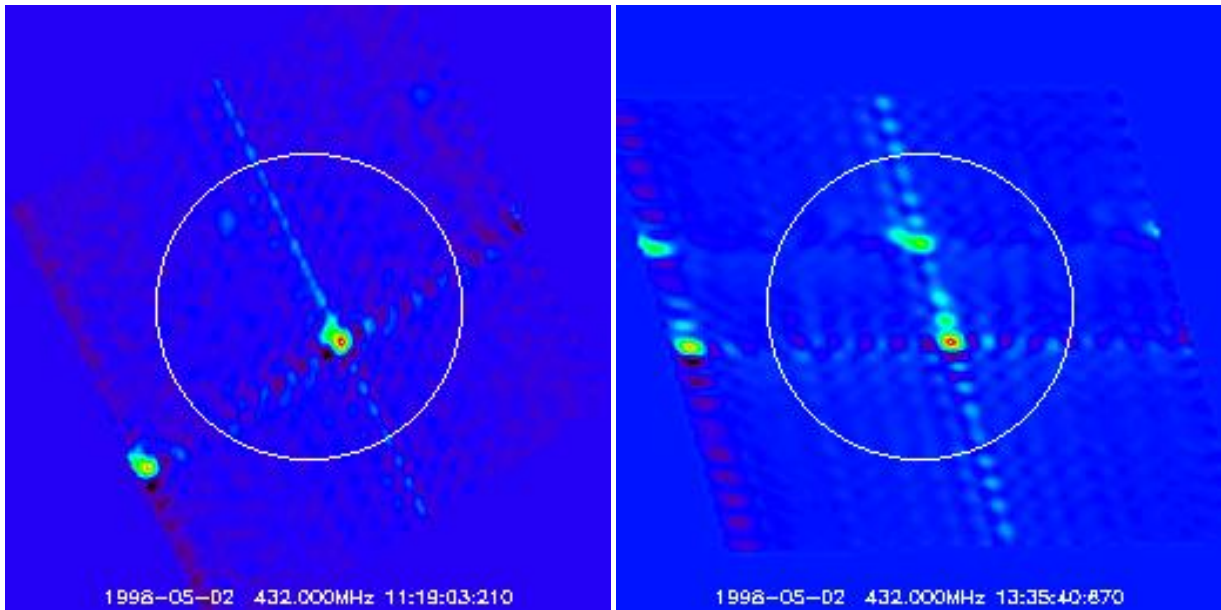


Figure 4.25: Nancay interferometric pattern + uncleaned source at 432 MHz

Interferometers - Owens Valley Solar Array (OVSA):

2 x 27-m + 3 x 2-m + 2 new 2-m antennas

1-18 GHz (tunable, phase lock in 20 ms)

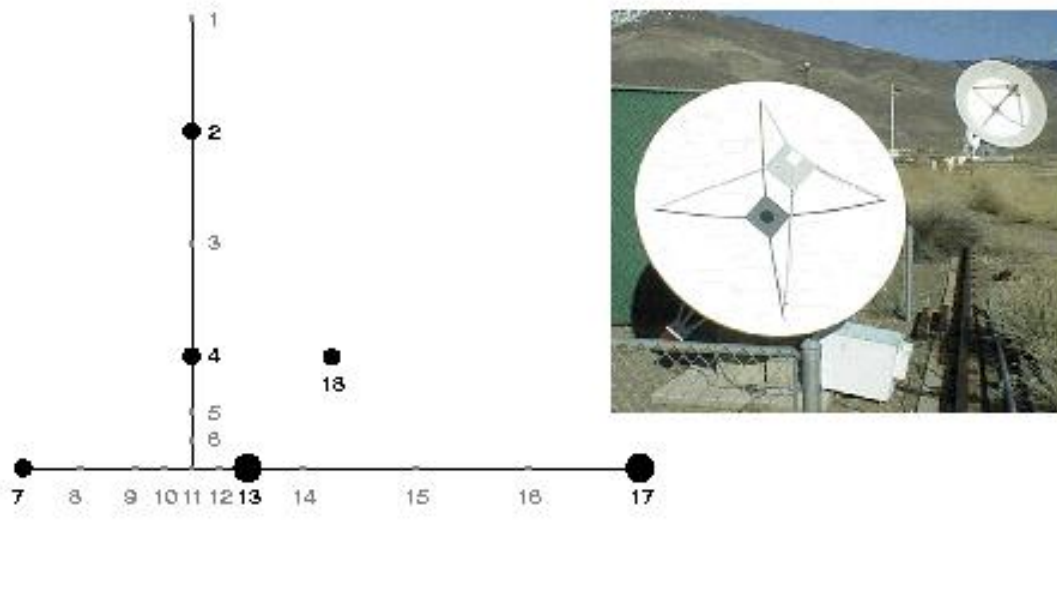


Figure 4.26: Owens Valley Solar Array (OVSA), USA

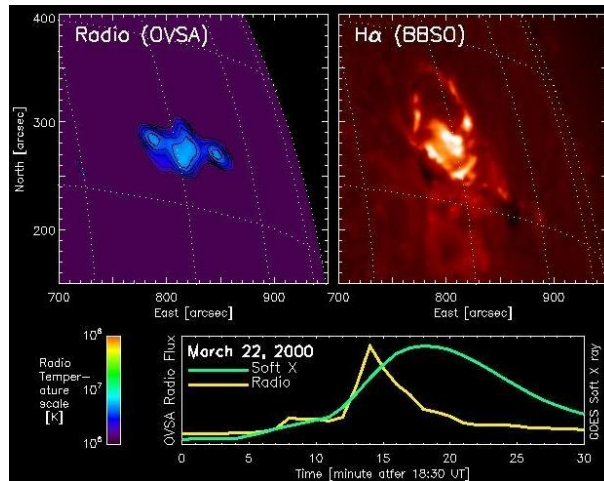


Figure 4.27: Owens Valley Solar Array (OVSA) flare observations, partial field-of-view



Figure 4.28: VLA, Socorro New Mexico, recently upgraded as Karl G. Jansky Very Large Array, with state-of-art receivers and electronics, enabling dynamic imaging spectroscopic observations of the Sun.

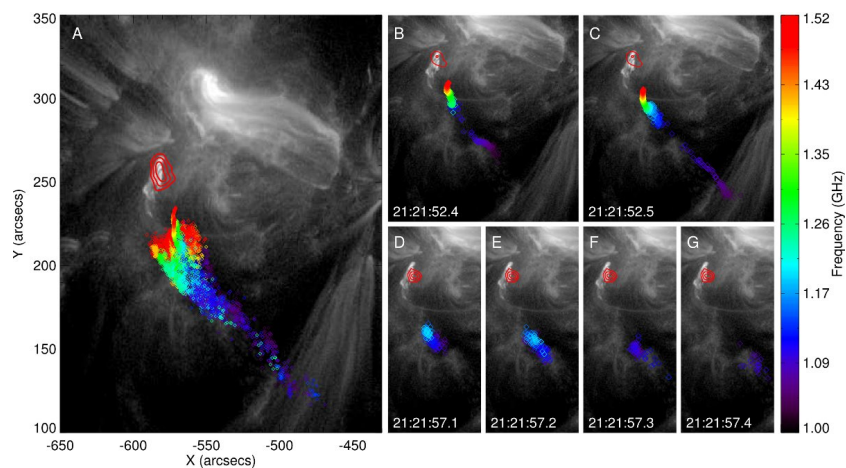


Figure 4.29: Type III dm burst centroids as a function of frequency (colored from red to blue for decreasing frequencies), showing trajectories of fast electron beams in the solar corona. See RHESSI Science Nugget at http://sprg.ssl.berkeley.edu/~tohban/wiki/index.php/Passages_of_Electron_Beams

4.5.6 Radio spectrometers

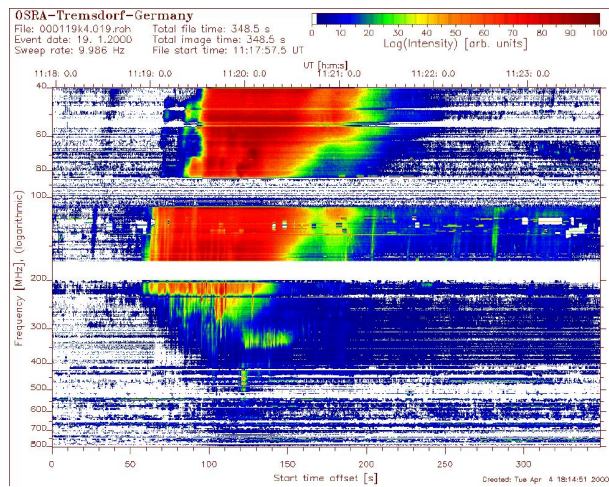


Figure 4.30: Note the missing frequencies, removed because of man-made interferences.

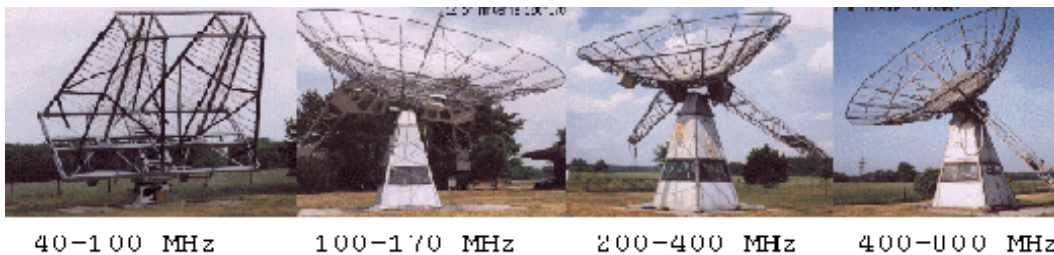


Figure 4.31: Examples of radio spectrometers: Tremdorf in Germany. The systems consists of 4 sweep spectrographs (10 sweeps per second): 40-90 Mz, 100-170 MHz, 200-400 MHz, 400-800 MHz. The antennas are a pair of crossed double-log Yagis, 1 x 10.5-m, 2 x 7.5-m paraboloids. There is strong interference at 85-108 MHz (UHF radio), 170-200 MHz (UHF TV), 550-700 MHz (VHF TV). Calibration between frequency ranges can also be tricky.

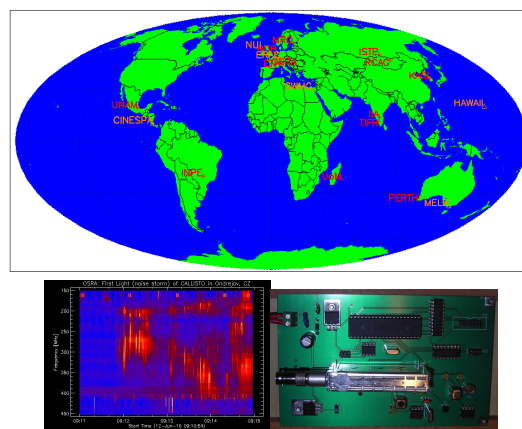


Figure 4.32: New cheap and smart technology: e-Callisto (operated by Christian Monstein, ETH Zurich)

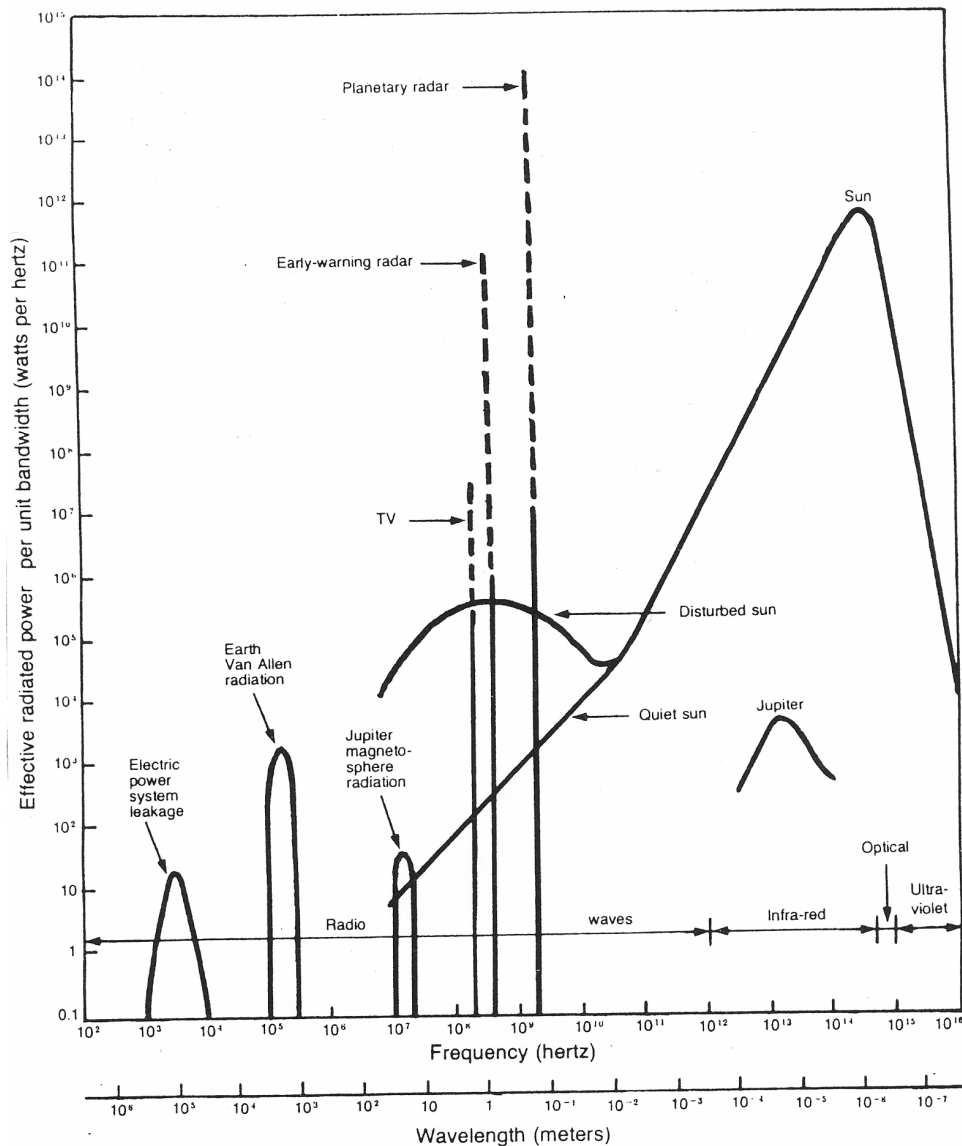


Fig. 8-51. Electromagnetic spectrum of the solar system from radio to UV showing the spectral power (W Hz^{-1}) as a function of frequency for sources of radiation from the earth, Jupiter and the sun. The largest spectral powers are from terrestrial radars.

Figure 4.33: Interferences may appear at IF, not just at observing frequencies. (Fig. from Kraus: Radio Astronomy)

The plasma frequency of the ionosphere is ~ 15 MHz on the day side of the earth near sunspot maximum and ~ 10 MHz on the night side near sunspot minimum, making the layer opaque to all lower frequencies. Even at preferred sites near the magnetic poles, such as Canada and Tasmania, and near sunspot minimum when ground based observations can be taken as low as $2\sim$ MHz, the available resolution is extremely poor (several degrees). Therefore, to study this last unexplored window on the electromagnetic universe, one must go to space.

The Wind **WAVES** investigation (launched in 1994), with two swept-frequency radio receivers RAD1 and RAD2, provides comprehensive coverage of radio and plasma wave phenomena in the frequency range from 20 kHz up to about 14 MHz. The Thermal Noise Receiver TNR extends the frequency range down to 4 kHz. STEREO (launched in 2006) and Solar Orbiter (to be launched around 2015) will provide similar radio spectral data.

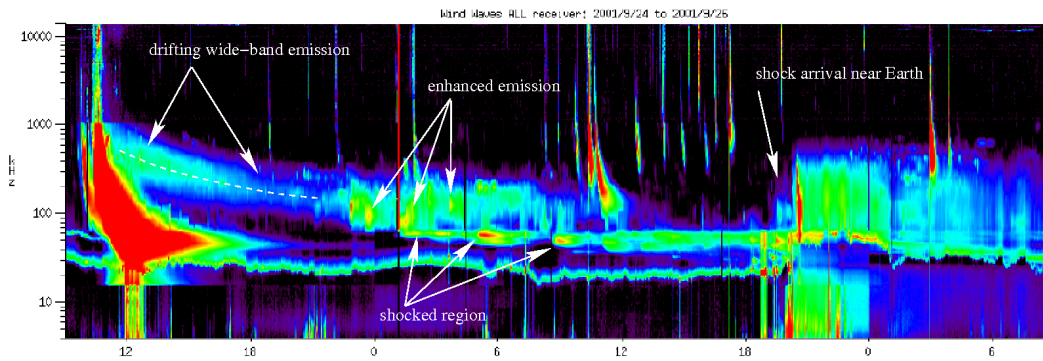


Figure 4.34: Radio spectrometers in space - Wind WAVES example.

4.5.7 Solar eclipse observations using Fresnel diffraction

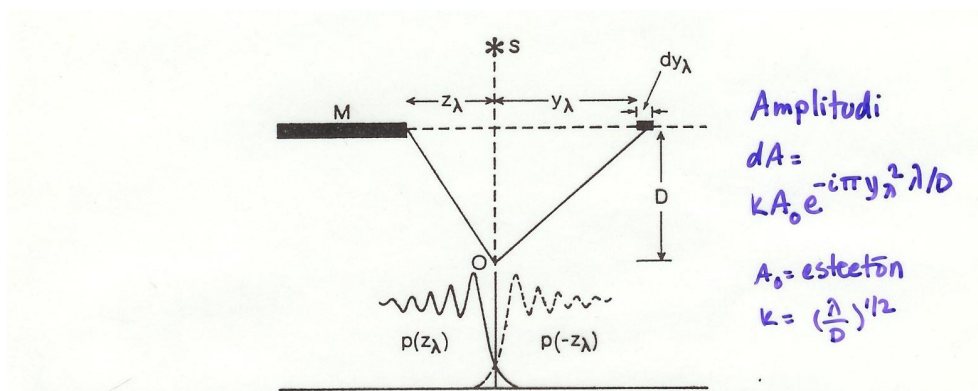


FIG. 1. Schematic representation of the generation of the occultation curve $p(z_\lambda)$, as the screen M at a distance D from the observer uncovers a source S . The occultation curve is the mirror image about the axis OS of the diffraction curve $p(-z_\lambda)$.

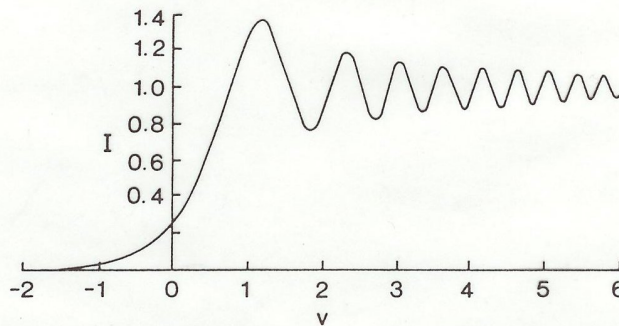
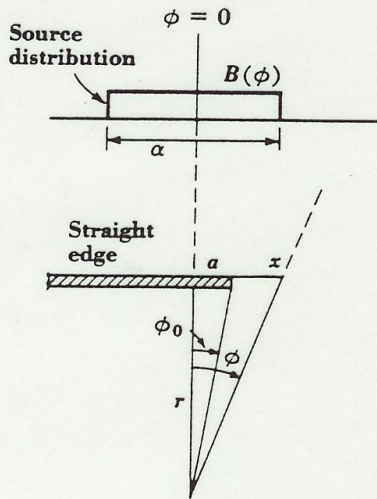


FIG. 2. The shape of the occultation curve of a point source. The horizontal scale is in units of v , the corresponding angular scale being given by $\theta = v(\lambda/2D)^{1/2}$, where λ is the wavelength and D the Moon's distance. For $\lambda = 1$ m, one unit of v corresponds to about 8 arc sec. $I = 1$ corresponds to the flux density of the unobstructed curve, while at the edge of the geometrical shadow $I = 0.25$.

Hazard, 1976



Kohteen nopeus diffraktioluvun yli (kohtisuoraan kuvun reunaa vastaan)

Aika $t / 1''$

$$t = \frac{1}{\frac{d\theta}{dt} \cos\theta}$$

$$\frac{d\theta}{dt} = \text{kuvun etenemisnopeus} \\ \text{arc sec/s} \approx 0.3/\text{s}$$

θ = kuvun etenemissuunnan ja kohteen välinen kulma

Fig. 6-35. Occultation of source of width α .

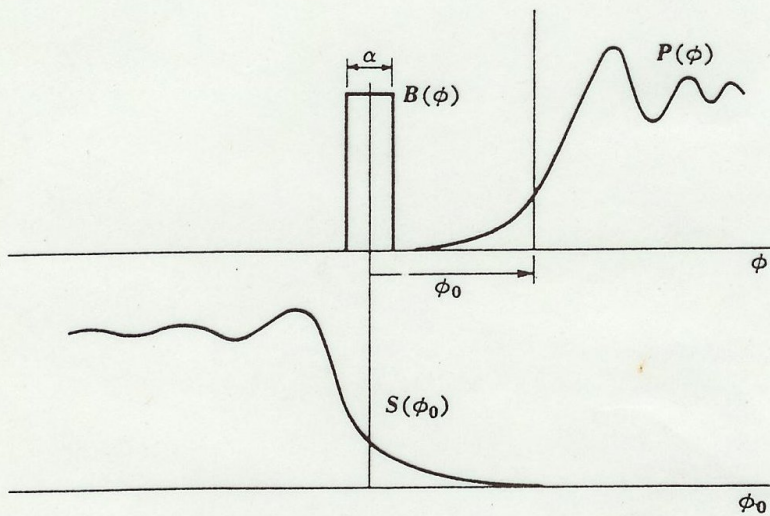
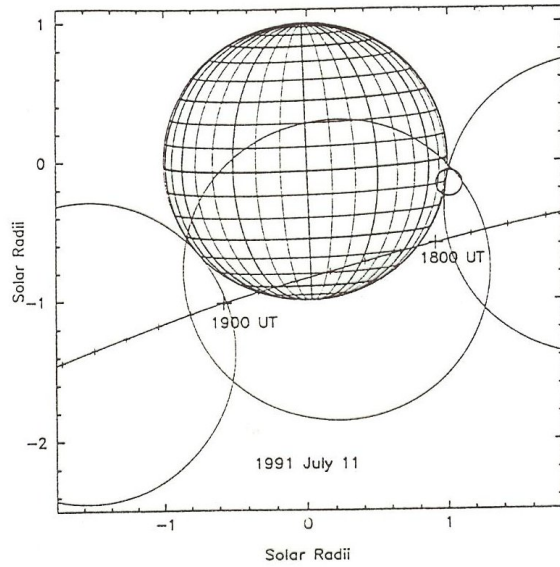


Fig. 6-36. The occultation curve is the convolution of the source distribution and the occultation pattern for a point source.

$$S(\phi_0) = \int_{-\alpha/2}^{+\alpha/2} B(\phi) \bar{P}(\phi_0 - \phi) d\phi$$

Kraus, 1986



Koon liike $0.4/5$
 integrointiaika $3.2/5$
 resoluutio $1/3$

FIG. 1.—Path of the Moon with respect to the Sun during the eclipse (north is at the top of the figure and west to the right). The relative size of the main beam is shown by a circle. The interferometer tracked a point $10''$ above the photospheric limb.

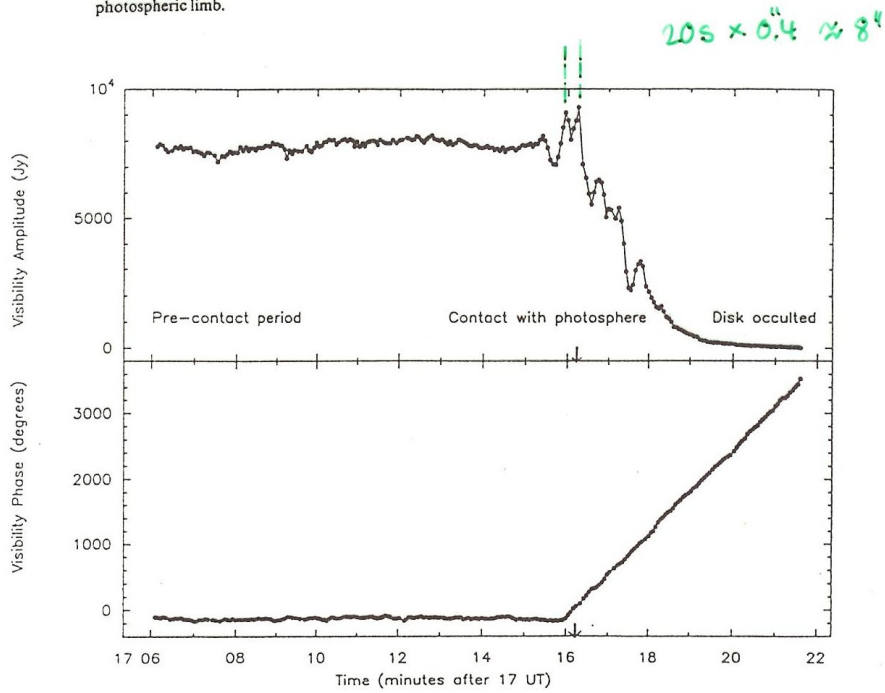


FIG. 2.—Amplitude (top panel) and phase (bottom panel) of the visibility around the time of first contact, for a baseline with fringes parallel to the limbs. The behavior of each is explained in the text. The arrows point to the time at which the photosphere was occulted.

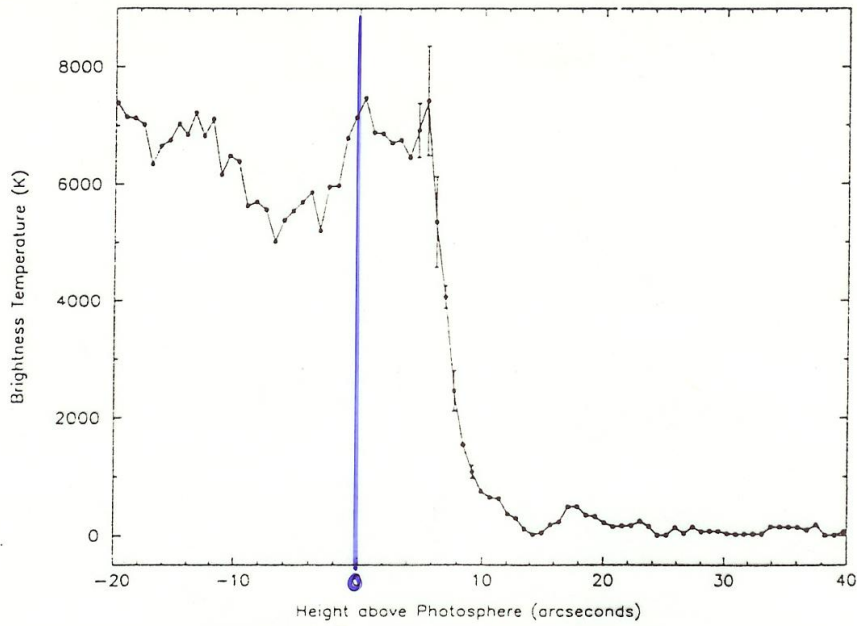


FIG. 5.—The limb profile, derived using the ephemeris phases. The attenuation due to the primary beam has been removed.

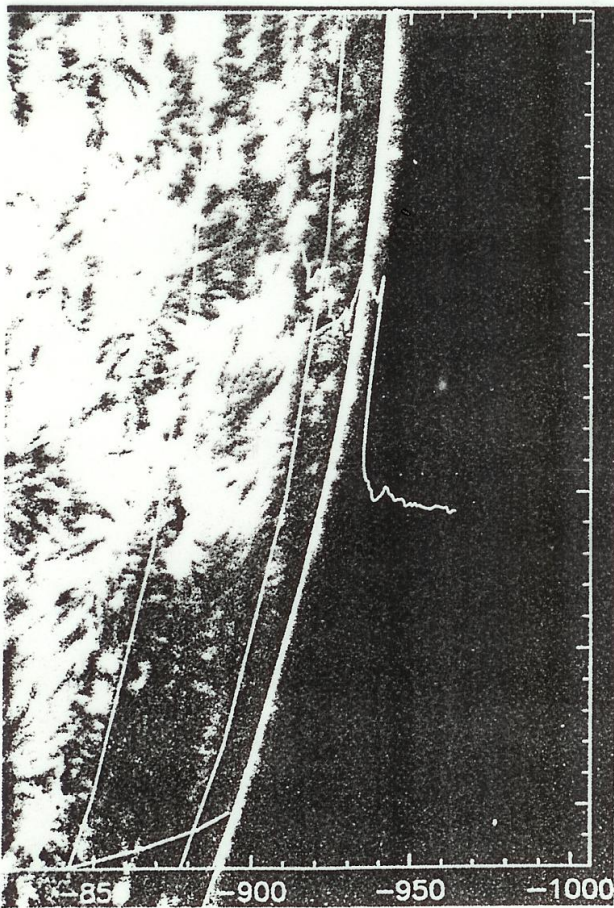
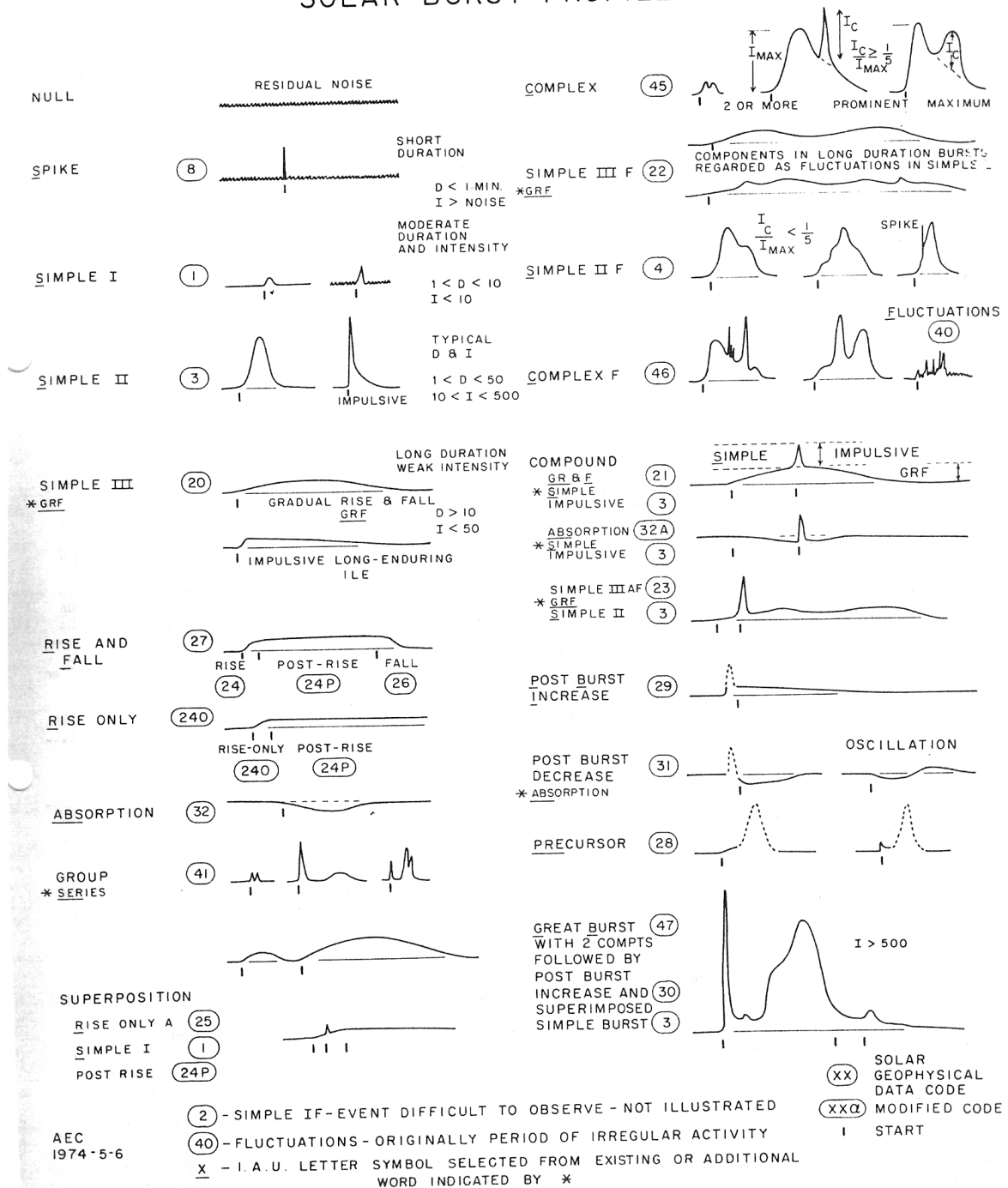


FIG. 6.—Off-band H α photograph of the region near the limb, taken at BBSO on the day of the eclipse, overlaid with solar latitude and longitude lines at 10' intervals and with a plot of the 3 mm limb profile. The vertical scale of the radio profile is arbitrary. The plus sign shows the center of the beam. The spicules can be seen as a fuzzy edge above the optical limb, nearly at the same height as the sharp cutoff in the radio profile. The contrast of the H α spicules was photographically enhanced for clarity.

Belkora, ... 1992.

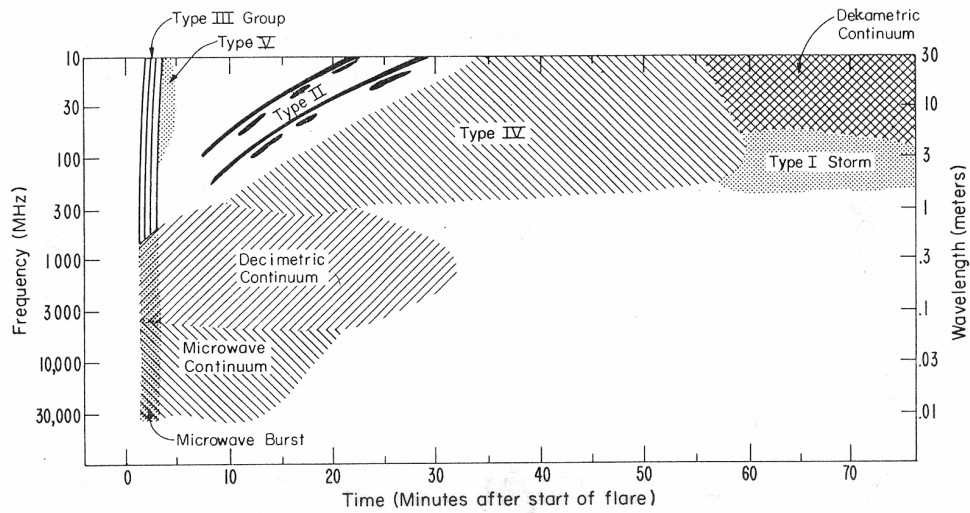
4.5.8 Burst classifications

2800-2700 MHz SOLAR BURST PROFILES



Solar burst classification using radio emission at 2.8 GHz. Many flare forecasts are done using this wavelength

F10.7 = 2800 MHz = 10.7 cm flux



Spectral type --

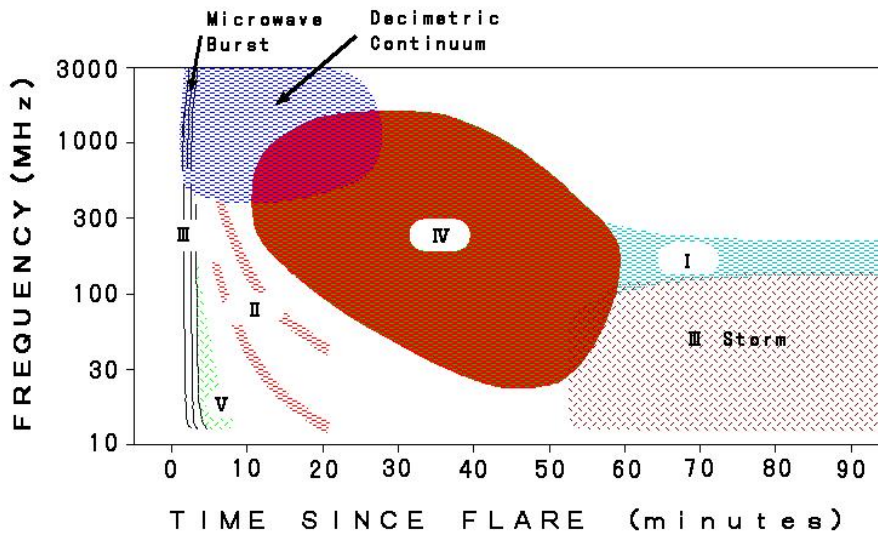
- I = storm bursts
- II = slow drift bursts
- III = fast drift bursts
- IV = prolonged continuum
- V = brief continuum (normally following Type III burst)

CONTINUUM = continuum in close association with Type III burst storms, often with reverse drift bursts and often, but not always, associated with noise storms on metric wavelengths (used by SMGR);

DCIM = decimetric burst defined by very fast drift spike or group of spikes with very high degree of polarization extending usually less than one octave in or close to decimeter range;

UNCLF = unclassified activity.

Solar Geophysical Data classification



Hiraiso Solar Observatory classification (reversed frequency scale)

Chapter 5

Optical, EUV, and X-ray observations

5.1 Satellite orbits

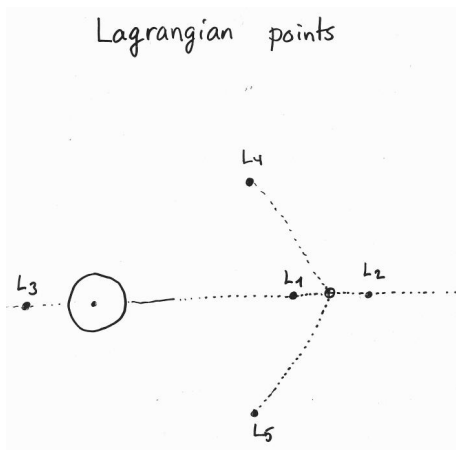


Figure 5.1: The Lagrangian points are positions in an orbital configuration where a small object (like a satellite) is affected only by gravity and can theoretically be stationary relative to the two larger objects (like the Sun and Earth). L1 is a favourable place for solar satellites because it allows a constant view of the Sun and the position is near enough to the Earth to allow good telemetry. L1 is about 1 million km from the Earth and about 148 million km from the Sun.

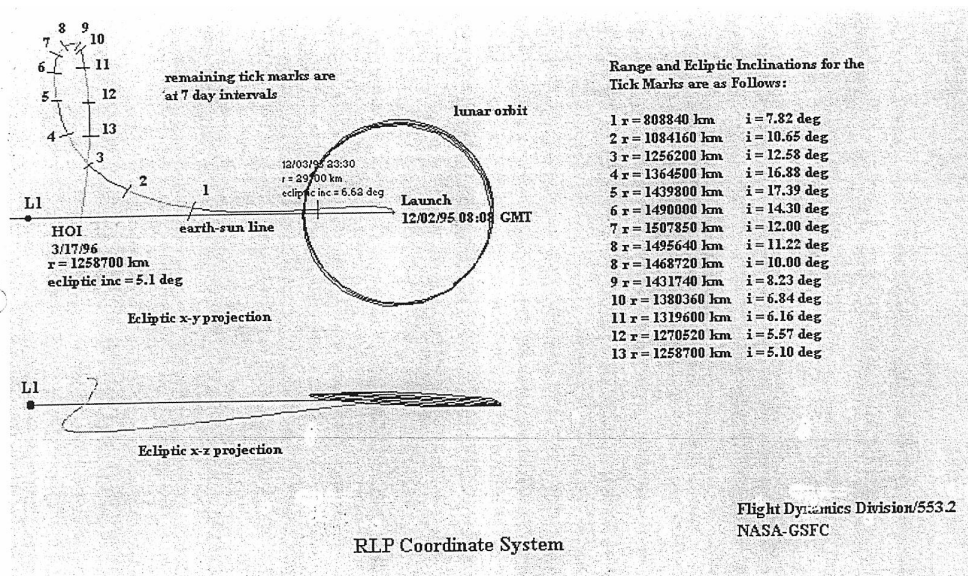
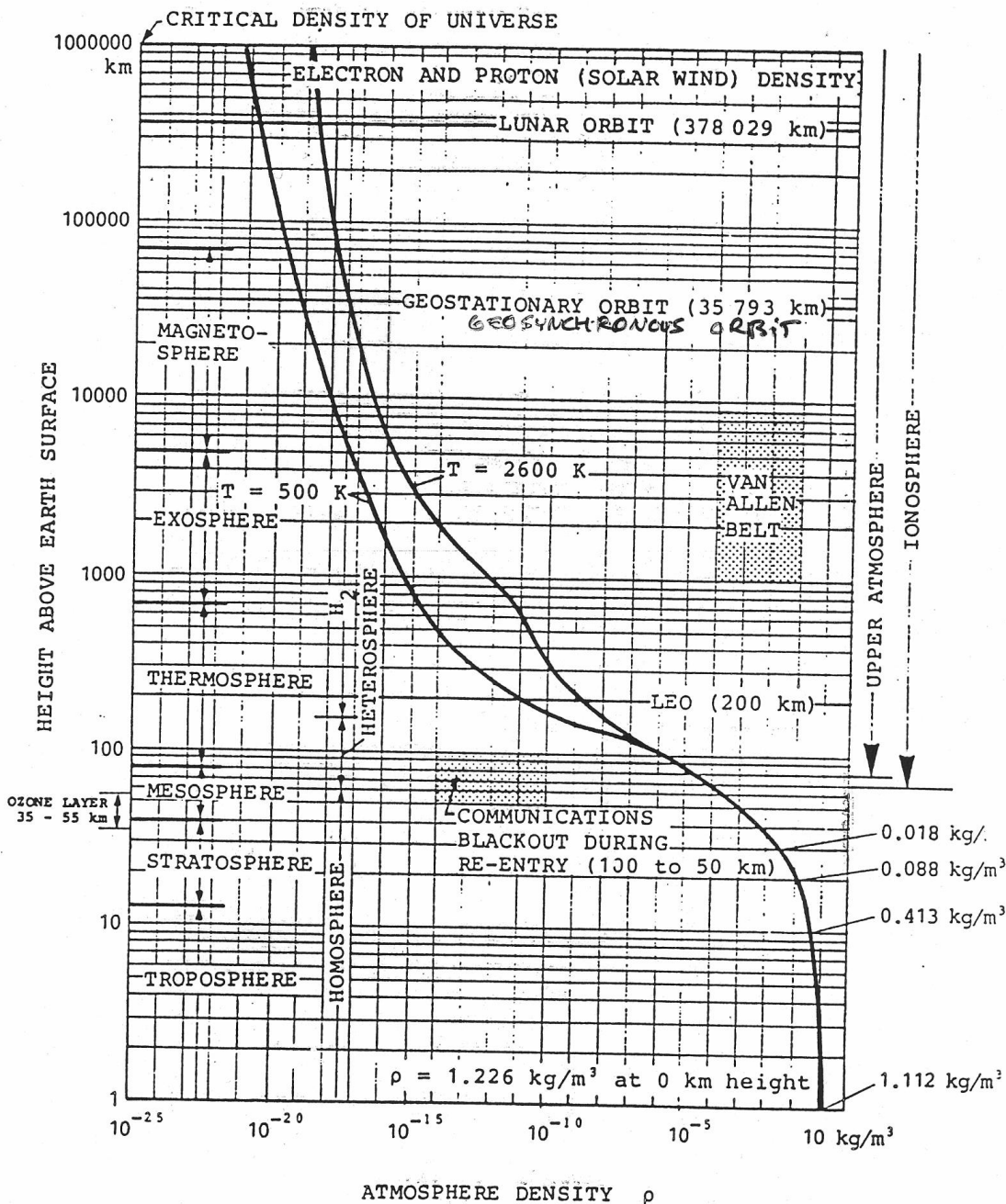


Figure 5.2: SOHO satellite moves around the Sun in step with the Earth, by slowly orbiting around the First Lagrangian Point L1.

Satellites on low-Earth orbits will experience 'satellite night times', i.e., the Sun cannot be observed when the satellite is behind the Earth. The on-off periods get repeated every 40–70 minutes. This affects also the telemetry.



ATMOSPHERIC DENSITY WITHIN EARTH'S INFLUENCE SPHERE

FIGURE 4

Figure 5.3: The NOAA GOES satellites have geosynchronous orbits, near height 36 000 km. The Japanese solar satellite Yohkoh (1991–2001) was on a low Earth orbit at height 570–730 km, and it regularly passed the van Allen radiation belts so near that the most sensitive instruments had to be turned off. This is the so-called 'South Atlantic Anomaly', SAA region, where the van Allen belt is at 200 km height at the lowest.

5.2 X-ray and EUV instruments

These instrument designs include:

- Geiger counters (1962-, saturates easily)
- Proportional counters
- Scintillation detectors
- Gas scintillation proportional counters
- Solid state detectors
- Microchannel plates
- Collimators
- Grazing incidence telescopes
- Glancing incidence telescopes
- Grating spectrometers
- Bragg crystal spectrometers

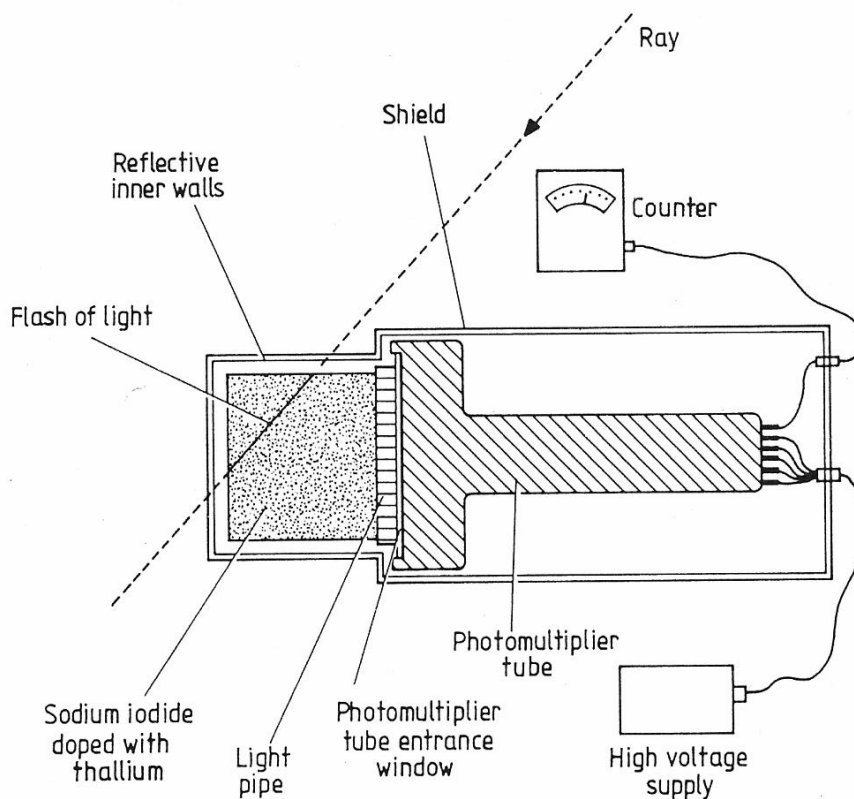


Figure 1.3.2 Schematic experimental arrangement of a scintillation counter.

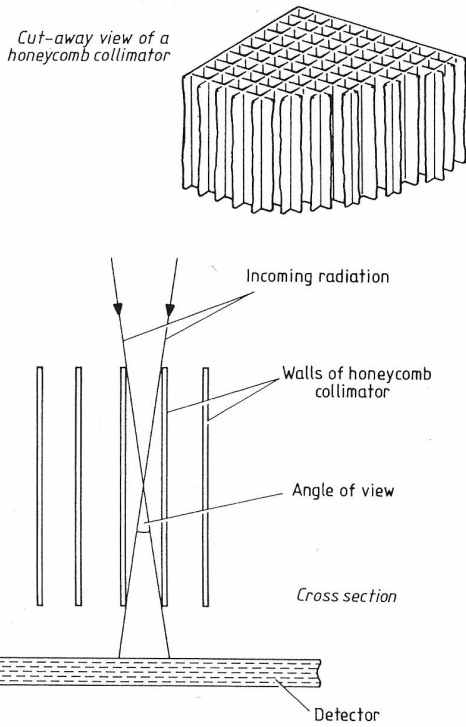


Figure 1.3.5 Honeycomb collimator.

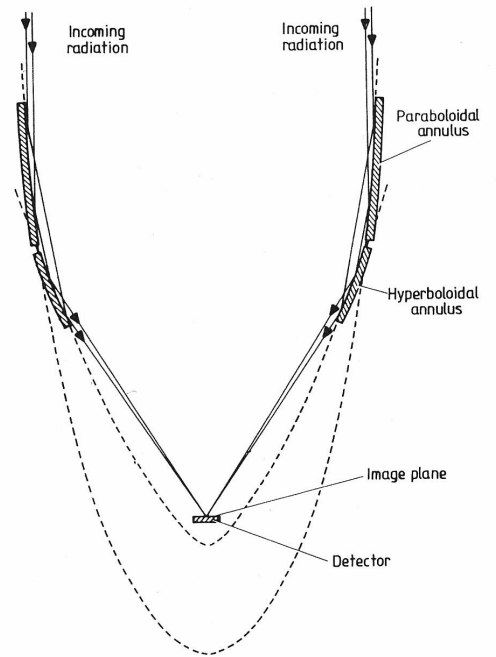


Figure 1.3.8 Cross section through a grazing incidence x-ray telescope.

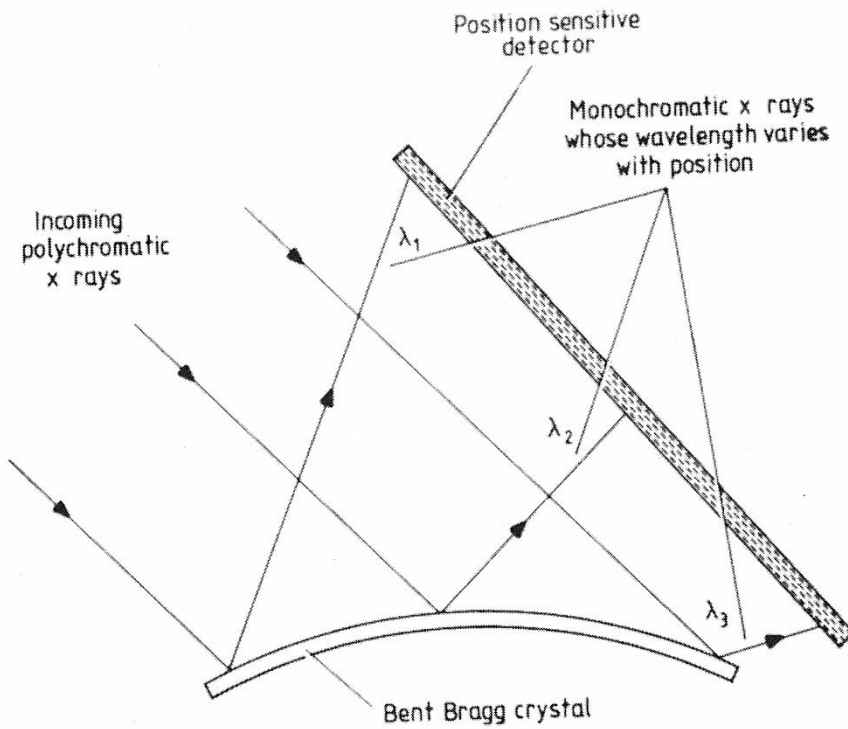


Figure 1.3.15 Bent Bragg crystal x-ray spectrometer.

The Yohkoh Satellite (1991–2001)

The satellite was launched into space from the Kagoshima Space Center (KSC) in Southern Japan. This satellite, known as Yohkoh ("Sunbeam"), is a project of the Japanese Institute of Space and Astronautical Science (ISAS). There were four instruments on the satellite,

Bragg Crystal Spectrometer (BCS)

Wide Band Spectrometer (WBS)

Soft X-Ray Telescope (SXT)

Hard X-Ray Telescope (HXT).

The BCS consisted of four bent crystal spectrometers. Each was designed to observe a limited range of soft x-ray wavelengths containing spectral lines that are particularly sensitive to the hot plasma produced during a flare. The observations of these spectral lines provide information about the temperature and density of the hot plasma, and about motions of the plasma along the line of sight. Images were not obtained.

The WBS consisted of three detectors: a soft x-ray, a hard x-ray, and a gamma-ray spectrometer. They were designed to provide spectra across the full range of wavelengths from soft x-rays to gamma rays with a time resolution on the order of one second or better. Like the BCS, images were not obtained.

The SXT (glancing incidence mirror/CCD sensor) imaged X-rays in the 0.25 - 4.0 keV range. It used thin metallic filters to acquire images in restricted portions of this energy range. SXT could resolve features down to 2.5 arc seconds in size. Information about the temperature and density of the plasma emitting the observed x-rays is obtained by comparing images acquired with the different filters. Flare images were obtained every 2 seconds. Smaller images with a single filter were obtained as frequently as once every 0.5 seconds.

The HXT (Fourier Synthesis Telescope) observed hard x-rays in four energy bands through sixty-four pairs of grids. These grid pairs provide information about 32 spatial scales of the x-ray emission. This information can be combined on the ground to construct an image of the source in each of the four energy bands. Structures with angular sizes down to about 5 arc seconds can be resolved. These images could be obtained as frequently as once every 0.5 seconds.

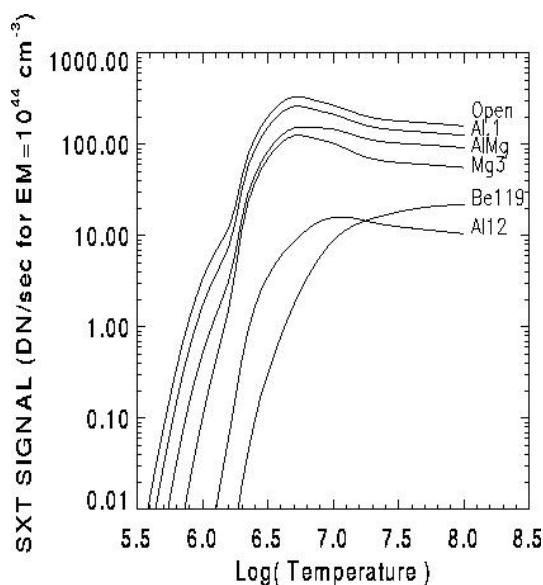


Figure 5.4: The temperature ranges of different Yohkoh SXT filters. The names of the filters come from the materials that were used in their making. The 'AlMg' filter is generally known as the 'sandwich'. The filter ratios can be used to calculate EM and T.

The Yohkoh spacecraft used a slightly elliptical low-earth orbit, with an altitude ranging from approximately 570 km to 730 km. The orbital period was 90 minutes. Sixty-five to seventy-five

minutes of this time was spent in sunlight. During five to six of its orbits per day, Yohkoh passed through the radiation belts of the South Atlantic Anomaly where the instruments using high voltages had to be turned off (the BCS, HXT, and most WBS channels). Otherwise the radiation could have destroyed the instruments or the satellite.

Observations from the instruments were stored in the spacecraft Bubble Data Recorder (BDR). The capacity of the BDR was 10 Mbytes. In order to optimize the recorder, it could operate at several bit-rates; high, medium, and low. Switching between the bit-rates was controlled two different ways, by the on-board deferred commands and automatically. This switching was necessary since the high-bit rate only holds 42 minutes worth of data. Some overwriting of the data was permitted.

The satellite could operate in a large number of spacecraft modes and several different subsystem modes. The two modes of principal interest are the Quiet Mode and Flare Mode. Switching between these two particular modes was controlled by a flare flag generated by the WBS instruments. Allocation of which instruments could collect what data and how much of it depended on which mode Yohkoh was operating in. Generally, more HXT data was taken during the Flare Mode as opposed to the Quiet Mode.

During each orbit, about five or six times a day, Yohkoh passed over the Kagoshima Space Center. Commanding of the satellite could be performed at this time. (The rest of the time the satellite was controlled by on-board deferred command storage.) In addition, Kennedy Space Center also received data from the Data Recorder. At other locations in the orbit, the data got sent to ground stations in the NASA Deep Space Network.

RHESSI (2002 –)

The Reuven Ramaty High Energy Solar Spectroscopic Imager (RHESSI) was known as HESSI before launch. It is a NASA Small Explorer (SMEX) mission. Its launch was very much delayed, and it missed most of the last solar activity maximum. Hopefully it will last until the next one.

RHESSI Spectroscopy

Detectors: Nine segmented, hyperpure germanium crystals, cooled to ~ 75 K

Energy Range: ~ 3 keV – ~ 17 MeV

Spectral Resolution: 1 keV (FWHM) in the front segment up to ~ 100 keV; 3 keV in the rear segment up to ~ 1 MeV increasing to ~ 5 keV at 20 MeV

RHESSI Imaging

Technique: Fourier-transform imaging with 9 rotating modulation collimators (grid pairs)

Field of View: Full Sun (~ 1 degree)

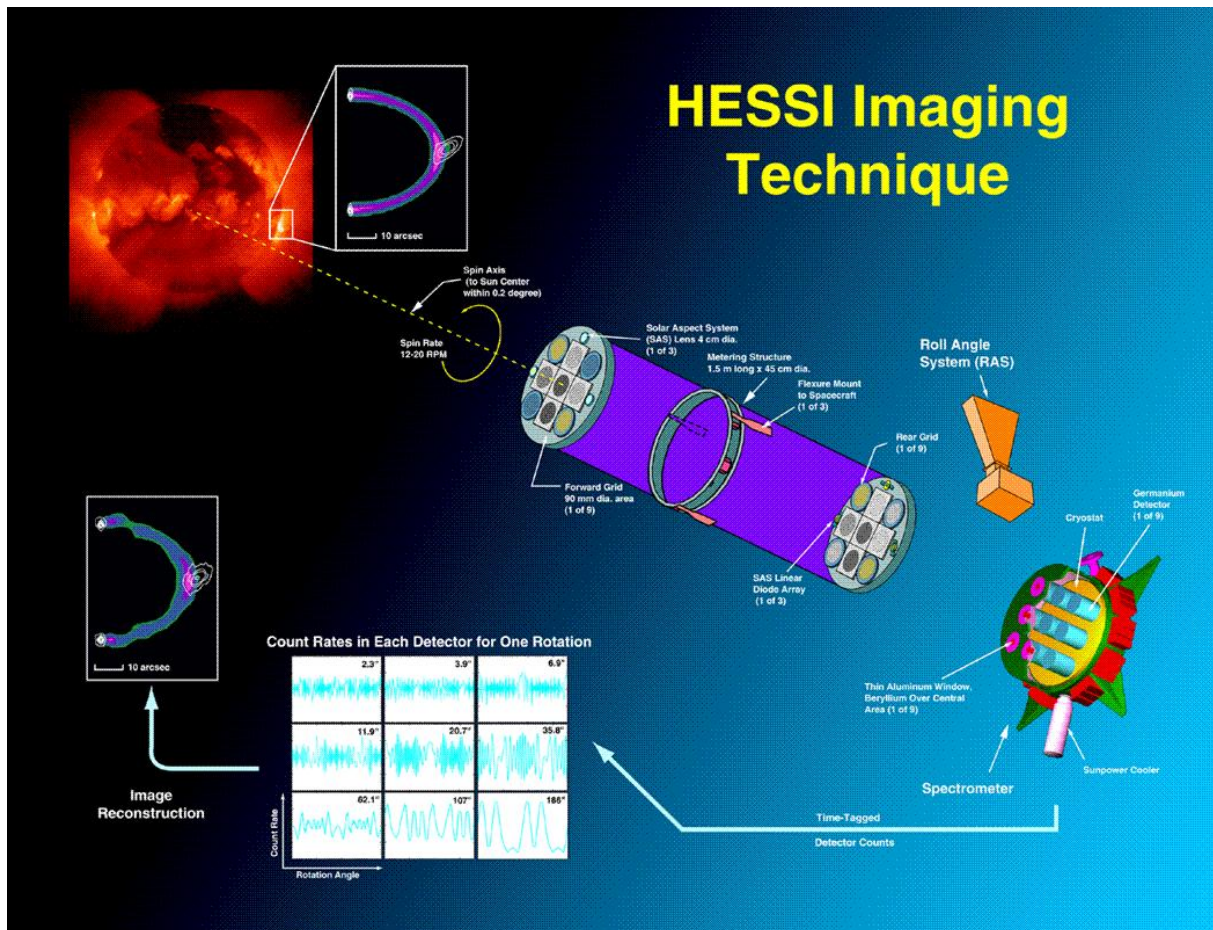
Angular Resolution: 2 arc sec to 100 keV; 7 arc sec to 400 keV; 36 arc sec above 1 MeV

Temporal Resolution: tens of milliseconds for a basic image; 2 seconds (half a rotation of the spacecraft) for a detailed image

RHESSI Aspect System:

Solar Aspect System (SAS) determines the direction to Sun-center to better than 1.5 arc sec.

Roll Angle System (RAS) determines the roll angle to better than 3 arc min.



GRANAT (1989–1999)

The Russian x-ray satellite was launched to a high apogee orbit (200 000 km), where it operated for almost 10 years. It carried 4 major instruments: French SIGMA coded-mask hard x-ray telescope (30-1000 keV), Soviet ART-P coded-mask telescope, Danish all-sky monitor WATCH (6-150 keV), and a gamma-burst detector PHEBUS.

The Danish WATCH experiment was composed of four units. One of these units had the Sun in its field-of-view and observed in the deka-keV range with approximately 6.5 s time resolution. WATCH was based on the rotation-modulation-collimator (RMC) principle. It contained two independent detectors, one based on a NaI- the other on a CsI-scintillator. The direction of the incoming X-rays could thus be derived from the modulation of the detected signal as a function of the rotation phase of the collimator grids. The modulation patterns were used in determining the positions and strengths of the X-ray sources in the field-of-view. The WATCH solar burst catalogue consists of 1551 flares and it was created by systematically going through the approximately 2.5 years of count rate time profile observations. WATCH observations are grouped in dumps associated to telemetry periods. See further details in Crosby et al., *Astron. Astrophys. Suppl. Ser.* 130, 233-234 (1998).

The CGRO Mission (1991 - 2000)

The Compton Gamma Ray Observatory was launched on April 5, 1991 aboard the space shuttle Atlantis. Compton was deorbited and it re-entered the Earth's atmosphere on June 4, 2000. Compton had four instruments that covered six decades of the electromagnetic spectrum, from 30 keV to 30 GeV.

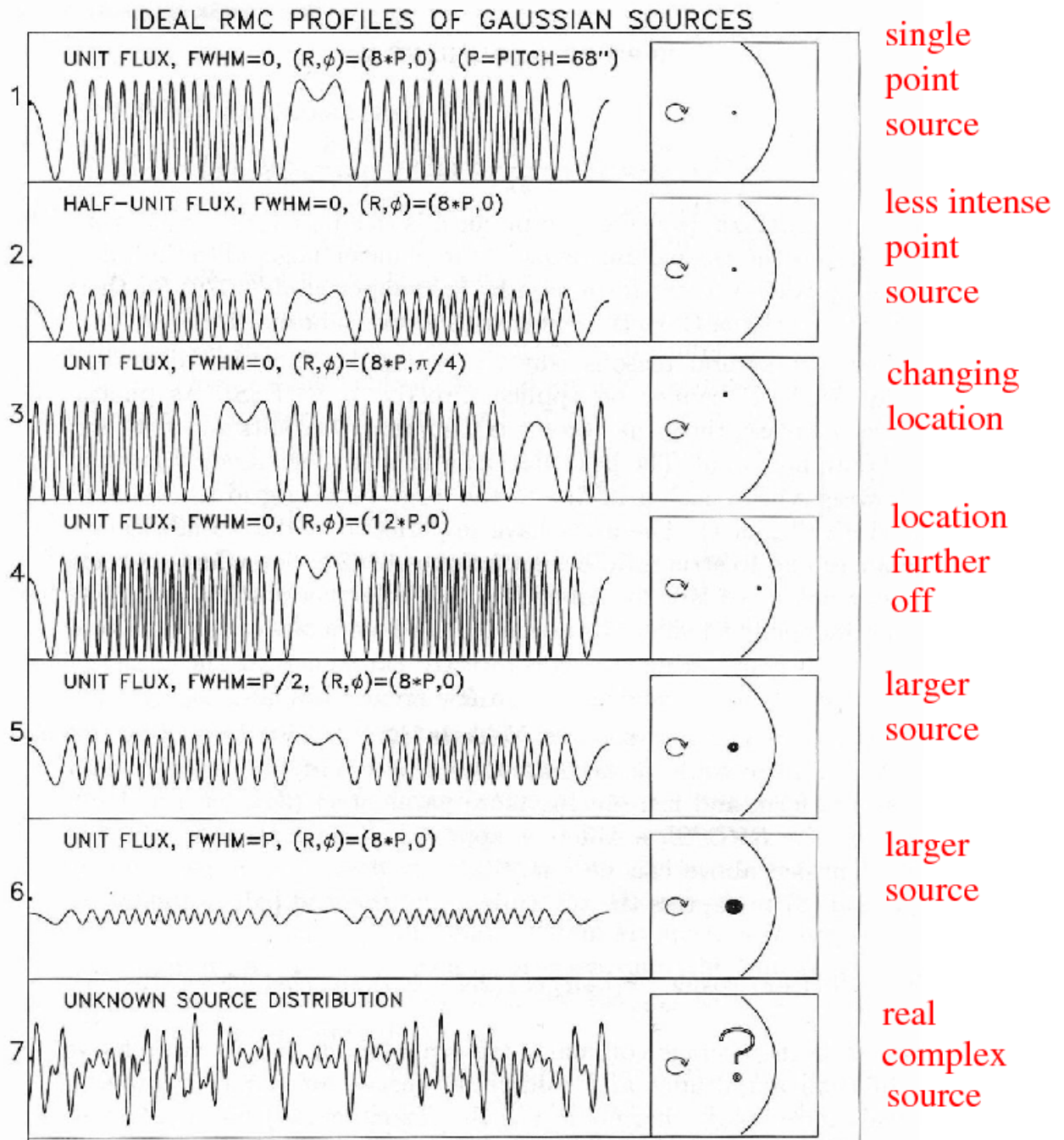


Figure 3. Modulation profiles plotted for one complete rotation for various configurations of an off-axis source, assuming ideal grids of pitch p with equal slits and slats mounted on a collimator that is rotating uniformly about a fixed axis. As discussed in the text, successive panels show the effect on the modulation profile of changing the source characteristics. R and ϕ are the radial offset and the azimuth of the source position relative to the axis of rotation.

Figure 5.5: The RHESSI imaging technique resembles the techniques used in radio interferometry - the 'dirty map' is cleaned using CLEAN, MEM or PIXON algorithms.

The CGRO instruments were the Burst And Transient Source Experiment (BATSE), the Oriented Scintillation Spectrometer Experiment (OSSE), the Imaging Compton Telescope (COMPTEL), and the Energetic Gamma Ray Experiment Telescope (EGRET). For each of the instruments, an improvement in sensitivity of better than a factor of ten was realized over previous missions.

Although BATSE was optimized for the detection of gamma-ray bursts, it was also a sensitive instrument regularly available for the detection of hard X-ray solar flares. As such, it was of great value in providing high time resolution spectral observations over a broad energy range for up to 50% of all flares. A BATSE solar flare catalog was built during the mission. Plots of quick-look orbital data and flare time profiles can be obtained, and ASCII or binary data files can be downloaded for further analysis.

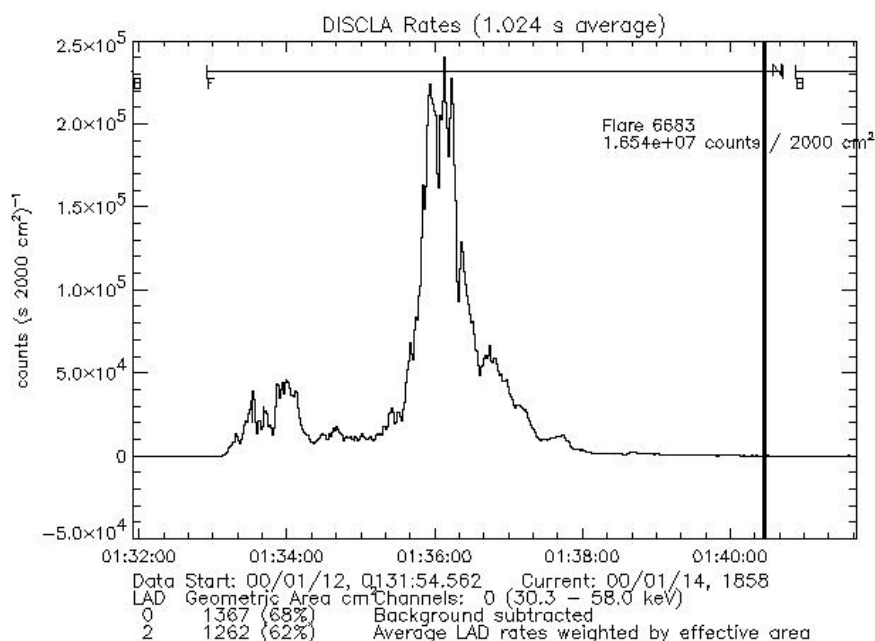


Figure 5.6: A solar flare detected with CGRO BATSE.

SOHO EIT (1995–)

The SOHO EIT is able to image the solar transition region and inner corona in four, selected bandpasses in the extreme ultraviolet (EUV):

- He II, 304 Å (80 000 K)
- Fe IX/X, 171 Å (1.3 MK)
- Fe XII, 195 Å (1.6 MK)
- Fe XV, 284 Å (2 MK)

Using either full-disk or subfield images, the EIT can image active regions, filaments and prominences, coronal holes, coronal "bright points," polar plumes, and a variety of other solar features. The instrument was designed to be used in conjunction with other SOHO instruments, particularly the LASCO visible-light coronagraphs and the SUMER and CDS imaging spectrographs, as well as with ground-based instruments. EIT image cadence is 8–12 minutes.

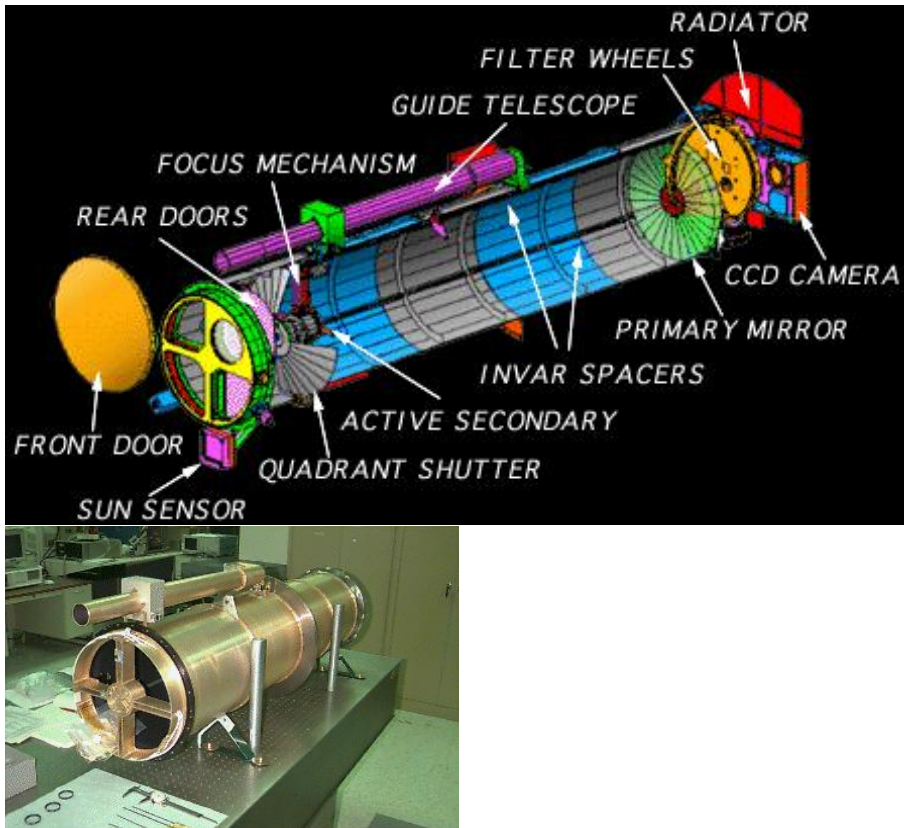


Figure 5.7: TRACE telescope

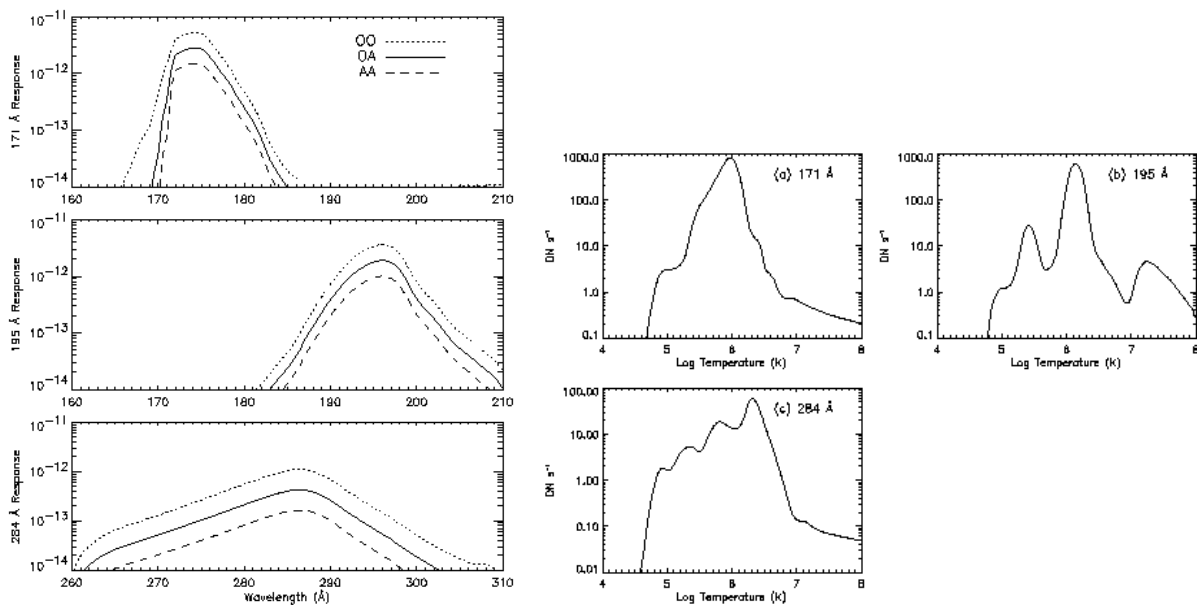


Figure 5.8: Left: Spectral response in the TRACE EUV quadrants ($\text{electrons sr cm}^2 \text{ photon}^{-1} \text{ pixel}^{-1}$). Right: Signal at the CCD for each of the TRACE EUV quadrants as a function of source temperature for an emission measure of 10^{44} cm^{-3} . **Conclusion:** plasma diagnostics are possible only from instruments with narrow response functions (like SOHO CDS or SUMER)

Hinode (2006–)

The Japanese Hinode (Solar-B before launch) is a highly sophisticated observational satellite equipped with three advanced solar telescopes. Its solar optical telescope (SOT) has an unprecedented 0.2 arcsec resolution for the observation of solar magnetic fields. This corresponds to about 140 km on the solar surface. The X-ray telescope (XRT) has a resolution of three times as high as Yohkoh, and the EUV imaging spectrometer (EIS) has sensitivity ten times as high as SOHO EIT. Hinode is a quiet Sun mission, and its aim is to answer questions like why does a hot corona exist above the cool atmosphere, what drives explosive events such as solar flares, and what creates the Sun's magnetic fields.



STEREO (2006–)

The Solar TERrestrial RELations Observatory (STEREO) is the third mission in NASA's Solar Terrestrial Probes program. The mission employs two nearly identical space-based observatories - one ahead of Earth in its orbit, the other trailing behind - to provide the first-ever stereoscopic measurements to study the Sun and the nature of its coronal mass ejections. Four instrument packages are mounted on each of the two STEREO spacecrafts, including coronagraphs and radio burst trackers (for plasma emission).

In 2011 the two STEREO spacecraft will be separated by more than 90 degrees from the Earth. With the help of observations from SDO and SOHO, a 360-degree view of the Sun is possible for the first time.

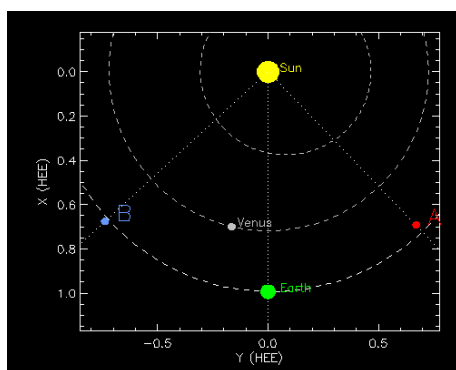


Figure 5.9: Positions of the STEREO Ahead (red) and Behind (blue) spacecraft relative to the Sun (yellow) and Earth (green) on Mar 6, 2009. The dotted lines show the angular displacement from the Sun.

Solar Dynamics Observatory, SDO (2010–)

SDO has three scientific experiments: Atmospheric Imaging Assembly (AIA), EUV Variability Experiment (EVE), and Helioseismic and Magnetic Imager (HMI). SDO is a sun-pointing semi-autonomous spacecraft that allows nearly continuous observations of the Sun, with a continuous science data downlink rate of 130 Megabits per second. The spacecraft is 4.5 meters high and over 2 meters on each side, weighing a total of 3100 kg (fuel included). SDO's inclined geosynchronous orbit was chosen to allow continuous observations of the Sun, and enable its high data rate through the use of a single dedicated ground station.

ATMOSPHERIC IMAGING ASSEMBLY

[HOME](#) | [SOLAR INFO AND SPACE WEATHER](#) | [RESULTS - PUBLICATIONS](#) | [RELATED LINKS](#) | [THE HOME](#) | [Recent Reported Events](#)
[SCIENCE INVESTIGATION](#) | [INSTRUMENT](#) | [OPERATIONS](#) | [DATA](#) | [TEAM SITE](#)

The Sun 2011-1-31

AIA images shown were taken at about 31-Jan-11 12:51:29.120 UT "What's this?"

Image Channels

"When were these images taken?"

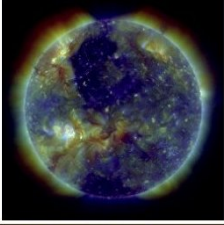
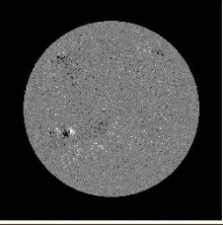
			
4500: [1K] [4K]	094_335: [1K] [4K] [PFSS]	211_193: [1K] [4K] [PFSS]	HMI: [1K] [4K] [PFSS]
1600: [1K] [4K] [PFSS]	193: [1K] [4K] [PFSS]	171: [1K] [4K] [PFSS]	B(los): [1K] [4K] [PFSS]
1700: [1K] [4K] [PFSS]	094: [1K] [4K] [PFSS]	211: [1K] [4K] [PFSS]	B(los): [1K] [4K] [PFSS]
304: [1K] [4K] [PFSS]	335: [1K] [4K] [PFSS]	193: [1K] [4K] [PFSS]	171: [1K] [4K] [PFSS]
304_211: [1K] [4K] [PFSS]	193: [1K] [4K] [PFSS]	171: [1K] [4K] [PFSS]	
171: [1K] [4K] [PFSS]	131: [1K] [4K] [PFSS]		

Figure 5.10: The Sun Today - SDO. AIA and HMI data can be accessed through the <http://jsoc.stanford.edu/> website.

5.3 Ground-based optical telescopes

NSST, La Palma

The best spatial resolution obtained from ground-based observations is with the New Swedish Solar Telescope in La Palma, Canary Islands. Adaptive optics are used to clean the images from atmospheric effects. The large, almost 1-meter diameter lens was made by Opteon in Tuorla (Turku, Finland).

In addition to the atmospheric effects, solar telescopes suffer from heating by sunlight of the optics and the air within the telescope tube. This causes the image to shiver and become blurred. Modern solar telescopes are either vacuum telescopes, filled with helium or use careful control of the optic's temperature to reduce heating of the air in the telescope. The NSST is a vacuum telescope.



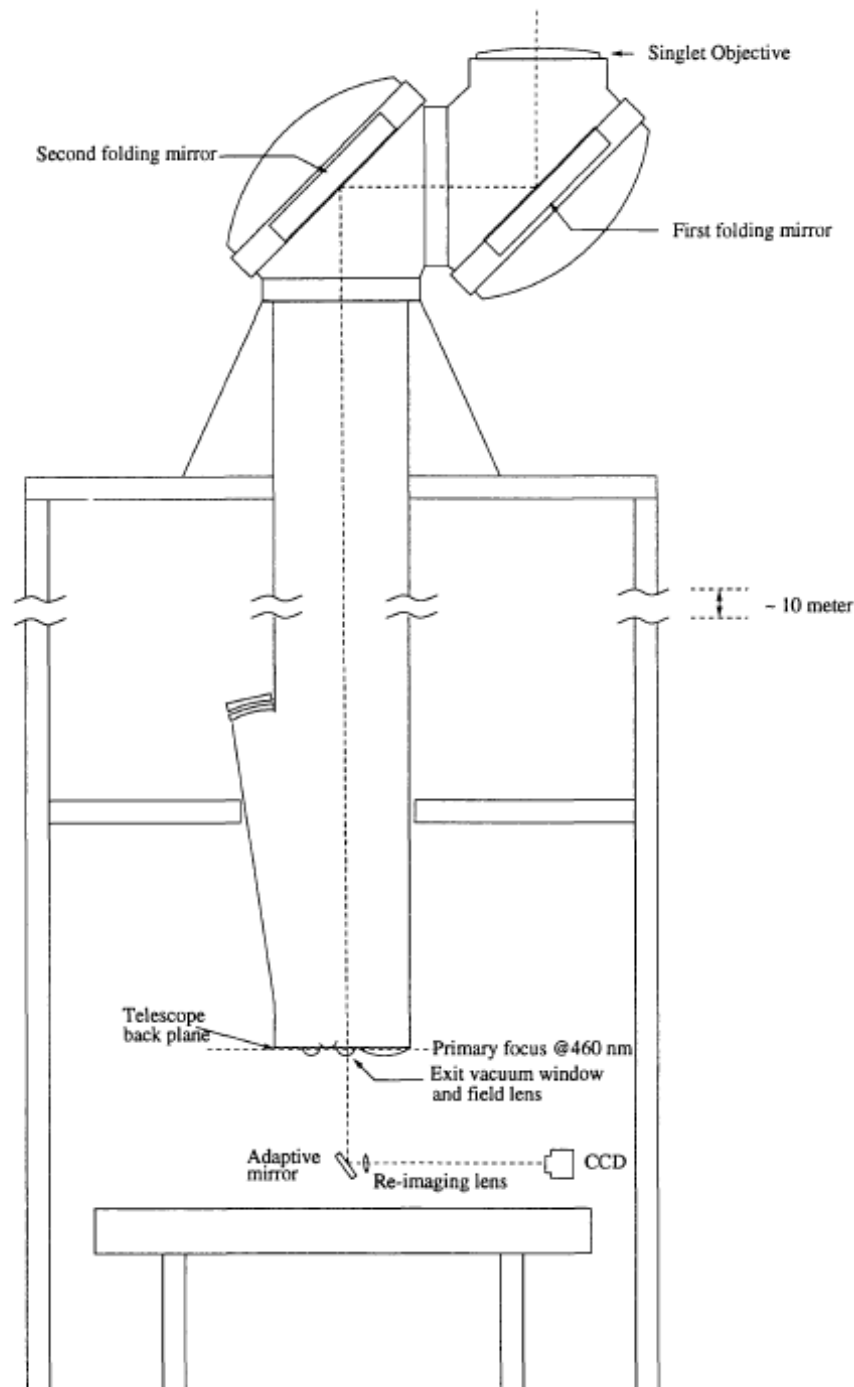


Figure 1. Schematic optics for high-resolution, narrow-band imaging with a conventional flat adaptive mirror, used also as folding mirror. The combined vacuum window and field lens re-image the singlet objective on a small adaptive mirror. Note the simplicity of the optical system and the small number of optical surfaces.

Figure 5.11: The NSST construction (Scharmer et al., ASP Conference Series 183, 1999)

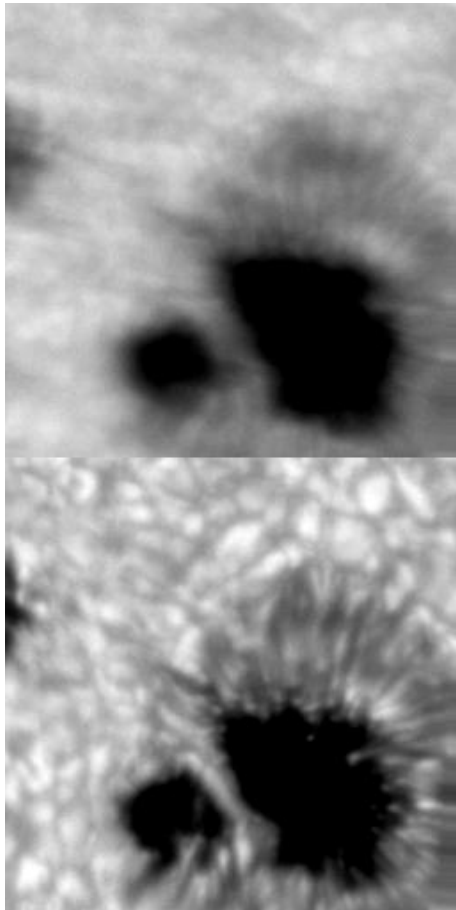


Figure 5.12: The NSST mirror system uses adaptive optics to correct for seeing. The problem is that the atmosphere changes quickly, and the adaptive optics systems have to correct the adaptive mirror at least several hundred and preferably more than 1000 times per second. The obtained diffraction limit is about 100 km on the Sun (0.1 arc sec).

Global High-resolution H-alpha network

The global high-resolution H-alpha (656.3 nm) network utilizes facilities at the Big Bear Solar Observatory (BBSO) in California, the Kanzelhöhe Solar Observatory (KSO) in Austria, the Catania Astrophysical Observatory (CAO) in Italy, Meudon Observatory in France, the Huairou Solar Observing Station (HSOS) and the Yunnan Astronomical Observatory (YNAO) in China. All these observatories have over 300 sunny days a year, good seeing conditions, adequate observing staffs and well established H-alpha telescope systems. Each of the three stations has a 1K x 1K or 2K x 2K CCD detectors available to monitor the Sun with a spatial resolution of 1 arcsec per pixel. Observations of 1 minute cadence are obtained at each station with higher cadence which can be triggered by automated filament eruption detection. The largest time difference in the network is about 9.4 hours between BBSO and YNAO. The difference between BBSO and KSO is about 8.7 hours and that between YNAO and KSO about 5.9 hours. In summer each station can observe 12 hours on clear days. Therefore, normally there is no night gap in the summer. In winter, when each station is expected to operate 8 hours, the BBSO/YNAO gap will be about 1.6 hours and the BBSO / KSO gap about 0.7 hours.

SOONSPOT

The name SOONSPOT stands for SOON Solar Patrol on Tape, where SOON refers to the Solar Observing Optical Network of four solar observatories maintained and operated by the U.S. Air Force 50th Weather Squadron. The refracting telescopes have apertures of 25.3 cm (10-inches) and have vacuum optics. The digitally recorded data are written onto 8-mm Exabyte tapes. The images are written in extended FITS format with header information on timing, pointing coordinates, image scale and sky transparency. The site at Palehua was dismantled and shipped to Sacramento Peak in New Mexico in April of 1997 to facilitate a major upgrade to the SOON system (see map of the sites).

GLOBAL HIGH-RESOLUTION H α NETWORK



Figure 5.13: Big Bear - Kanzelhöhe - Catania - Meudon - Yunnan - Huairou High resolution H α network. The number of observatories in the network has been increasing, the network was founded in the 1990s by only three facilities, Big Bear, Kanzelhöhe and Yunnan.

Solar Observing Optical Network

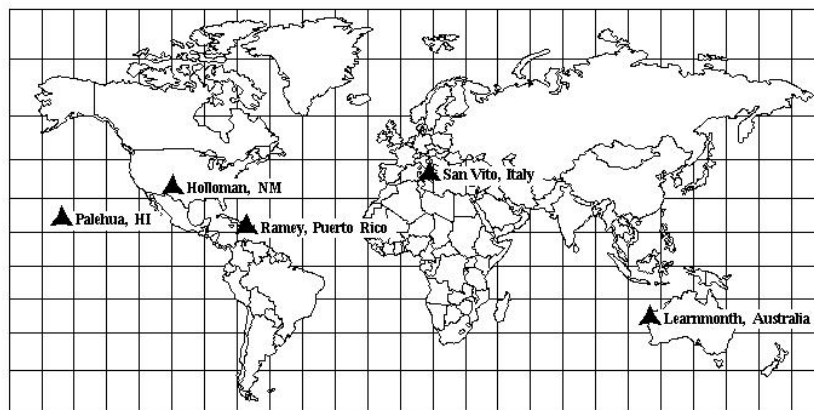


Figure 5.14: The locations of SOON observatories (U.S. Airforce). The data can be searched using the SOONSPOT web archive.

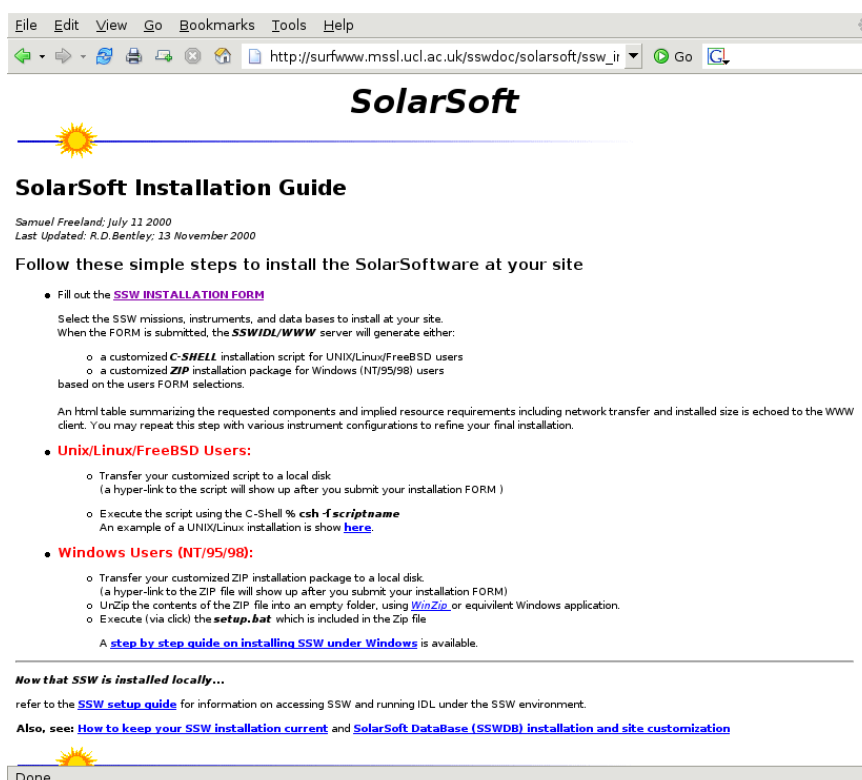
Chapter 6

Software and data archives

Solarsoft

The SolarSoft system is a set of integrated software libraries, data bases, and system utilities which provide a common programming and data analysis environment for solar physics. The SolarSoftWare (SSW) system is built from Yohkoh, SOHO, SDAC and Astronomy libraries and draws upon contributions from many members of those projects. It is primarily an IDL based system, although some instrument teams integrate executables written in other languages. Software is used either with command lines or widgets.

The SSW capabilities include: time series analysis, time conversions, UTPLOT, spectral fitting, image and image cube (movies) display, IDL data manipulation (structure, string, array, mathematics...), file I/O (generic binary, ascii), FITS, solar limb fitting, grid overlay, coordinate tranformations... Object oriented programming (OOP) is also widely used.



The screenshot shows a web browser window with the address bar containing the URL `http://surfwww.mssl.ucl.ac.uk/sswdoc/solarsoft/ssw_i`. The page title is "SolarSoft" and the main heading is "SolarSoft Installation Guide". The page content includes the following text:

Samuel Freeland; July 11 2000
Last Updated: R.D.Bentley; 13 November 2000

Follow these simple steps to install the SolarSoftware at your site

- Fill out the [SSW INSTALLATION FORM](#)
Select the SSW missions, instruments, and data bases to install at your site. When the FORM is submitted, the **SSWIDL/WWW** server will generate either:
 - a customized **C-SHELL** installation script for UNIX/Linux/FreeBSD users
 - a customized **ZIP** installation package for Windows (NT/95/98) users based on the users FORM selections.An html table summarizing the requested components and implied resource requirements including network transfer and installed size is echoed to the WWW client. You may repeat this step with various instrument configurations to refine your final installation.
- **Unix/Linux/FreeBSD Users:**
 - Transfer your customized script to a local disk (a hyper-link to the script will show up after you submit your installation FORM)
 - Execute the script using the C-Shell `% csh fscriptname`
An example of a UNIX/Linux installation is show [here](#).
- **Windows Users (NT/95/98):**
 - Transfer your customized ZIP installation package to a local disk (a hyper-link to the ZIP file will show up after you submit your installation FORM)
 - UnZip the contents of the ZIP file into an empty folder, using [WinZip](#) or equivalent Windows application.
 - Execute (via click) the **setup.bat** which is included in the Zip fileA [step by step guide on installing SSW under Windows](#) is available.

Now that SSW is installed locally...
refer to the [SSW setup guide](#) for information on accessing SSW and running IDL under the SSW environment.

Also, see: [How to keep your SSW installation current](#) and [SolarSoft DataBase \(SSWDB\) installation and site customization](#)

Keyword Standards for Events File Primary Headers

This file will contain examples of keywords found in typical FITS events files. Comments precede some keywords, and others are hotlinked to the appropriate section of OGIP FITS working group documents. Comments are italicized. There are often several examples for some of the keywords to give a feel for possible values as some keywords have been interpreted by developers in different ways.

Please refer to [OGIP 93 003](#) for full information about this type of file.

Events file [definition](#) from OGIP_93_003.

```
SIMPLE = T / file does conform to FITS standard
BITPIX = 32 / number of bits per data pixel
NAXIS = 0 / number of data axes
EXTEND = T / FITS dataset may contain extensions
```

These comments are automatically generated by FITSIO.

```
COMMENT FITS (Flexible Image Transport System) format defined in Astronomy and
COMMENT Astrophysics Supplement Series v44/p363, v44/p371, v73/p359, v73/p365.
COMMENT Contact the NASA Science Office of Standards and Technology for the
COMMENT FITS Definition document #100 and other FITS information.
```

DATE is also generated automatically by FITSIO among others.

```
DATE = ' 5/10/94' /FITS creation date (DD/MM/YY)
```

Content provides quicklook "HDUCLASS-like" information in the primary header.

```
CONTENT = 'BASIC ' / file contains time intervals and events
CONTENT = 'EVENT LIST' / this is an event list file
CONTENT = 'RAW ' / TARGET EVENTS
REVISION= 1 / revision number of processed data
```

The ORIGIN keyword is the original processing point. Subsequent processing and reduction is then kept in the REVISION and/or HISTORY and/or CREATOR keywords.

```
ORIGIN = 'ESA/SSD ' / processing site
ORIGIN = 'HEASARC/GSFC' / origin of FITS file
ORIGIN = 'MPE Garching, FRG' / origin of processed data
ORIGIN = 'USRSDC ' / origin of processed data
```

```
OBSERVER= 'ESA/ESTEC' / Principle Investigator
OBSERVER= 'MPE, ROSAT-TEAM' / PI name
OBSERVER= 'NONE ' / Principal Investigator
OBSERVER= 'PSPC CAL TEAM' / PI name
```

```
OBS_ID = '41 ' / Observation ID 00-64
OBS_ID = 'CA999998P-3.N1' / observation ID
OBS_MODE= 'POINTING' / Observation mode
OBS_MODE= 'SCAN ' / obs mode: POINTING, SLEW, OR SCAN
OBS_MODE= 'SLEW ' / obs mode: POINTING, SLEW, OR SCAN
```

```
OBJECT = '2S2251-178' / Name of observed object
OBJECT = 'ALUMINUM 1.47 keV calibration' /name of object
OBJECT = 'CRAB ' / Name of observed object
```

```
TELESCOP= 'ASCA ' / Telescope (mission) name
```

Other telescope values for [CGRO](#), [ROSAT](#), [EXOSAT](#), [HEAO 1](#), [XTE](#)

```
INSTRUME= 'GIS2 ' / Instrument name
INSTRUME= 'LECS ' / instrument name
INSTRUME= 'PSPCB ' / instrument name
```

```
EQUINOX = 2000.0 / equinox
RADECSYS= 'FK4 ' / Stellar reference frame in use
RADECSYS= 'FK5 ' / World Coordinate System
```

```
RA NOM = 8.429000E+01 / nominal RA (deg)
```

File Edit View Go Bookmarks Tools Help

http://www.lmsal.com/solarsoft/ssw_install.html

How do I use this form to install the SolarSoftWare (SSW) on my machine?

Desired SSW Host	Installation Type	Installation Source	Firewall Constraints
sohoftp.nascom.nasa.gov	New Installation	Internet	None

Enter desired local path for top level SSW tree. You may select one of suggested locations from menu or enter an explicit path if you don't like any of those options. If this is an **Upgrade** rather than a **New Installation** then your path *must* match your existing SSW top level path.

SSW Path Suggestions -OR- Explicit Path

SSW Site email contact (USER@HOSTNAME)

Windows Options: Enable daily upgrade task (NT Only for now)

Select those SolarSoft instruments which you plan to analyze at your site:

SOHO: [EIT] [LASCO] [CDS] [SUMER] [MDI] [UVCS]

Yohkoh: [SXT] [BCS] [HXT] [WBS]

Orbital Observatories: [SXI-GOES12] [TRACE] [HESSI] [SMEI] [HXRS] [BATSE] [SPARTAN]

Optical Observatories: [SOON] [NSO] [MEES] [LaPalma SVST]

Radio Observatories: [ETHZ] [NRH] [NoRH] [NoRP] [OVSA]

Virtual Observatories: [CoSEC] [EGSO] [VSO]

Solar-B: [EIS]

STEREO: [SECCHI] [SSC]

Packages: [BINARIES] [SPEX] [CHIANTI] [PINTofALE] [XRAY] [PFSS] [HYDROSTATIC] [FINDSTUFF] [ANDRIL] [LPARL] [VDPM] [ANA] [ZTOOLS] [MMASTERED] [NGDC] [CMES] [NLFFF] [PDL]

SMM: [XRP] [UVSP] [HXRBS] [CP] [GRS] [HXIS] [ACRIM]

Generate Installation Script | Reset (to re-initialize all fields)

Done

File Edit View Go Bookmarks Tools Help

http://trace.lmsal.com/trace_cat.htm



Home | Data Policy | Data Catalog | Help

[Summaries Page](#)
[Most Recent 24 hour TRACE Movie Sampler \(JavaScript, MPEG, and GIF-Animation\)](#)
[Missing Data](#)
[Data Analysis Software \(solarsoft\)](#)
[Image History](#)

TRACE Catalog Search

Select times and image parameters and then press when ready or to clear.

UT time 

Start Time: : Date:

Stop Time: : Date:

wavelength 

ALL 171Å 195Å 284Å 1216Å 1550Å 1600Å 1700Å WL TEST PREV

image identification and description 

Observing Program **Wild Cards OK**

NX **NY** **Pixel Size"** **EW" (W+)** **EW FOV Tolerance** **NS" (N+)** **NS FOV Tolerance**

Done

```

File Edit View Terminal Tabs Help

> mreadfits, '/sswdata/lz/2004/10/efz20041030.042410', index, data
> eit_prep, index, data=data, eind, edat
> index2map, eind, edat, map0424
> plot_map, map0424, /log
> xloadct ; change color scale

alternative way to do it (ok for some image data):
> fits2map, 'smdi_maglc_fd_19980331_1117.fts', map, header=header
> loadct, 0
> plot_map, map

> doc_library, 'fits2map'; see documentation on the procedure

> help, map0424, /st ;prints structure of map
> dmap=drot_map(map0424, 2, /days) ;corrects for differential rotation
> sub_map, map0424, smap, xrange=[200,500], yrange=[300,600] ;sub image in arc sec
> dmap=diff_map(map1, map2, /rotate) ; rotates to same time before differencing
> plot_map, map1
> plot_map, map2, /over, levels=[100,200,300] ; overplotting in contours

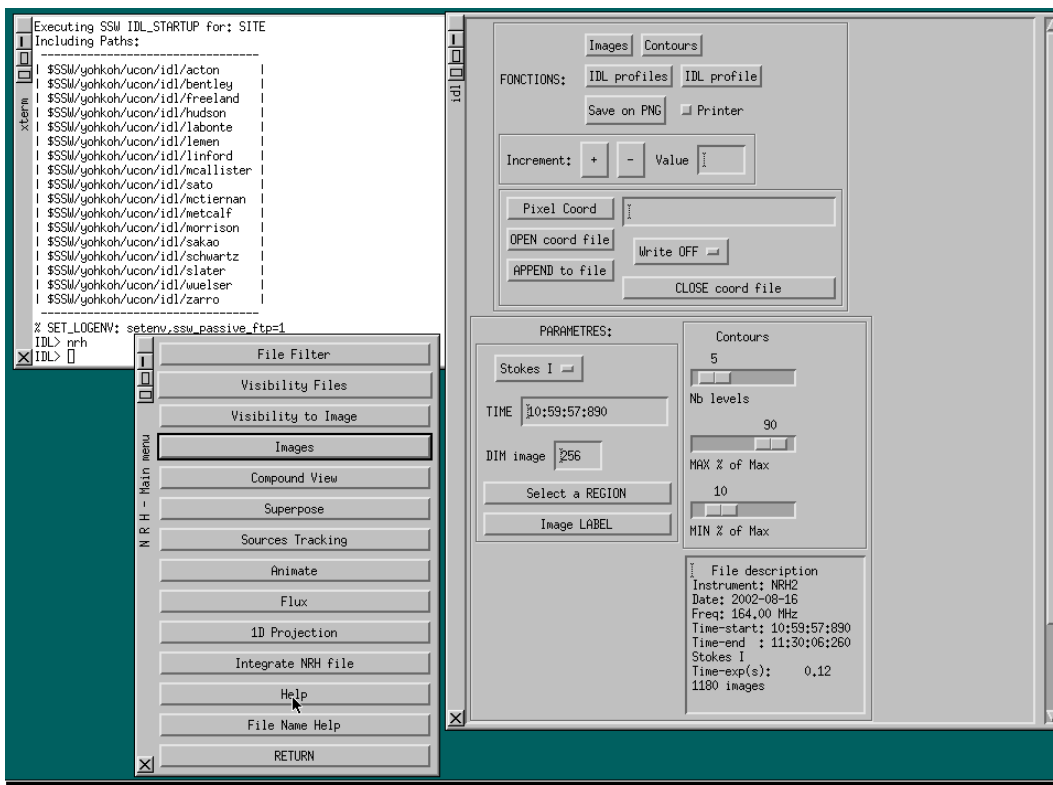
> earth0248=map2earth(m0248) ; SOHO L1 view to Earth view, need to do it
; when overplotting with ground based data
; (program should complain if forgotten)

Plotting on white background:
> !p.color=0
> !p.background=255

Plotting multiple images:
> !p.multi=[0,2,2]
and back
> !p.multi=[0,1,1]

Size of plot:
> xs=768
> ys=256
> wdef, 0, xs, ys

```



Chapter 7

Shock waves in the solar corona

7.1 Moreton waves and EIT waves

Wave-like fronts were observed in $H\alpha$ by Moreton & Ramsay (1960). They were interpreted as fast MHD (flare) waves that propagate to the corona, their chromospheric “skirt” being observed in $H\alpha$ (Uchida 1968, 1974). SOHO EIT observed “EIT waves” in 1997, which brought back the question on solar waves. Later on, wave-like fronts were also detected in soft X-rays, He I, microwaves, etc.

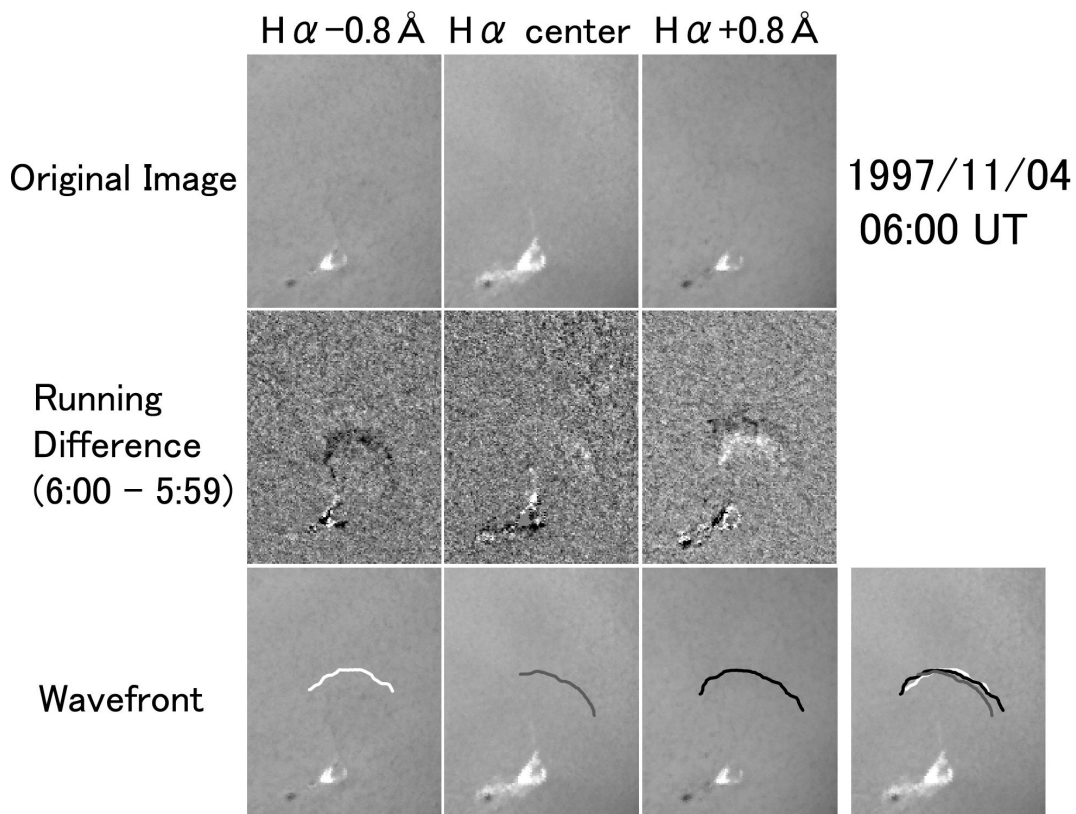


Figure 7.1: Example of a Moreton wave front that is best observed in difference images. The waves sometimes slow down when they encounter other (dense) structures.

EIT wave (Eto et al.,2002)

1997/11/04 NOAA 8100

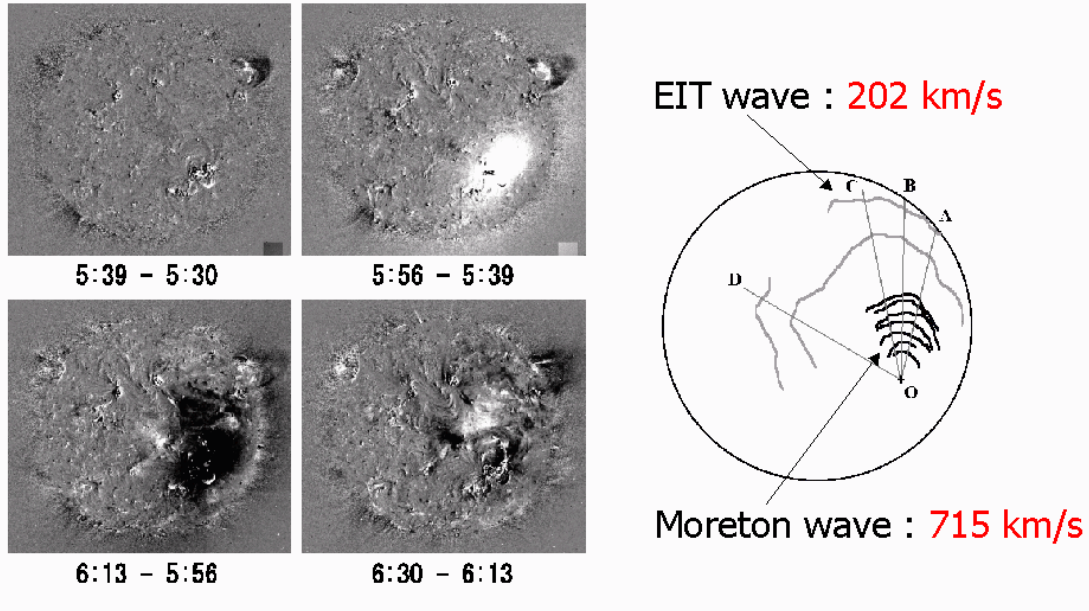


Figure 7.2: Example of a Moreton wave observed together with an EIT wave.

Filament oscillation (winking filament) due to Moreton wave

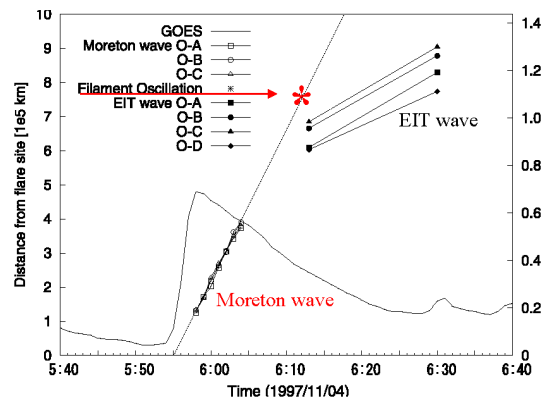
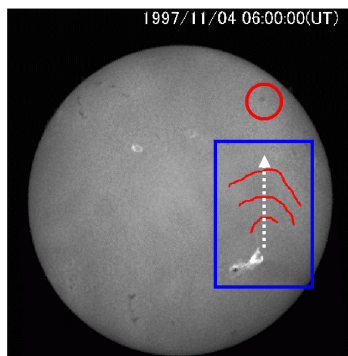


Figure 7.3: The speeds of Moreton waves and EIT waves look different. On the other hand, we do not know where and when EIT waves are formed, and therefore comparisons are difficult. Also instrument time cadence is often insufficient to determine start times for waves.

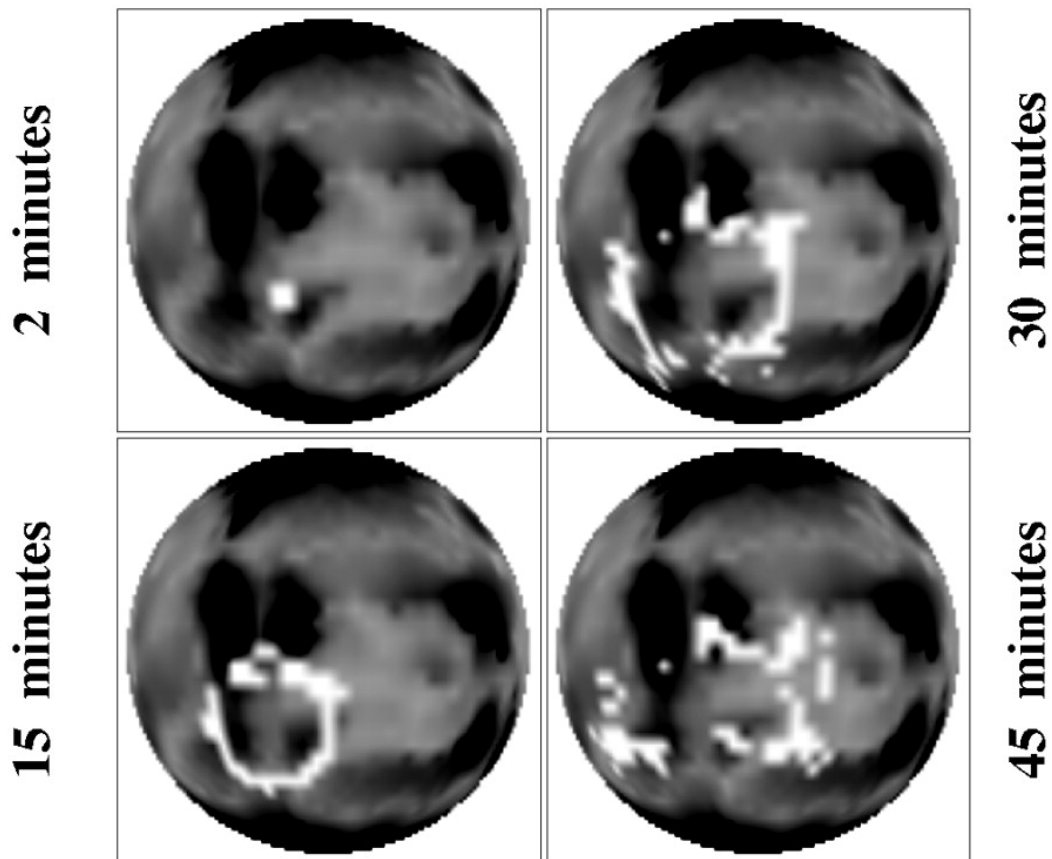


Figure 7.4: Simulation of the April 7 (Wang, ApJ 543, 2000) EUV transient. The wave is deflected away from the large northern hemisphere active region and from the south polar hole, so that the wave front eventually becomes elongated in the direction of the weaker fields to the northwest and southeast of the source. The surface-projected expansion speeds are initially of order 300 km/s but subsequently decrease to less than 200 km/s.

- Uchida et al.: Moreton waves are fast (600–1000 km/s) and EIT waves are slow (200–350 km/s), so the waves must be different
- Warmuth et al., Pohjolainen et al.: Cases of cospatial Moreton and EIT waves observed, associated with type II bursts
- Wang: Moreton waves can create EIT waves, but simulations do not produce any fast EIT waves or associated type II bursts
- Alternative interpretations for EIT waves: they are signatures of magnetic field evolution during CME lift-off (Delannée, ApJ 2000)
- Or, the waves may be due to Joule heating, resulting from the generation of electric currents (Delannée et al., 2007)
- Or, they are a signature of reconnection between the expanding magnetic cloud (CME) and low-lying fields (Attrill et al., 2007)

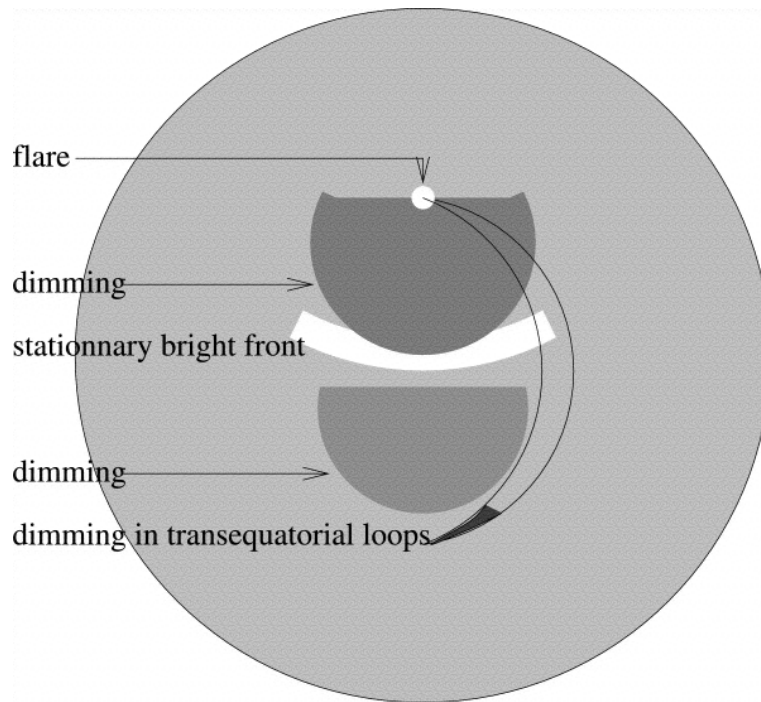


Figure 7.5: Delanée, ApJ 2000: EIT waves are a signature of magnetic field evolution during CME lift-off?

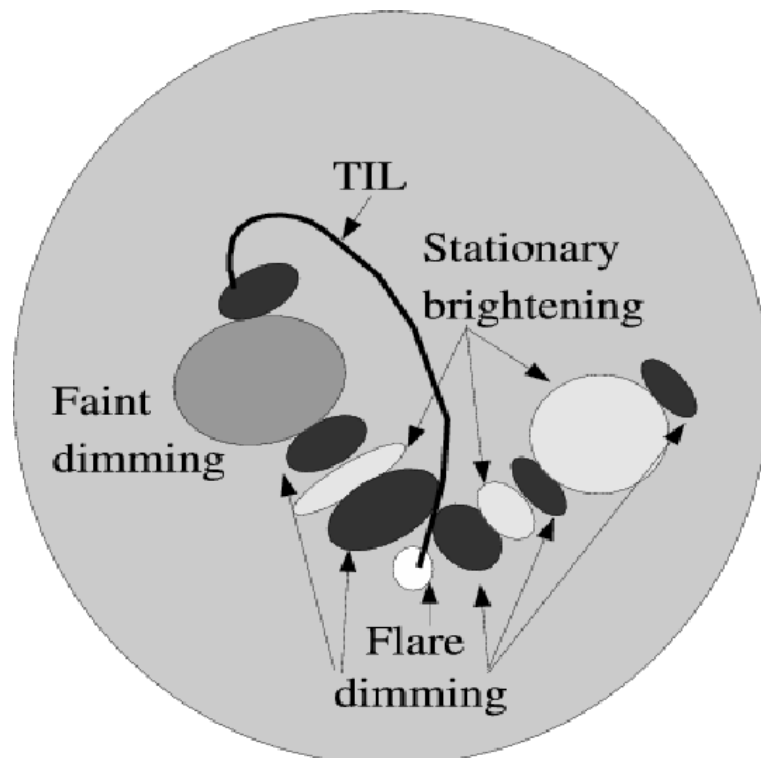


Figure 7.6: EIT and Moreton waves present stationary brightenings - the waves may be due to Joule heating resulting from the generation of electric currents in the neighboring area of the drastic jumps of magnetic connectivity, while the magnetic field lines are opening during a CME (Delanée et al., 2007).

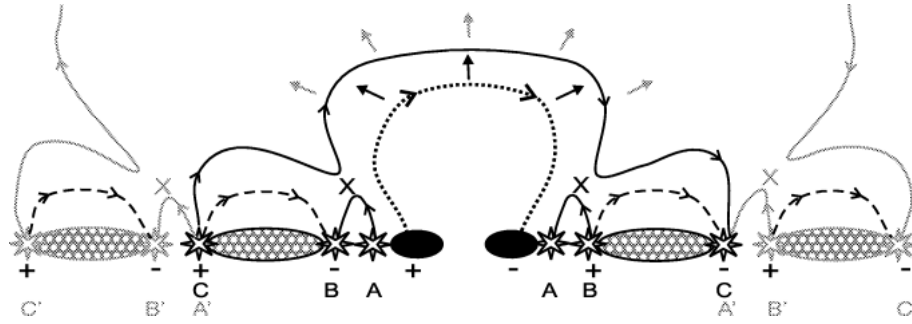


Figure 7.7: Magnetic reconnection model proposed to generate the bright, diffuse coronal "wave" front, with the observed dual brightenings. The expanding CME (dotted line) reconnects with favourably orientated quiet-Sun magnetic loops (dashed lines), displacing the footpoints of the expanding CME (solid line). The crosses mark regions where magnetic reconnection occurs (Attrill et al., 2007).

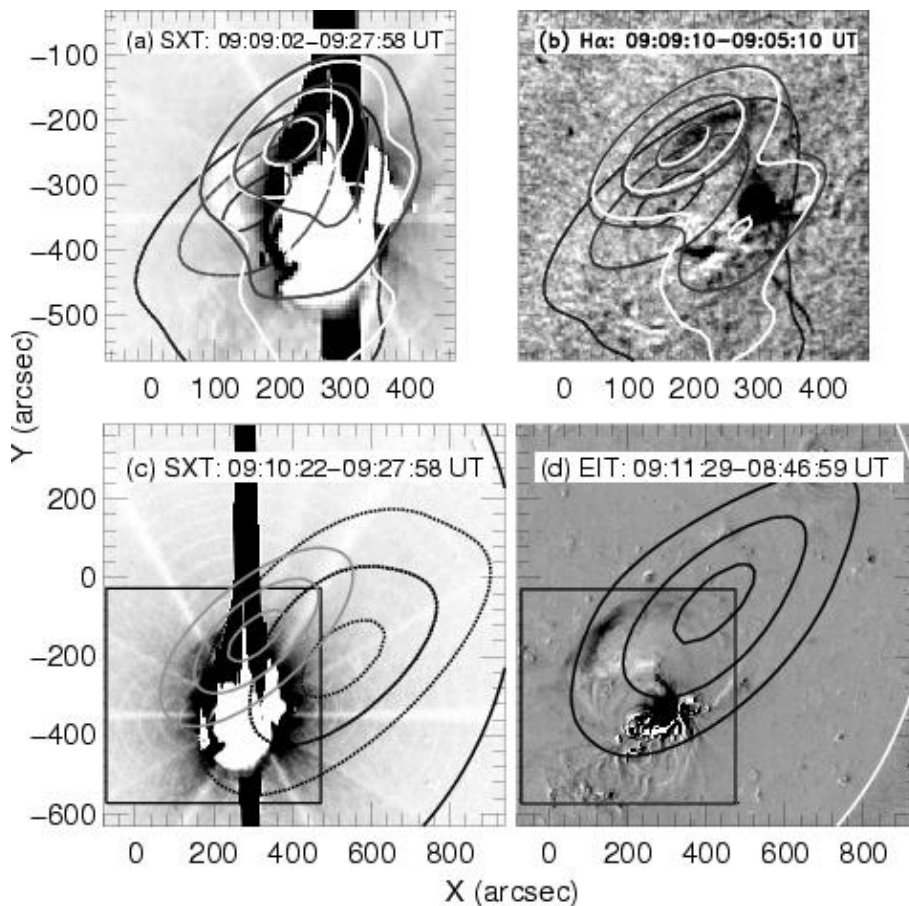


Figure 7.8: Portions of soft X-ray, $H\alpha$, and EUV difference images with overplotted Nancay Radioheliograph image contours during the type II burst emission. The image shows how the type II burst emission is located near the soft X-ray, EIT, and Moreton wave fronts. (Khan & Aurass, A&A, 2002).

7.2 Radio type II bursts

Frequency-drifting emission is observed at the fundamental plasma frequency and its harmonics (twice or three times the fundamental frequency).

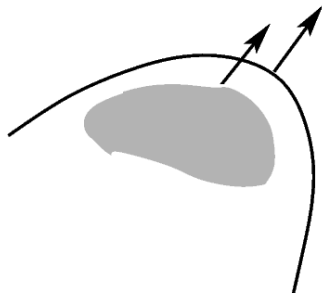
- Coronal type II bursts are observed at 400 – 15 MHz.
- Interplanetary type II bursts are observed at 14 MHz – 30 kHz.
- Calculated source velocities are $\sim 500 - 1000$ km/s.

Radio type II emission is created by accelerated particles that produce Langmuir waves, these waves then convert to radio waves. Best continuous accelerator for particles is a shock wave. However, there are several candidates for the sources and origins of shock waves:

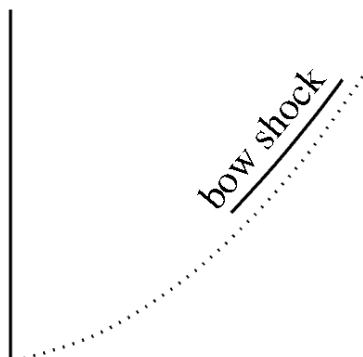
- Flare (blast) waves
- Bow shocks ahead of CMEs or fast ejecta
- CME-driven shocks
- Shocks at the flanks of CMEs

Basic shock types that are commonly associated with CMEs are bow shocks and piston-driven shocks. The basic differences can be described with the following cartoons:

BOW SHOCK

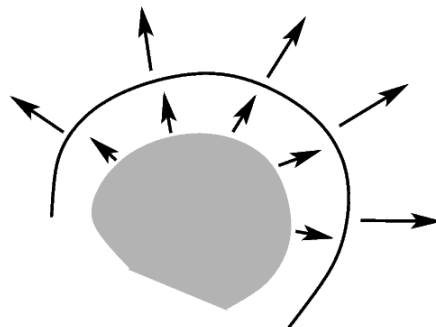


$$v_{\text{projectile}} > v_{\text{magnetosonic}}$$

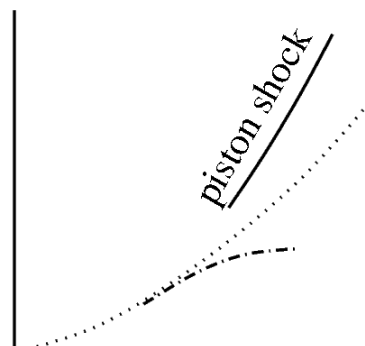


shock speed \approx projectile speed

EXPANDING 3-D SHOCK



$$v_{\text{piston}} \gtrsim v_{\text{magnetosonic}}$$



shock speed $>$ piston speed

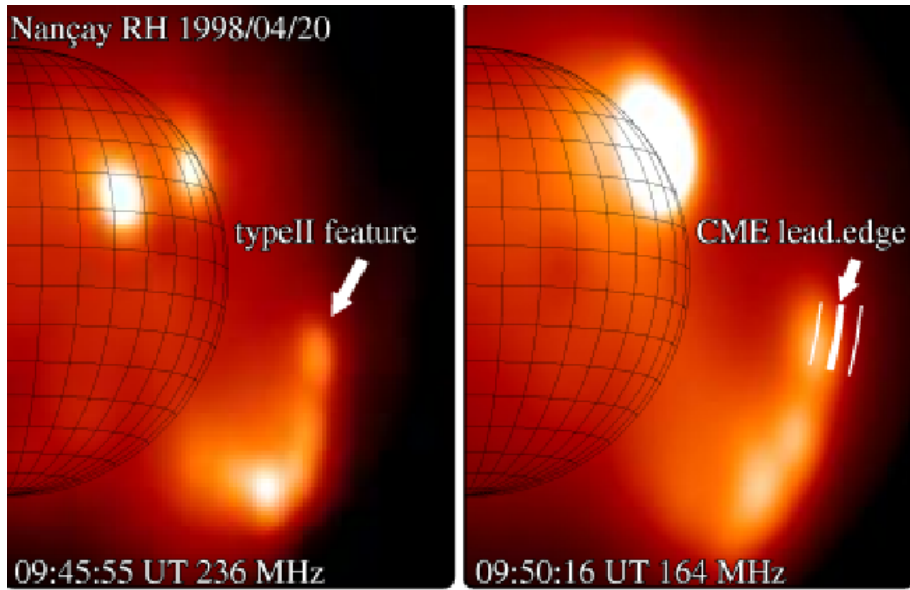


Figure 7.9: Observations of radio type II burst origins: Type II burst driver is the CME bow shock (Maia et al. ApJ, 2000).

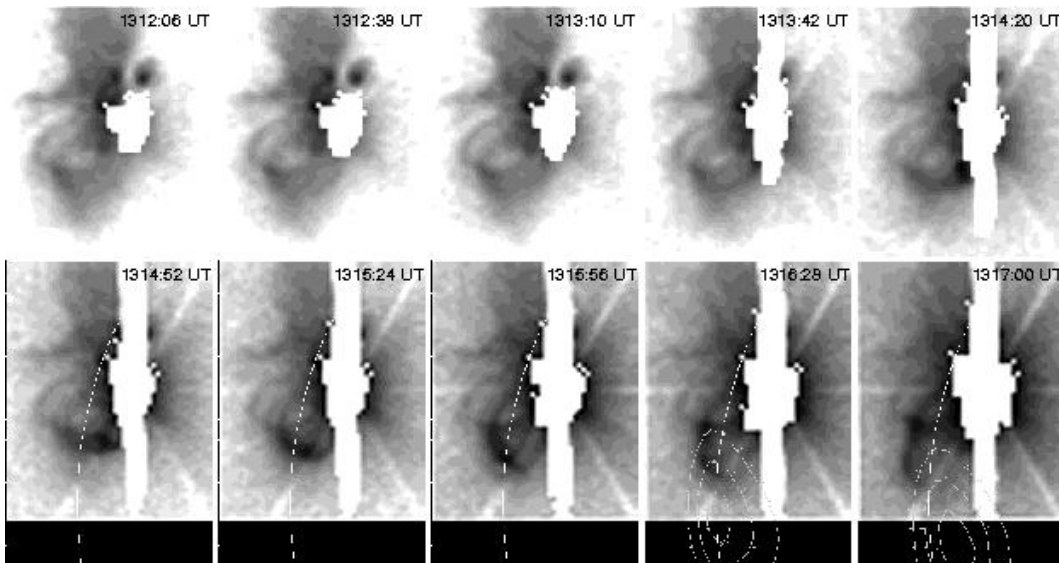


Figure 7.10: Observations of radio type II burst origins: Type II burst driver is a plasmoid (Klein et al., 1999). A sequence of Yohkoh SXT flare-mode, partial frame images of AR 8113 and its surroundings before and at the onset of a type II burst. The first images show diffuse and highly inclined loops extending south-eastward from the inner active region whose emission saturates the detector. In the subsequent images a localized brightening seems to rise along the southern legs of these loops at a projected speed of 770 km s^{-1} . When this blob reaches the loop top near 13:16 UT, the loop expands and seems to disrupt. The first high-frequency signature of the type II burst becomes visible near the time of disruption, and just above the loop top.

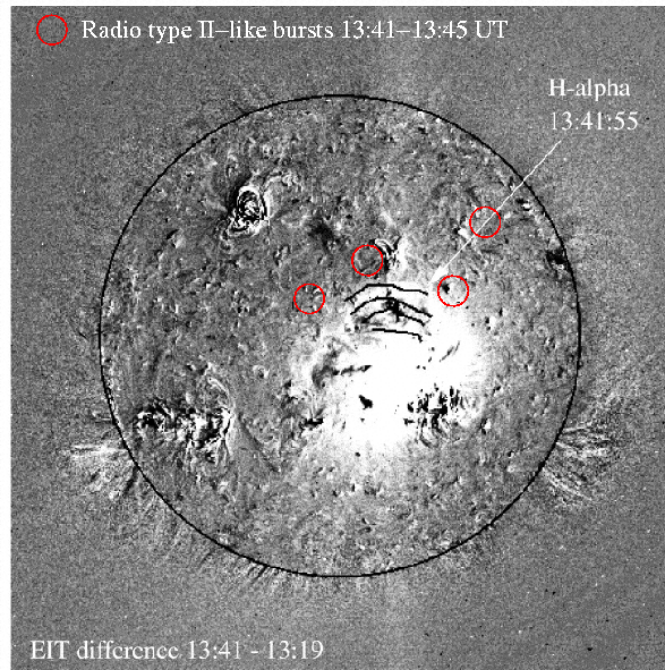


Figure 7.11: Observations of radio type II burst origins: Type II burst driver is the Moreton/EIT wave (Pohjolainen et al. 2001).

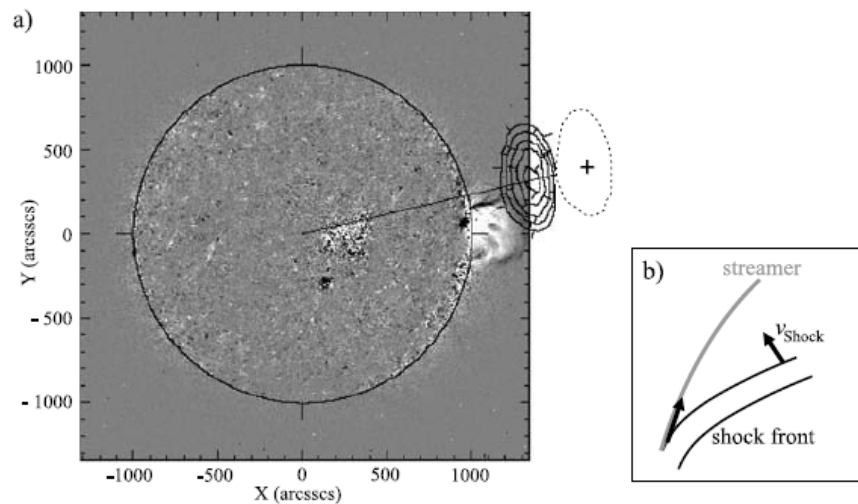


Figure 5 (a) NRH radio source (13:10:07 UT), corresponding to the harmonic band of the 1st type II burst (H1), superposed on the EIT image (13:14:14 UT). The corrected position of the radio source is marked by the cross and dashed curve. (b) Geometry of the shock front and the field line of the streamer; such an interaction between the shock front and the streamer can lead to a significant overestimate of the radio source velocity.

Figure 7.12: Observations of radio type II burst origins: The type II burst is located much higher than the CME front (Magdalenic et al. 2008). Note that the background EIT image was taken at 13:14 UT and the type II burst (contours) was observed at 13:10 UT - and hence the corrected even higher height (center marked with cross) for the type II burst at the time when the EIT image was taken.

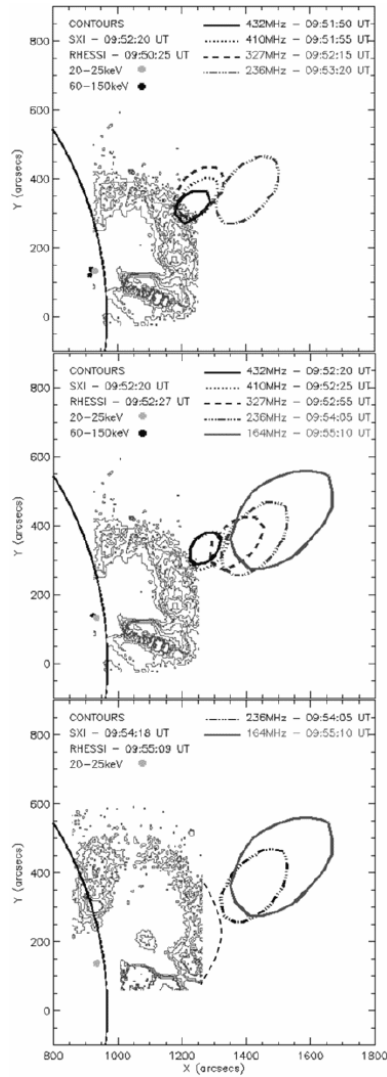


Figure 7.13: Observations of radio type II burst origins: Type II burst driver is the rising SXR loop (Dauphin et al. 2006).

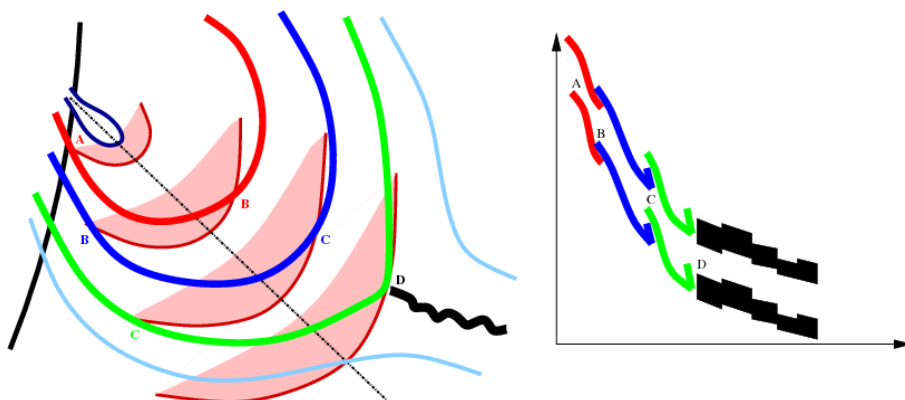
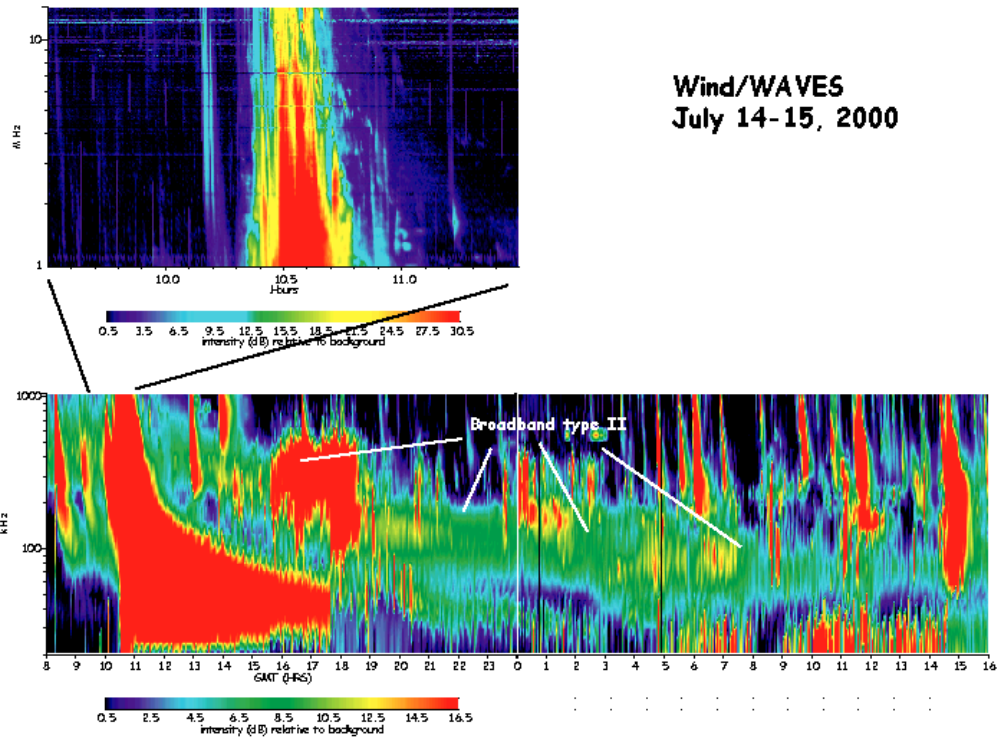


Figure 7.14: Observations of radio type II burst origins: Fragmented type II bursts are observed when shock wave passes through high-density loops (Pohjolainen, Pomoell & Vainio, 2008).



Wind/WAVES
July 14-15, 2000

Figure 7.15: Wind WAVES dynamic radio spectrum at two frequency bands, 1–14 MHz (top) and 20 kHz – 1 MHz (bottom). A propagating (interplanetary, IP) shock is visible at decameter - hectometer waves. Plasma frequency near L1 is 30 – 50 kHz. If electron density is dropping as $\sim 1/r^2$, the speed of the shock driver is about 2400 km/s.

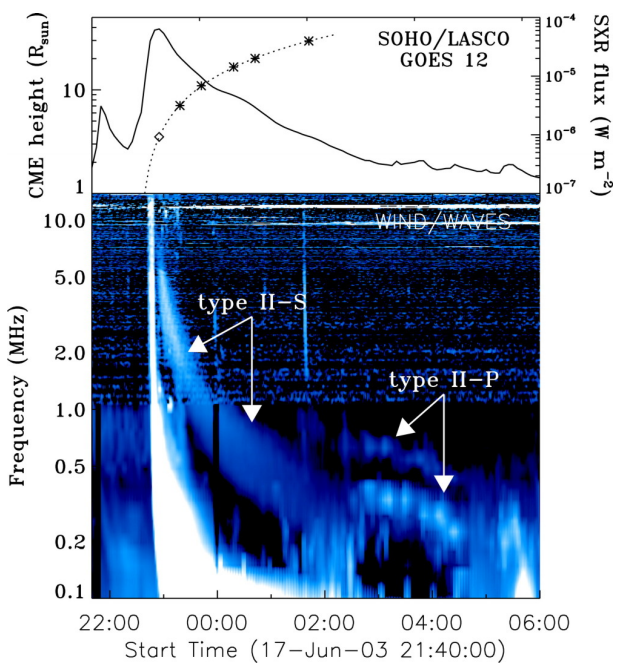
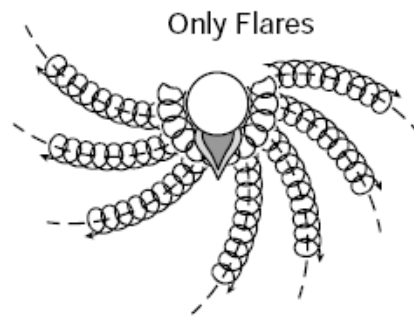


Figure 7.16: But, radio emission at low frequencies is not always plasma emission. Bastian, 2008: plasma (II-P) vs. synchrotron (II-S) emission in IP space.

Old Picture:



New Picture:

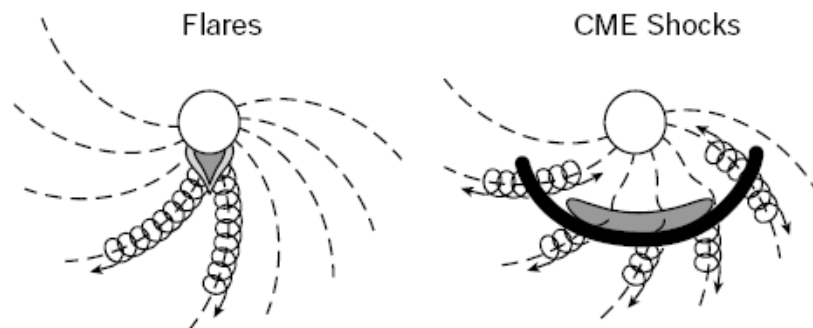


Figure 7.17: Gradual/impulsive SEP paradigm: are impulsive SEP events flare-accelerated and gradual SEP events CME-accelerated? (Reames, Space Science Reviews, 1999).

7.3 Solar energetic particles

For solar energetic particle (**SEP**) events, onset time = start of intensity rise at counting detector; injection time = start of acceleration near Sun; travel time = from injection to onset. You need to correct the times for 8 minutes when compared to electromagnetic emission.

For determining travel times, the methods are

- fixed path length method, assuming that the travel path is 1.2 AU
- velocity dispersion analysis (VDA), based on the fact that particles with higher energies arrive earlier and you can determine one path length and injection time for all energies.

SEP events can be divided into two classes, impulsive and gradual events.

Impulsive events are usually relatively low-intensity and short-duration (from hours to days) events. They are associated with short-duration soft X-ray emission, have high electron to proton intensity ratio and enhanced abundances of heavy elements. There is an association with flare acceleration processes and typical maximum particle energies in impulsive events are ~ 10 MeV per nucleon, the events are usually observable only if the accompanying flare occurs close to the nominal root (at $\sim W60$) of the interplanetary (IP) magnetic field lines connected to the observer. The particles in these events are generally believed to be accelerated in impulsive solar flares.

In contrast, gradual SEP events have higher particle intensities and power-law energy spectra extending to higher energies (in the case of protons beyond 1 GeV in extreme cases). The SEP events have long durations (days to weeks), and they are associated with long-duration soft X-ray emission and with interplanetary shocks driven by CMEs. The electron to proton ratios are smaller and on average elemental abundances and ionic charge states are in consistency with solar coronal abundances and temperatures.

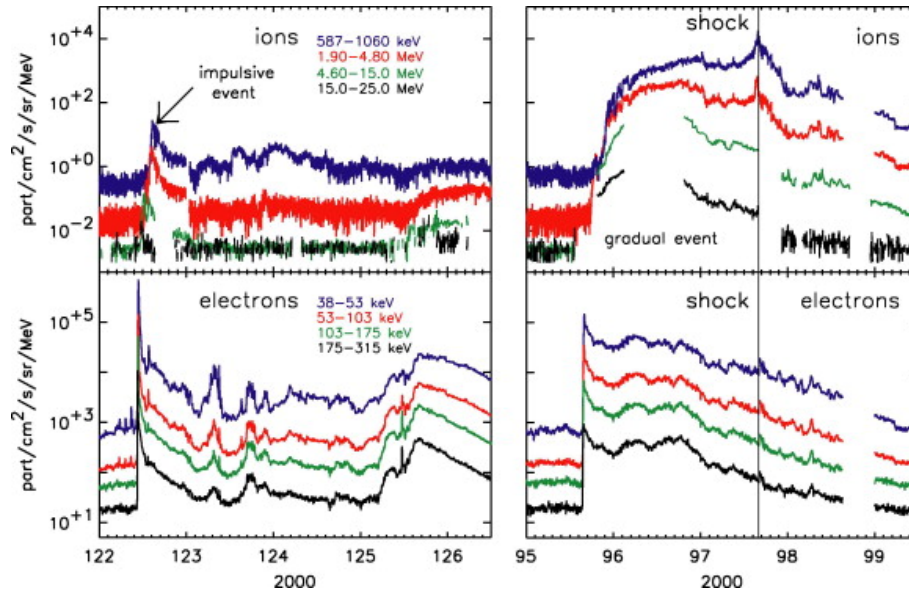


Figure 7.18: From: Lario D., Advances in Space Research, Vol 36, Issue 12, 2005

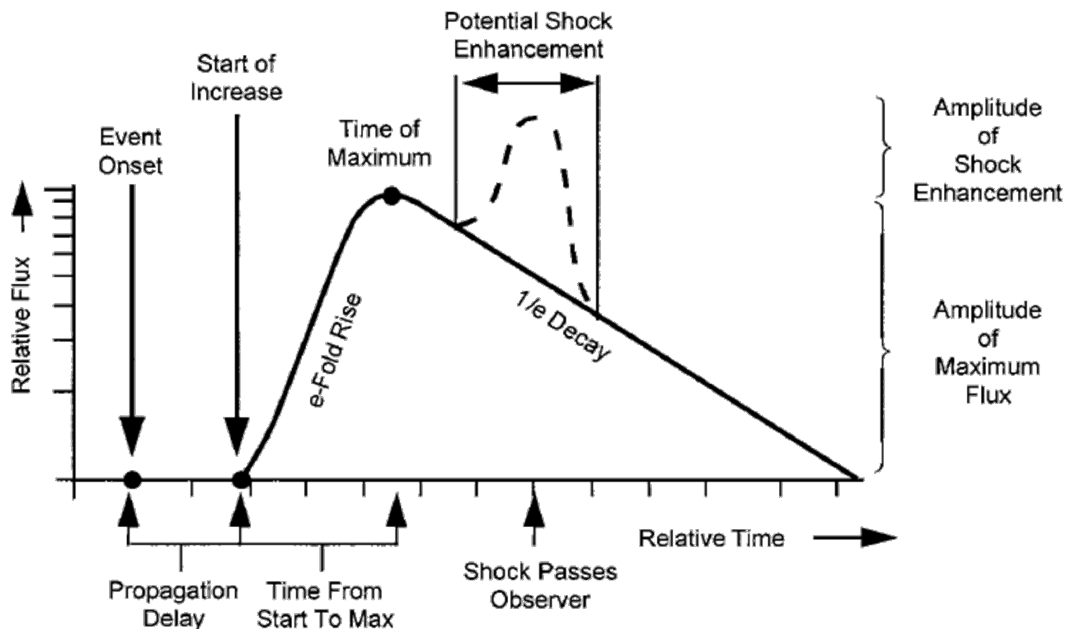


Figure 7.19: From: http://dev.sepem.oma.be/help/sep_intro.html

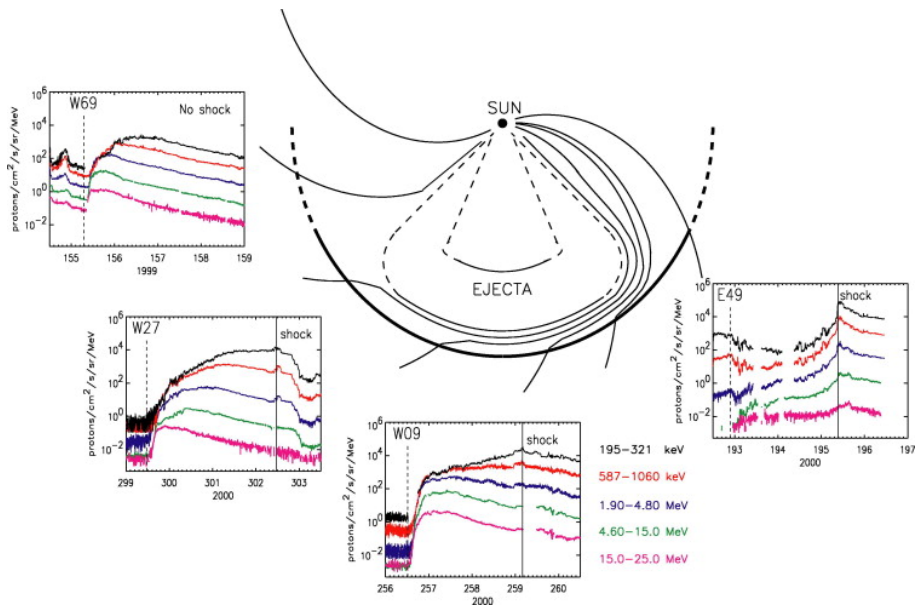


Figure 7.20: From: Lario D., *Advances in Space Research*, Vol 36, Issue 12, 2005

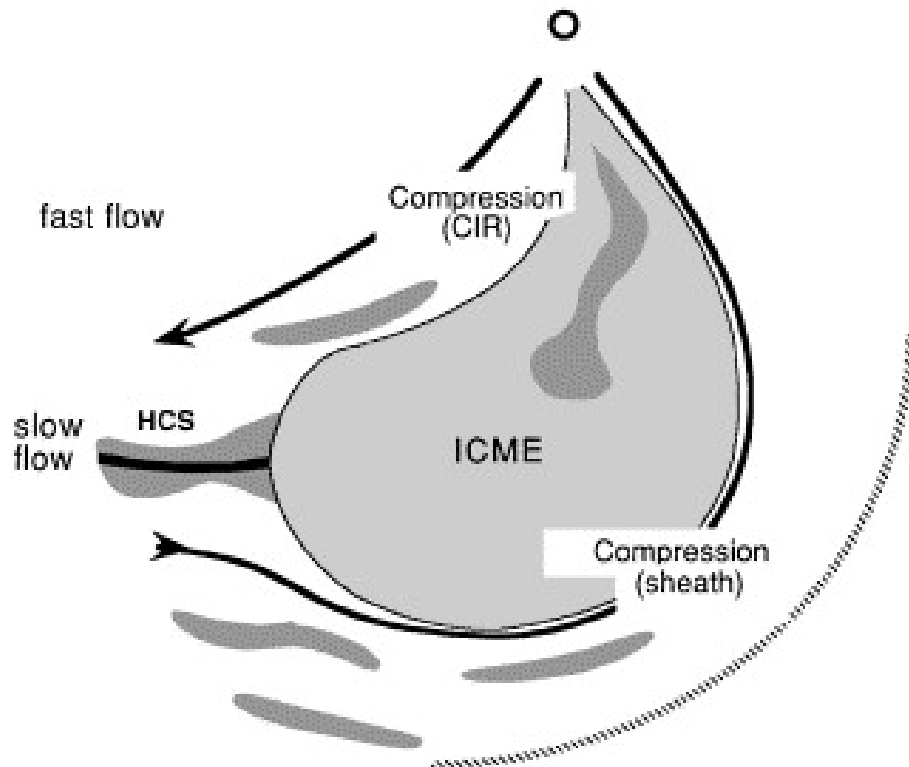


Figure 7.21: Interplanetary CME (ICME) and corotating interaction region (CIR). From: Crooker N., *Journal of Atmospheric and Solar-Terrestrial Physics*, Volume 62, Issue 12, August 2000

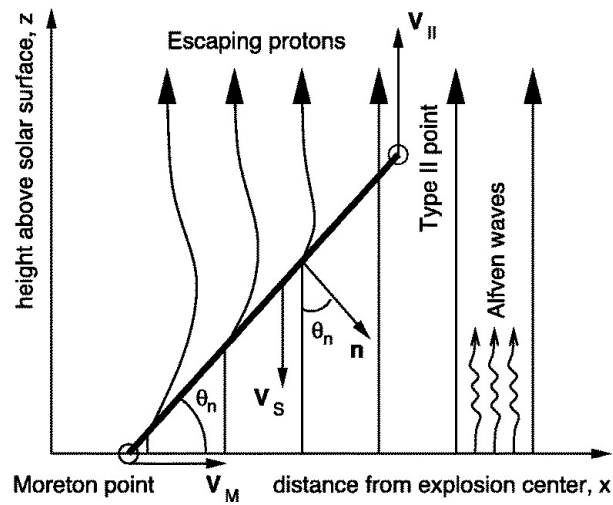


Figure 7.22: Simplified model of the acceleration region. V_M is the Moreton wave speed, θ_n is the (constant) angle between the shock normal n and the magnetic field, V_{II} is the vertical speed deduced from the metric type II drift rate, and $V_S = V_M \tan \theta_n$ is the shock speed projected along the field lines (Vainio & Khan, ApJ 2004).

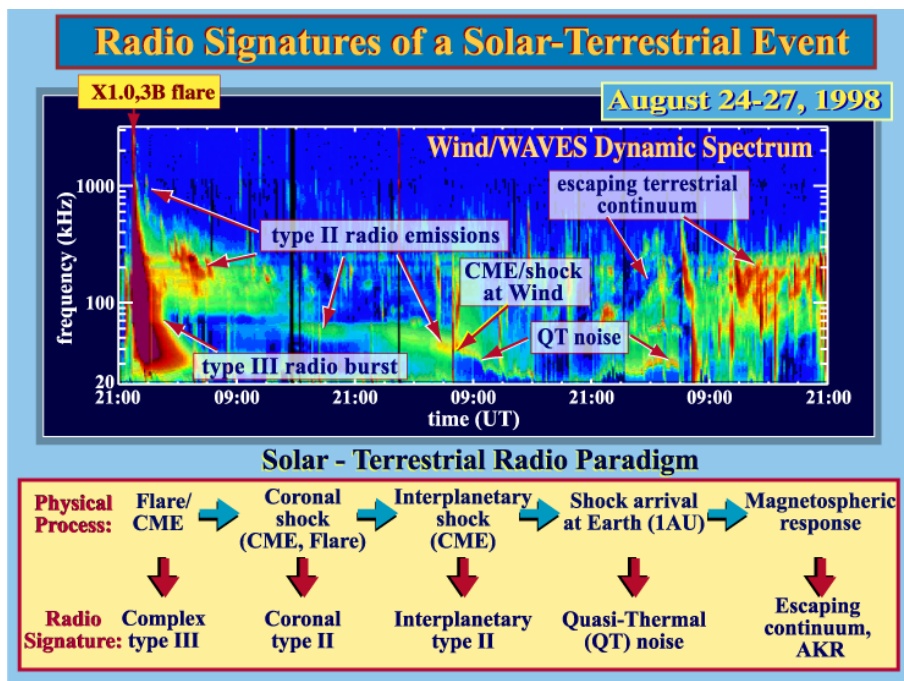


Figure 7.23: From: http://swaves.gsfc.nasa.gov/content_images/swavesf1.png

Chapter 8

Solar flares

8.1 Basic concepts

A solar flare is a sudden release of magnetic energy that has been stored in the field. Flares are associated with particle acceleration and heating. There have been many attempts to classify solar flares, but many of the classifications are outdated, mainly because they have been based on the outlook and appearance of events and not on the physical processes. The “impulsive – gradual” separation is still used, and it has worked best in describing energetic particle events. The “small – large” classification depends on the wavelength, but “confined – ejective” is still useful because it describes plasma motions and also makes a difference between magnetic field configurations (if the field opens or not).

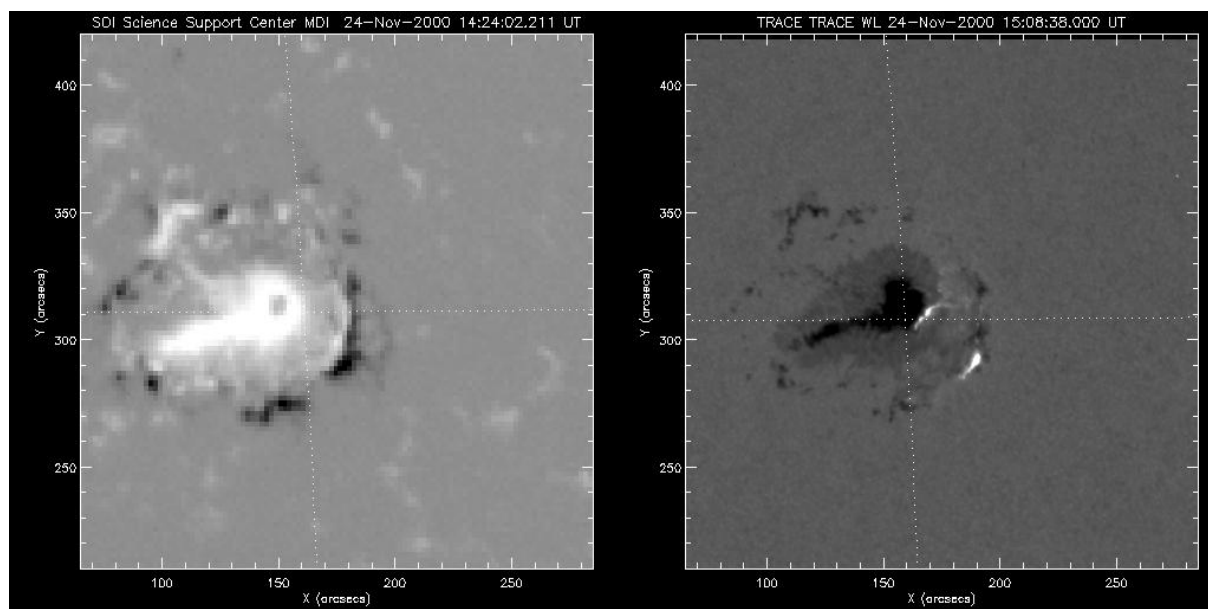


Figure 8.1: A solar flare is a sudden release of magnetic energy, stored in the field. The earlier definition required an H-alpha brightening. The TRACE image on the right shows a two-ribbon flare observed in white light and the SOHO MDI image on the left shows the magnetic polarities and the field strength within the region. Eruptions often occur on the edges of sunspots, where the opposite polarity fields meet.

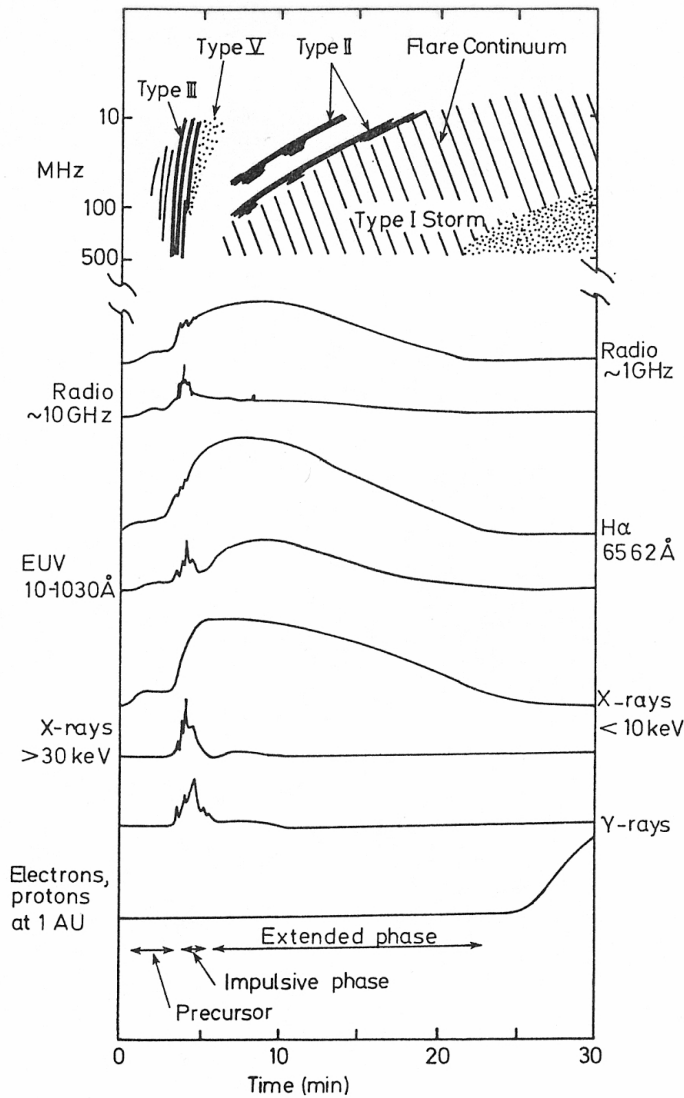


Fig. 4.1 - A schematic representation of the different phases of a typical solar flare as observed in electromagnetic and particle radiation. (Adapted from Kane 1974.)

G. A. Dulk et al.: Solar flares

Impulsive – Gradual

- Impulsive: Fast flux changes and non-thermal emission in hard X-rays and radio, may include a later thermal “tail” or “post-burst increase”
- Gradual: Almost purely thermal emission, hot plasma loops radiate thermal bremsstrahlung in soft X-rays and radio

Confined – Eruptive

- Depends whether magnetic fields open or not
- Diagnostics with radio type III emission (electron beams stream out along open magnetic field lines – or field lines stay closed and no type III bursts are observed)

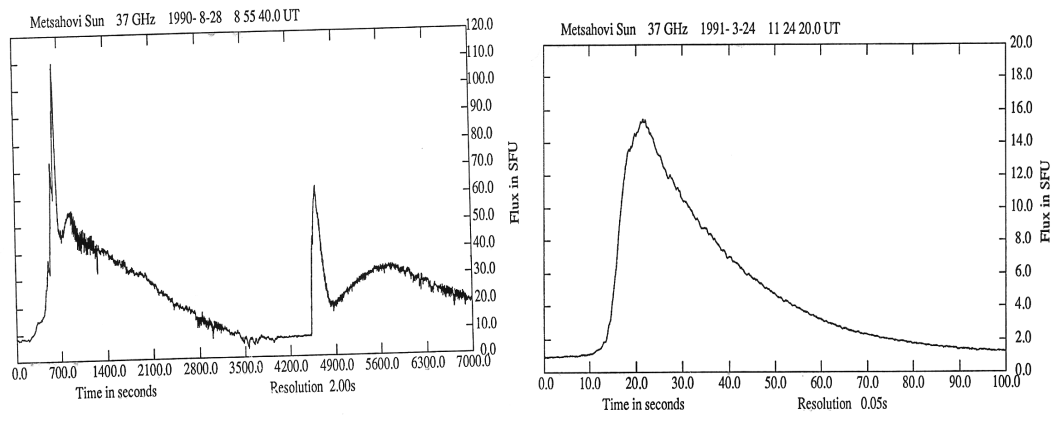


Figure 8.2: On the left: Impulsive burst + thermal tail. On the right: short impulsive burst without thermal emission (Metsähovi radio observations at 37 GHz).

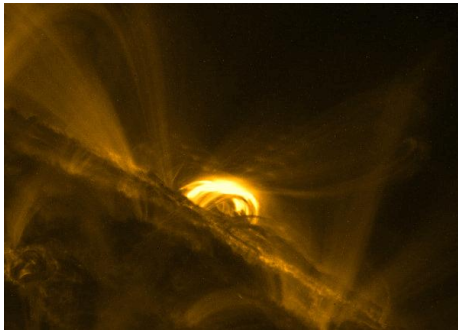


Figure 8.3: Flaring loop observed by TRACE at 171 Å.

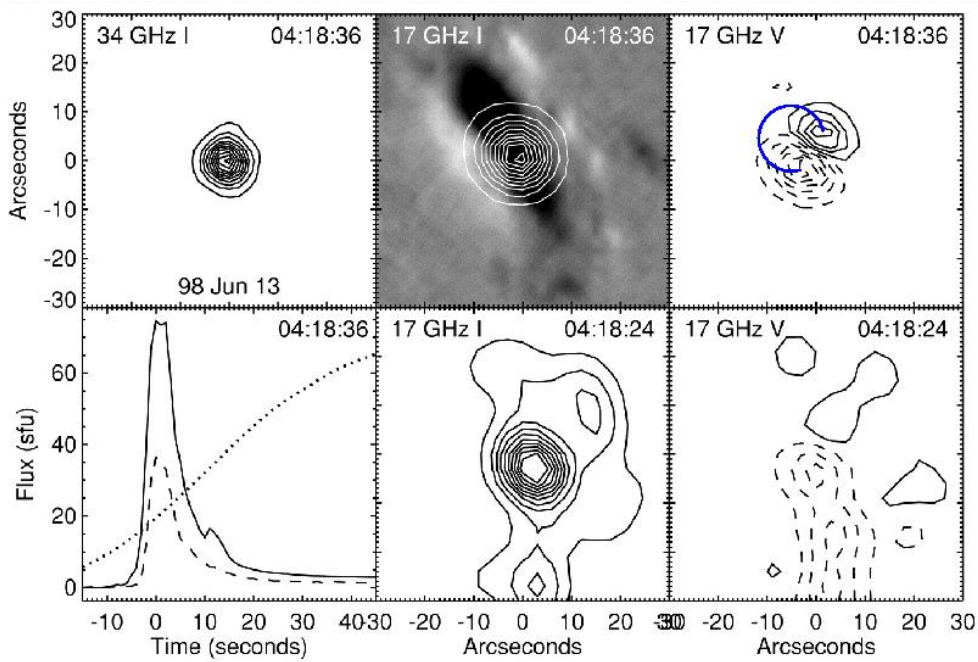


Figure 8.4: The 17 GHz emission (upper right plot; $I=L+R$, $V=L-R$) shows loop footprints that have opposite polarization. The trapped particles are emitting gyrosynchrotron emission, and the direction of gyration is different at different loop ends. (Kundu et al., ApJ 547, 2001)

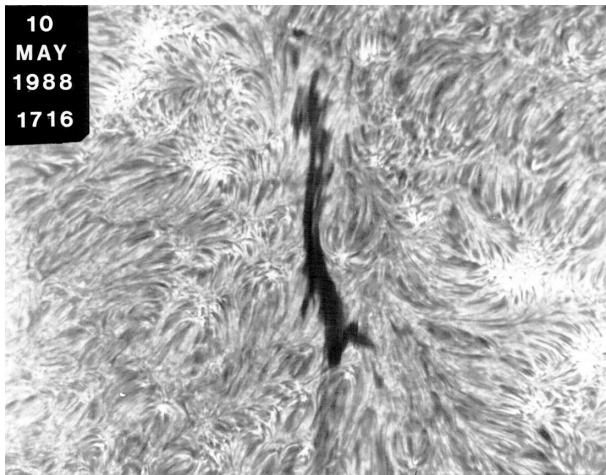


Figure 8.5: Filaments are cool and dense structures and they look dark in H_{α} as they are observed against the bright solar disk. The same happens at most radio wavelengths.

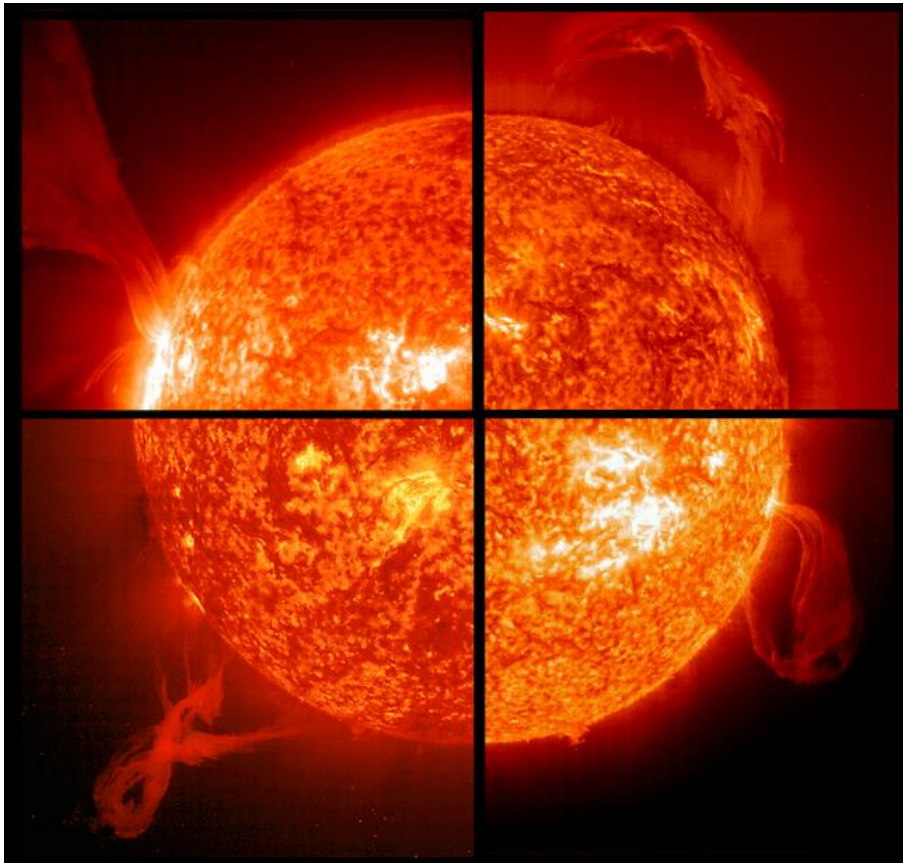
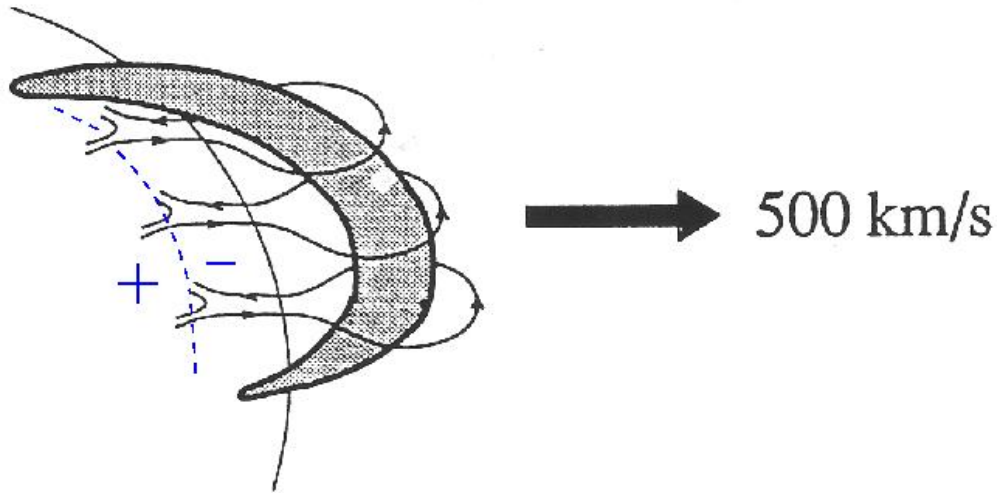


Figure 8.6: Filaments look bright when observed above the limb. Their appearances can be quite different (SOHO EIT, He II images).

Eruption Energetics



$$\text{Kinetic energy} = 2.5 \times 10^{31} \text{ ergs}$$

Figure 8.7: A filament “floats” in the solar atmosphere but is kept in place by magnetic field lines. Filaments are located above neutral lines, they are lines that separate oppositely polarized fields. If the oppositely directed fields reconnect below the filament, this may cause the filament to erupt. (From the MHD lectures by Terry Forbes)

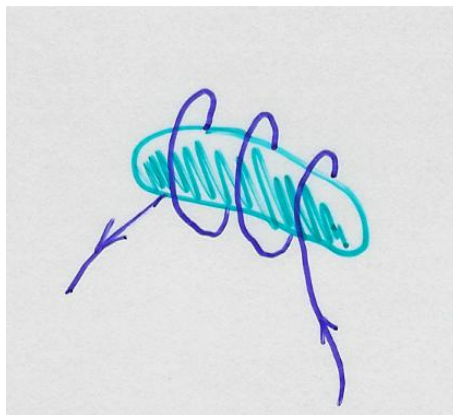


Figure 8.8: A flux rope scenario that is sometimes used for modeling filament eruptions - re-connecting field lines are now at the ends of the filament.

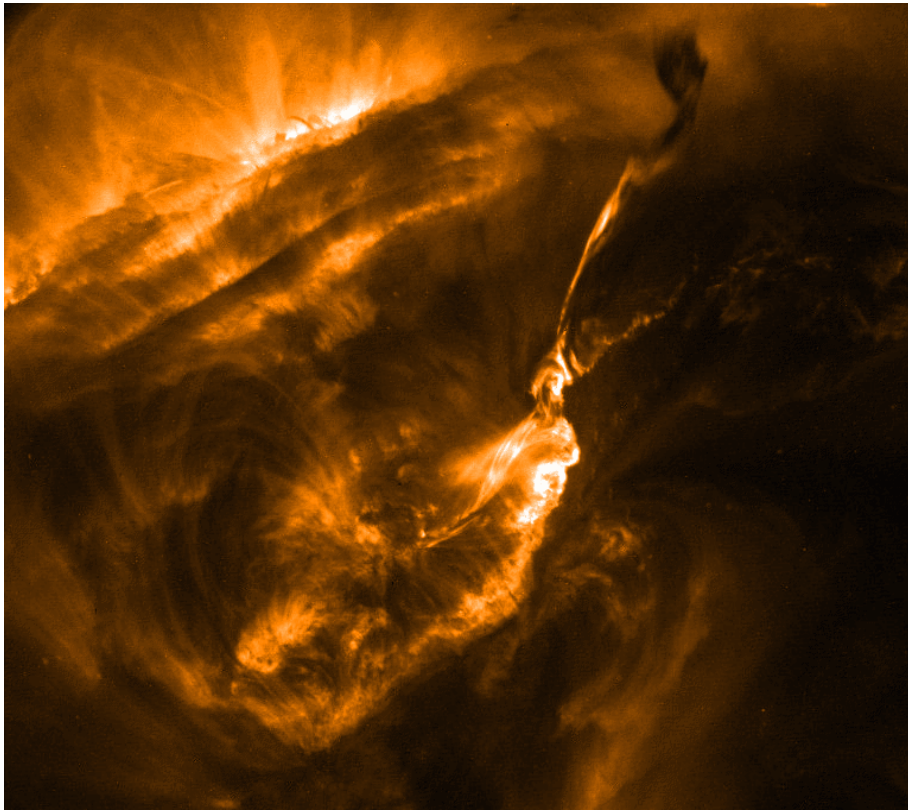


Figure 8.9: Filament eruptions are often (but not always) associated with flares. TRACE image shows bright regions at 1.5 MK temperature (more images at the TRACE web archive, by Karel Schrijver).

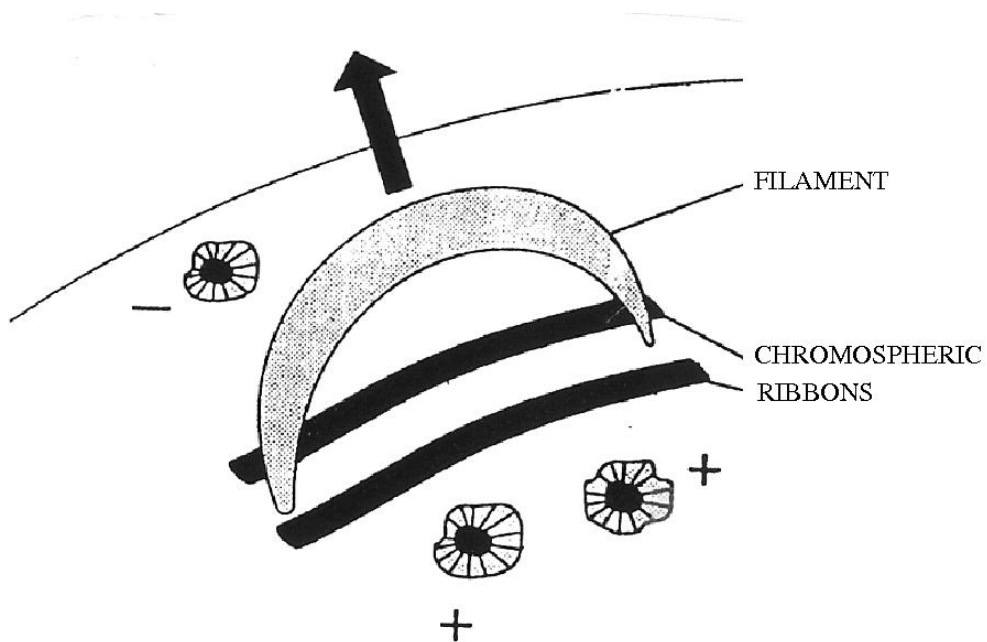


Figure 8.10: Filament eruption cartoon.

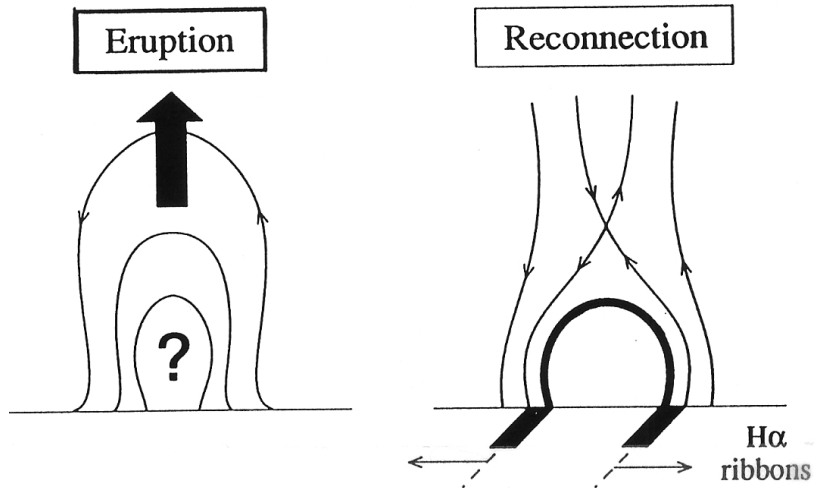


Figure 8.11: Eruption cartoon with a big question mark for trigger.

8.2 Flare models

Solar flare models have evolved from solenoids (Carmichael, 1963) to different types of reconnection scenarios (Sturrock 1966, Hirayama 1974, Kopp & Pneumann 1976) - hence the shortening CSHKP. The Grand Archive by Hugh Hudson contains practically all the available cartoons, see <http://solarmuri.ssl.berkeley.edu/~hudson/cartoons/overview.html>

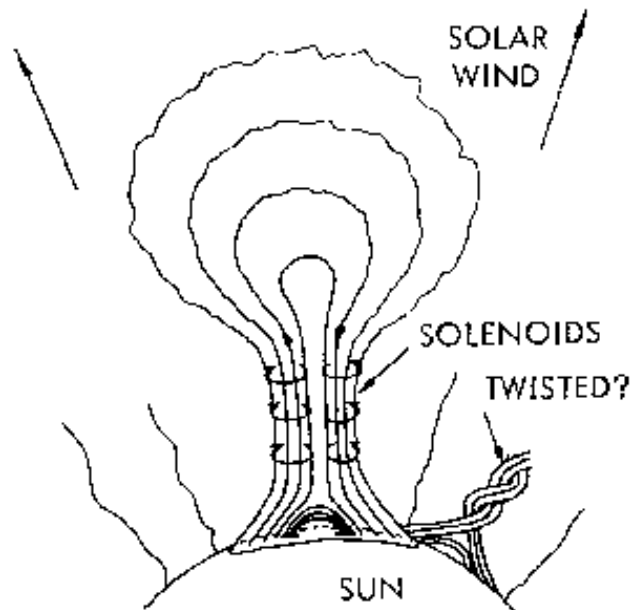


Figure 8.12: Development of flare models: Carmichael, 1960.

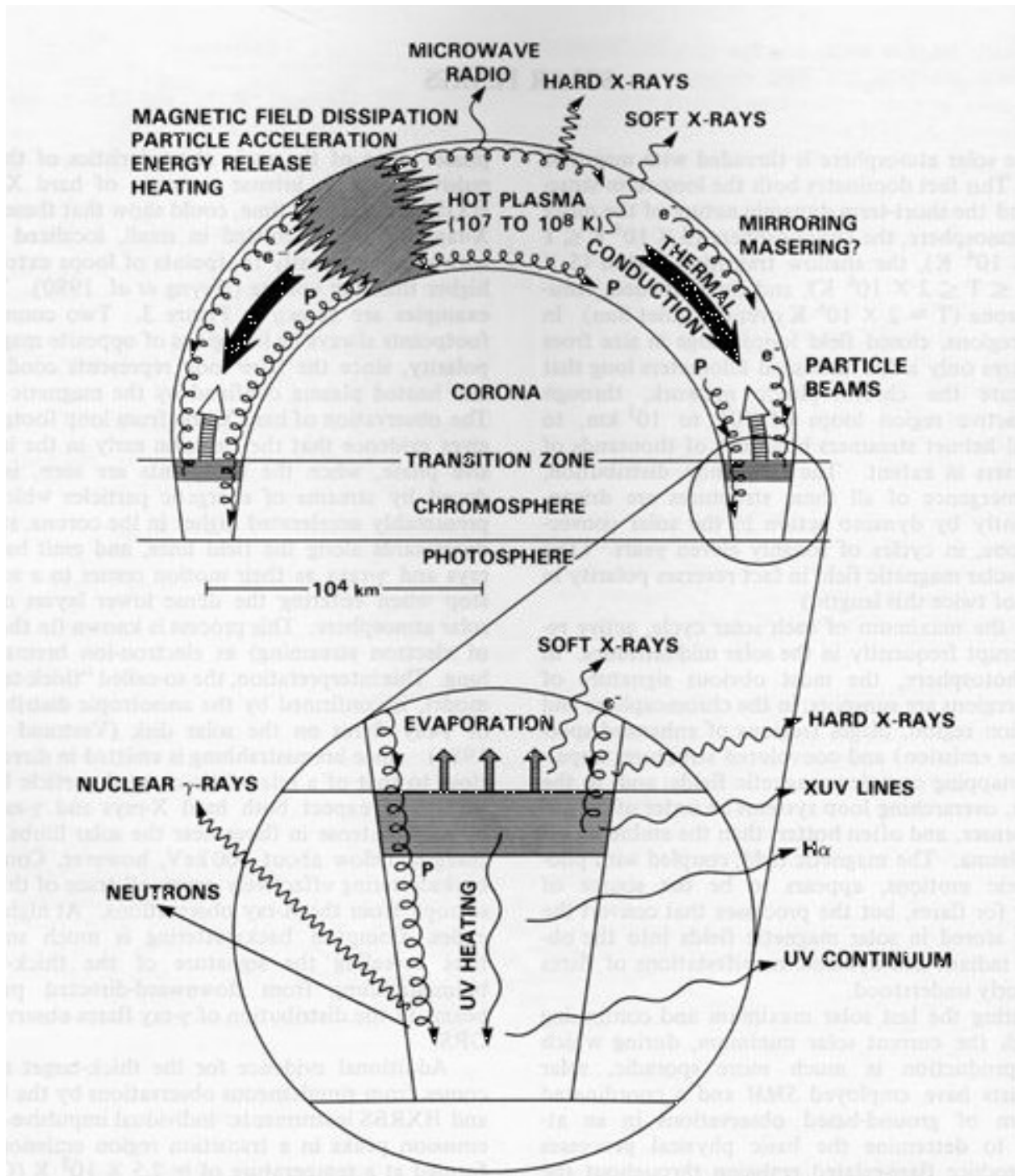


Figure 8.13: A simple model for a flare loop and associated emission (Gurman, 1987).

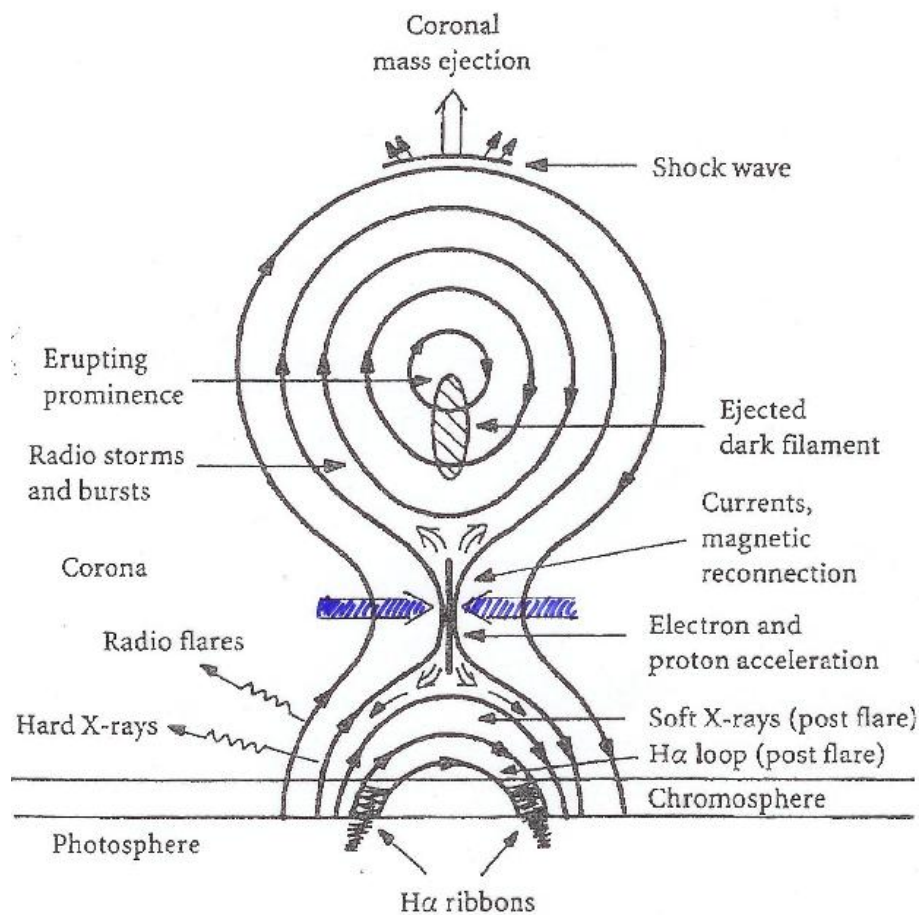


Figure 8.14: Filament eruption + flare in cross-section. This model also presents the connection between flares, filament eruptions, and coronal mass ejections. (K. Lang, 1995, copied from Kallenrode: Space Physics, 1998.)

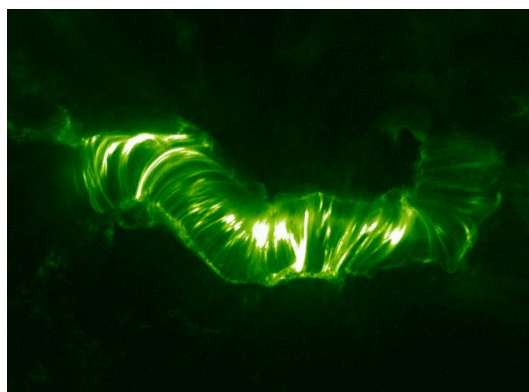


Figure 8.15: Post-flare loops form a rapidly cooling arcade of loops, in between the ribbons (TRACE: Bastille Day flare).

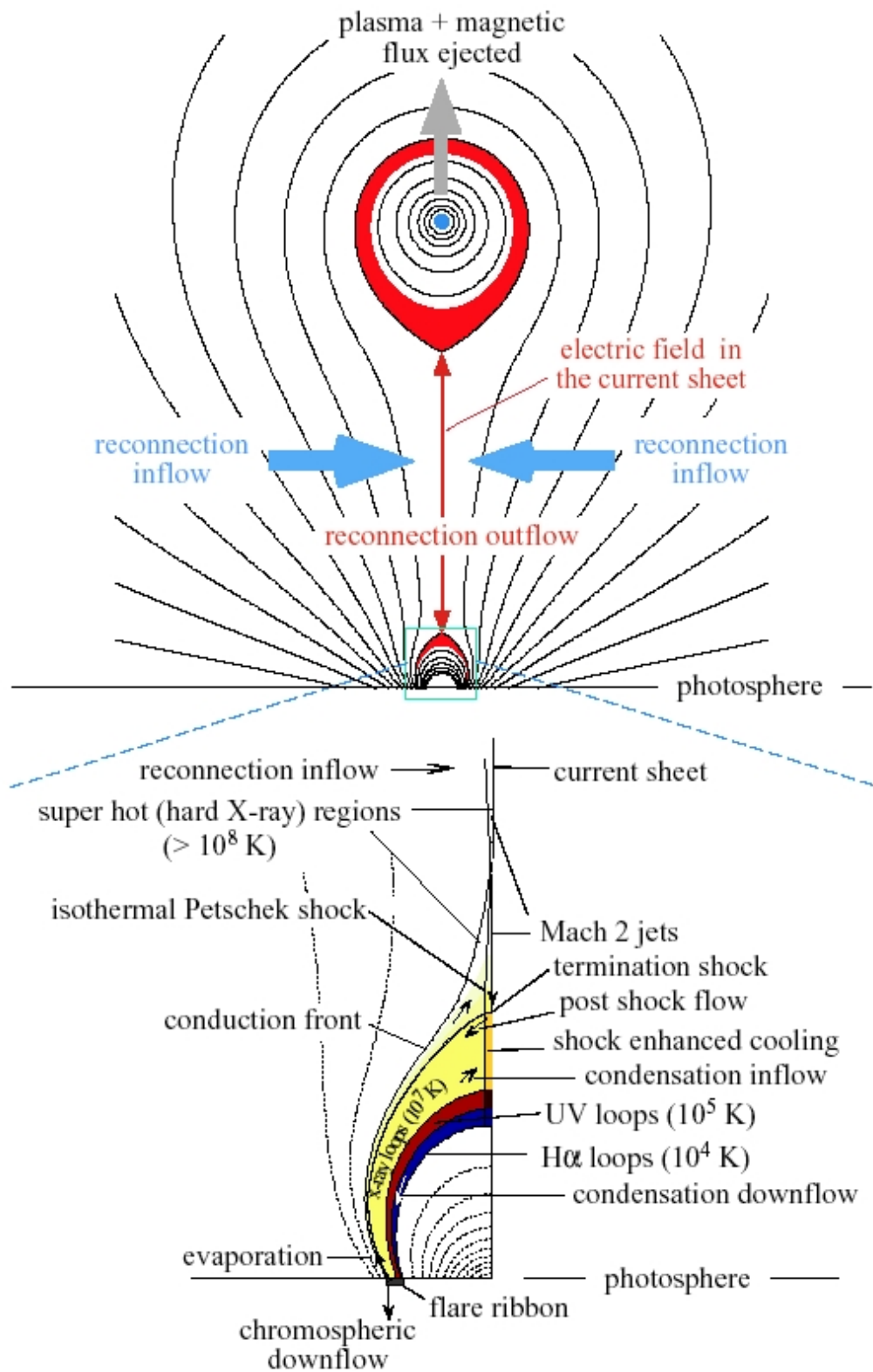


Figure 8.16: A more recent model (CSHKP+) contains many features that are not easily observed, but verified from theoretical considerations (Lin & Forbes 2002).

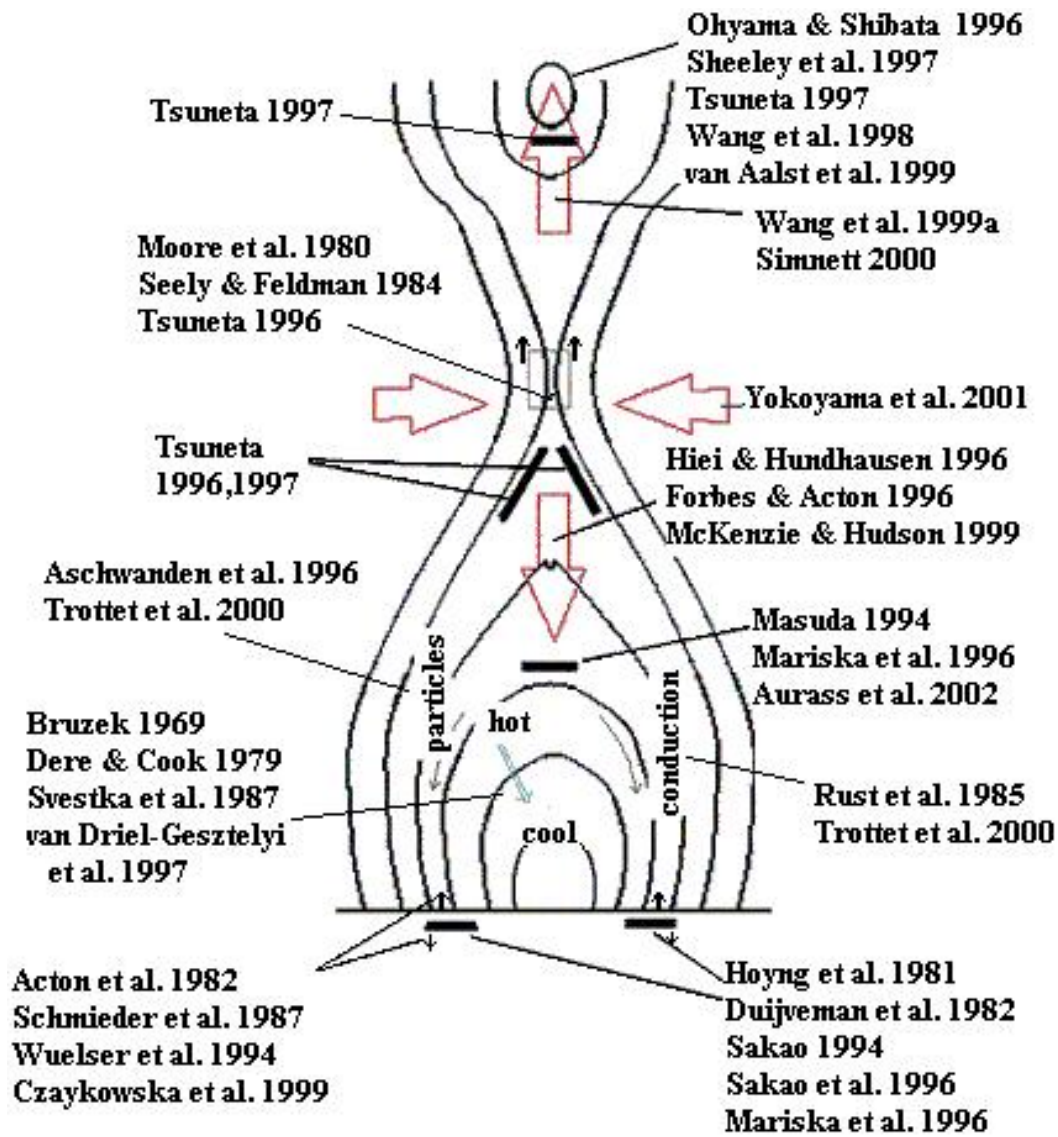


Figure 8.17: A summary of the different models was presented by McKenzie in the 10th Yohkoh Anniversary Meeting in 2001.

8.3 Predictions for activity

Mount Wilson Magnetic Classifications

Alpha: Denotes a unipolar sunspot group

Beta: A sunspot group having both positive and negative magnetic polarities, with a simple and distinct division between the polarities

Gamma: A complex active region in which the positive and negative polarities are so irregularly distributed as to prevent classification as a bipolar group

Delta: A complex magnetic configuration of a sunspot group consisting of opposite polarity umbrae within the same penumbra – **most probable to erupt**

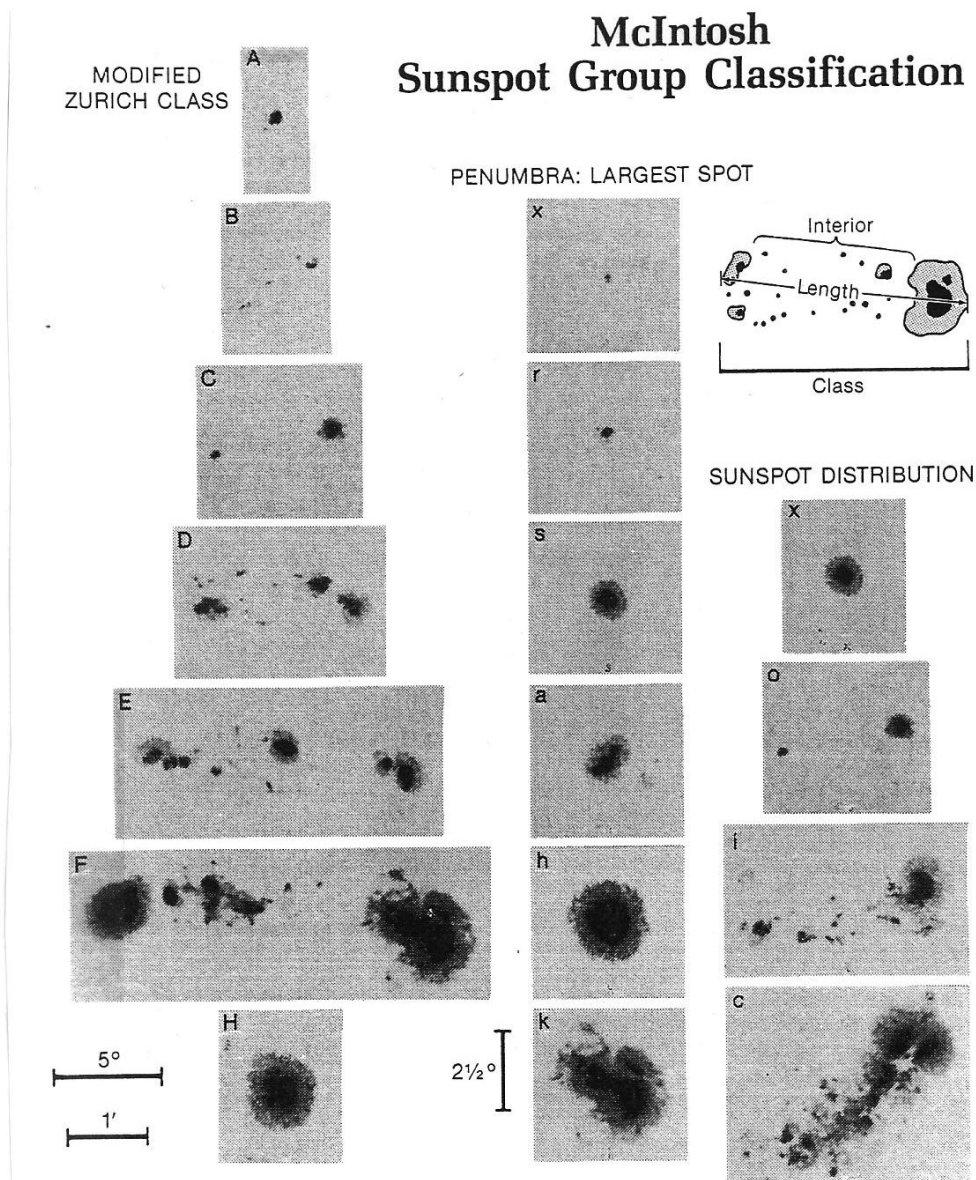
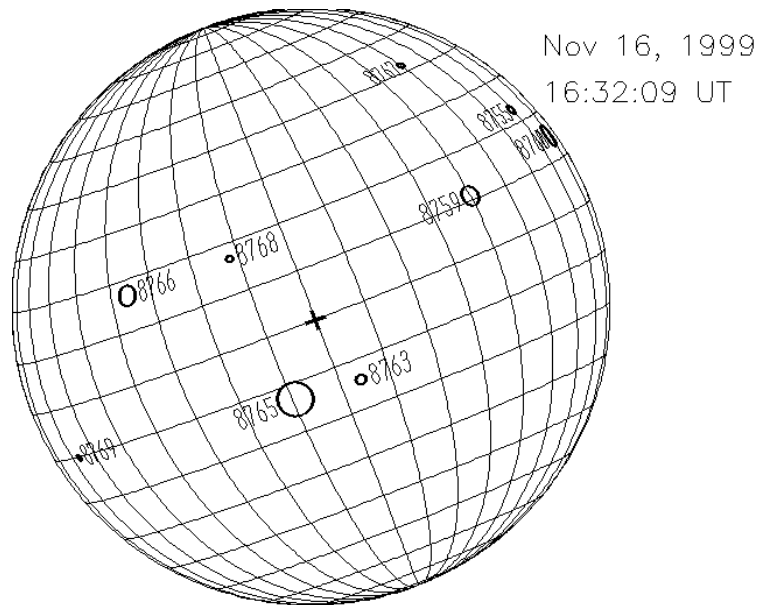


Fig. 6.4 The McIntosh sunspot classification scheme. Three letters describe in turn the class of sunspot group (single, pair or complex group), the penumbra of the largest spot in the group, and the spot distribution. (Courtesy P. S. McIntosh, NOAA (1990))



Joint USAF/NOAA Solar Region Summary (NOV 16,1999 00:00:00 UT)

NMBR	LOCATI	LO	AREA	Z	LL	NN	MAG	TYPE
8755	N23W61	315	0080	HSX	02	01		ALPHA
8759	N11W32	286	0270	FAI	21	44		BETA-GAMMA
8760	N15W70	324	0420	FKO	17	11		BETA
8763	S14E04	250	0070	CSO	06	07		BETA
8765	S13E19	235	0820	EKC	14	34		BETA-GAMMA
8766	N17E44	210	0270	DKI	07	13		BETA-DELTA
8767	N42W42	296	0040	CSO	05	05		BETA
8768	N17E20	234	0030	DSO	06	07		BETA
8769	S10E76	178	0030	HSX	01	01		ALPHA

Figure 8.18: Sunspot regions are identified with their NOAA number, given by the National Oceanic and Atmospheric Administration, USA. Daily measurements are made of the sunspot group positions, magnetic classification, maximum magnetic field strength, group number, Zurich class, Penumbra class, compactness class, number of spots, longitudinal extend in degrees, total spot areas, individual spot areas, etc.

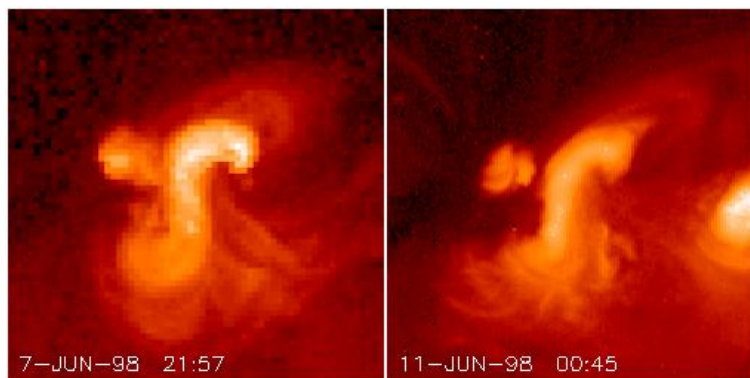


Figure 8.19: Sigmoid (S-shaped) structures in active regions forecast eruptions. However, not all sigmoid regions erupt. (Yohkoh soft X-ray image of a hot, coronal S-shaped region).

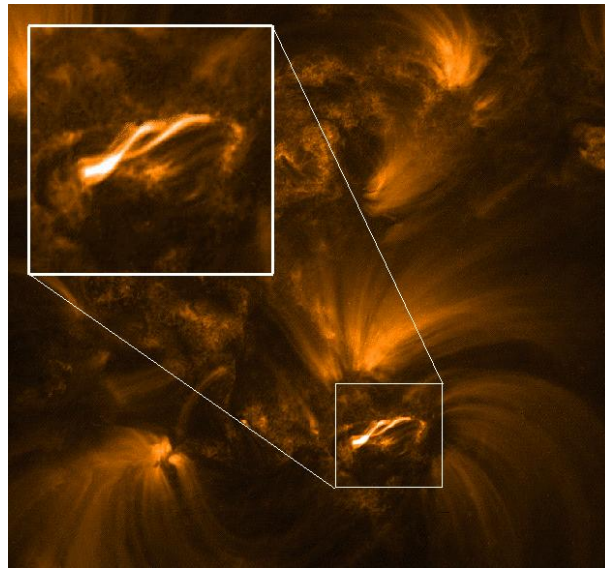


Figure 8.20: Low-lying wrapped loops (TRACE EUV image of chromospheric loops, that are cooler than the coronal soft X-ray loops).

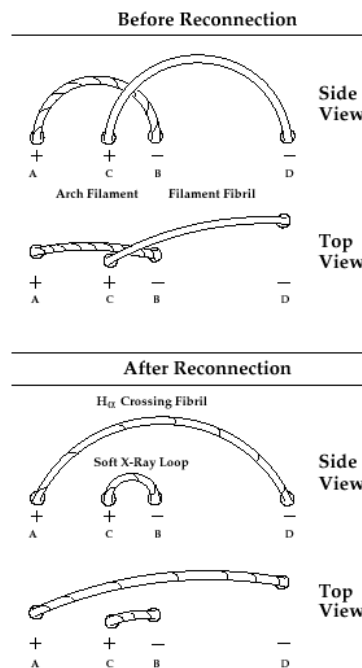


Figure 8.21: Simple reconnection model for wrapped loops. Note that the loops can appear as S-shaped structures when looked from above with instruments that have low spatial resolution (cartoon by Canfield & Reardon, *Solar Phys.*, 1998).

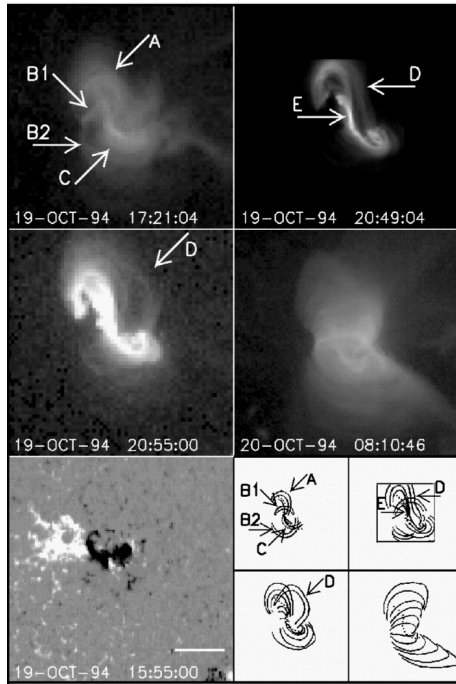


Figure 8.22: Sigmoids often evolve into ejective eruptions (Moore et al. ApJ 552, 2001).

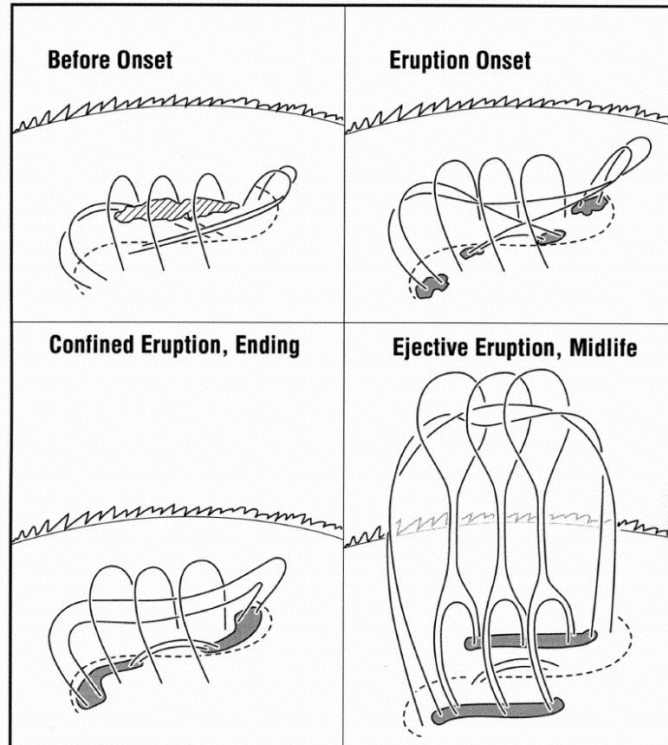


Figure 8.23: The separation between confined and ejective eruptions. Moore et al. (2001) found that 4 out of 6 analysed S-shaped region events were ejective.

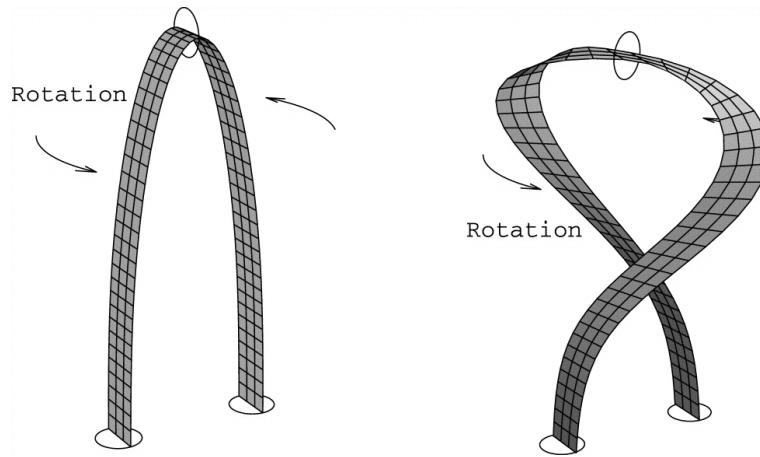


Figure 8.24: Twist and writhe of magnetic flux tubes: Plasma flows, solar rotation, etc. can cause footpoint movement and twisting of loops, that lead to reconnection (Lopez Fuentes et al., 2000).

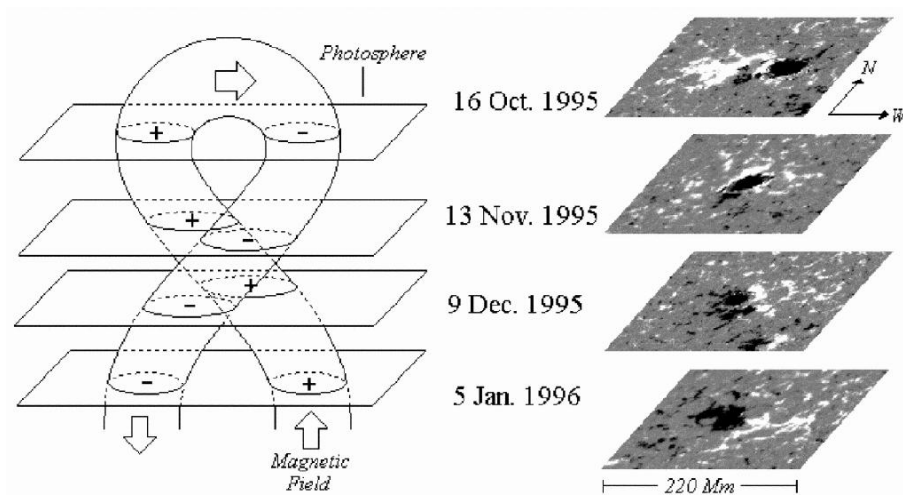


Figure 8.25: Emergence of twisted flux tubes is also possible. The twist will “unfold” during and after emergence, which can be observed as rotating magnetic polarities (see magnetograms on the right; from Lopez Fuentes et al., 2000).

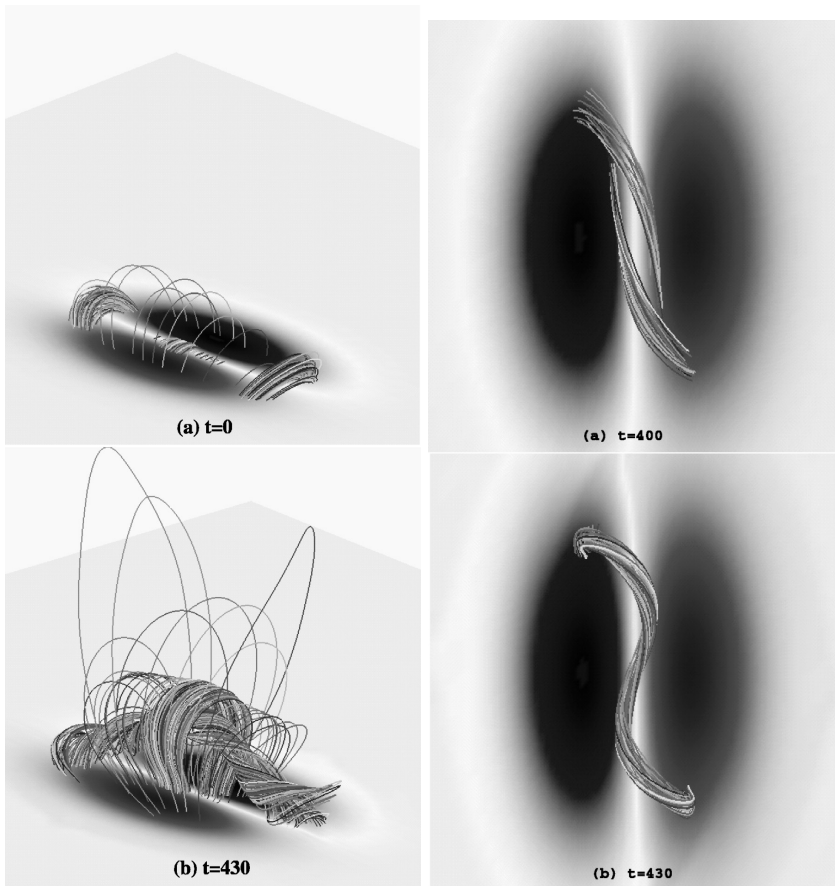


Figure 8.26: MHD simulations of the evolution of an S-shaped region: Selected field lines of the configuration when a twisted flux rope has been created. Top view of selected field lines showing the merging of two inverse J-shaped structures visible at $t = 400$ into a single inverse S-shaped structure at $t = 430$. (Amari et al. ApJ, 2000)

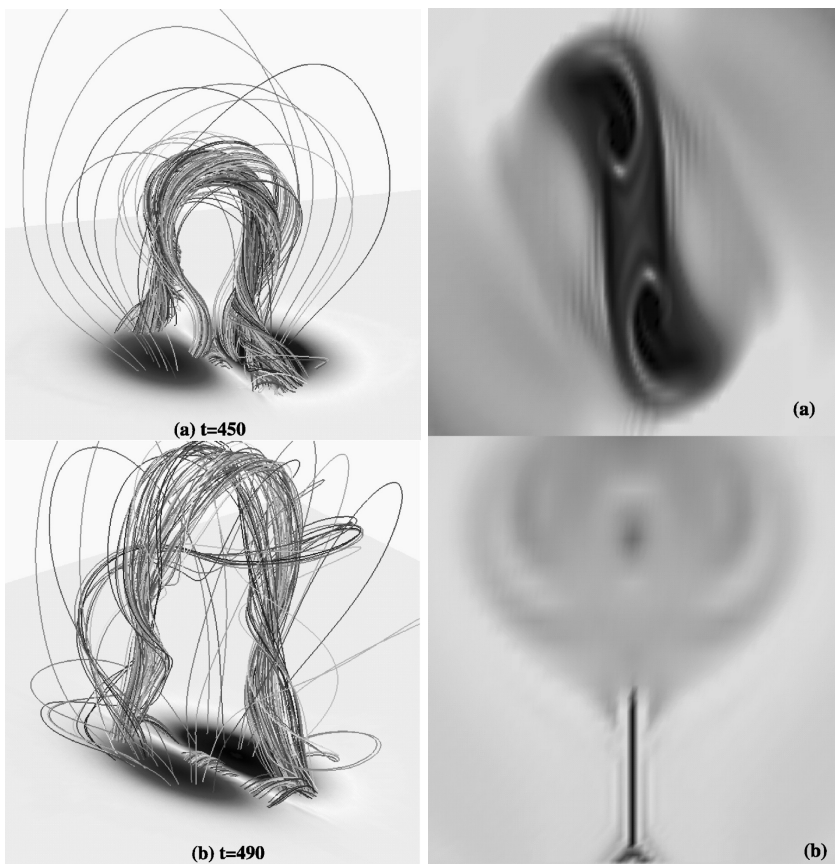


Figure 8.27: For $t = 430$ the configuration experiences a major global disruption. The twisted flux rope expands very rapidly; evolution of the configuration at two steps during a relaxation phase at $t = 450$ and $t = 490$. No neighboring equilibria exist, and the configuration experiences a major disruption. (Amari et al. ApJ, 2000)

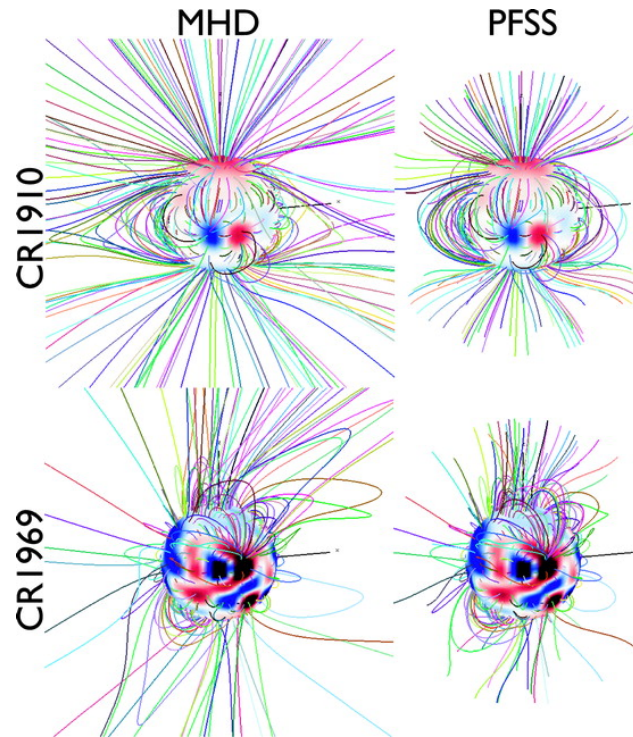


Figure 8.28: Magnetic field extrapolations can be done with the Solarsoft software, using potential field source surface (PFSS) code. PFSS solutions have been found to match MHD results for configurations based on untwisted coronal fields (i.e., when driven by line-of-sight magnetograms). It remains an open question whether MHD solutions will differ more substantially from PFSS solutions when vector magnetograms are used as boundary conditions. This will be addressed in the near future when vector data from the Solar Dynamics Observatory and Hinode become incorporated into the MHD models. (Riley et al., ApJ 653, 2006).

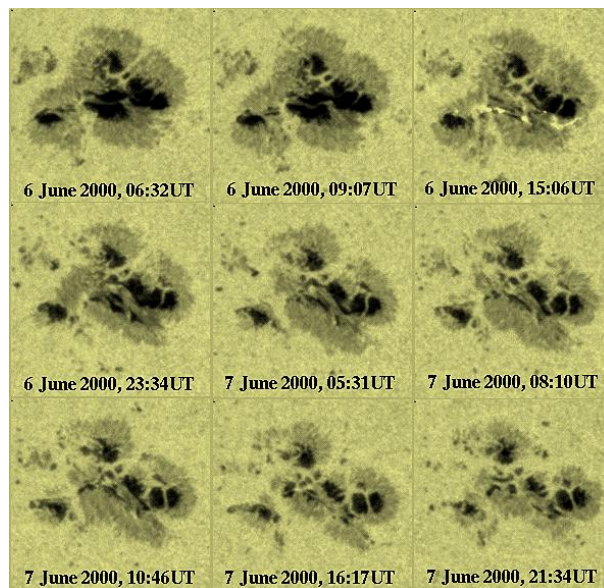


Figure 8.29: Sunspot regions disintegrate within time.

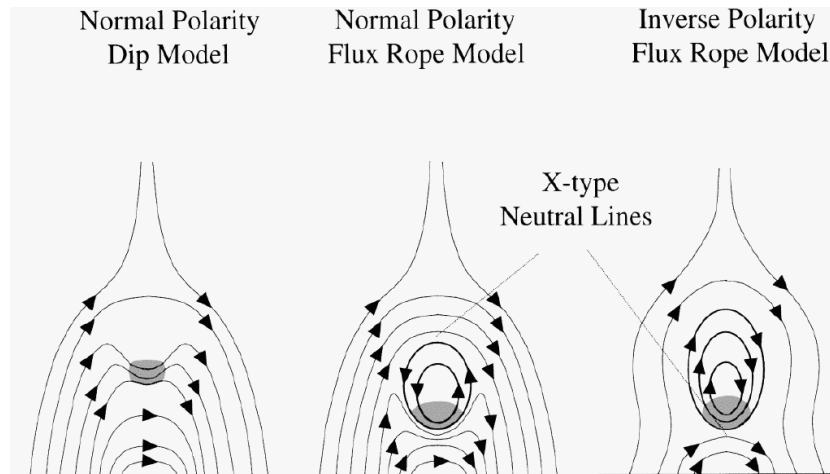


Figure 8.30: Filament support models: Dip model \rightarrow flux rope model when filament moves downward until reconnection occurs above (X-type neutral line). In inverse polarity model flux rope emerges from below (Gilbert et al. ApJ 537, 2000).

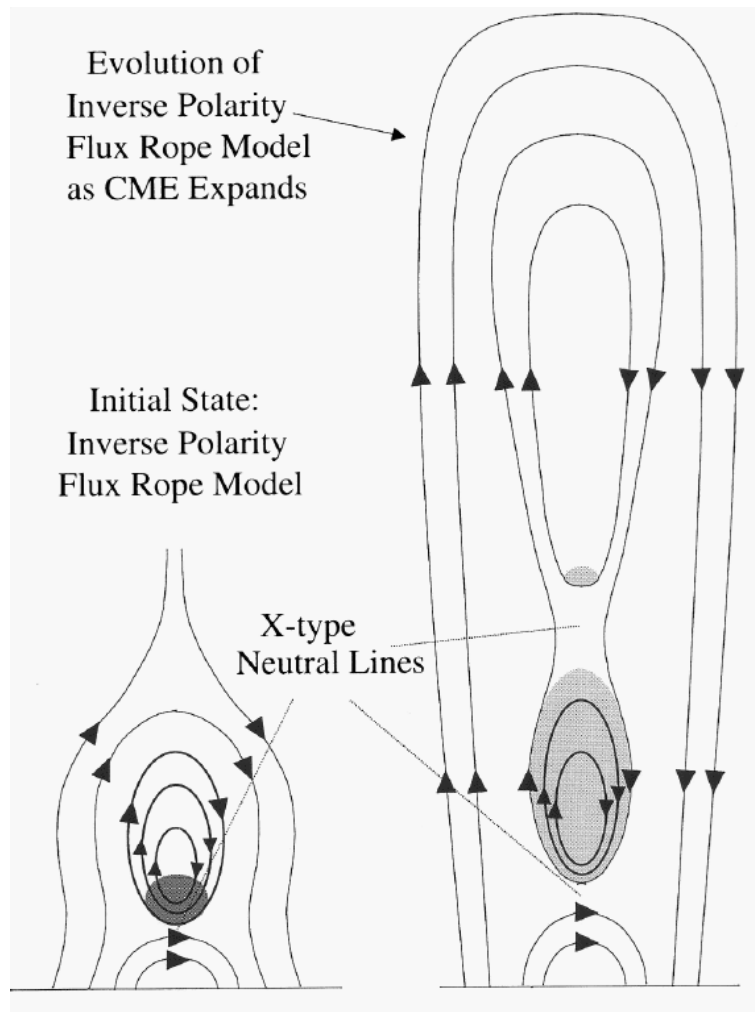


Figure 8.31: Filament eruption model (Gilbert et al. 2000)

8.4 Reconnection models

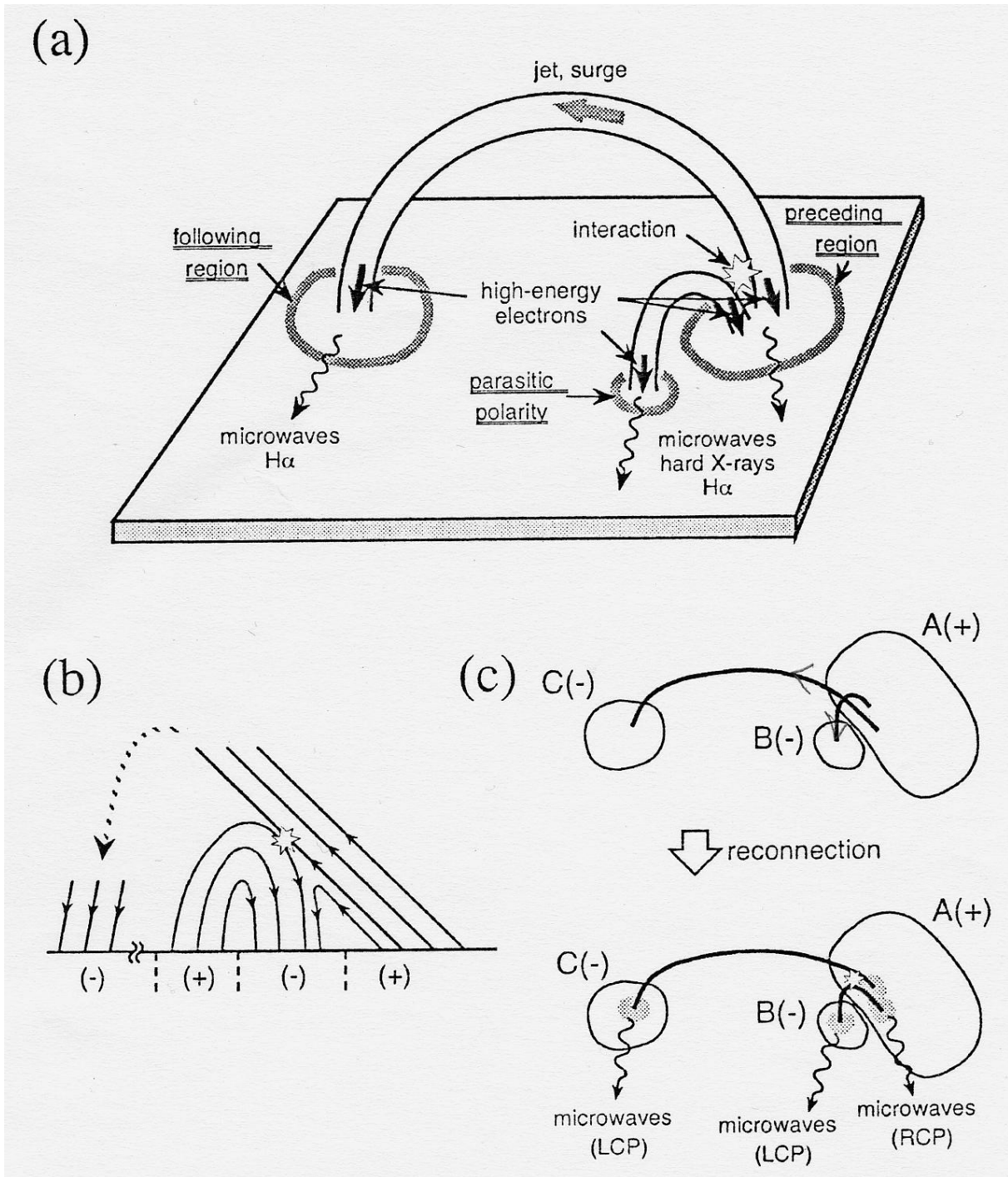
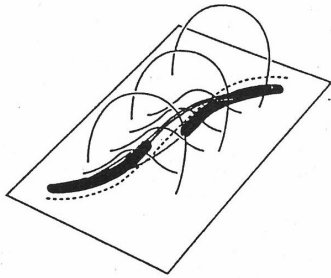


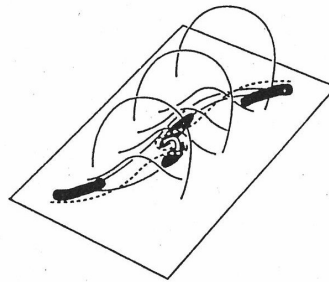
Figure 8.32: Emerging flux is a simple way to cause reconnection: the rising opposite polarity region reconnects with the existing flux and the new loop interacts with the older one that lies above in this plot. Hanaoka (PASJ 51, 1999) shows a schematic drawing of a double-loop flare and behaviour of high-energy electrons. The interaction region of the two loops is the origin of high-energy electrons and thermal plasma flows, such as jets and surges.

ONSET:

WITHOUT EMERGING FLUX



WITH EMERGING FLUX ON MAIN INVERSION LINE



WITH EMERGING FLUX OFF MAIN INVERSION LINE

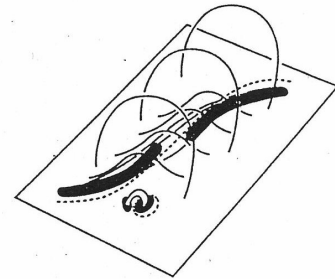
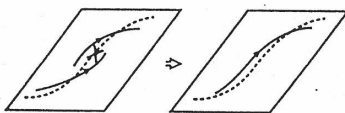


Figure 2. Typical onsets of eruptive flares; left: no emerging flux; center: emerging flux on main inversion line; right: emerging flux off main inversion line. Here, as in Figure 1, the dashed lines are magnetic inversion lines, dividing areas of opposite polarity in the photosphere; black areas are ribbons of chromospheric flare brightening. In all three cases, at flare-ribbon onset the sheared core field along and above the main inversion line has begun to erupt upward, distending the surrounding envelope field, and the initial flare ribbons along the main inversion line are tucked under the erupting core.

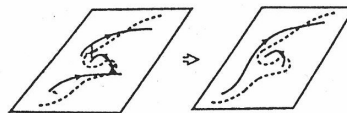
TRIGGER:

SLOW RECONNECTION IN FLUX CANCELLATION

① **TETHER CUTTING WITHOUT EMERGING FLUX:**



② **TETHER CUTTING WITH EMERGING FLUX:**



③ **TETHER WEAKENING BY RECONNECTION WITH EMERGING FLUX:**

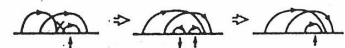
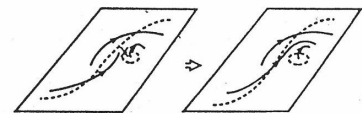


Figure 4. Inferred process for triggering typical onsets of eruptive flares; left: no emerging flux; center; emerging flux on main inversion line; right: emerging flux off main inversion line. The field lines shown are in the core of the preflare field configuration shown in Figures 1-3. The sequences of 2-D sketches below the perspective sketches show the reconnection, emergence, and submergence of field in an end view along the main inversion line. X's mark reconnection. Vertical arrows below the 2-D sketches mark flux emergence (upward arrow) and flux submergence (downward arrow).

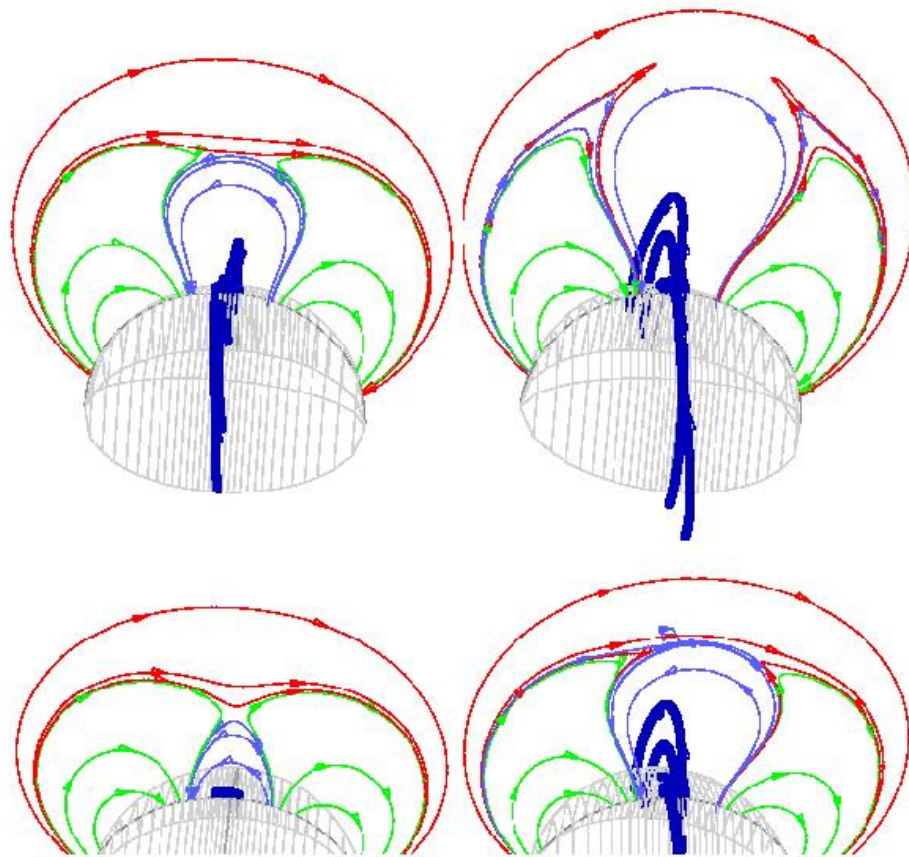


Figure 8.33: Reconnection models: magnetic breakout (Antiochos et al., 1999). A magnetic breakout is the opening of initially low-lying sheared fields, triggered by reconnection at a null point that is located high in the corona and that defines a separatrix enclosing the sheared fields). DeVore & Antiochos (ApJ 628, 2005): In this model, the magnetic free energy that drives the eruption is stored readily in the pre-reconnection state: the energy required to open the stressed flux in the initial configuration can be much greater than that in the post-reconnection state, because more overlying flux must be opened in the former than in the latter. Once the breakout reconnection begins, it accelerates inexorably as the open energy declines, progressively and rapidly. The resultant excess magnetic free energy is converted into kinetic and gravitational energy of the CME plasma, which escapes in an ideal expansion. Subsequently, flare reconnection across the current sheet trailing the ejected flux produces a flux rope and a closed coronal arcade, similar to those in other models. Unlike those scenarios, however, in the breakout model flare reconnection results from, rather than causes, the eruption.

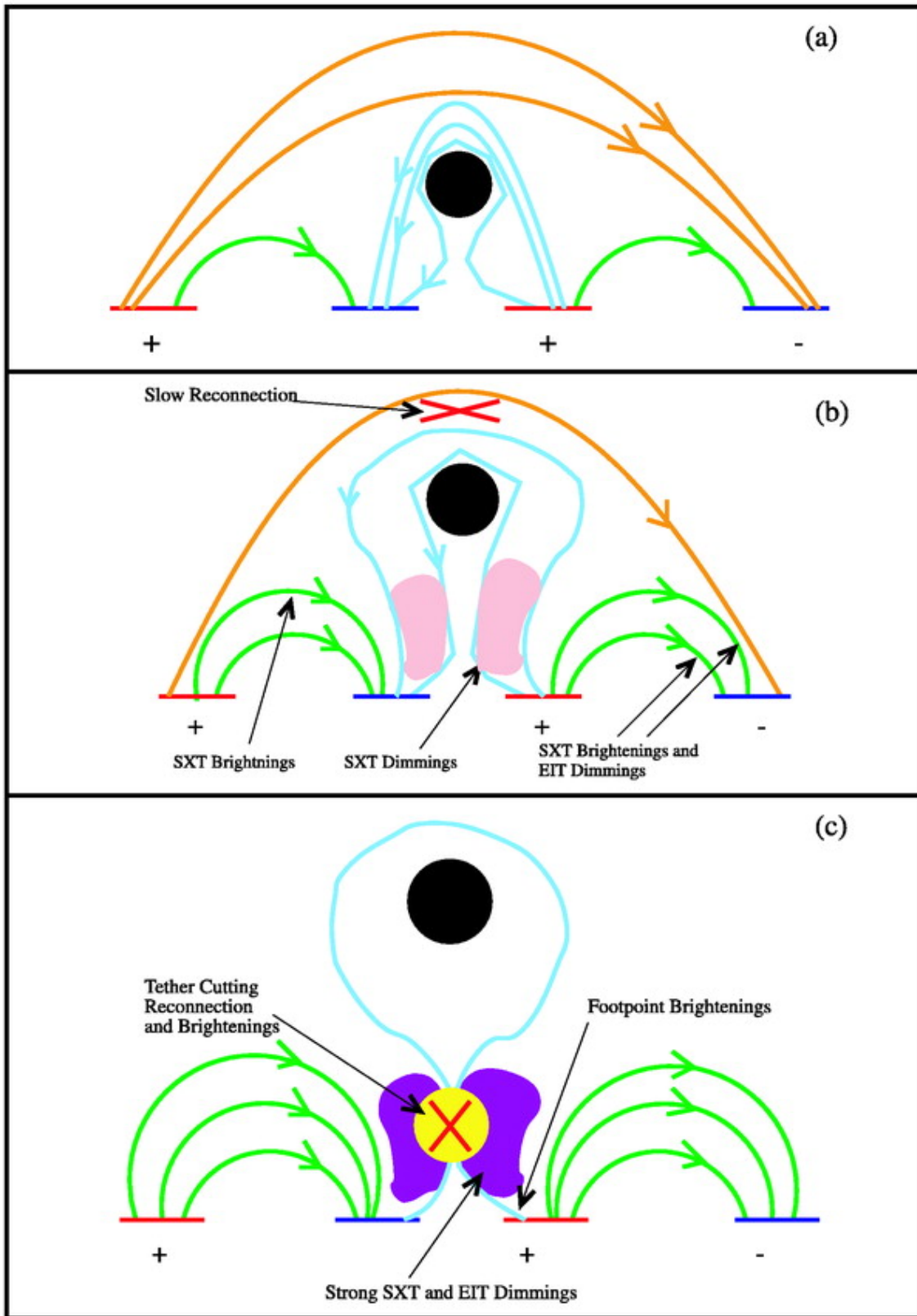


Figure 8.34: Tether cutting + breakout (Sterling & Moore 2004).

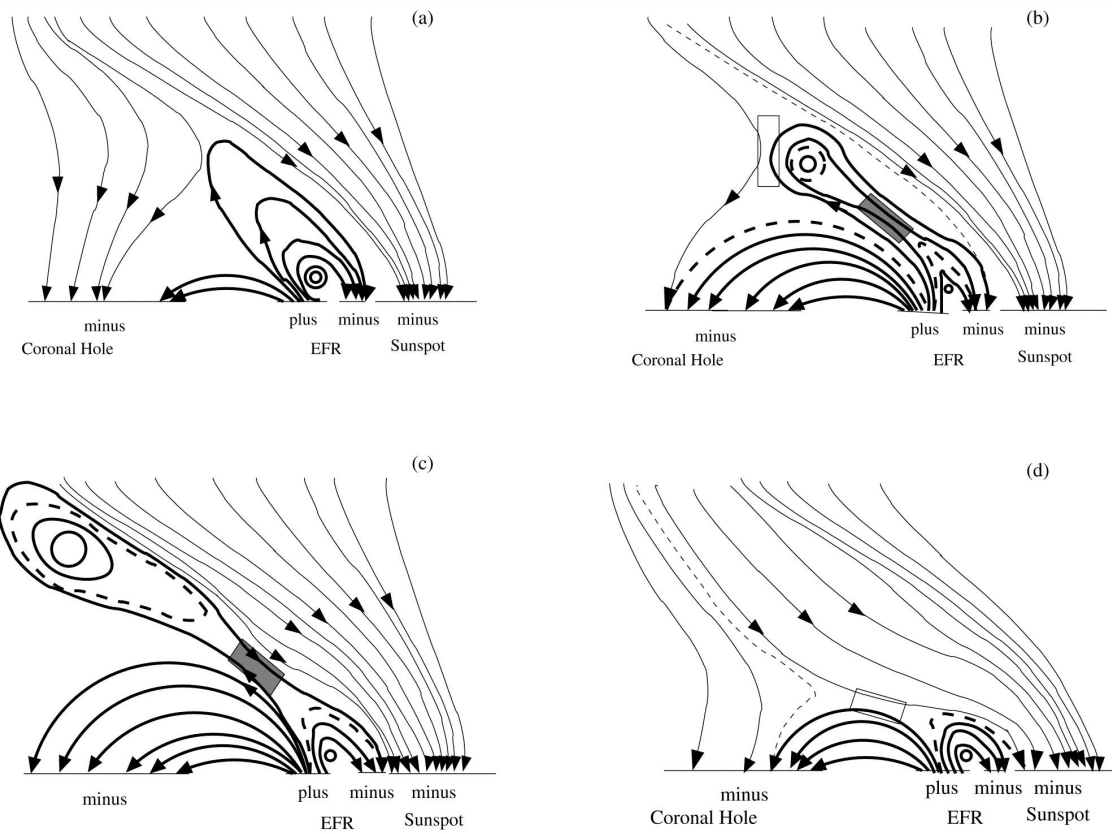


Figure 8.35: Emerging flux region (EFR) meets coronal hole field lines and creates outer reconnection, followed by inner reconnection (Sterling et al. 2001).

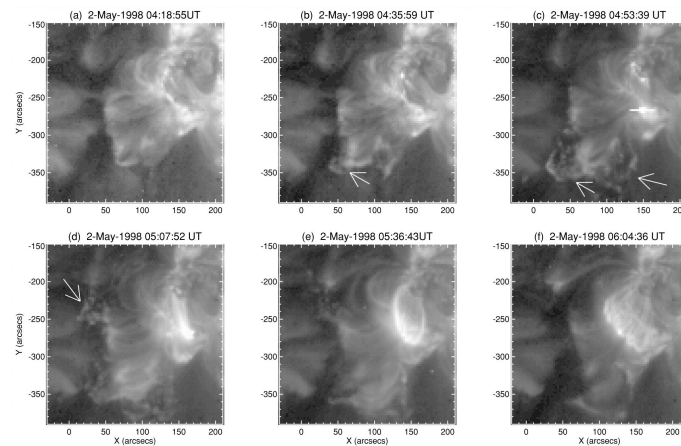


Figure 8.36: EIT crinkles would then be caused by the heated plasma and enhanced density region that is pushed toward the coronal hole (Sterling et al. 2001).

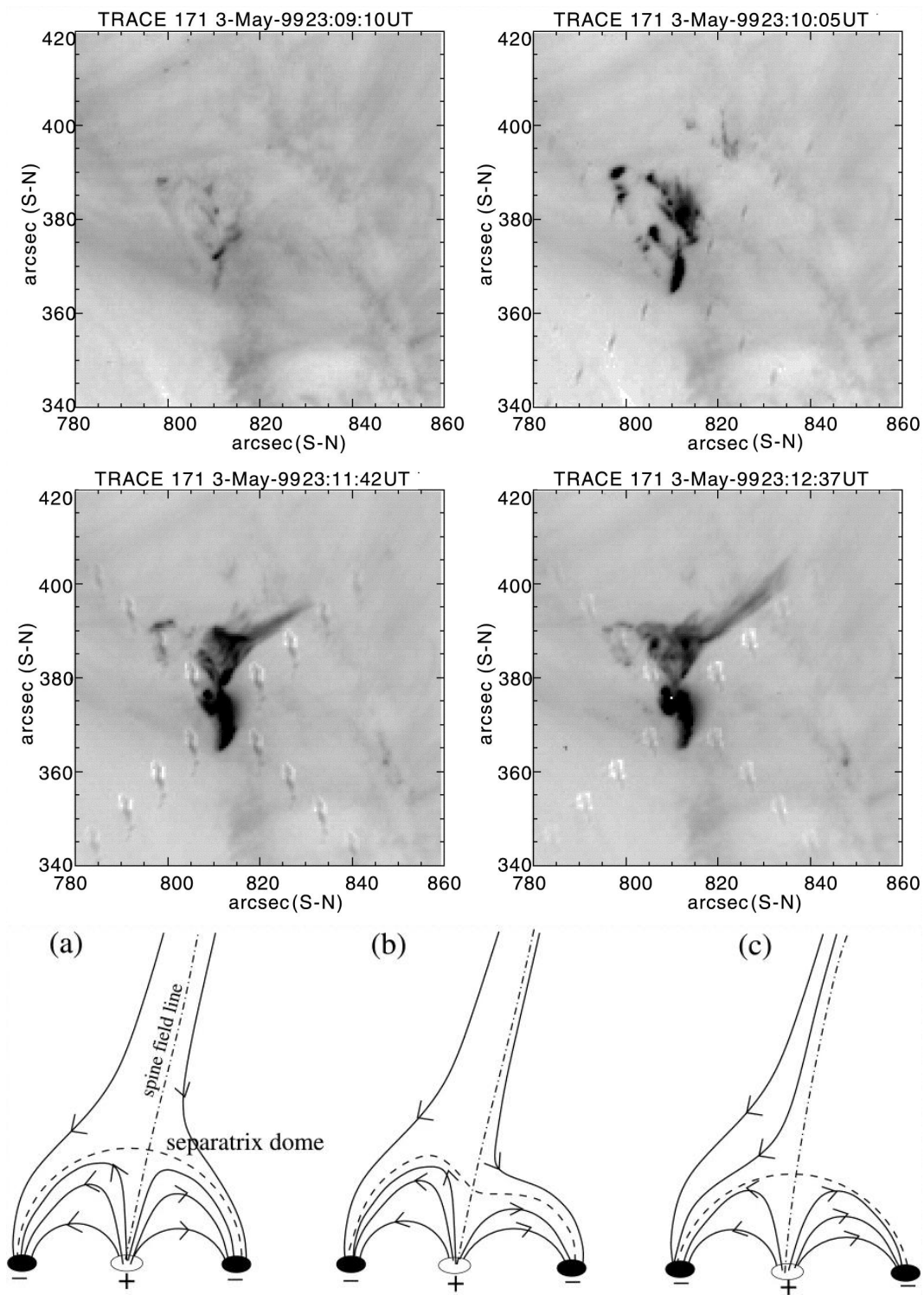


Figure 8.37: Creation of plasma jets: TRACE 171 Å images of the flare site made around the impulsive phase. Near the time of the HXR impulsive phase the TRACE emission is confined to a few bright kernels; shortly thereafter, the kernels disappear, a small loop brightens, and material ejection starts. Two-dimensional representation of the process of reconnection via a separator dome (Fletcher et al. *Astrophysical Journal*, 2001)

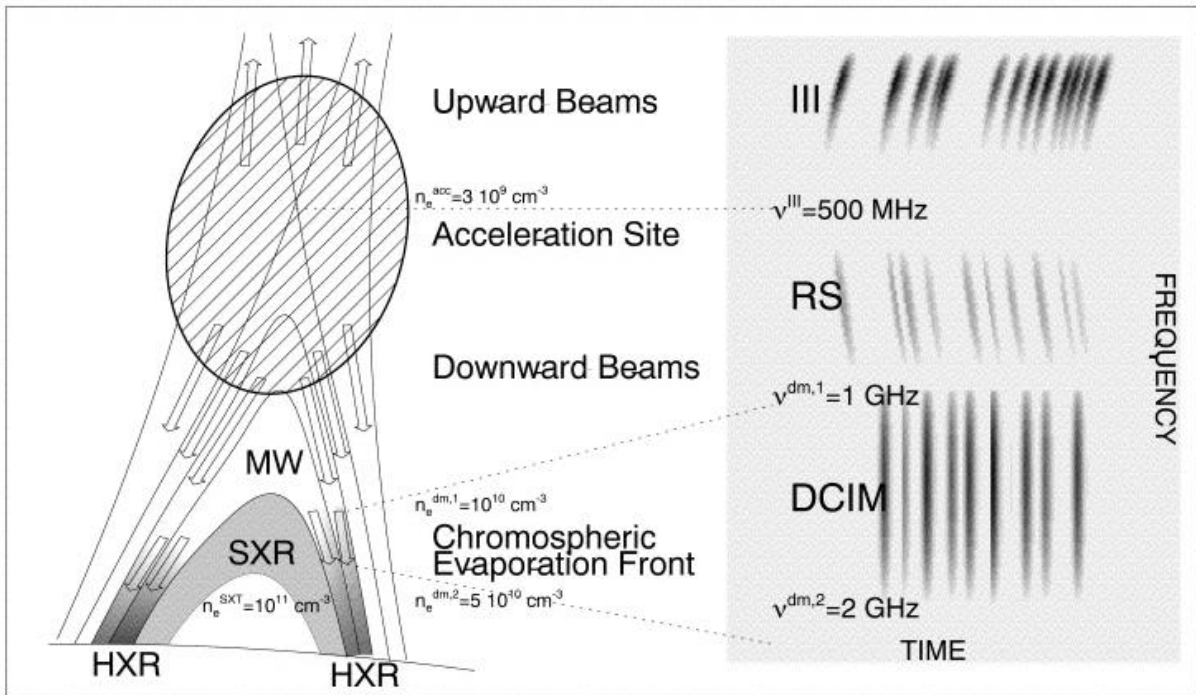


Figure 8.38: Diagram of a flare model envisioning magnetic reconnection and chromospheric evaporation processes in the context of electron density measurements. The panel on the right illustrates a dynamic radio spectrum with radio bursts indicated in the frequency-time plane. The acceleration site is located in a low-density region (in the cusp), from where electron beams are accelerated in upward (type III) and downward (RS bursts) directions (Aschwanden & Benz, ApJ 480, 1997).

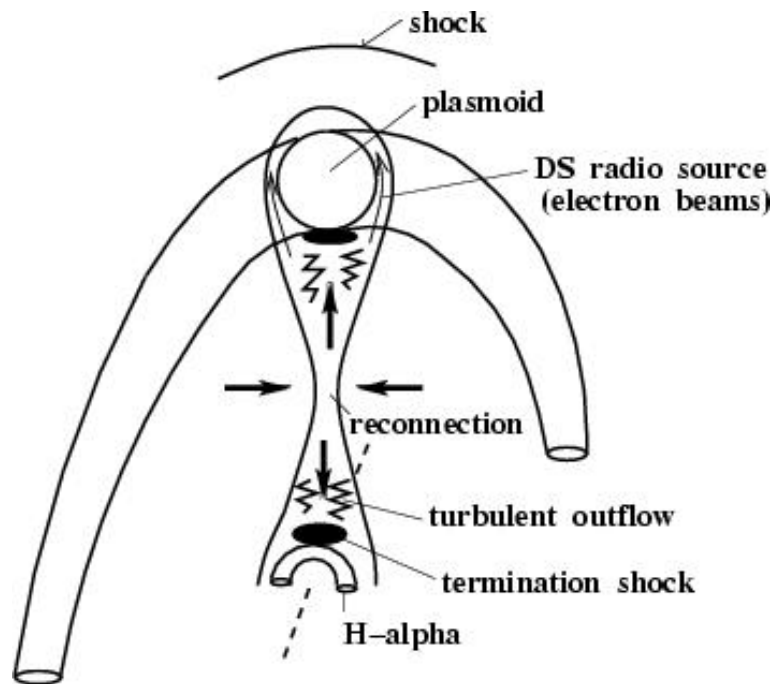


Figure 8.39: Decimetric radio sources (Karlicky, 2004).

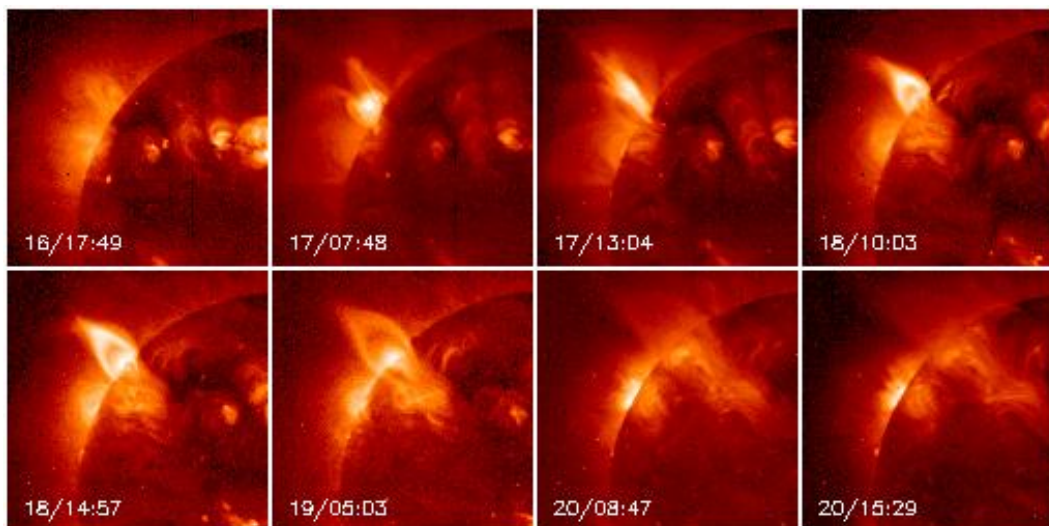


Figure 8.40: Long duration cusp-like sources - no reconnection?

8.5 Accelerated particles

The basic principle of the thick-target model is that the observed hard X-rays result from bremsstrahlung emitted by a beam of electrons accelerated in the corona, but then "precipitating" into the dense atmosphere where they stop collisionally (via Coulomb collisions). The term "thick target" describes just this property of collisional termination of a particle beam. The resulting X-ray spectrum has a fixed dependence on the beam properties. That simplification is one of the model's virtues, permitting an easy use of inverse theory to learn about the (assumed) electron beam. (See more from the RHESSI Science Nugget by Lyndsay Fletcher and Hugh Hudson, at http://sprg.ssl.berkeley.edu/~tohban/nuggets/?page=article&article_id=44)

- Thick target: Double-footpoint, need 10^{37} electrons per second to explain the HXR emission (typical loop 10^{37} electrons!)
- Thin target: Superhot thermal source $> 10^8$ K (Masuda-flare)

HXR thin target – thick target

$$E^{\delta_{thin}} : \quad \delta_{thin} = \gamma - 0.5 \quad (8.1)$$

$$E^{\delta_{thick}} : \quad \delta_{thick} = \gamma + 1 \quad (8.2)$$

where γ is the photon power-law index (Brown, 1971).

Practical example:

observed photons with $\epsilon = 70$ keV \rightarrow mean energy of electrons

E_x thin-target = 100–130 keV

E_x thick-target = 120–180 keV

Comparison:

Outstreaming electrons in type III bursts have velocities between 0.1c and 0.5c, meaning sub-relativistic electron energies of 2–80 keV.

Gyrosynchrotron radio – HXR

$$N(E) \propto E^{-x} \quad \text{Electron energy spectrum} \quad (8.3)$$

$$I(\nu) \propto \nu^{\alpha_r} \propto \nu^{-(x-1)/2} \quad \text{Gyrosynchrotron radiation} \quad (8.4)$$

$$N_x(\epsilon) \propto \epsilon^{\alpha_x} \propto \epsilon^{-(x+1/2)} \quad \text{X-ray emission} \quad (8.5)$$

$$\alpha_r = 0.5\alpha_x - 0.75 \quad (8.6)$$

These are general relations – no model assumptions, gyrosynchrotron is optically thin, no directional effects assumed (Longair: High-energy Astrophysics)

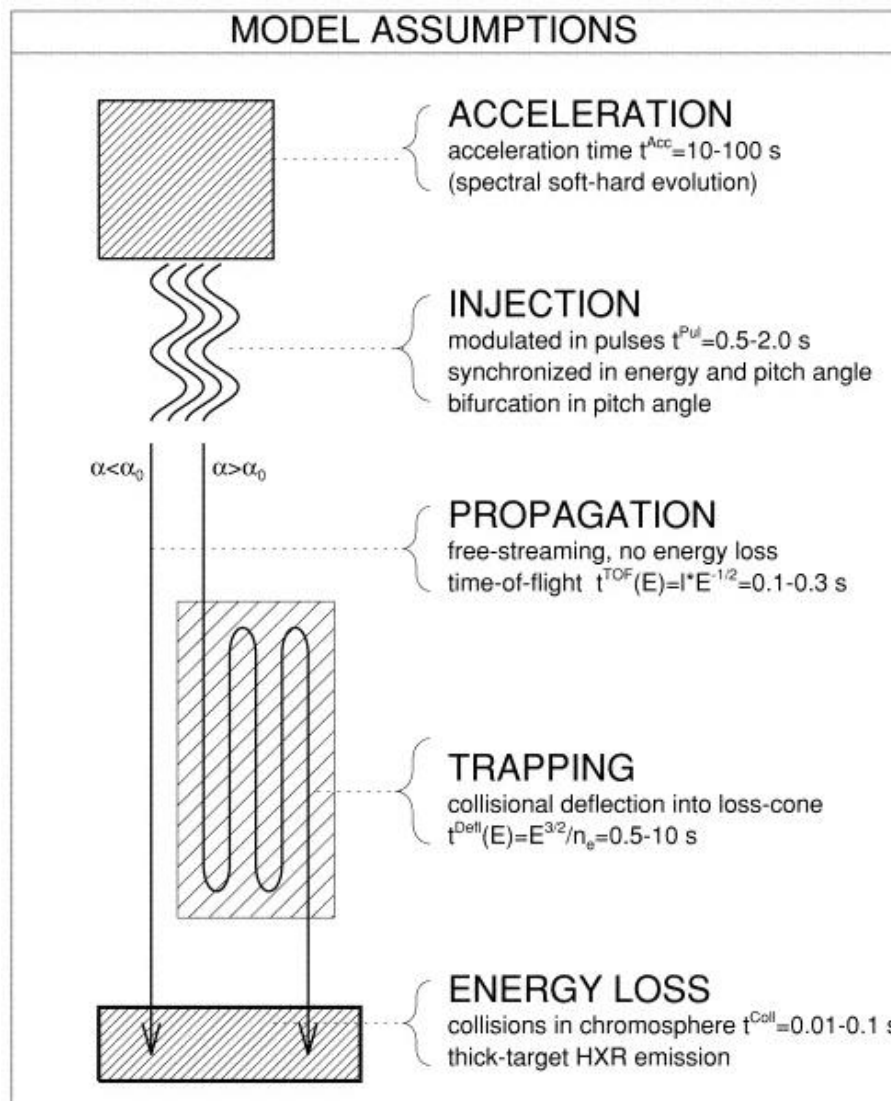


Figure 8.41: Summary of model assumptions used in the deconvolution method of hard X-ray time profiles (Aschwanden, 1998)

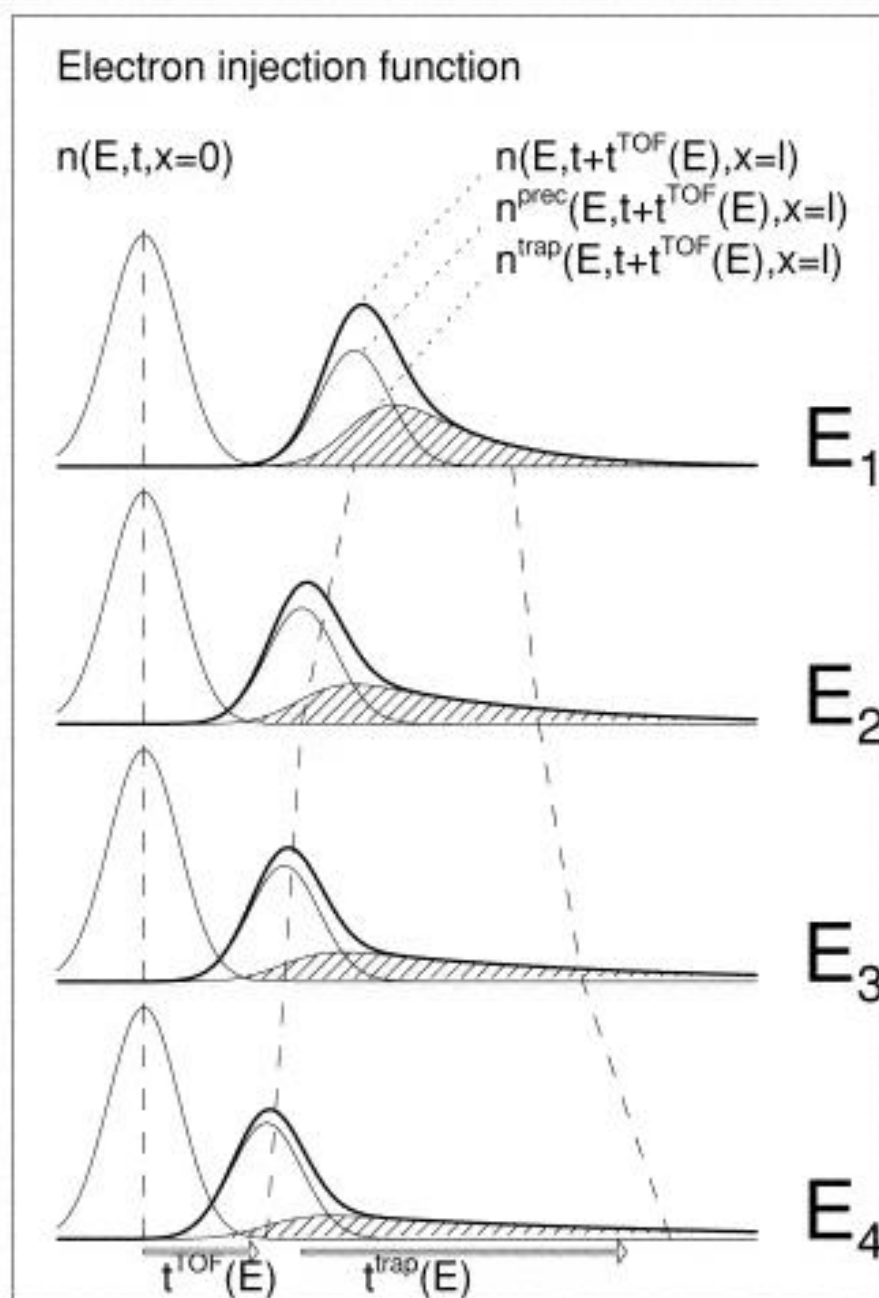


Figure 8.42: Temporal relation of the electron injection function $n(E, t, x=0)$ at the injection site and at the HXR emission site $n(E, t + t^{TOF}(E), x = l^{TOF})$, delayed by an energy-dependent electron time-of-flight interval $t^{TOF}(E)$, schematically shown for four different energies $E_1 < E_2 < E_3 < E_4$. The injection function at the HXR emission site (thick curve) is broken down into a directly precipitating component (thin curve) and the trap-precipitating component (hatched area). Note that the (e-folding) trapping time $t^{trap}(E)$ increases with energy E , whereas the time-of-flight delays $t^{TOF}(E)$ decreases.

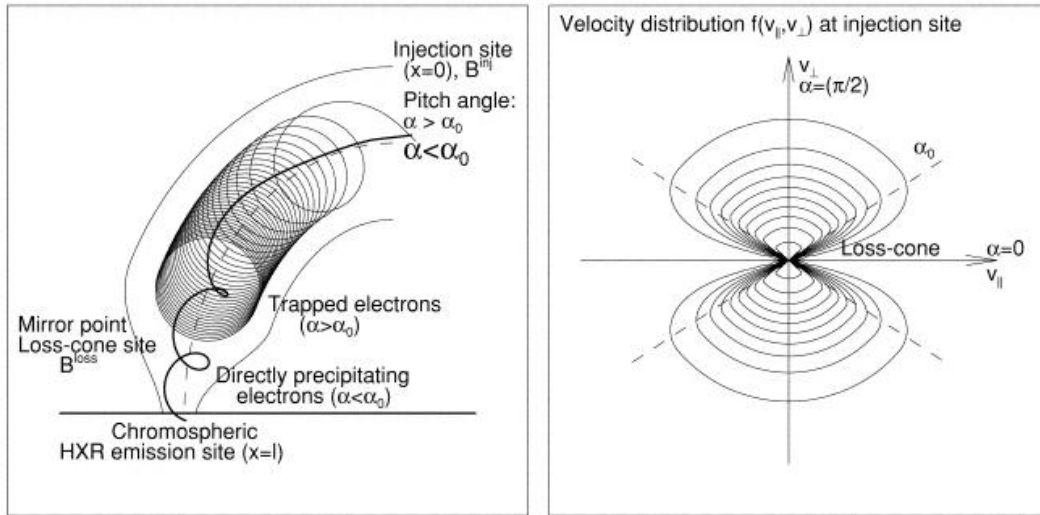


Figure 8.43: Spatial configuration of injection site, loss cone site, and HXR emission site in a flare loop. Electrons with small initial pitch angles precipitate directly, while electrons with large pitch angles become temporarily trapped. Right: The velocity distribution at the injection site has a loss cone for pitch angles $\alpha \leq \alpha_0$. (Aschwanden, ApJ 1998)

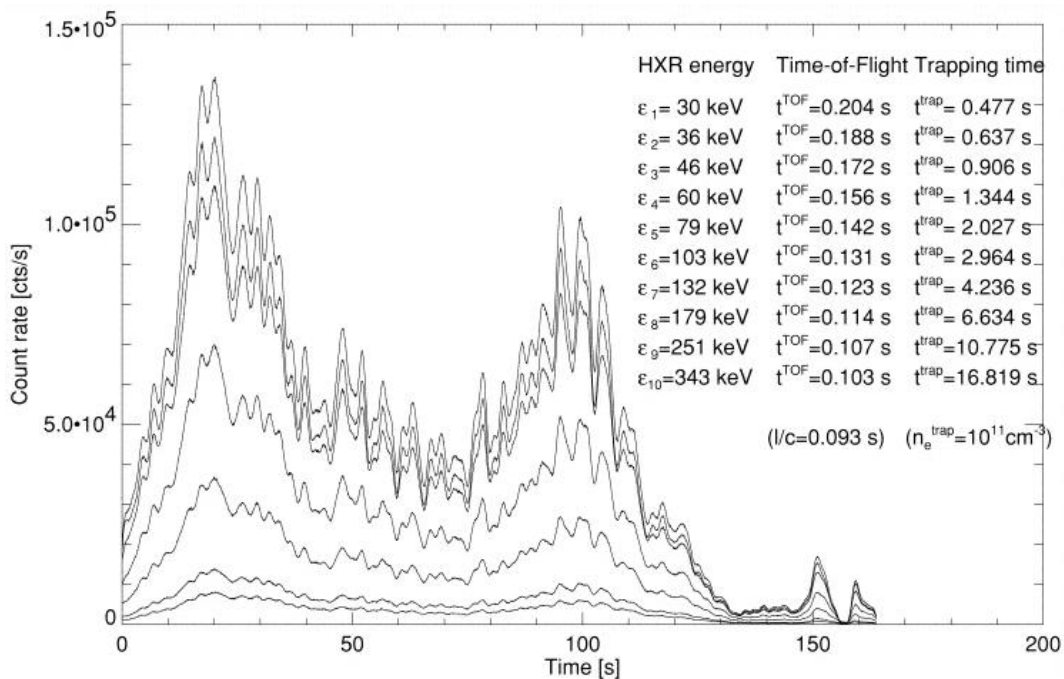


Figure 8.44: Simulated data set of HXR time profiles $I(\epsilon, t)$ for 10 energy channels (ϵ_i , $i = 1, \dots, 10$). The first channel is taken from observed BATSE/MER count rates of the solar flare 1991 November 13, 21:15:55 UT, while the time profiles of the other channels were convolved with TOF delays (occurring over a projected distance of $l = 15,000$ km) and trap delays (based on collisional deflection times in a plasma with an electron density of $n_e = 10^{11} \text{ cm}^{-3}$). The fluences of all channels are scaled proportionally to the fluences of the observed BATSE/MER channels. Data noise on timescales of 1 s has been filtered out with a Fourier filter.

Chapter 9

Coronal mass ejections

9.1 Basic concepts and observational constraints

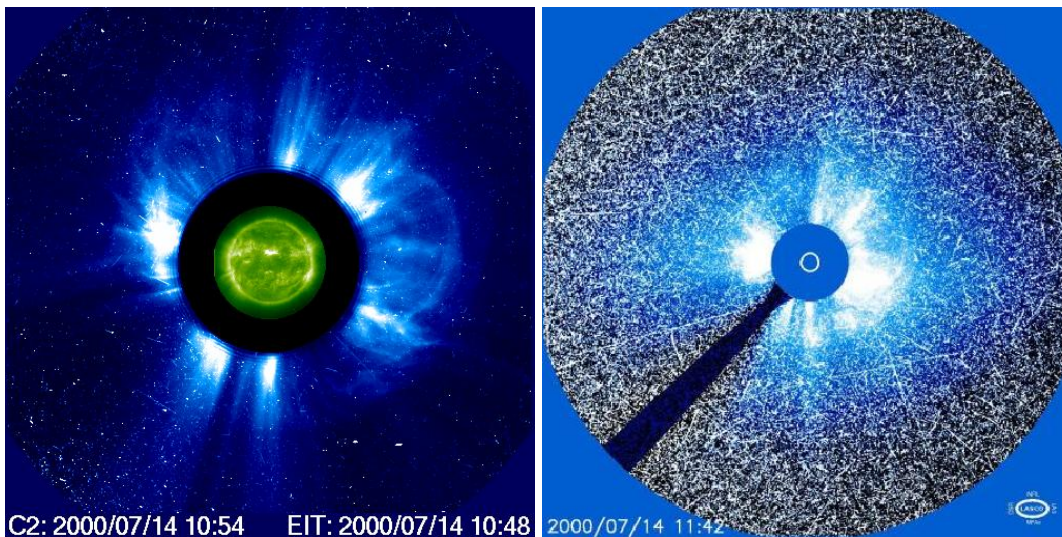


Figure 9.1: CMEs are observed with coronagraphs that block emission from the bright solar disk (SOHO LASCO images).

CME characteristics:

- Observed in white light (Thomson scattering of sunlight from electrons)
- Observed CME speeds $\sim 10 - 3000$ km/s
- Typical CME mass $2 \times 10^{14} - 4 \times 10^{16}$ g
(solar mass 2×10^{33} g)
- Different sizes and shapes
- Activity maximum: several CMEs per day
Activity minimum: one per week or less

For speed determination, we need to

- define the CME front
- consider that these are plane-of-the-sky observations
- remember that CME speed consists of expansion velocity + propagation velocity

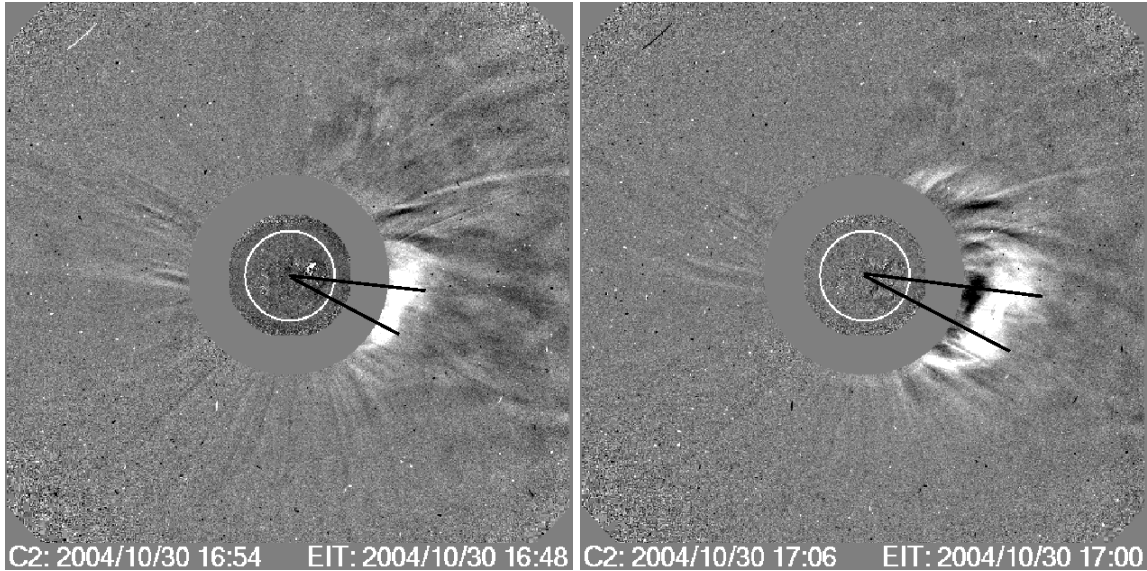


Figure 9.2: Consecutive CME difference images for CME front speed determination.

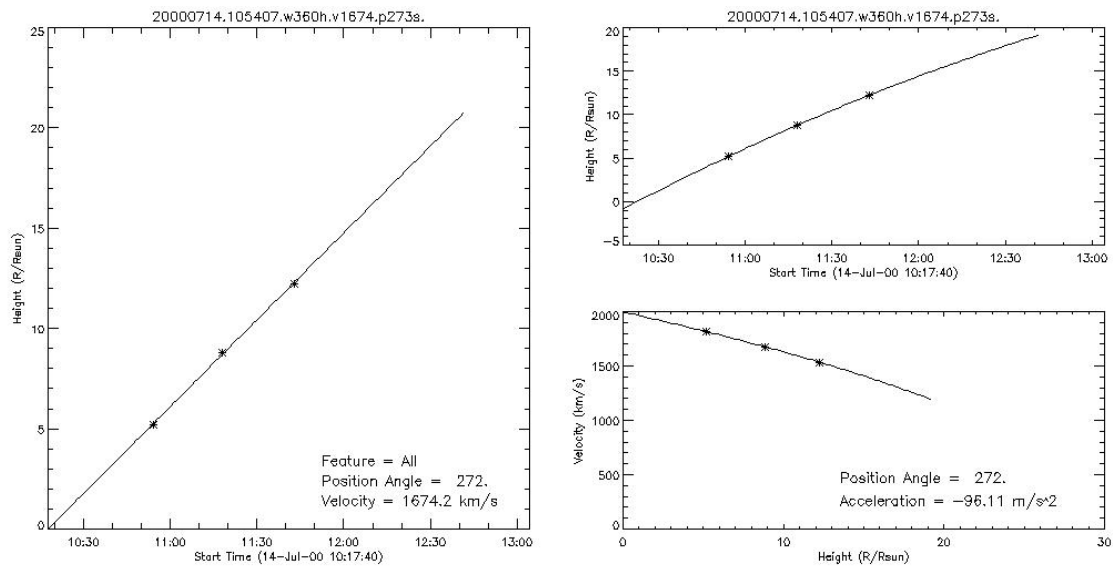


Figure 9.3: Height-time plot from the LASCO CME Catalog (on the left), and the estimated speed based on a second-order fit (on the right). The solar limb is at $R = 1 R_{\odot}$.

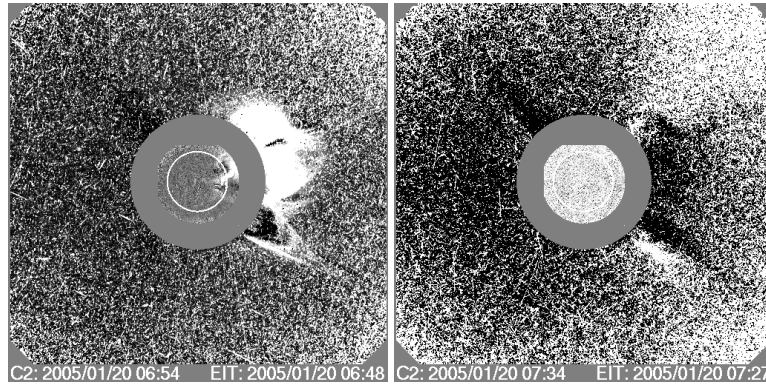
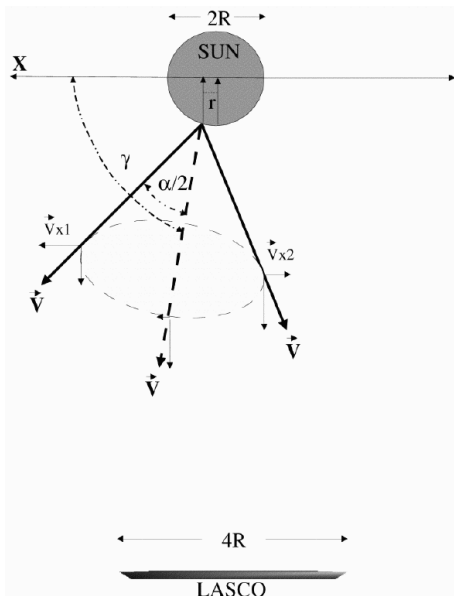


Figure 9.4: In many cases we simply lack good data: Halo CME first observed at 06:54 UT, flare X7.1 in AR N14W61, protons and lots of particle hits (left). However, the next available image (right) does not give much information.



By simple inspection we see from [Figure 1](#) that on the left (eastern) side of the occulting disk, the CME has to travel a distance $2R - r$ with velocity V_{x1} to appear in coronagraph at time T_1 such that

$$T_1 = \frac{(2R - r)}{V_{x1}} .$$

Similarly, the CME will appear on the right (western) side of the occulting disk after a time

$$T_2 = \frac{(2R + r)}{V_{x2}} .$$

From these equations, we determine the time difference

$$\Delta T = T_2 - T_1 = \frac{(2R + r)}{V_{x2}} - \frac{(2R - r)}{V_{x1}} . \quad (1)$$

From the geometry of the CME shown in [Figure 1](#), we get rest of the necessary equations:

$$\cos(\gamma) = \frac{r}{R} , \quad (2)$$

$$\cos\left(\gamma - \frac{\alpha}{2}\right) = \frac{V_{x1}}{V} , \quad (3)$$

$$\cos\left(180^\circ - \gamma - \frac{\alpha}{2}\right) = \frac{V_{x2}}{V} . \quad (4)$$

We have four equations and four parameters to determine r , α , V , and γ . The inputs V_{x1} , V_{x2} , and ΔT need to be obtained from observations. In our considerations, we use data from the *SOHO*/LASCO C2 coronagraph with a

Figure 9.5: Michalek et al. 2003: velocity estimates for halo CMEs that have constant velocities, are symmetric, and propagate with constant angular widths.

- Michalek et al. 2003: A New Method for Estimating Widths, Velocities, and Source Location of Halo Coronal Mass Ejections (*ApJ* 584, 472)
- Michalek 2006: An Asymmetric Cone Model for Halo Coronal Mass Ejections (*Solar Physics*, Vol. 237, 101)
- Michalek et al. 2009: Expansion Speed of Coronal Mass Ejections (*Solar Physics*, Vol. 260, 401)
- Michalek 2010: Is the Asymmetric Cone Model for Halo Coronal Mass Ejections Correct? (*Solar Physics*, Vol. 261, 107)

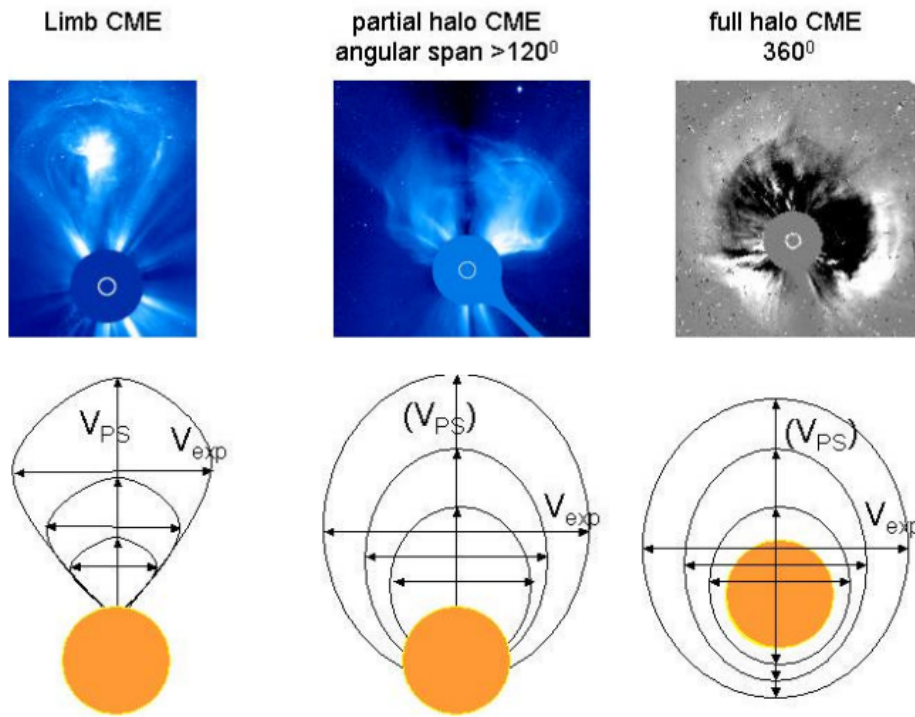


Figure 9.6: Expansion speed (V_{exp}) can be determined for all types of CMEs while the apparent plane-of-the-sky speed (V_{PS}) contains an unknown speed component towards the observer (Schwenn et al. Ann. Geophys., 23, 1033, 2005).

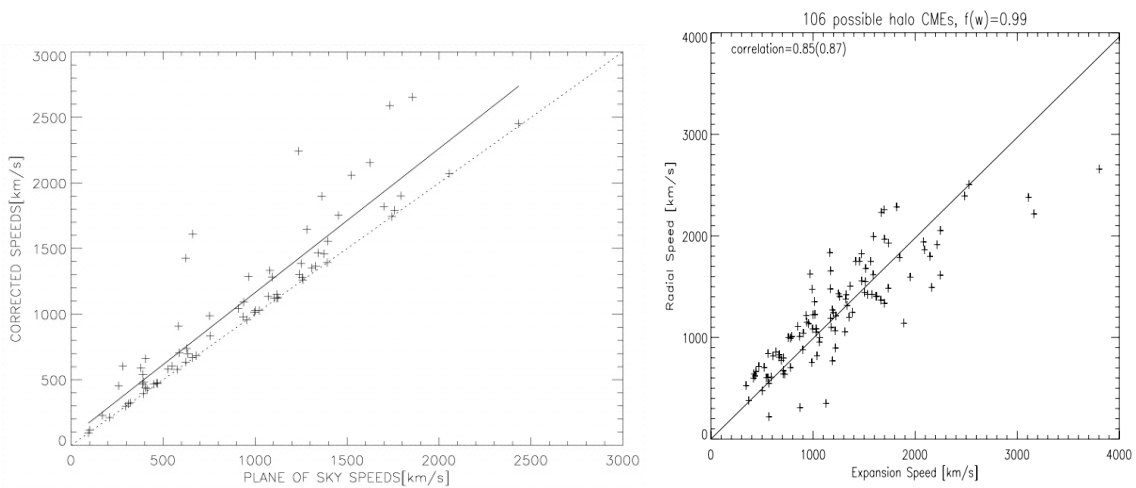


Figure 9.7: Left: plane-of-sky speeds vs. corrected (real) speeds. The solid line shows the linear fit to the data (Michalek et al., 2003). Right: expansion speed (rate of change of the lateral dimension of a CME at its widest part) vs. radial speed (Michalek et al., 2010).

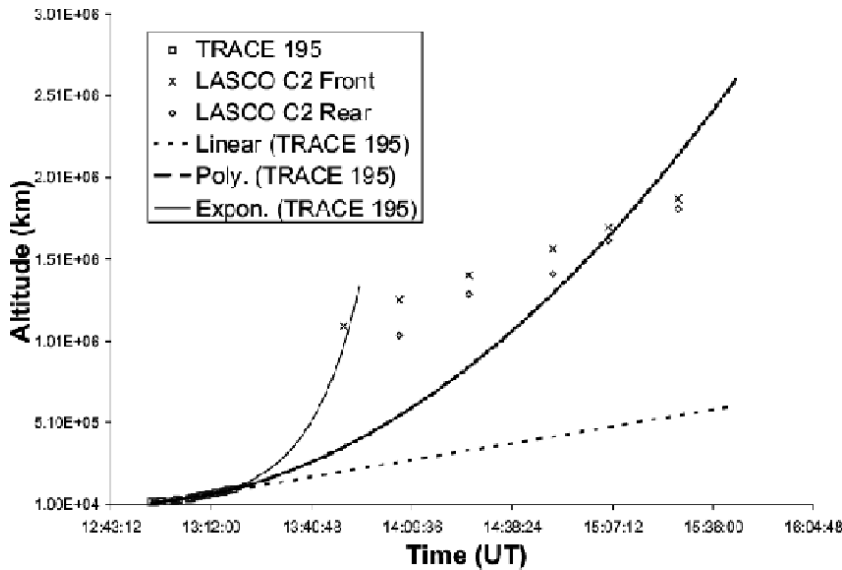


Figure 9.8: CME height-times indicate velocity changes that are difficult to account for (Goff et al., A&A 434, 761, 2005)

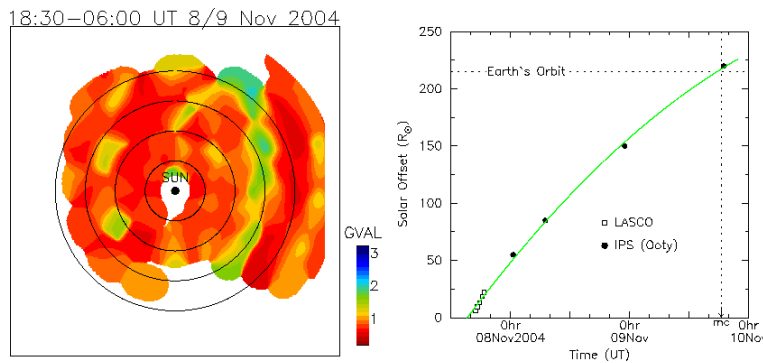


Figure 9.9: At larger distances from the Sun, radio scintillation experiments become useful in estimating CME locations (figures from Manoharan and Pohjolainen et al., 2007).

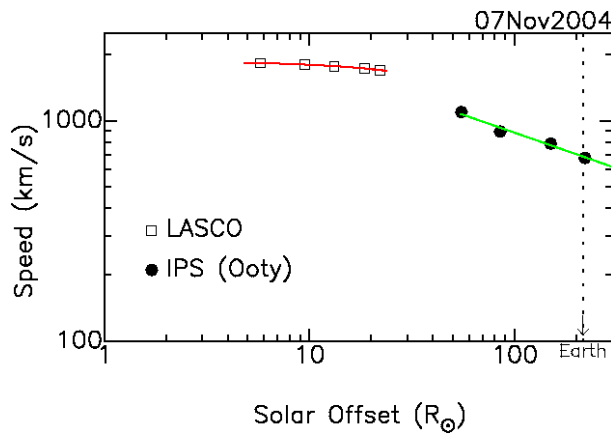


Figure 9.10: Atmospheric drag – or a push when the CME velocity is low and the solar wind speed is high – play a role CME velocity changes

Intensity scintillations of compact radio sources (galaxies or quasars having angular diameter of < 0.5 arcsec) are produced by the density fluctuations in the solar wind plasma. The presence of solar wind transients (e.g., CMEs) can be identified by the enhanced g-values (normalized scintillation index) which are due to the increase in the density-fluctuation (i.e., turbulence) level. Radio observations are made in Ooty (India) and Nagoya (Japan) at 327 MHz (Manoharan et al. 2001).

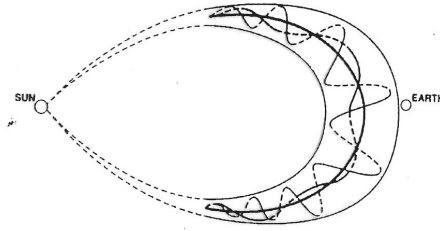


Figure 9.11: The footpoints of magnetic clouds can stay attached to the Sun quite a long time after eruption (Kallenrode, Space Physics).

Questions related to flares and CMEs:

- How does the energy needed for eruption build up? (observations of 'inflow'?)
- How does the magnetic field open up? (from the inside or the outside?)
- What can affect the particles/magnetic clouds during their travel? (solar wind anisotropies, CME interaction, etc.)

There are still open issues:

- There are CMEs with and without flares
- Filament eruptions do not always produce CMEs
- CME speeds are surprisingly different: 10...3000 km/s
- CMEs can accelerate/decelerate suddenly
- Energetic particles (observed in situ near Earth) are produced somewhere along the processes (flare-accelerated vs. CME-accelerated)

and questions to be answered:

- How do filaments and flares fit in the picture of CME formation?
What is the cause and what are the effects?
- Can we really say when a CME "starts"?
- The old classification, filament eruption -> slow CME, and flare -> fast CME, can be questioned?
- When and how do CMEs accelerate/decelerate?
In the SOHO era there has been an observational gap between $1.3-2.1 R_{sun}$, but STEREO observations could now give some more information.

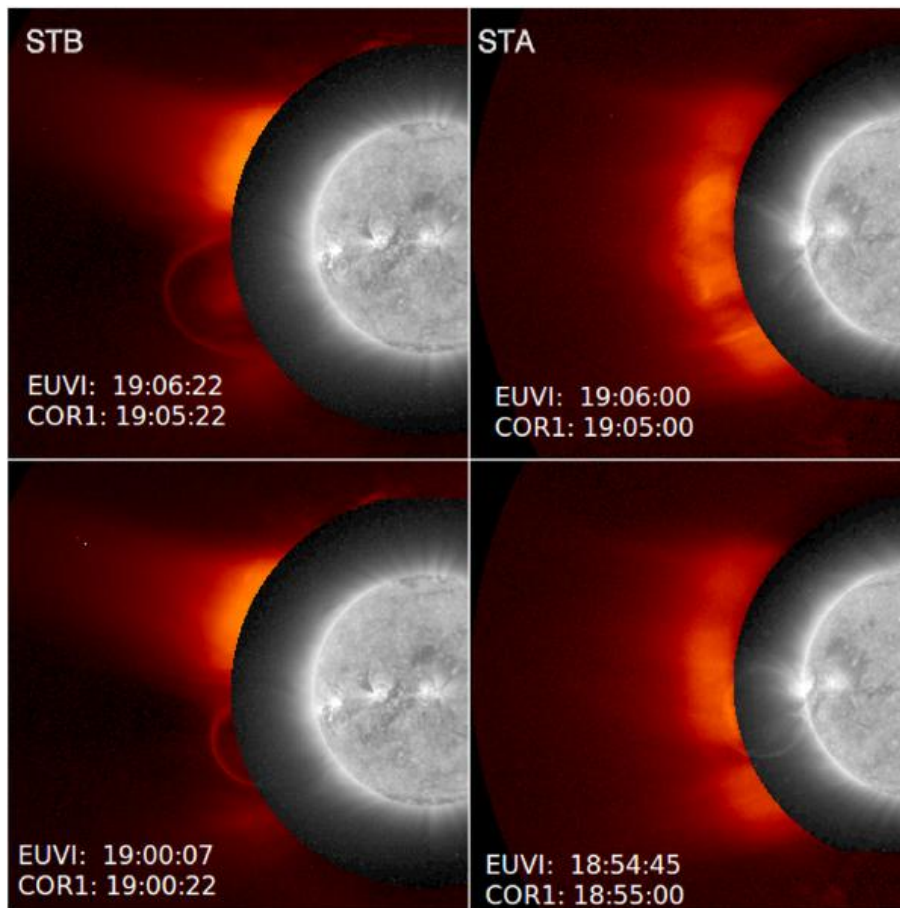


Figure 9.12: STEREO A and B observations of the emergence of an EUVI bubble into the COR1 field of view, where it becomes the cavity of a typical three-part CME (Patsourakos et al. A&A 522, 2010).

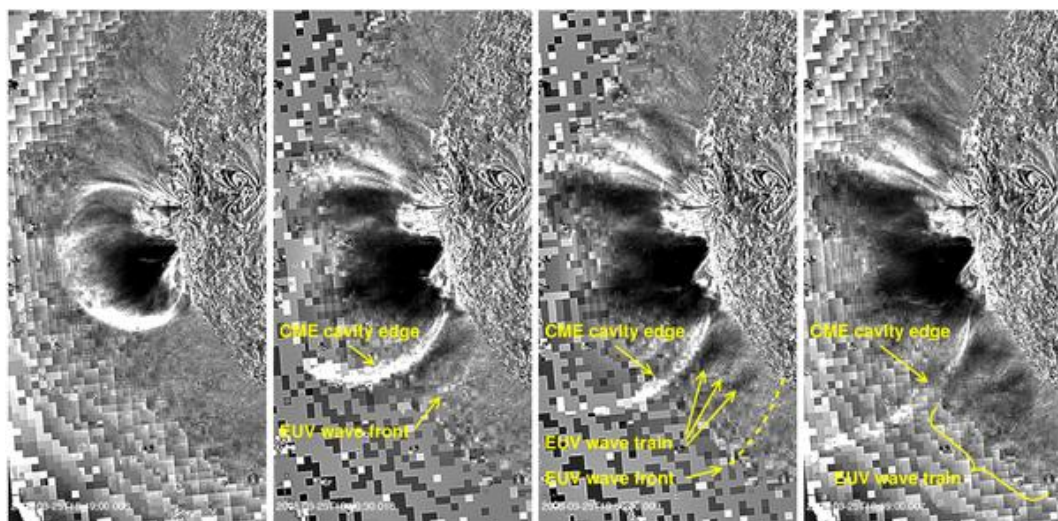


Figure 9.13: Launch of an EUV wave by the horizontal (over)expansion of the CME cavity (Patsourakos et al. A&A 522, 2010).

9.2 Dimmings

Dimming regions are identified by their strong depletion in coronal EUV emission within \sim half hour of the estimated time of CME lift-off. They include areas which are as dark as quiescent coronal hole areas, as well as other regions with weaker brightness depletions. The extended dimming areas in analysed events generally map out the apparent “foot-print” of a CME, as observed by white-light coronagraphs (see more details in Thompson et al., Geophysical Research Letters, 2000).

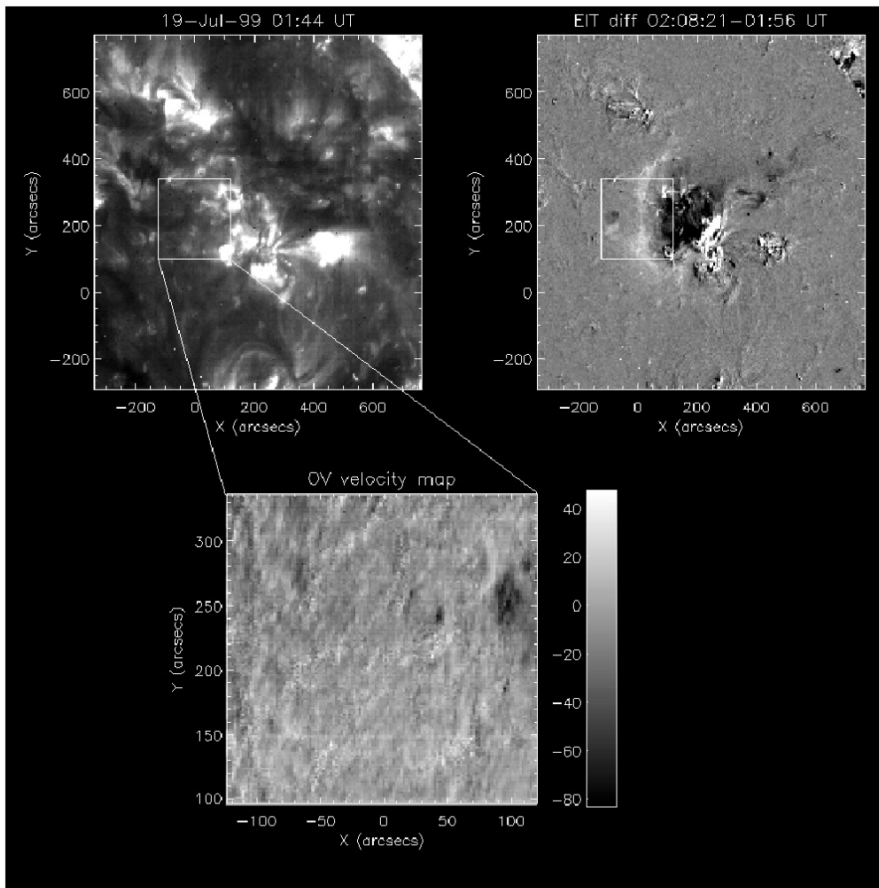


Figure 9.14: Evidence of CME launch: rising material is observed in blueshift in chromospheric spectral lines (Harra & Sterling, 2001)

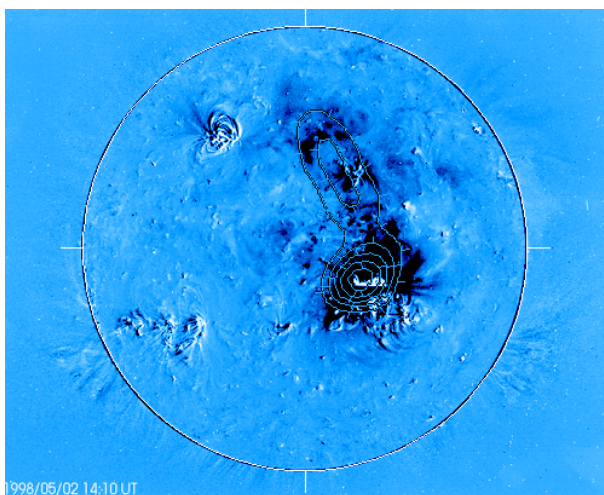


Figure 9.15: Radio sources have been found to match with disappearing features: in this case radio type IV emission (interpreted as emission from trapped particles within a magnetic cloud) was observed over an EUV dimmed region (Pohjolainen et al., 2001)

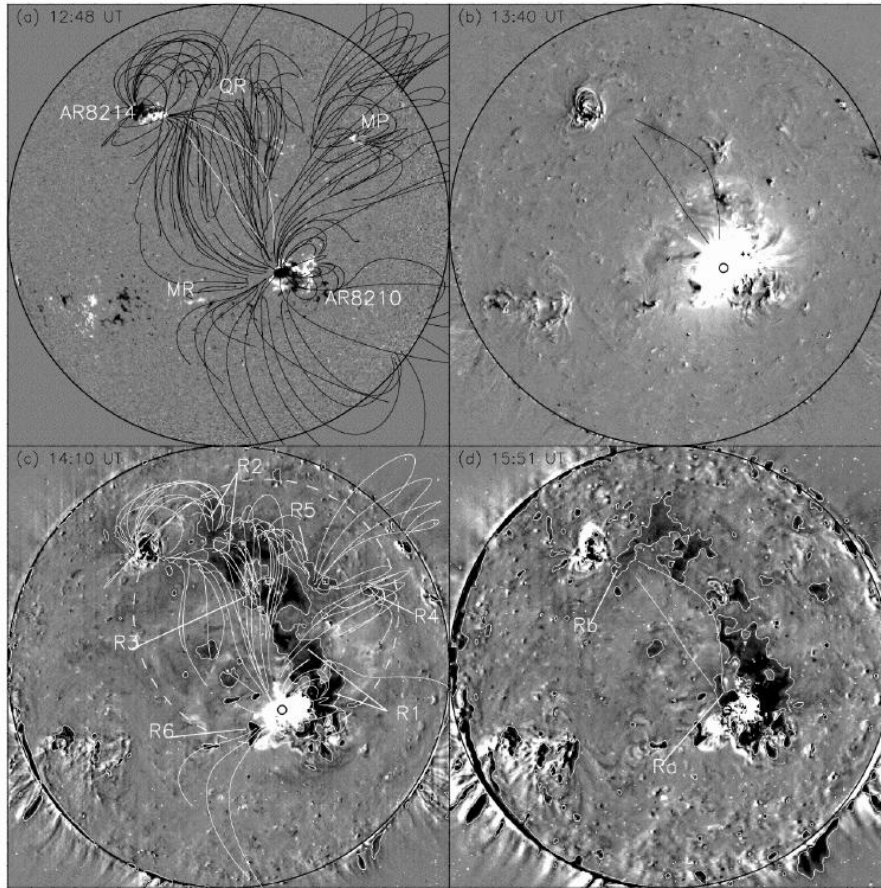


Figure 9.16: Magnetic field extrapolations verify the locations and connections of loops which are later found to disappear (Wang et al., 2002). Remember that structures are visible only if their temperatures and densities fall within those of the observing instruments.

The sudden dimming of parts of the corona, as observed in soft X-rays, can be recognized as (see Yohkoh Science Nugget December 10, 1999, by Hugh Hudson):

- Transient coronal holes (discovered with Skylab observations)
- Above-the-arcade dimming
- Enveloping dimming
- Moving cloud
- Disappearing trans-equatorial (large-scale) loops

Disappearance may also mean that the structure expands (electron density decreases) and cools down, and therefore it is no longer detected by the instrument. We can estimate the time scales with

$$\tau_{rad} = \frac{3kT}{\Lambda n_e} \sim 10^5 \text{ s} \sim 1\text{day}, \quad (9.1)$$

$$\Lambda = 3 \times 10^{-23} \text{ erg cm}^3 \text{ s}^{-1},$$

$$\tau_{cond} = \frac{2nk l^2}{\kappa_0 T^{2.5}} \sim 10^4 \text{ s} \sim 3\text{hours}, \quad (9.2)$$

$$\kappa_0 = 10^{-6} \text{ erg (cm K}^{3.5}\text{)}^{-1}.$$

Mass estimate for the moving and disappearing soft X-ray cloud was 4×10^{14} g, which corresponds to a small coronal mass ejection. The observed movement was ~ 100 km/s (too slow to create any shock waves). The observed timescale for the disappearing SXT structure was $< 3 \times 10^3$ s (uncertainty due to Yohkoh entering satellite night time at the wrong moment!), so the disappearance could not be due to heat transfer by radiation or conduction.

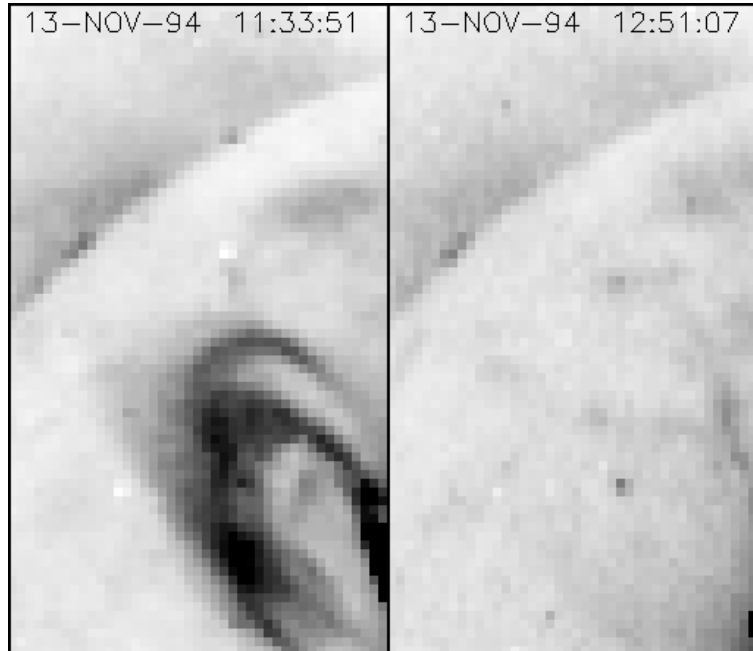


Figure 9.17: Disappearing SXT cloud (H. Hudson, Yohkoh Science Nuggets)

9.3 CMEs, filaments, type IIs, and flares - all connected?

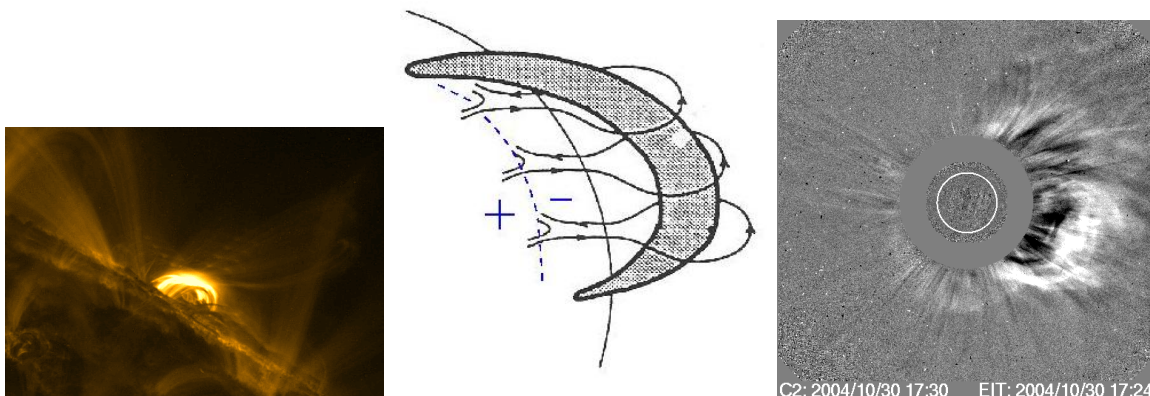


Figure 9.18: Are flares, filament eruptions and CMEs always connected?

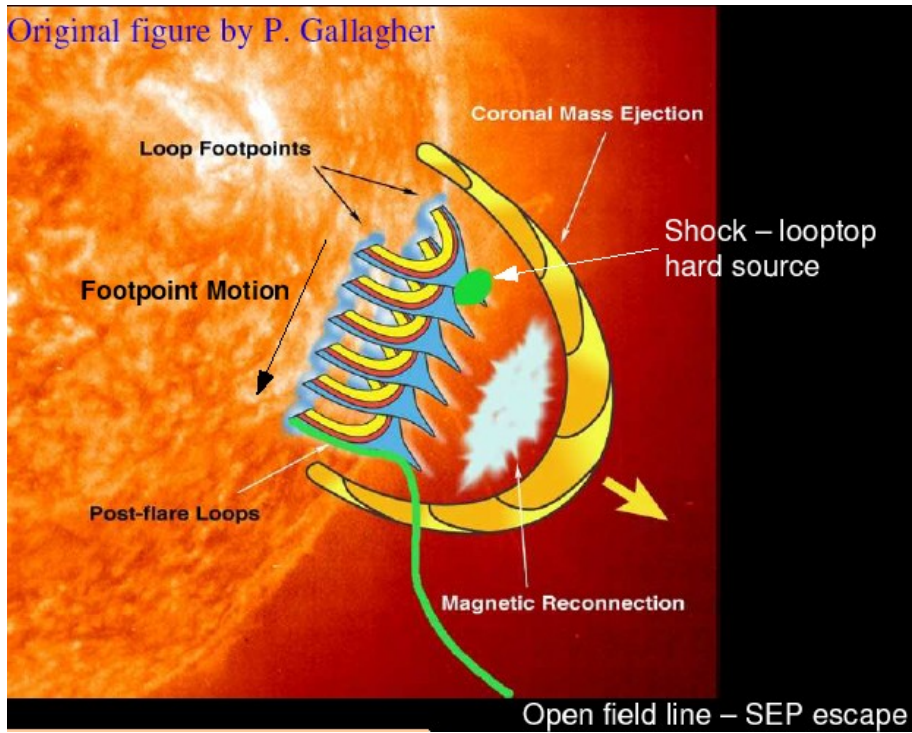


Figure 9.19: Unifield models can explain all features! (Smith & Gallagher, 2004).

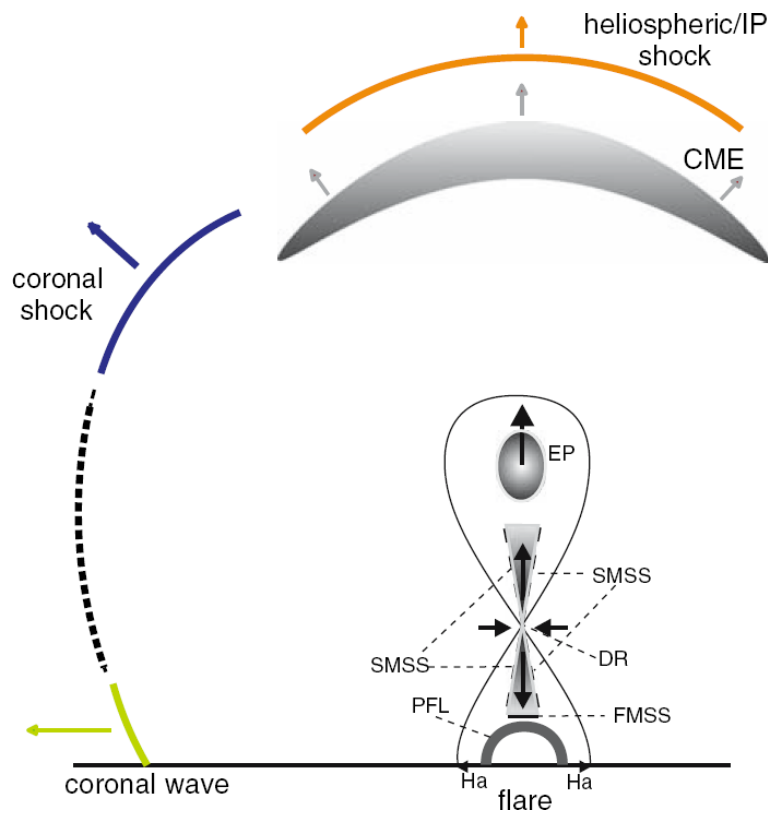


Figure 9.20: ... even shocks? (Warmuth, LNP 2007/ Aurass et al., A&A 2002)

Things to evaluate in type II burst emission:

- Atmospheric density models -> speed from density change
- Scale height + frequency drift -> may give different speed
- Corona: second harmonic stronger
- IP space: fundamental stronger
- Emission lanes can be band-split
- May not be plasma emission at all

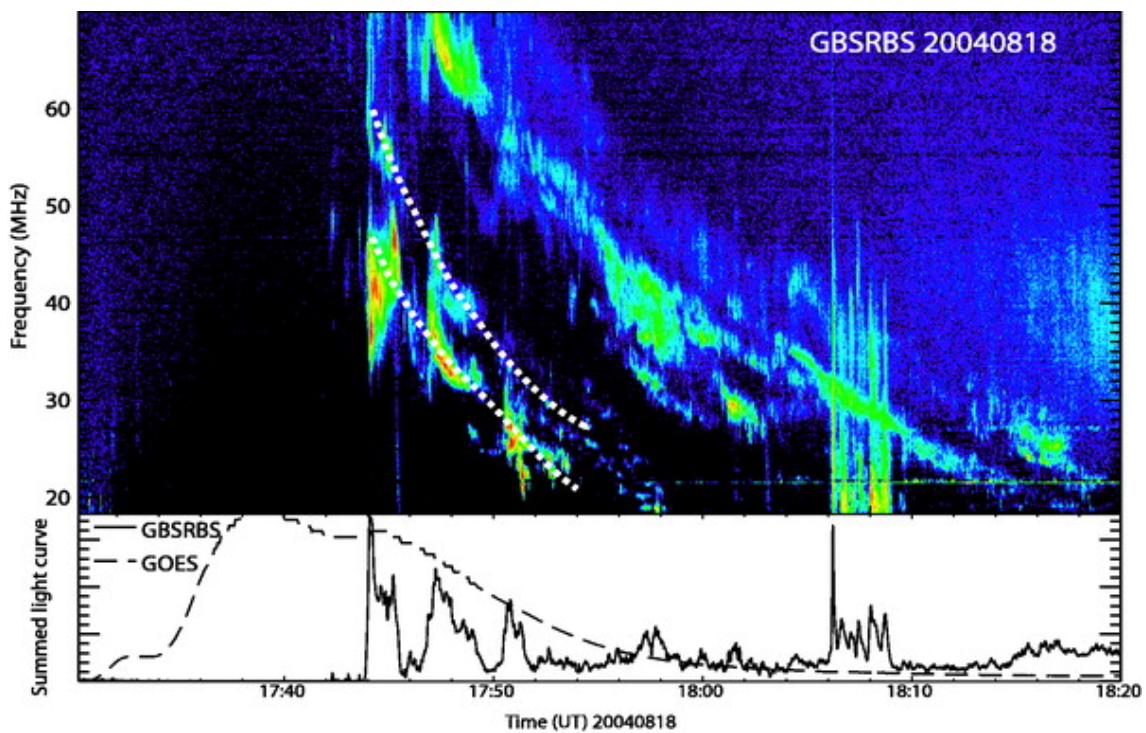


Figure 9.21: Emission at the upper (HFB) and lower (LFB) frequency branches in the fundamental band of the type II burst (dotted lines). Band-split reveals the shock Mach number if it is a consequence of the plasma emission from the upstream and downstream shock region. Shock speed can be inferred from the frequency drift \rightarrow Alfvén velocity and magnetic field can be estimated (Cho et al. ApJ 665, 799, 2007; Vrsnak et al. ESA SP-506, 2002).

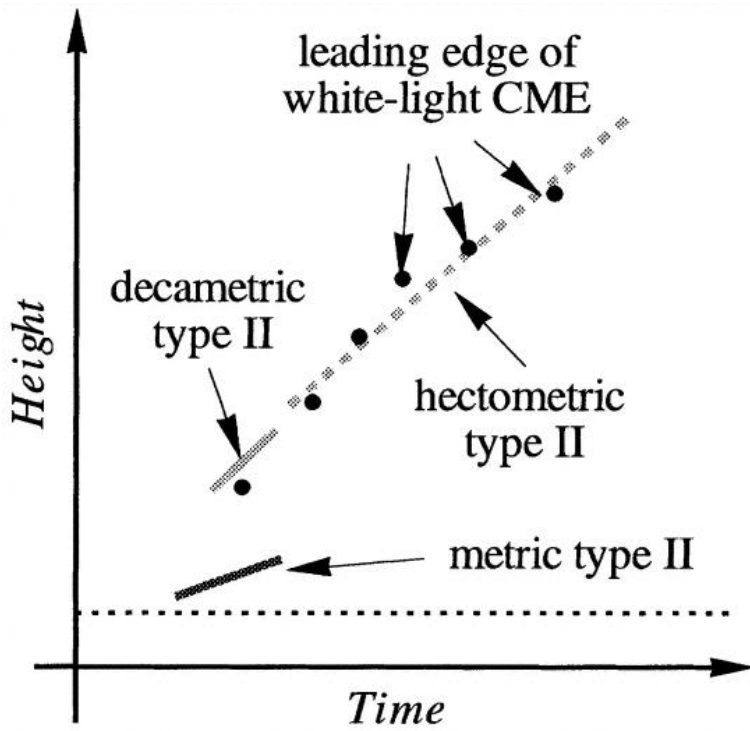


Figure 9.22: A unified model? (Magara et al. ApJ, 538, L175, 2000)

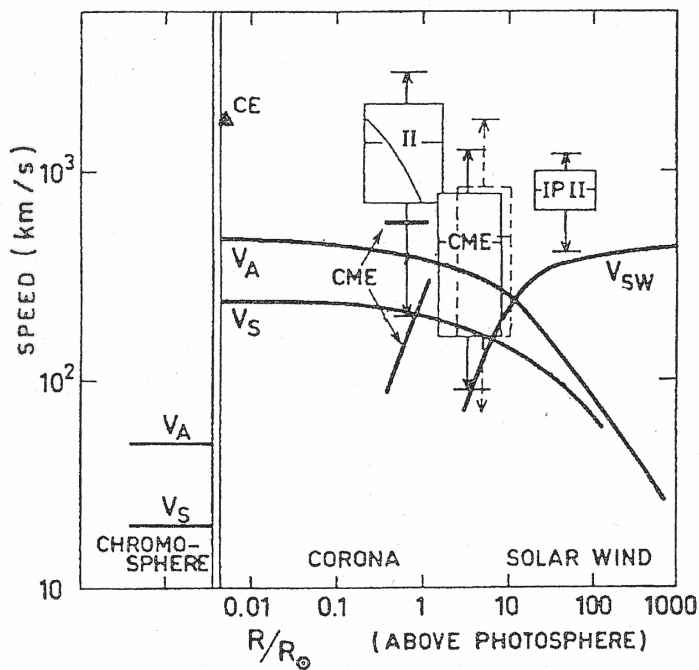


Figure 9.23: Observations of coronal type II, interplanetary (IP) type II, and CME speeds, compared to the Alfven speed, sound speed, and solar wind speed (Kallenrode: Space Physics).

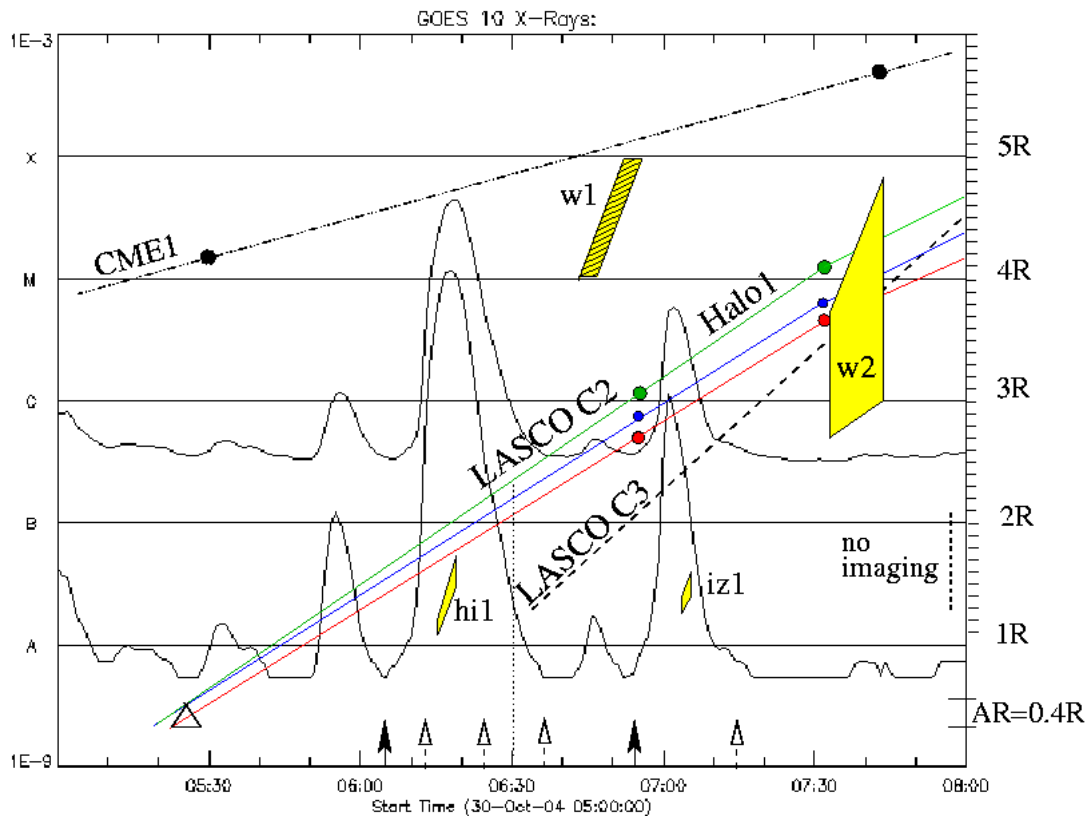


Figure 9.24: There are many studies that try to combine and interpret all available observations. This example from Pohjolainen & Lehtinen (2006) shows data for one halo CME event. The estimated heliocentric CME heights, in solar radii (R) along the selected radials, are plotted over the GOES X-ray flux curve. An extrapolated linear fit on the height-times from the later LASCO C3 observations is also shown. Vertical dotted line shows the time of the earlier LASCO C2 observation when the CME could have been observed if it was within the field of view. The height-times of the preceding CME1 are also shown. Type II burst times and estimated heights (height ranges defined by using 2-fold Newkirk and 2-fold Saito coronal density models) are marked in the plot: "hi1" denotes Hiras observations where fundamental emission starts at 06:15 UT at 150 MHz, "iz1" denotes Izmiran observations where fundamental emission starts at 06:42 UT at 90 MHz, "w1" denotes WIND RAD2 observations of a DH type II burst starting at 06:42 UT at 3.2 MHz, and "w2" denotes a burst starting at 07:32 UT at 10 MHz. Triangle indicates the time of an $H\alpha$ filament eruption around 05:25 UT. The Yunnan observations were limited due to bad weather conditions, but there is some indication of another filament eruption near 06:26 UT. Black arrow shows the start times of two GOES flares at 06:04 and 06:54 UT, and dashed arrows show the times when EIT dimmings were observed (note that there were no available 195 Å EIT images near the start of the second flare, between 06:48 and 07:13 UT). The EIT field of view ends at height ≈ 1.3 R and the LASCO C2 field of view begins around 2.1 R, and thus there is a wide range of heights where imaging is not available. The flaring active region and the dimmed areas were located approximately at 0.4-0.6 R on the disk. This study found support that the cause of metric type II bursts, for two of the analysed three events, was flare-related.

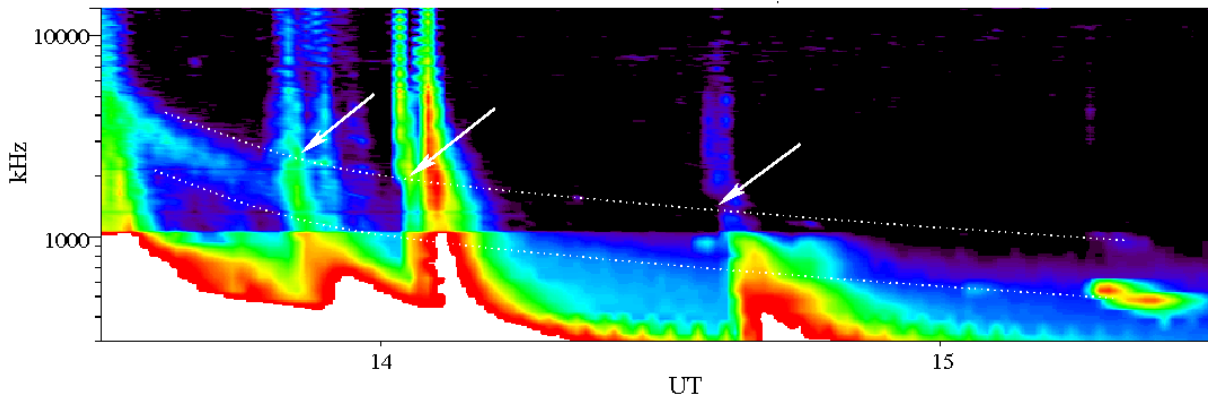


Figure 9.25: Shocks on the way: tilted type III burst lanes (Lehtinen et al., 2008).

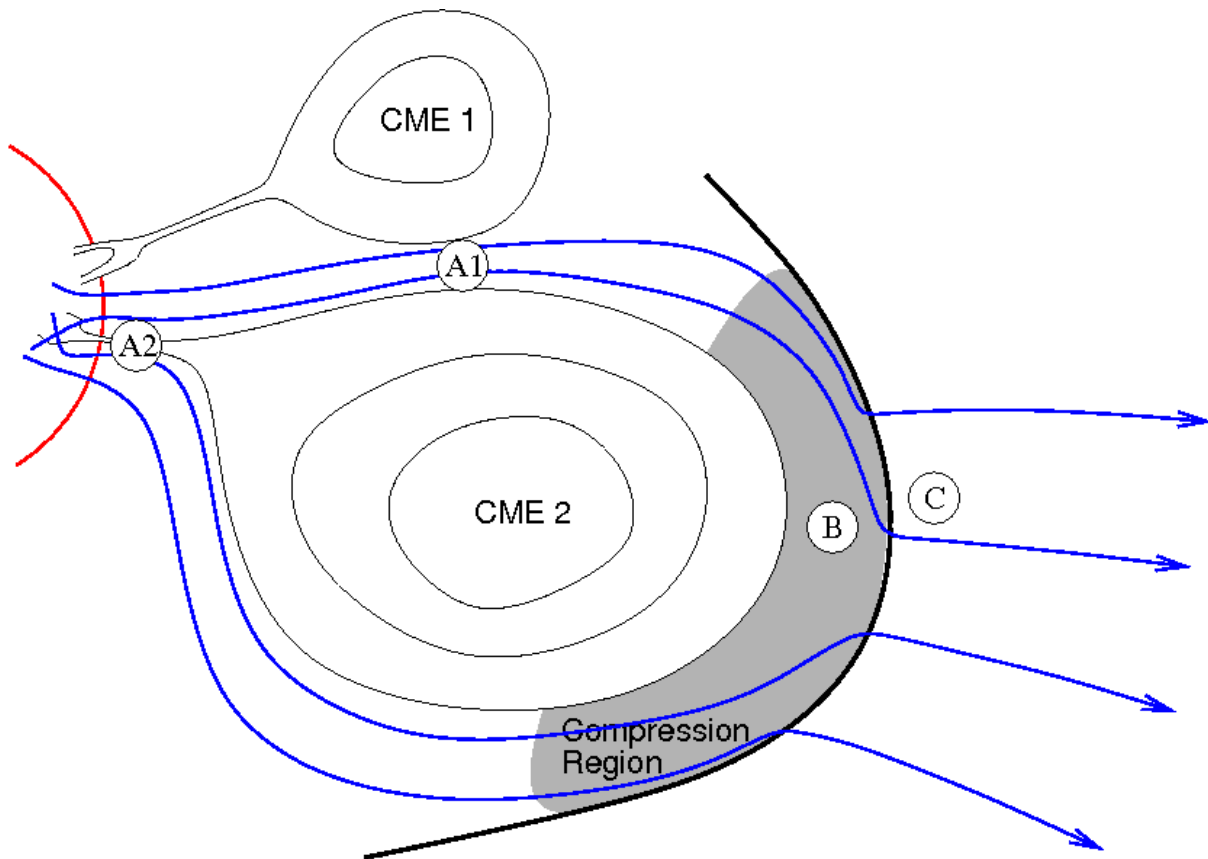


Figure 9.26: Tilts could be due to electron streams passing through shock fronts.

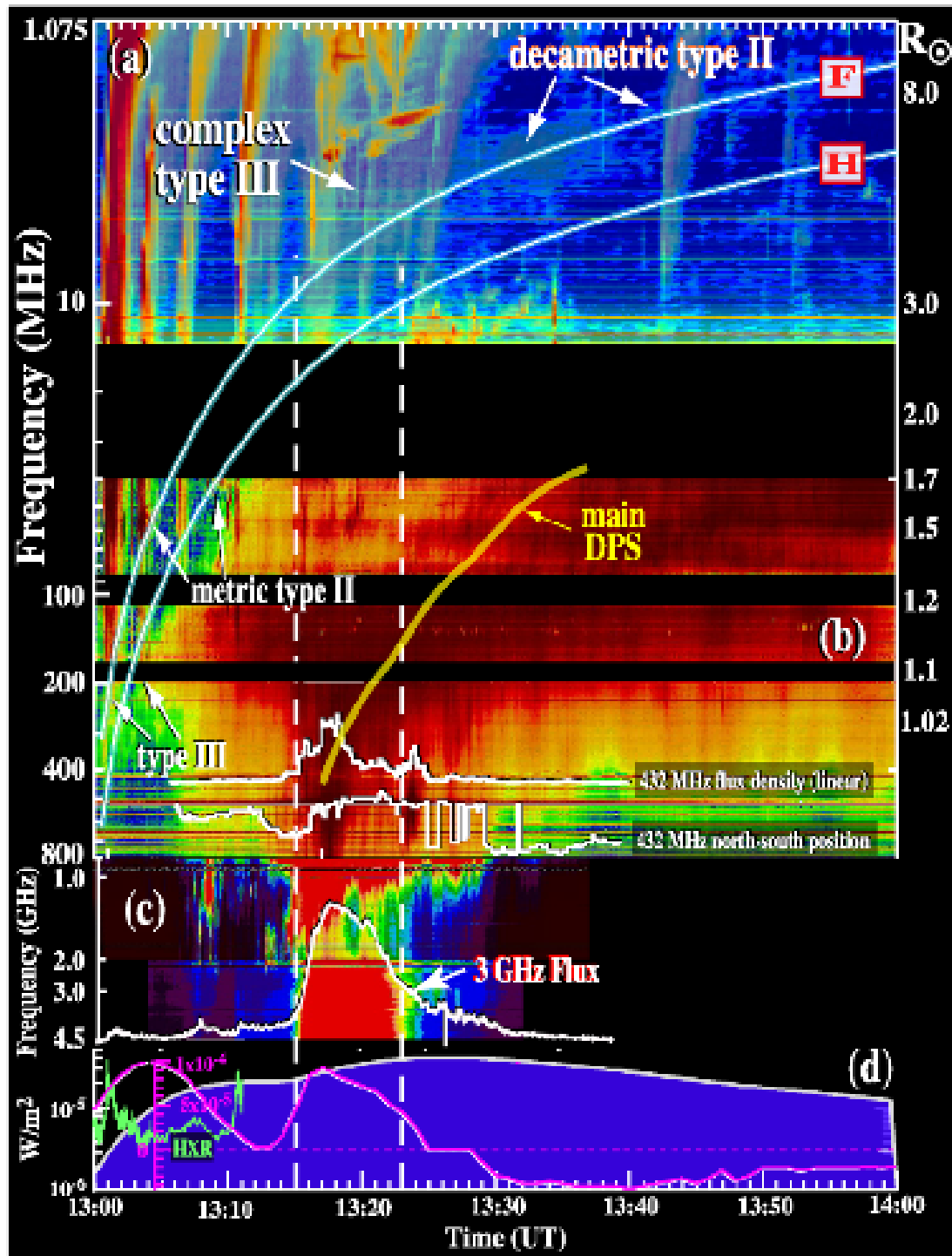


Figure 9.27: Reiner et al., 2008 (see also Hilary Cane and shock-accelerated 'SA-events')

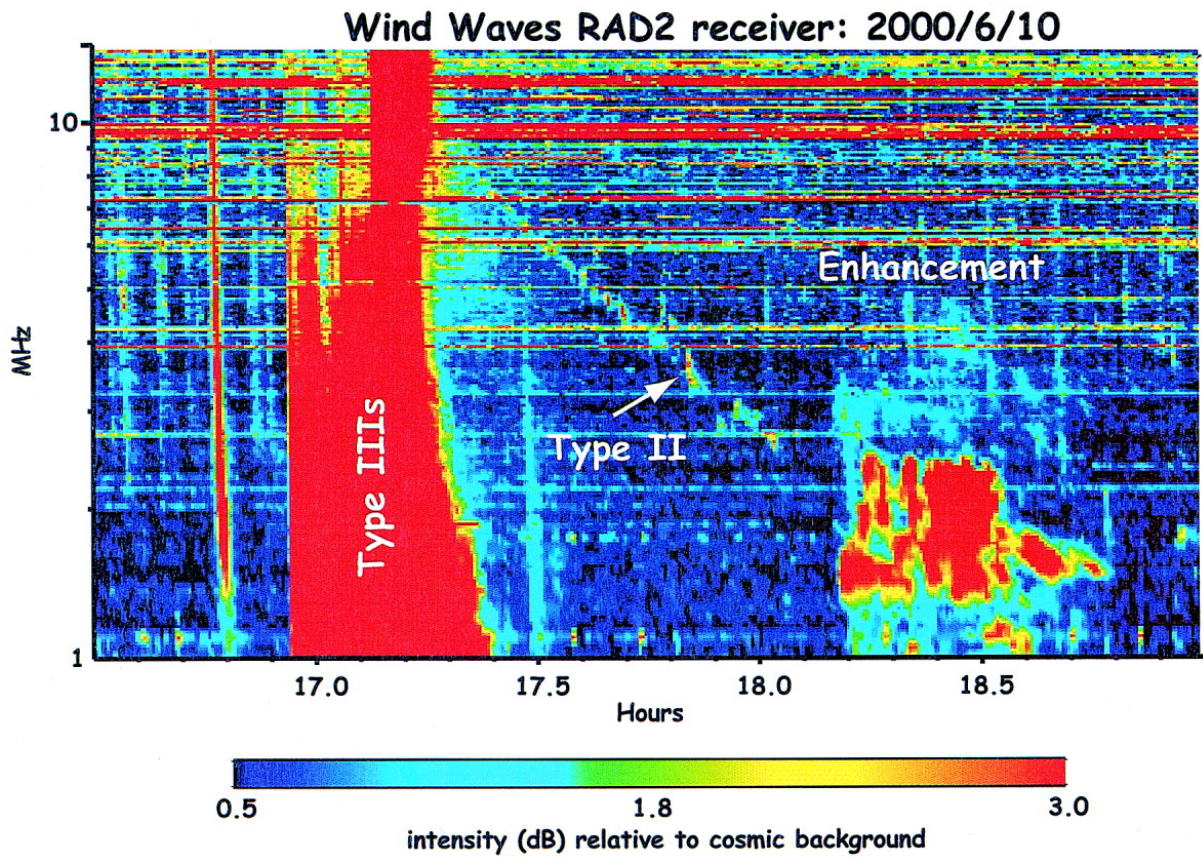


Figure 9.28: Radio features from interacting CMEs? (Gopalswamy et al. ApJ, 2001)

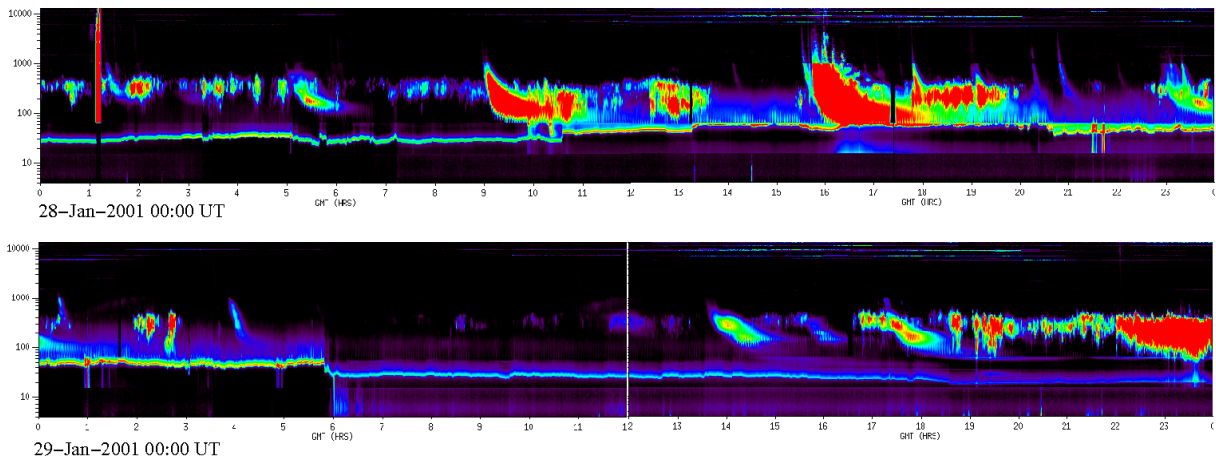


Figure 9.29: AKR - auroral kilometric radiation - appears usually at 80 – 400 kHz causing radiation episodes every 12 hours that affect observations of radio emission originating from the Sun.

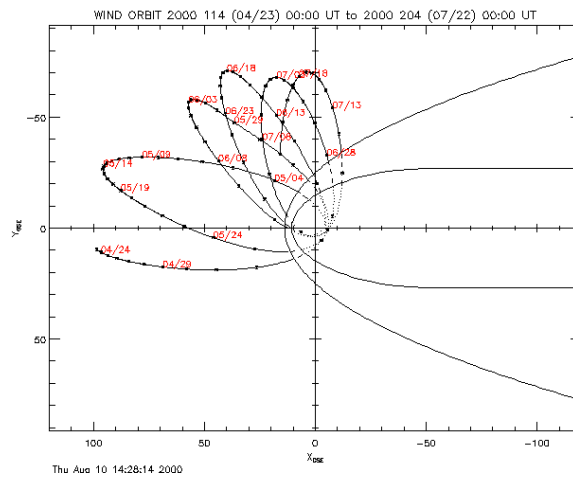


Figure 9.30: Wind WAVES orbit takes the satellite near Earth – and AKR gets more intense.

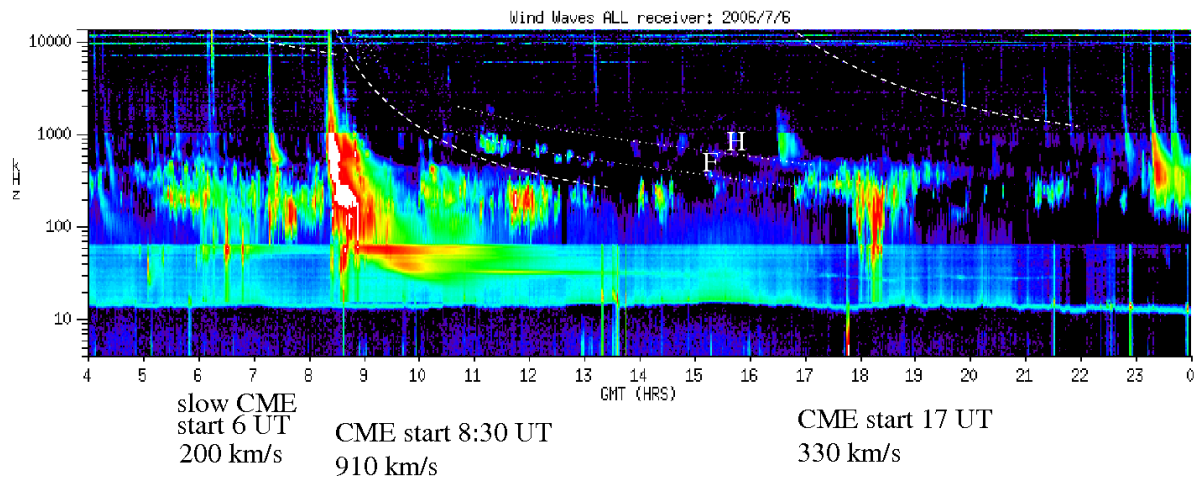


Figure 9.31: Radio emission in the IP space can consist of propagating CMEs, type II shocks, type III bursts, and AKR, all mixed together.

Statistics on CMEs, type IIs, and flares:

- 2/3 of metric type IIs are accompanied by fast CMEs
- 2/5 of CMEs are without metric type IIs
- 1/2 of CMEs without metric type IIs are fast CMEs (> 450 km/s)
- 90% of flares are without CMEs
- 60% of CMEs are without flares
- Energy released in a CME is larger than in a flare
- In 65% of CME–flare events the CME starts first

Chapter 10

Small and large scale solar features

10.1 Coronal holes

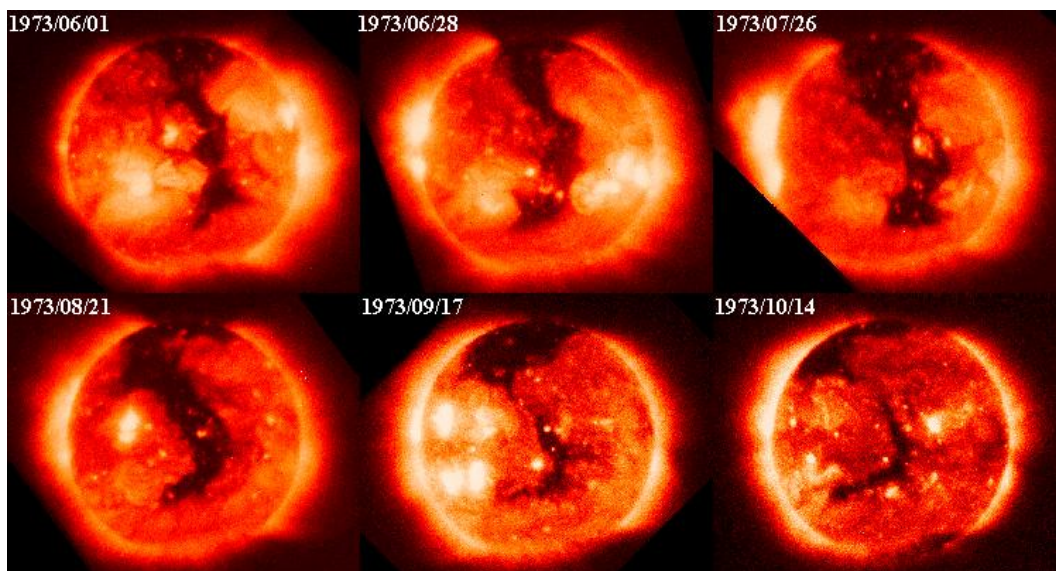


Figure 10.1: Skylab observations of a “boot of Italy” coronal hole. It survived over 4 months in 1973.

Definition of a coronal hole

- Brighter than the average solar surface at He I (10830 Å)
- Low contrast in cell structures
- Unipolar magnetic field
- High contrast at hole edges

+ particle density 2-3 times lower than in “quiet sun” regions.

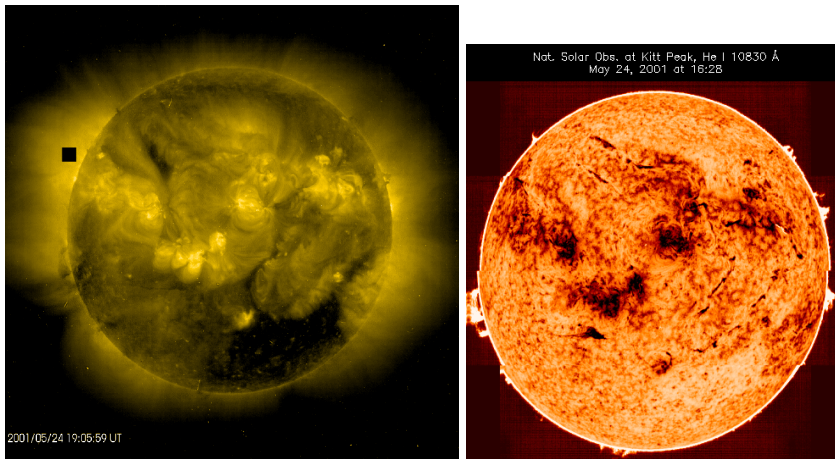


Figure 10.2: Left: EIT 284 Å (coronal hole visible as dark region). Right: Kitt Peak He I at 10830 Å (CH observed as bright).

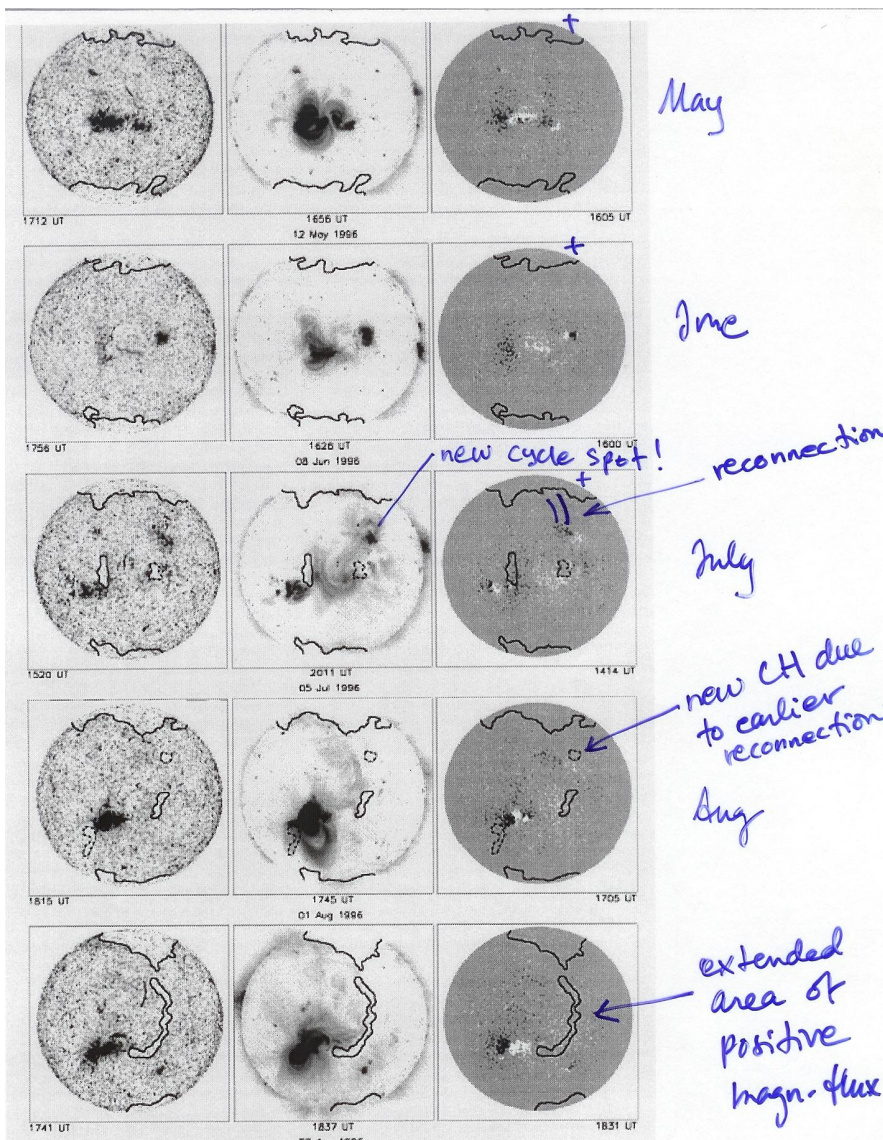


Figure 10.3: Harvey & Hudson (1998) explain CHs through emerging flux and reconnection. In this example, a new active region at $\sim N25$ and the positive polarity polar region get connected and 'open' a new small coronal hole.

10.2 Radio-bright coronal holes

Polar radio brightenings:

- Discovered in the 1970s with the Crimean Astrophysical Observatory 22-m radio telescope
- Polar regions were observed to be brighter than the quiet Sun at 15–48 GHz (at <15 GHz they were depressed)
- At 22 GHz enhancement is about 1500 K, at 37 GHz 800 K (observed with 1-2 arc min spatial resolution)
- later Nobeyama high-resolution radio images showed diffuse brightenings near the poles but also compact bright separate sources

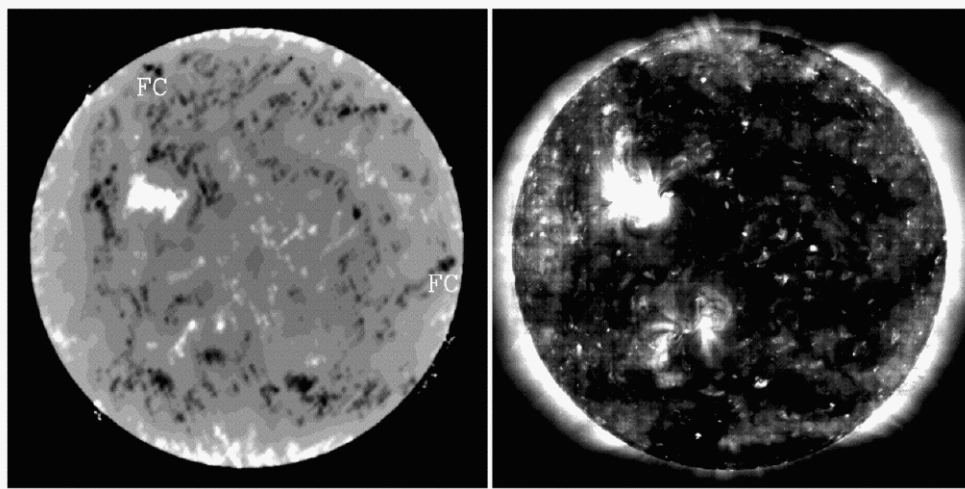


Figure 10.4: Polar radio brightenings: Nobeyama 17 GHz and EIT 195 Å observations of the Sun on 1997 March 11. The gray-scale range is chosen to emphasize the structure at the poles: in the 17 GHz image it ranges from 8000 K to 12,500 K in brightness temperature (Nindos et al., *ApJ* 527, 415-, 1999)

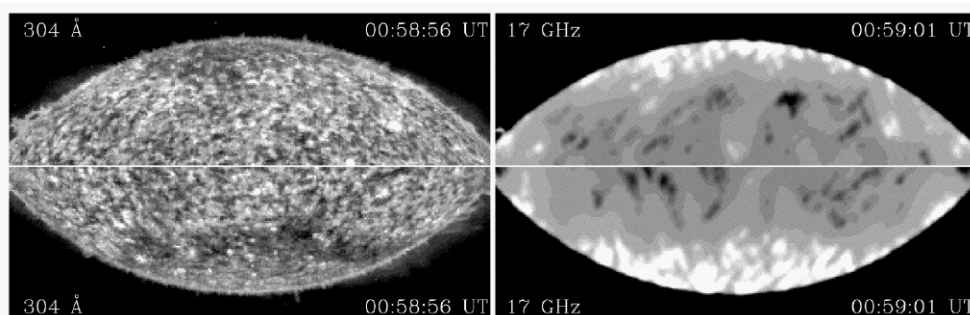


Figure 10.5: Polar radio brightenings: EIT images taken in the chromospheric line of He II at 304 Å on 1997 March 19 and the corresponding NRH 17 GHz maps. Top: north pole; bottom: south pole. The south pole 17 GHz emission is clearly more prominent (Nindos et al., *ApJ* 527, 415-, 1999)

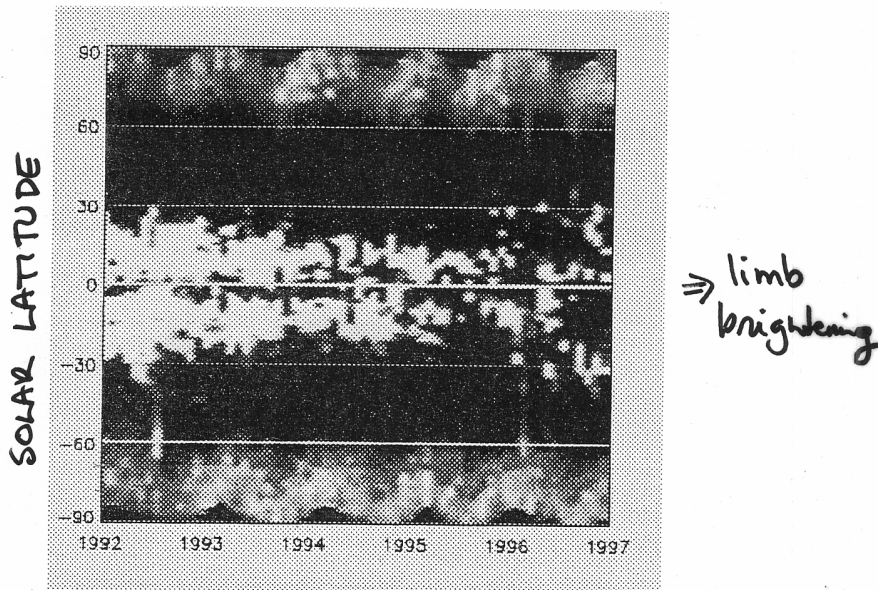
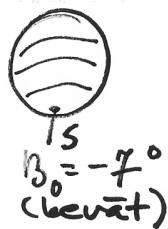
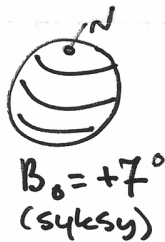


Figure 2. A radio butterfly diagram from July 1992 to July 1997



vuoden aikaan nähden
 B_0 -kulma muuttuu

Equatorial coronal hole brightenings (radioheliograph observations at 17 GHz):

- CHs are basically unipolar magnetic field regions
- Diffuse brightenings (+500 K) inside network cells
- Compact brightenings (+2000 K) at network cell boundaries
- Temporal changes

Problems in measuring radio bright regions:

- Interferometers: how to deconvolve faint sources
- Single dish telescopes: not enough spatial resolution + instrumental limb darkening
- Magnetograms: difficult to measure field strengths near poles
- EUV and optical: difficult to define plasma volume

Candidates for the radio enhancements: bright points, bases of plumes, coronal hole edges, network structures, etc.

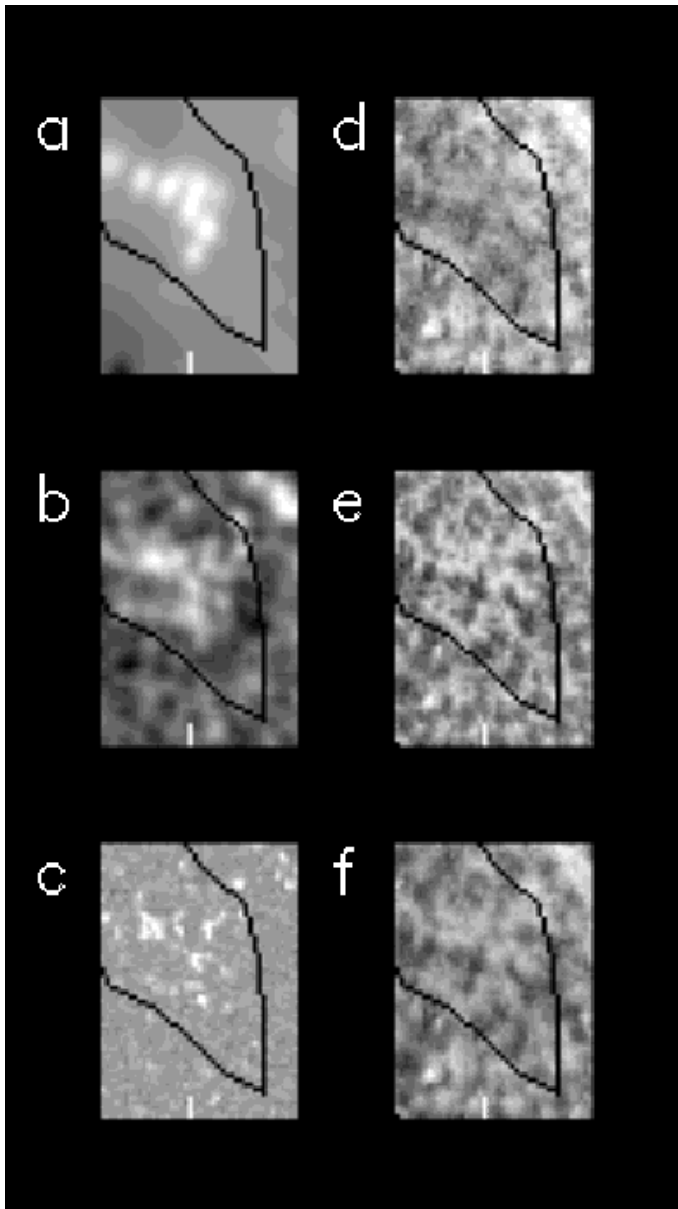


Figure 10.6: SUMER field of view subframes of the October 24, 1999 observations of an equatorial coronal hole (outlined with a black line). a) 17 GHz radio data, b) re-binned, smoothed $H\alpha$ image, c) magnetogram, and SUMER d) O I 948.7 Å, e) HI Ly4 949.7 Å, and f) He II 958.6 Å images. Radio brightenings seem to correspond best to $H\alpha$ structures (Moran et al., 2001).

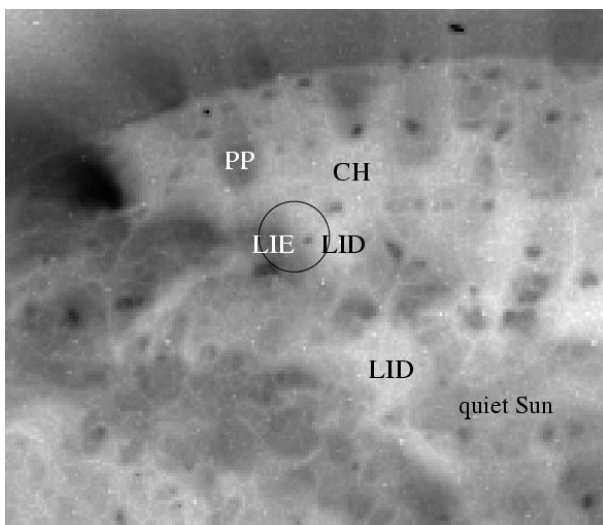


Figure 10.7: EIT map with radio beam size (circle), local intensity enhancement in EUV ('LIE') and local intensity decrease in EUV ('LID'). PP = polar plume and CH = coronal hole. It is evident that the radio flux within the beam is a convolution of several emission sources (Pohjolainen et al. 2000).

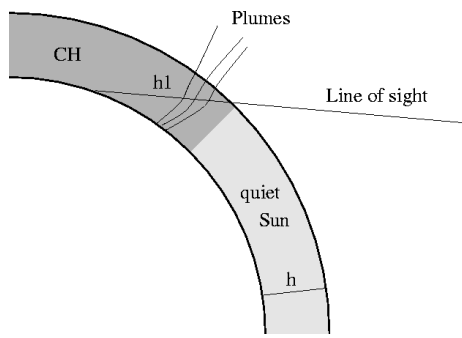


Figure 10.8: Geometry for observing the solar atmosphere at high latitudes: Polar coronal hole (CH) and the quiet Sun have scale height h and source length (radio path) $L =$ near the poles. If the same atmospheric layer is viewed near the center of the disk, the source length $L = h$. Note that L for polar plumes is not significant unless the plumes are seen along the line of sight (from the top).

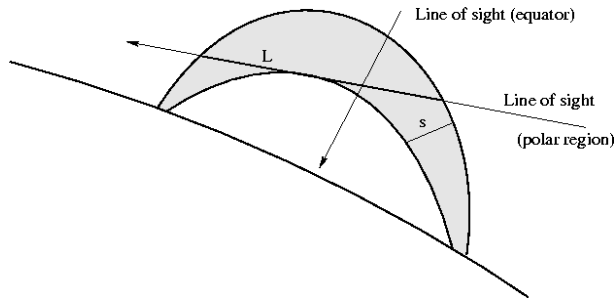


Figure 10.9: Observations of high latitude bright points with source length (radio path) L . If the loop (or a system of loops between two regions of opposite polarities) is viewed from the top (e.g., near the solar disk center), the source length L is equal to the loop diameter s .

10.3 Bright points

- Bipolar magnetic structures, size 10–50 arcsec
- Lifetime \sim 8 hours
- $T \sim$ 2 MK, density $\sim 2 \times 10^9 \text{ cm}^{-3}$
- Hot plasma in small-scale loops
- Flaring bright point \Rightarrow cancelling flux / rising flux / rotational shear (convective motion) or ...?
- Images needed with better spatial resolution

Example: Brightness temperature of a bright point

$$T_b = T_{eff} (1 - e^{-\tau})$$

$$\text{when } \tau \ll 1, T_b = T_{eff} \tau_\nu$$

$$\text{where } \tau_\nu = \kappa L \approx 0.01 L \frac{n_e^2}{\nu^2 T^{3/2}} \times (24.5 + \ln T - \ln \nu)$$

For a bright point,

$$s = 3500 \text{ km and } L = 10\,000 \text{ km}$$

$$T = 2 \times 10^6 \text{ K}$$

$$n_e = 1.5 \times 10^9 \text{ cm}^{-3}$$

and at $\nu = 87 \text{ GHz}$, the temperature enhancement on top of the quiet Sun emission would be $\Rightarrow T_b \sim +30 \text{ K}$

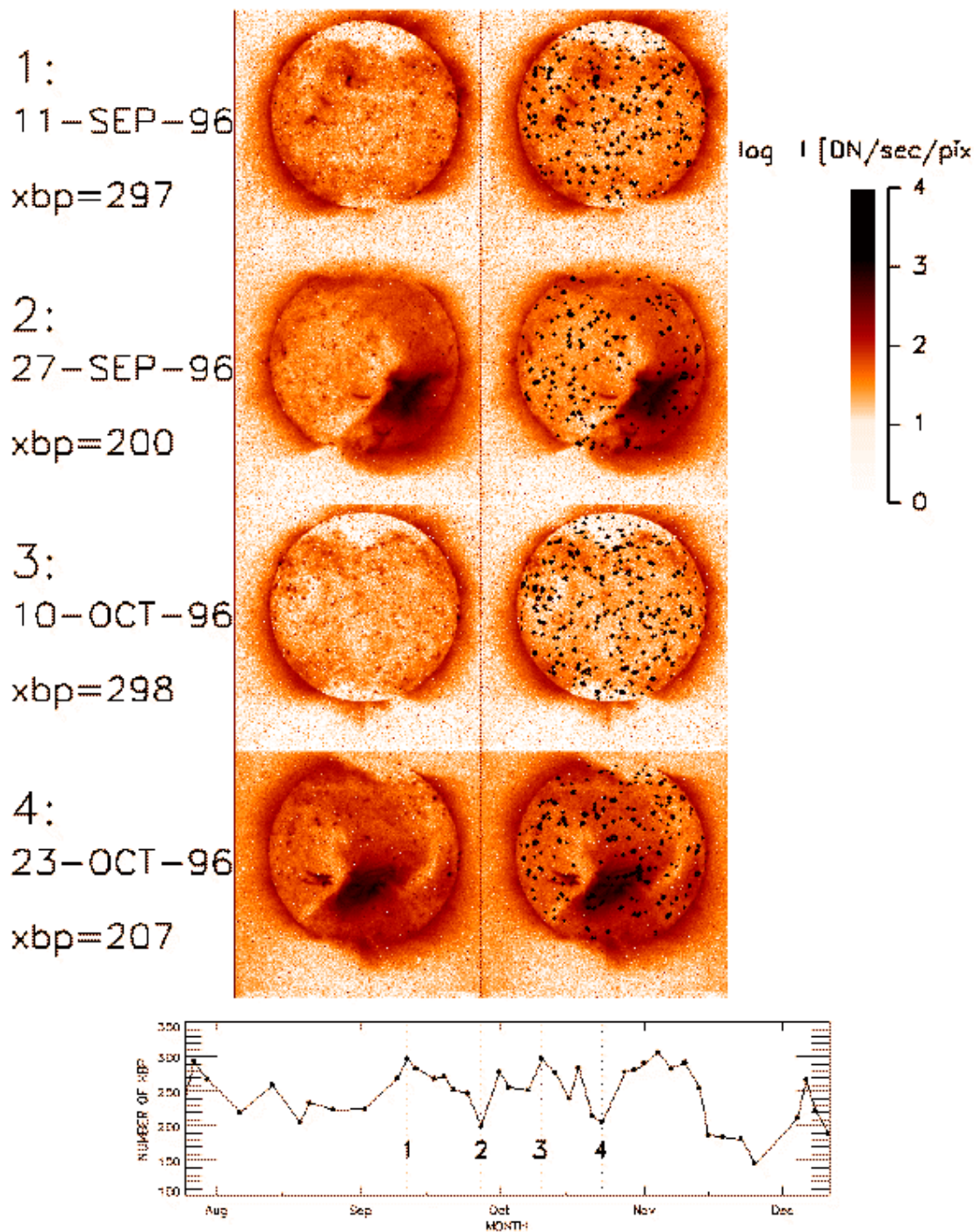


Figure 10.10: Bright points (observed number in soft X-rays, K. Nakakubo, NAOJ)

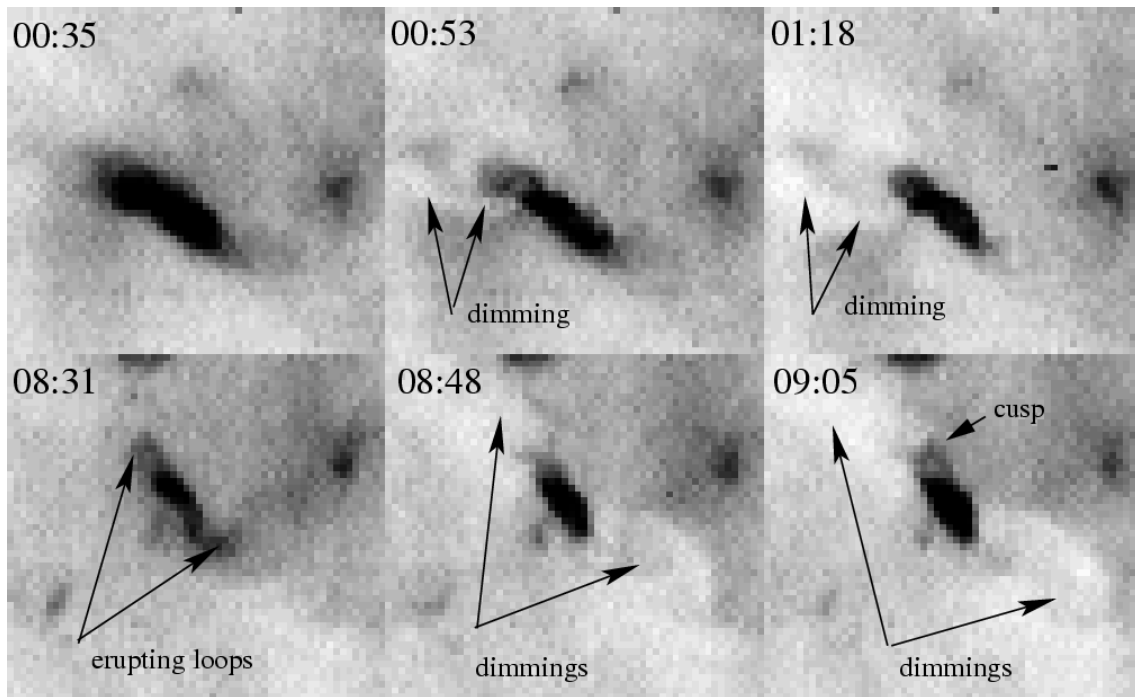
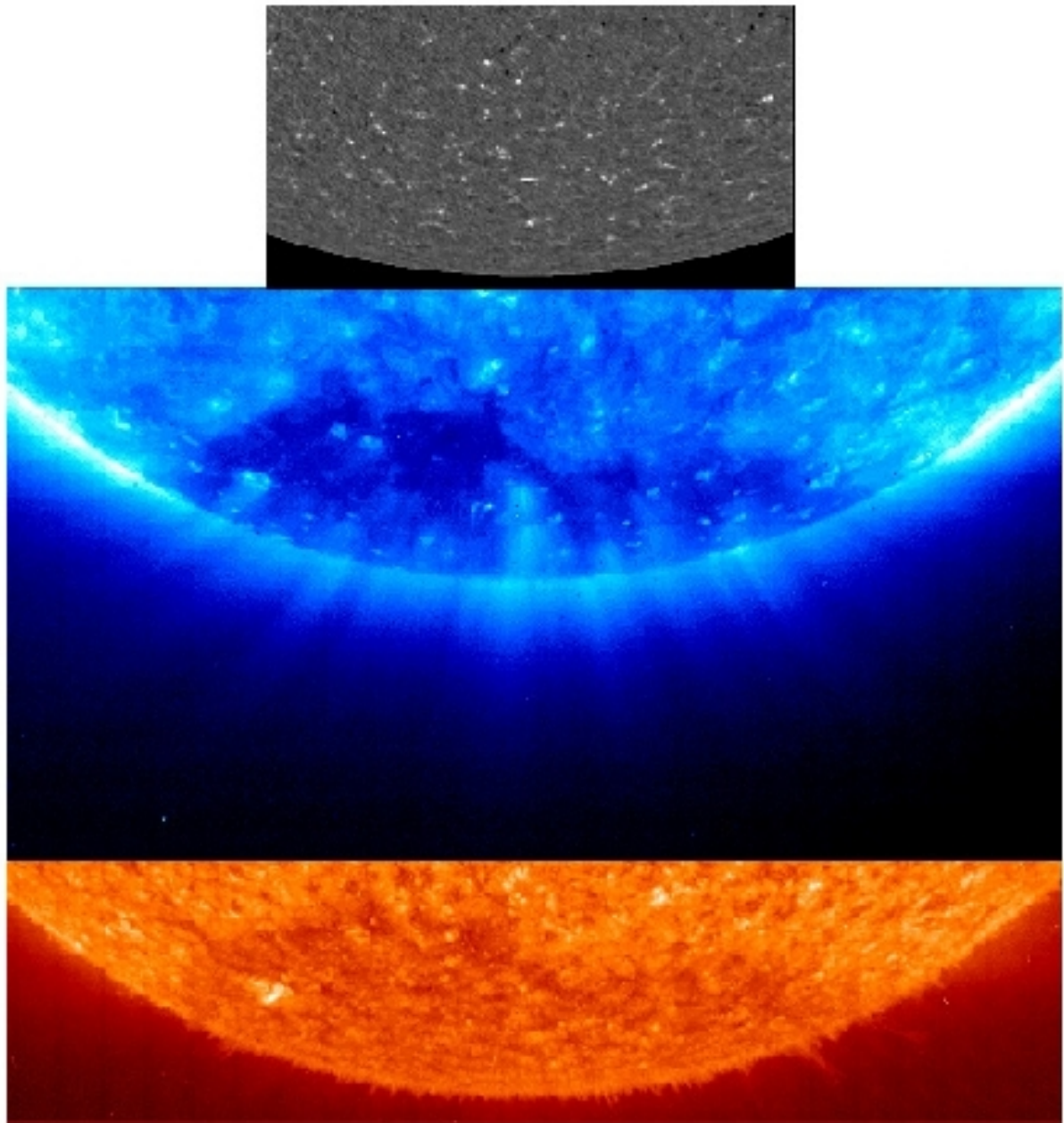


Figure 10.11: Bright points are sometimes 'mini active regions', that form S-shaped structures and erupt. This region showed even small-scale EIT dimmings. And surprisingly, the ejecta was identified near Earth, as coming from this region. Details can be found in the paper Mandrini et al., 2005: Interplanetary flux rope ejected from an X-ray bright point. The smallest magnetic cloud source-region ever observed.

10.4 Plumes

- Long, feathery jets with heights of about $30 R_{\odot}$
- In unipolar regions (CH), but formed when bipolar flux emerges ('base' ~ bright point)
⇒ small-scale reconnection driven by supergranular motion
- Dense: $3\text{--}5 \times$ interplume densities
- SOHO CDS: temperature along plume structure $\sim 1\text{MK}$, base at $\sim 2\text{MK}$
- Plume speeds $0\text{--}65\text{ km/s}$, interplume speeds $105\text{--}150\text{ km/s}$
- Oscillations of $20\text{--}25\text{ min}$ (slow magnetoacoustic waves?)
- Note that also fast solar wind is created in same CH regions



SOHO views of polar plumes
1996 March 7

Top to bottom:
MDI hi-res magnetogram
EIT Fe IX/X 171 Å image
EIT He II 304 Å image

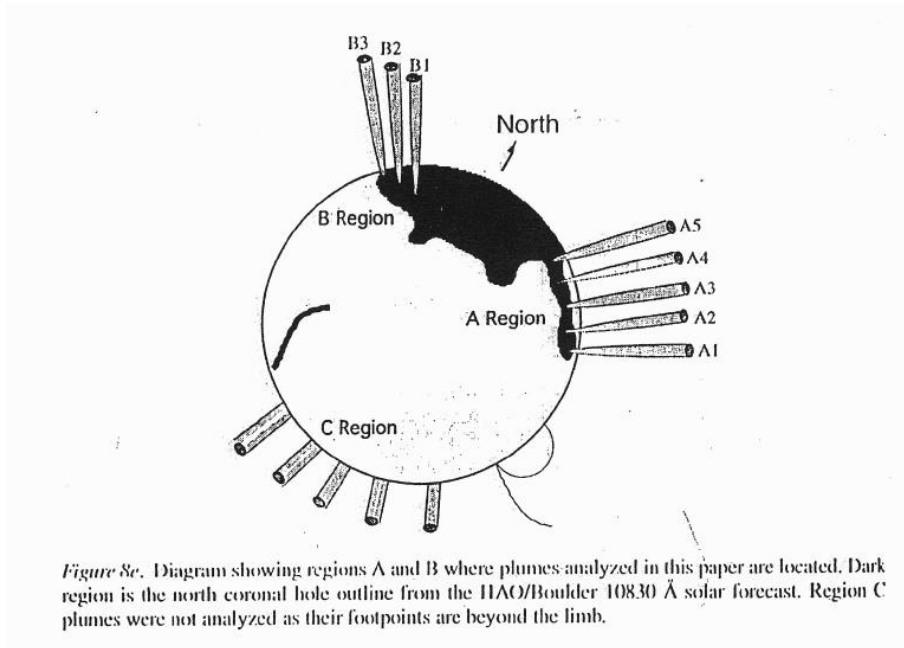


Figure 10.12: Allen & al. 1997, rocket experiments (still done, cheap and fast!)

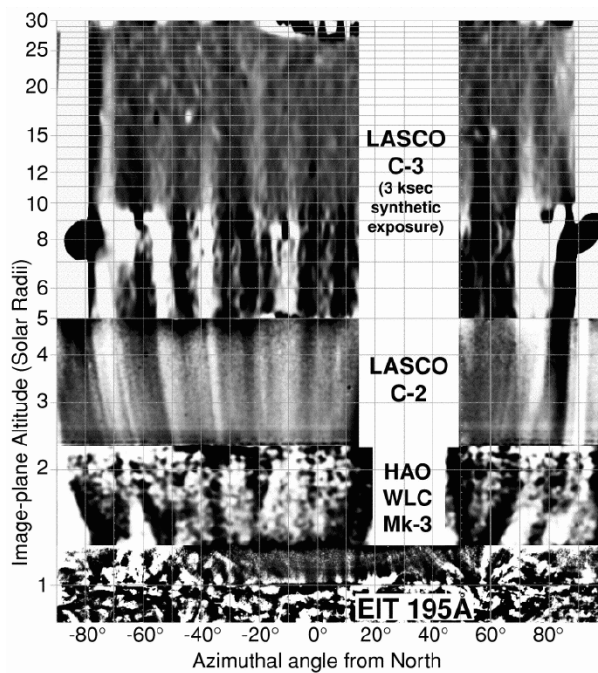
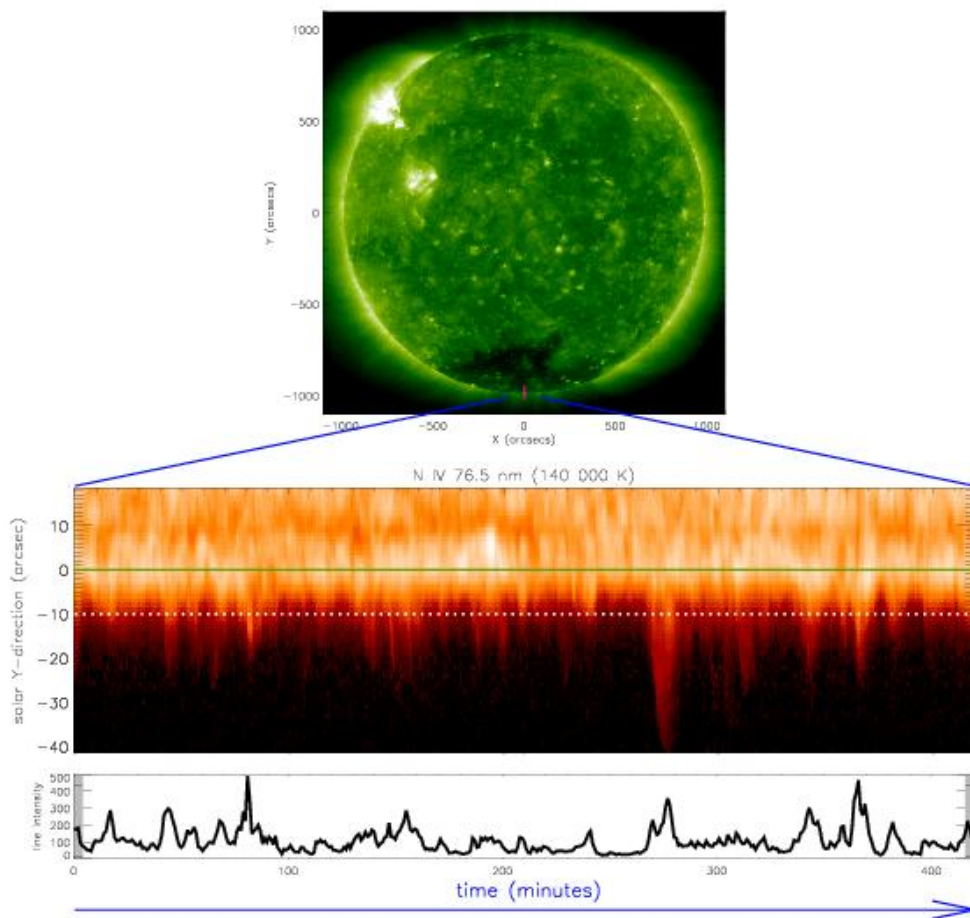


Figure 10.13: Polar plumes extending from the surface of the Sun out to $30 R_{sun}$ above the surface (in the image plane). Image is in conformal azimuthal coordinates. Vertical lines in image represent radial lines in normal space, and the radial direction is scaled logarithmically. Four instruments' data are presented. C-3, HAO K-Coronameter, and EIT images have been smoothed and detrended as described in text. C-2 image has been subjected only to radial filtering, to demonstrate by coalignment that the C-3 features are solar and not artificial. (DeForest et al, ApJ 546, 569-, 2001)

10.5 Spicules

- Fine, narrow jet-like structures near network boundaries, appear often in groups
- Heights 3000–9000 km (radio observations: ~7000 km)
- Speeds (Doppler) 10–30 km/s
- Lifetime ~ 10 min
- Unipolar magnetic field



10.6 Photospheric network

- Granules (1000–2000 km)
- Mesogranules (5000–10 000 km)
- Supergranules (20 000–30 000 km)

Granules are created by cellular convection but larger structures are due to granular movements. At bright centers the flow is up and at dark edges the flow is downward.

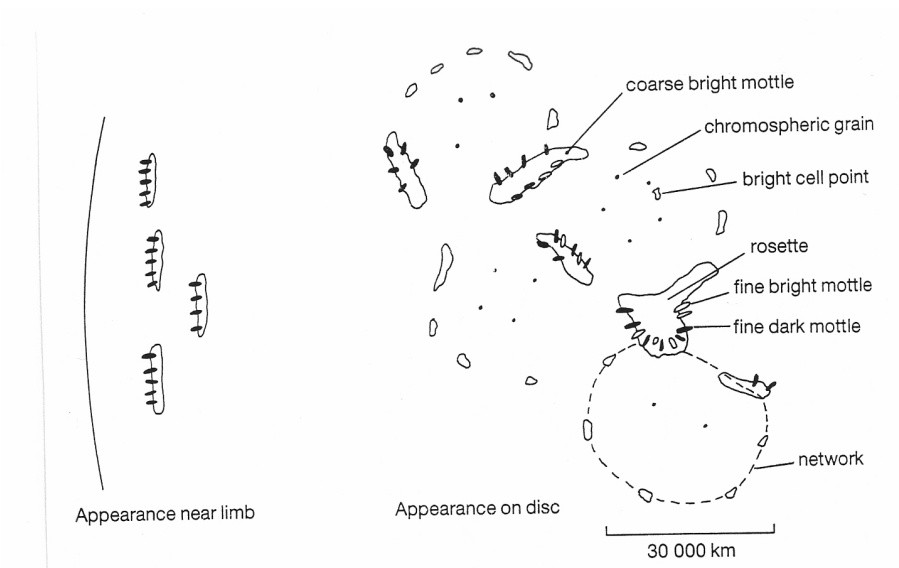
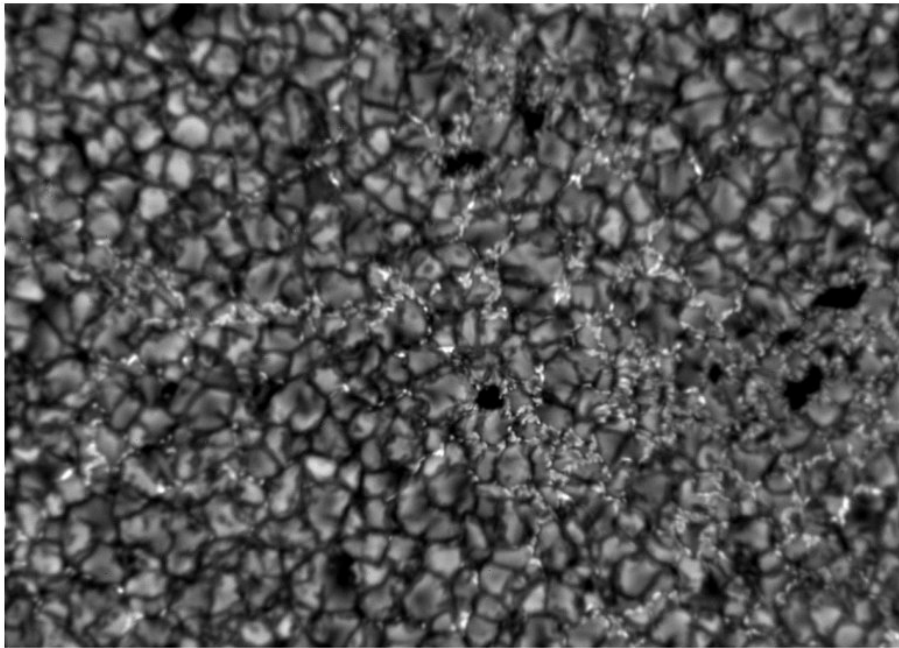


Fig. 4.8 Schematic diagram of quiet-sun chromospheric structures seen in $H\alpha$ and Ca II H and K line images. The coarse bright mottles outline the chromospheric network, and fine dark and bright mottles emanate from the coarse mottles. At the intersection of two or three network cells, the fine mottles form a rosette pattern. Chromospheric grains are small dark features within network cells visible in the violet wing of the $H\alpha$ line, while in Ca K bright cell points are small bright points that repeatedly brighten and fade. Near the limb the fine dark mottles seen in $H\alpha$ point towards the limb.

The chromosphere in profile

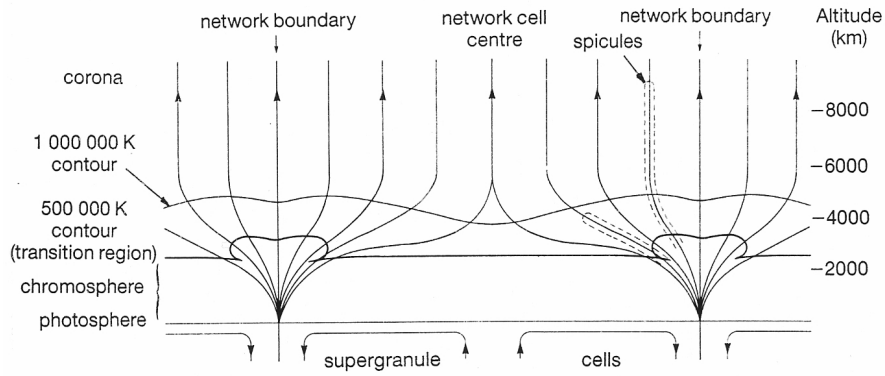


Fig. 4.2 Hypothetical section through chromosphere, showing the network structure and supergranules. Contours of temperature are shown for 500 000 K (taken to be the transition region) and for 1 000 000 K. The height scale on the right of the figure is only approximate. Spicules are represented by the dashed lines, the magnetic field lines by the arrowed lines: the field is swept horizontally towards the supergranule edges at low altitudes, but higher up the field lines spread out to form a canopy. (After Gabriel (1976))

Figure 10.14: (Plots from K.J.H. Phillips, Guide to the Sun, Cambridge Univ. Press)

10.7 Solar wind

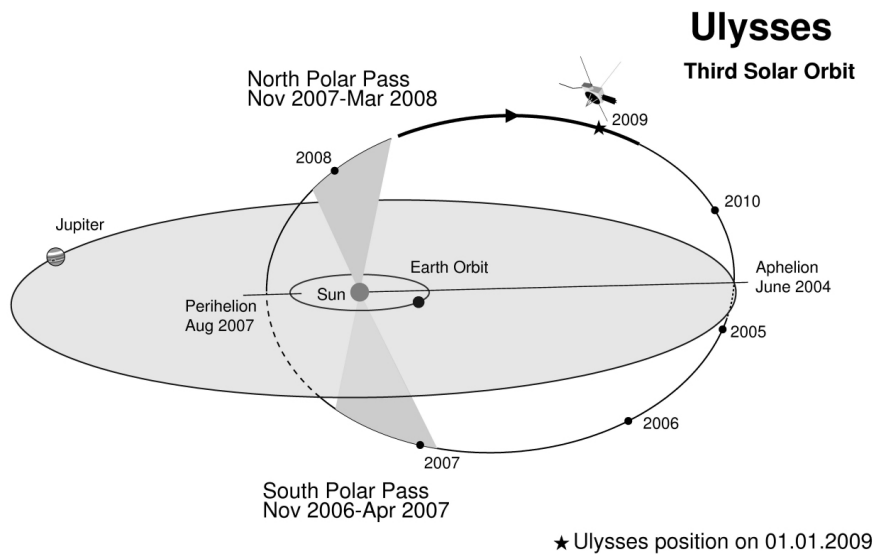


Figure 10.15: Ulysses spacecraft was launched in 1990. First south+north polar pass in 1994-95, second pass 2000-2001, third pass 2007-2008.

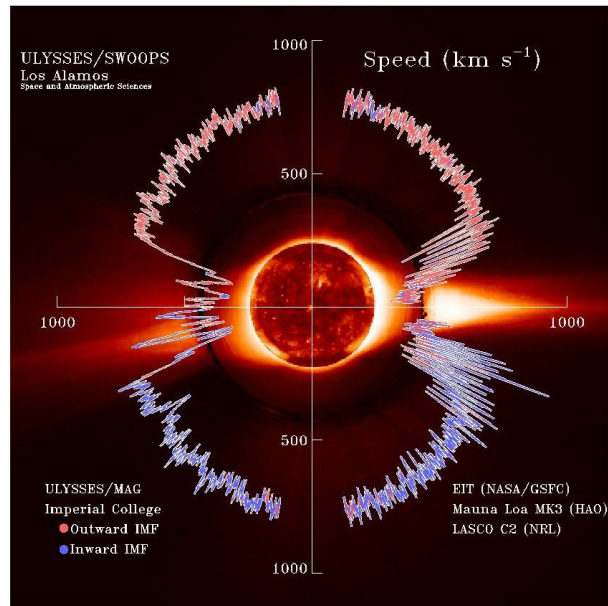


Figure 10.16: Solar wind speed (first solar pass)

Results from the first Ulysses bypass in 1994-95:

The solar wind is not uniform. Although it is always directed away from the Sun, it changes speed and carries with it magnetic clouds, interacting regions where high speed wind catches up with slow speed wind, and composition variations. The solar wind speed is high (800 km/s) over coronal holes and low (300 km/s) over streamers. These high and low speed streams interact with each other and alternately pass by the Earth as the Sun rotates. Many models of the solar magnetic field used prior to Ulysses assumed that the solar magnetic field was similar to that of a dipole; field lines near the solar equator were thought to form closed loops whereas field lines from the poles were dragged far into interplanetary space by the solar wind. For a dipole, the field strength over the poles is twice that at the equator. Ulysses found that the amount of outward magnetic flux in the solar wind did not vary greatly with latitude, indicating the importance of pressure forces near the sun for evenly distributing magnetic flux.

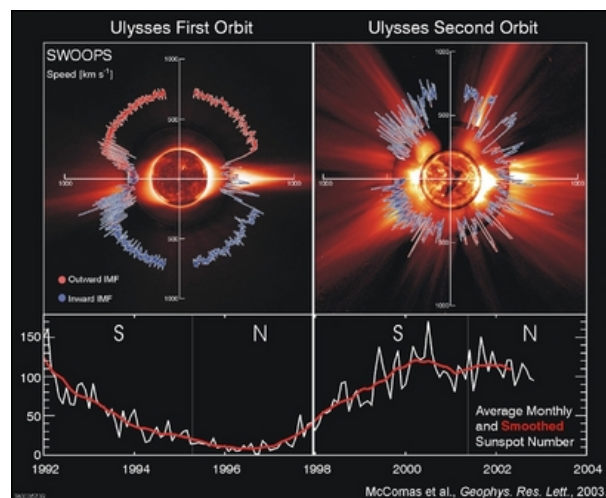


Figure 10.17: Solar wind speed during activity minimum (left, first pass) and during maximum activity (right, second pass).

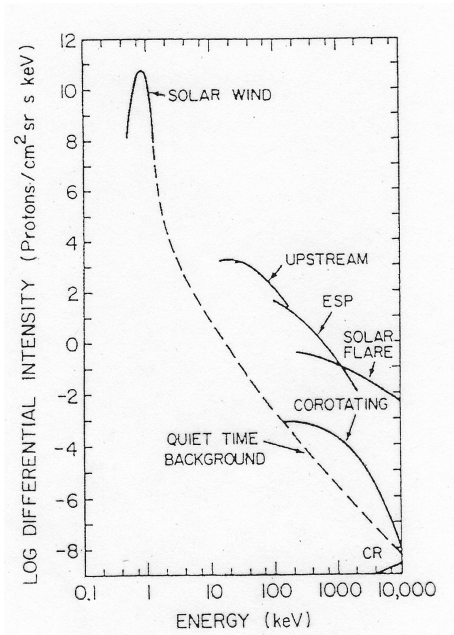


Figure 10.18: Energy spectra of different ion populations (Kallenrode, Space Physics). Particle loss due to solar wind is 1.3×10^{31} /s which is negligible when compared to the total solar mass.

10.8 Solar oscillations

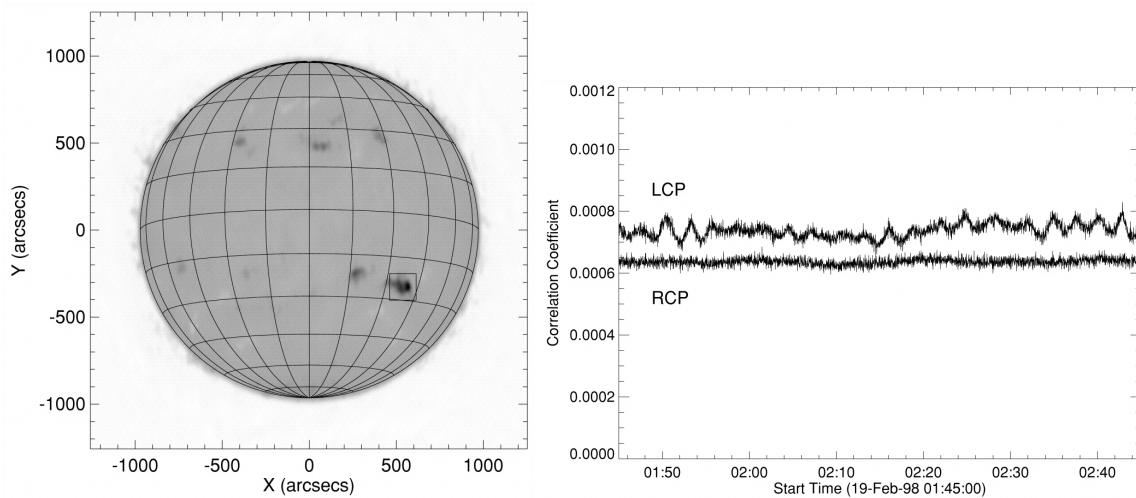


Figure 10.19: Full-disk intensity image of the Sun at 17 GHz (Nobeyama Radioheliograph). The active region is marked with a box. Correlation plot of 1 hour of observations for both RCP and LCP, showing that the emission was only left-hand polarized (Shibasaki, ApJ 550, 2001).

Gyrofrequency: $\nu_B \approx 2.8 \times 10^6 B$

If $B = 2000$ G, $\nu_B \approx 5.6$ GHz $\rightarrow 3^{rd}$ harmonic

The radio brightness temperature of an optically thin gyroresonance emission from the third harmonic layer is

$$T_b = T\tau \propto T^3 N$$

where T is the temperature and τ is the optical depth. The relative variation of the brightness temperature is then

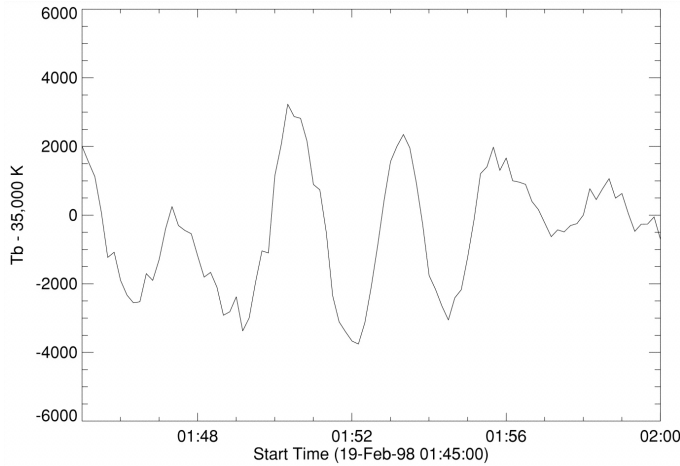


Figure 10.20: Time series of the peak brightness temperature during 15 minutes. The sunspot umbral oscillation was interpreted as density and temperature fluctuations due to upward-traveling acoustic waves through the third harmonic gyroresonance layer (2000 G).

$$\frac{\delta T_b}{T} = \frac{3\delta T}{T} + \frac{\delta N}{N}.$$

For an upward-travelling acoustic wave $\frac{\delta N}{N} = \frac{v}{c_s}$, where c_s is the sound speed, v is the oscillation velocity amplitude, and N and δN are the density and its oscillation amplitude. From SUMER observations in EUV, the density oscillations $\frac{\delta N}{N}$ are approximated to be around 0.05 and the temperature oscillations $\frac{\delta T}{T} = (5/3 - 1)\frac{v}{c_s}$ around 0.03. Therefore,

$$\frac{\delta T_b}{T} = \frac{3\delta T}{T} + \frac{\delta N}{N} = 3 \times 0.03 + 0.05 = 0.14$$

As observed at 17 GHz, the oscillation intensity was $\frac{3000K}{25000K} = 0.12$,

and therefore the 3-minute oscillation period could be due to acoustic waves in sunspot umbra (Shibasaki, 2001).

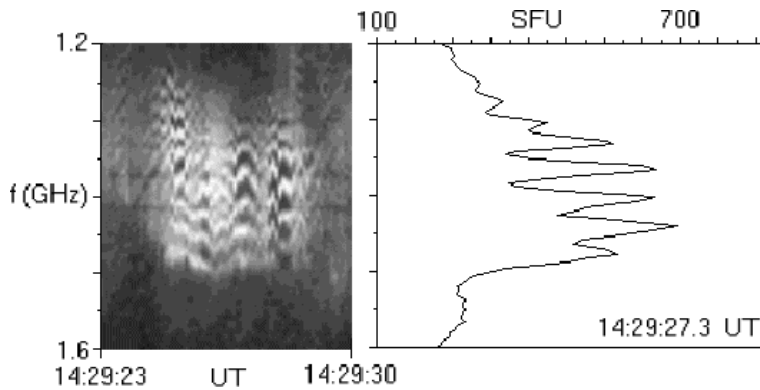


Figure 10.21: Example of an observed zebra-pattern, for which many alternative interpretations exist and this type of radio burst has already attracted attention for many years (Barta & Karlicky, A&A 450, 2006).

Solar radio pulsations show a large variety in their periods, bandwidths, amplitudes, temporal and spatial signatures. Most of them have been attributed to MHD oscillations in coronal loops, while alternative interpretations consider intrinsic oscillations of a nonlinear regime of kinetic plasma instabilities or modulation of the electron acceleration. In the umbral photosphere, oscillations with periods in the 5-minute range as well as in the 3-minute range occur. At chromospheric levels the intensity and velocity oscillations with periods of 150 – 200 s show larger amplitudes and are observed in the inner part of the umbra (Nindos & Aurass, Lecture Notes in Physics 725, 2007).

Microwave bursts often display quasi-periodic pulsations with periods from about 40 milli-sec in narrow-band bursts up to 20 sec in broad-band bursts (Nindos & Aurass). Causes of microwave flux pulsations with periods $P \approx 1 - 20$ s are believed to be some kind of magnetic field variations that modulate the efficiency of gyrosynchrotron radiation or electron acceleration itself. Pulsations with longer periods can be associated with the slow magnetoacoustic mode which propagates almost along the magnetic field (Nakariakov & Stepanov, Lecture Notes in Physics 725, 2007).

10.9 Atmospheric models and coronal heating

One-dimensional atmospheric models were first built based on UV/EUV observations (e.g., the VAL model by Vernazza, Avrett, and Loeser, 1981; the FAL model by Fontenla, Avrett, and Loeser, 1993). It was soon discovered that these models predicted much higher radio brightness temperatures than what were observed at microwaves.

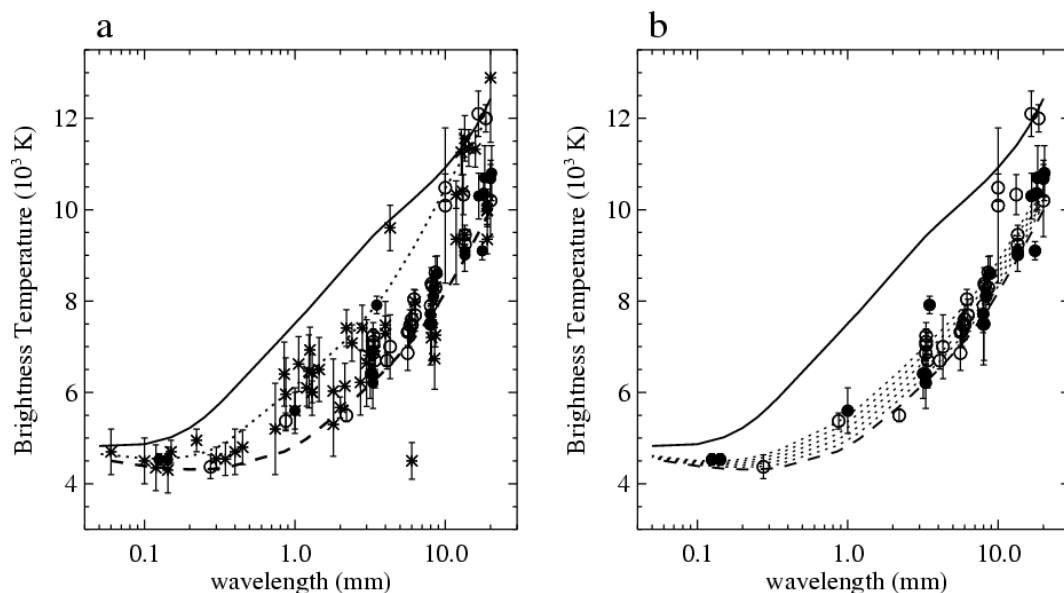


Figure 10.22: Observed brightness temperatures (circles and stars) and FAL models (dashed, dotted and solid curves), from Loukitcheva et al., A&A 419, 2004.

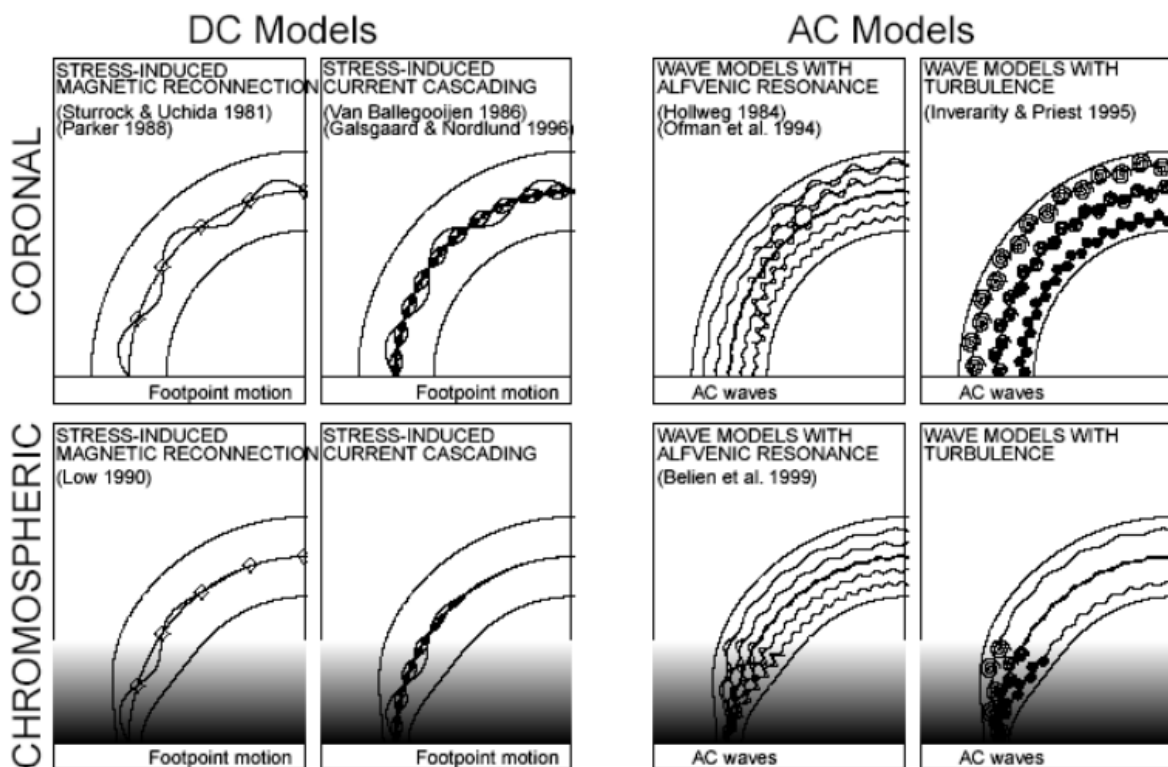
In 2003, Landi and Chiuderi Drago showed that a transition region model of the cell center, excluding any contribution from the magnetic network, can give an agreement with the observed radio brightness temperatures. The FAL models (a static atmosphere) and the dynamic simulations by Carlsson and Stein (1997 onwards) were compared with a large sample of radio observations in a study by Loukitcheva et al. (2004). The conclusion was that the dynamic picture of the solar internetwork chromosphere is consistent with the currently available millimeter and submillimeter brightness observations, although the chromospheric temperature rise is still absent in the simulations.

In other studies, a profound decrease in the computed temperatures have been obtained by assuming a tail of suprathermal electrons present in the solar atmosphere. Chiuderi and Chiuderi Drago (2004) modelled this with a two- component Maxwellian electron distribution and with a so-called kappa-function, and found both working.

Coronal heating

“There is no shortage of theoretical models that describe plasma-heating mechanisms that seem to be suitable for operating in the coronal environment (see discussion in Mandrini, Demoulin, & Klimchuk 2000), but the major dilemma is that either the theories are based on nonobservable parameters (e.g., currents, nonpotential magnetic energies, or coronal magnetic field) or the theoretical models have simply not been fitted to observed data. Another problem is that many theoretical models approximate a coronal loop with a straight cylindric tube, with a homogeneous density and magnetic field along the tube, while such an approximation is fully inadequate for large-scale loops observed in extreme ultraviolet (EUV), where the gravitational pressure scale height and heating scale height are much smaller than their half-length.” (From Aschwanden, *Astrophysical Journal*, 560, 1035, 2001)

- DC-models: energy source is magnetic, release happens by e.g. reconnection (flares, nano-flares, pico-flares, etc.). For DC currents the characteristic time is larger than the Alfvén transit time through the coronal magnetic structure.
- AC-models: energy source is convection or turbulence, transfer via MHD waves. AC coronal currents vary in a shorter time scale.



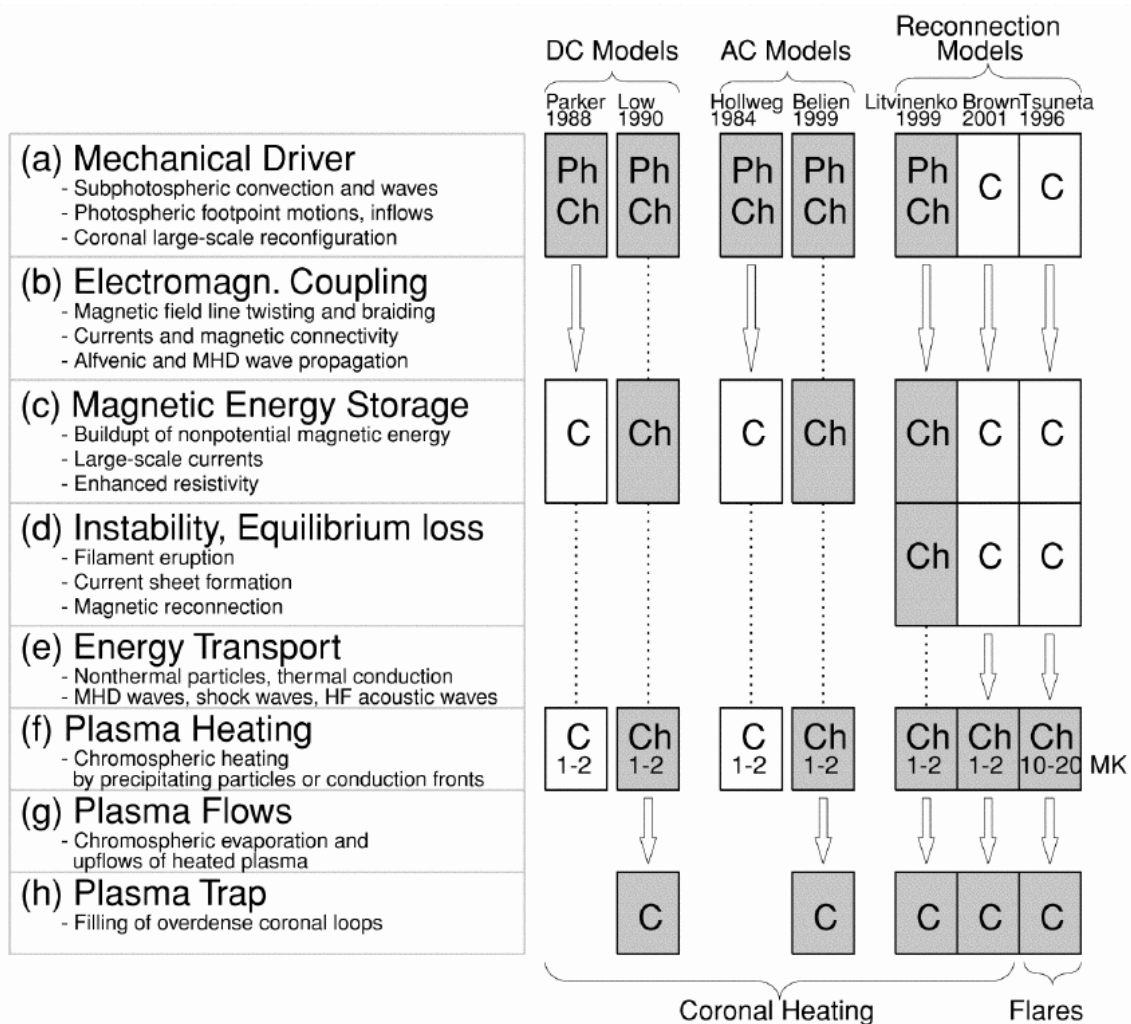


Figure 10.23: The eight main physical processes (ah) that occur in theoretical models of coronal heating are shown on the left side, and the corresponding flow charts of seven categories of theoretical models (with a reference to a typical representative listed at the top) are shown on the right side. Boxes mark the physical steps that are part of the models, arrows mark transport processes between different locations, and dotted lines mark cospatial locations. The boxes are colored in gray if the physical process takes place in a high-density region (photosphere, chromosphere, overdense coronal loops) and appear white for low-density regions (coronal background plasma). (Aschwanden ApJ 560, 1035-, 2001)

TABLE 1
CORONAL HEATING MODELS AND MATCHING OF OBSERVATIONAL CONSTRAINTS

Theoretical Model	Overdensity	Chromospheric Upflows	Heating Scale Height	References
Coronal DC Stressing				
Stress-induced reconnection				
Coronal	No	No	No	1, 2, 3, 4, 5, 6
Chromospheric	Yes	Yes	Yes	7
Stress-induced current cascade				
Coronal	No	No	No	8, 9, 10
Chromospheric	?	?	?	
Stress-induced turbulence				
Coronal	No	No	No	11, 12, 13, 14, 15, 16
Chromospheric	?	?	?	
Coronal AC Wave Models				
Alfvénic resonance				
Coronal	No	No	No	17, 18
Chromospheric	?	?	?	
Resonant absorption				
Coronal	No	No	No	19, 20, 21, 22, 23, 24, 25
Chromospheric	Yes	Yes	Yes	26
Phase mixing				
Coronal	No	No	No	27, 28, 29
Chromospheric	?	?	?	
Current layers				
Coronal	No	No	No	30
Chromospheric	?	?	?	
Turbulence				
Coronal	No	No	No	31
Chromospheric	?	?	?	
Magnetic Reconnection Models				
Dipolar				
Coronal	Yes	Yes	Yes	32
Chromospheric	Yes	Yes	Yes	33
Photospheric	Yes	Yes	Yes	34, 35, 36, 37, 38
Tripolar				
Coronal	Yes	Yes	Yes	
Chromospheric	Yes	Yes	Yes	39
Photospheric	Yes	Yes	Yes	
Quadrupolar				
Coronal	Yes	Yes	Yes	40
Chromospheric	Yes	Yes	Yes	
Photospheric	Yes	Yes	Yes	41

REFERENCES.—(1) Sturrock & Uchida 1981. (2) Berger 1991. (3) Parker 1988. (4) Berger 1993. (5) Galsgaard & Nordlund 1997. (6) Parker 1983. (7) Low 1990. (8) Van Ballegoijen 1986. (9) Hendrix et al. 1996. (10) Galsgaard & Nordlund 1996. (11) Einaudi et al. 1996. (12) Dmitruk & Gomez 1997. (13) Heyvaerts & Priest 1992. (14) Inverarity et al. 1995. (15) Inverarity & Priest 1995a. (16) Milano et al. 1997, 1999. (17) Hollweg 1984. (18) Litwin & Rosner 1998. (19) Ionson 1978, 1982, 1983. (20) Mok 1987. (21) Davila 1987. (22) Steinolfson & Davila 1993. (23) Ofman et al. 1994a, 1994b, 1995. (24) Halberstadt & Goedbloed 1995a, 1995b. (25) Ruderman et al. 1997. (26) Belien, Martens, & Keppens 1999. (27) Heyvaerts & Priest 1983. (28) De Moortel et al. 1999. (29) De Moortel, Hood, & Arber 2000. (30) Galsgaard & Nordlund 1996. (31) Inverarity & Priest 1995b. (32) Brown et al. 2000. (33) Litvinenko 1999. (34) Longcope & Kankelborg 1999. (35) Furusawa & Sakai 2000. (36) Sakai et al. 2000a, 2000b, 2001a, 2001b. (37) Tarbell et al. 1999. (38) Ryutova et al. 2001. (39) Chae et al. 1999. (40) Aly & Amari 1997. (41) Sturrock 1999.

Figure 10.24: Coronal Heating Models and Matching of Observational Constraints (Aschwanden, ApJ 560, 1035-, 2001)

Chapter 11

Solar Physics in the Future

11.1 Instrumentation

Earlier missions, data still used:

Yohkoh 1991-2001

BATSE etc. onboard Compton 1991-2000

Closing missions:

Wind 1994-

SOHO 1995-

TRACE 1998-

Current missions:

RHESSI 2002-

Hinode 2006-

STEREO 2007-

SDO 2010-

Future missions:

Solar Orbiter (ESA proposed mission finalist, to be launched around 2017)

Future ground-based solar radio imaging:

FASR (solar dedicated, USA) 50 MHz – 20 GHz

ALMA 84 – 720 GHz

LWA (Long Wavelength Array, USA) 10 – 90 MHz

LOFAR 30 – 240 MHz

MWA (Murchison Widefield Array, Australia) 80 – 300 MHz

Special need to maintain NoRH, NRH, OVRO, and other existing solar-dedicated facilities

11.2 Unsolved problems in solar physics

See Hardi Peter lecture notes at

<http://www.star.uclan.ac.uk/summerschool2010/peter.pdf>

11.3 Solar activity

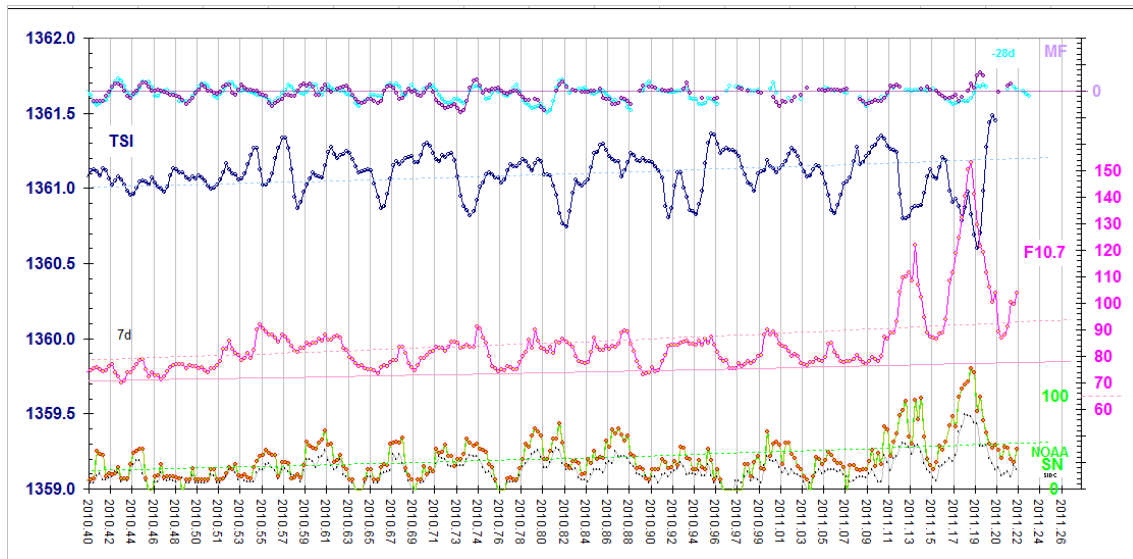


Figure 11.1: TSI = total solar irradiance, SSN = sunspot number, F10.7 daily 10-cm radio flux (from Leif Svalgaard's Research Page)

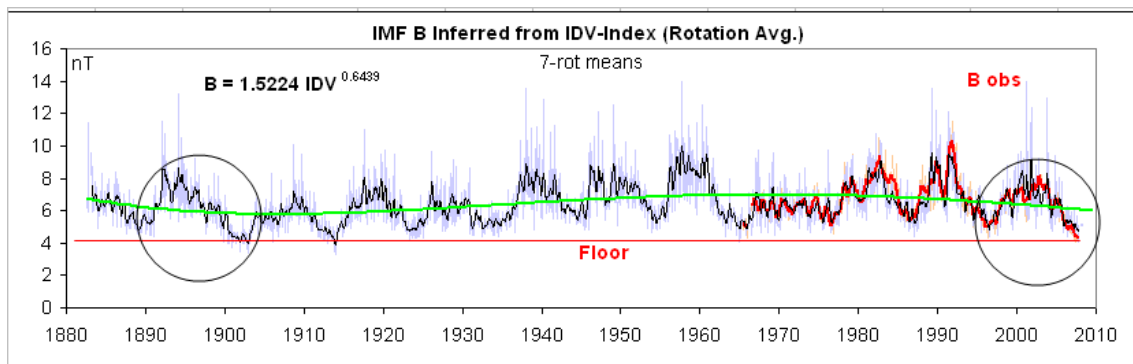


Figure 11.2: RHESSI Science Nugget number 99, see http://sprg.ssl.berkeley.edu/~tohban/wiki/index.php/RHESSI_Science_Nuggets

References and further reading

- Bastian T.S., Benz A.O., Gary D.E. 'Radio emission from solar flares', Annual Review of Astronomy and Astrophysics, 1998, 36, 131-188
- Benz A.O. 'Plasma Astrophysics (Kinetic processes in solar and stellar coronae)', Kluwer Academic Publishers, 1993
- Bruzek A. - Durrant C.J. 'Illustrated Glossary for Solar and Solar-Terrestrial Physics', Kluwer Academic Publishers, 2002
- Dulk G.A. 'Radio emission from the Sun and the stars', Annual Review of Astronomy and Astrophysics, 1985, 23, 169-224

- Foukal P.V. 'Solar Astrophysics', Wiley-VCH, 2004
- Gary D. 'PHYSICS 728, RADIO ASTRONOMY COURSE', <http://web.njit.edu/~gary/728/>
- Golub L.- Pasachoff J.M. (suom. T. Perhoniemi) 'Lähin tähtemme', Ursa 2004
- Harju J.-Juvela M.-Kontinen S.-Heikkilä A.-Wiik K. 'Johdatus radioastronomiaan', Helsingin yliopisto Observatorio, luentomoniste, 2001
- Hudson H., Ryan J. 'High-energy particles in solar flares', Annual Review of Astronomy and Astrophysics, 1995, 33, 239-282
- Kahler S.W. 'Solar flares and coronal mass ejections', Annual Review of Astronomy and Astrophysics, 1992, 30, 113-141
- Kallenrode M-B. 'Space Physics', Springer-Verlag, 1998
- Kitchin C.R. 'Astrophysical Techniques', Adam Hilger Ltd, 1991
- Kraus J.D. 'Radio Astronomy', Cygnus-Quasar Books, 1986
- Lehtinen N. 'Multiwavelength studies of solar eruptions' (PhD thesis), Annales Universitatis Tuekuensis AI 366, 2007
- Mursula K. 'Geokosmofysiikka', Oulun yliopisto luentomoniste, 1999, <http://spaceweb.oulu.fi/education/Geokosmofysiikka/>
- Phillips K.J.H. 'Guide to the Sun', Cambridge University Press, 1992
- Pohjolainen S. 'Energy release by solar flares: Observations at radio and X-ray wavelengths' (PhD thesis), Metsähovi Report 24, 1996
- Rohlfs K.-Wilson T.L. 'Tools of Radio Astronomy', Springer-Verlag, 1996
- Räisänen A.-Lehto A. 'Radiotekniikka', Otatieto 1993+
- Tayler R.J. 'The Sun as a Star', Cambridge University Press, 1997
- Vainio R. 'Astrophysical shock waves', lecture notes at website <http://vanha.physics.utu.fi/opiskelu/kurssit/XFY4410/>